THE UNIVERSITY *of* EDINBURGH

Next-generation Valve Actuation for Digital Displacement Machines

Andriy Tkachuk Volodymyrovych

A Thesis Submitted for the Degree of Doctor of Philosophy

The University of Edinburgh

2023

To my loving parents, Volodymyr and Valentina.

Abstract

A pump is the heart of a fluid-powered machine, which has a substantial impact on its efficiency. According to the state-of-the-art, the efficiency of a hydraulic excavator is about 16% due to a poor efficiency powertrain, combining a 40% efficient diesel engine and conventional hydraulic systems of between 30 and 40% efficiency. However, the efficiency of excavators can be significantly improved by using a Digital Displacement pump/motor (DDPM) instead of a conventional swash plate pump.

DDPM is a highly innovative hydraulic machine in which displacement and mode of operation are commanded by a dedicated computer by selective control of solenoid valves on a cycle-by-cycle basis. Optimal control of the valves is essential. This thesis is about the new solenoid valve actuation design development, aiming to extend the DDPM application by maximising the precision and efficiency of the valve control.

The development and testing of the new design of the coil driver for Digital Displacement (DD) valves are described. The new design of the coil driver is based on a combination of a new "smart" gate driver technology and pseudo-H-bridge topology. It was demonstrated that the new design benefits from a significant reduction of energy dissipation by implementing synchronous rectification during slow decay and energy regeneration at a fast decay mode of operation (up to 12.25%), improving reliability and fault tolerance by implementing fast overcurrent protection, the cost and footprint reduction (up to 40%).

Described the development, implementation, and testing of a method that allows for reliable detection of the low-pressure valve (LPV) reopening event, which applies to all existing designs of DD modules. It was demonstrated that the method enables the closed-loop motoring technique to apply to new DDPMs, which improves the safety and stability of operation of the DD machine and provides its auto-adjustment over the life span and self-calibration, which, in turn, allows for its mass production.

Development, implementation and testing of a new method to allow stabilisation of the response time of a cyclically operating solenoid valve at the turn-on phase were described. It was proven experimentally that the method enables precise control of the LPV closing angle within the established supply voltage and solenoid coil circuit resistance ranges, which improves the stability of operation and increases the displacement of the DDPM. Also, the implementation of the method cancels a need for the front-end DC-DC converter of the DD

controller, thus improving its efficiency, EMC performance, as well as reducing its cost and size.

Another new method to provide a sensorless diagnostic of the DD machine before its operation is described. The feasibility of the method was proven experimentally. Based on the method an algorithm that allows to determine the approximate level of the hydraulic fluid in the DD machine is proposed.

The test results from an electric powertrain demonstrator rig consisting of a DDPM DDP1X0, specifically designed for up to 30T excavators, powered by a high-efficiency Editron electric motor and controlled by the DDC15 controller based on the developed coil actuation design, are described and discussed. The test results demonstrate that the coil residual energy regenerating feature decreases the energy consumption of the DD controller by 10-11% at the pumping mode of operation. Up to 30% of displacement increment was demonstrated for the DDP1X0 by enabling the closed loop motoring mode of operation, which proportionally increases the developed torque, thus, leading to an increase in the regenerative efficiency of the DDPM. Also, it was proven that applying the valve response time stabilisation method allows for precise control of the DDPM displacement fraction at the static mode of operation.

Acknowledgements

I am thankful to my former and present colleagues from the Digital Displacement team to give me the opportunity to work on this project, be part of the research, and contribute to the development of such brilliant technology that is already changing the future of hydraulics. I am especially grateful to Dr Niall James Caldwell, Stewart Wilson, Stephen Liard, Dr Christian Norgaard, Mark Brett, Dominic Green, Peter McCurry, Daniil Dumnov, Vojtech Pavlis, and Mun Keong Chang for their support, guidance, and contribution.

Also, I am thankful to The University of Edinburgh for the academic support, especially to my academic supervisors: Dr Michael Merlin and Prof Stephen Finney, for their guidance and mentoring.

The financial support for this PhD project was provided by the Advanced Propulsion Centre (APC), which is a non-profit organization that funds the development of low-carbon emission powertrain technologies based in the UK.

Declaration

I certify that the work presented in this thesis, except where clearly credited to others, is of my own commitment, and that it has not been submitted for any other degree or professional qualification.

_____ _ A. Tkachuk Volodymyrovych

Contents

List of Acronyms

A

Alternating current
(AC) 114
American Wire Gauge
(AWG) 54
Analogue Digital Converter
(ADC) 24
Anti-aliasing filter
(AAF) 112
Artemis Modular Controller
(AMC) 20
Average
(AVG) 79

B

Bipolar junction transistor
(BJT) 42
Bottom dead centre
(BDC) 4
Bulk current injection
(BCI) 115

C

Carbon dioxide
(CO_2) 7
Centistokes, CGS unit for kinematic viscosity
(cSt) 185
Central processing unit
(CPU) 137
Charge pump undervoltage lockout
(CPUV) 28
Cross-section areas
(CSA) 130
Current Sense Amplifier
(CSA) 28
Current sense resistor
(CSR) 12

D

Digital Displacement Controller
(DDC) 3
Digital Displacement Controller, 15-channel
DDC15 193
Digital Displacement Pump/Motor
(DDPM) 2
Digital Displacement®
(DD) 1
Digital Pump Controller, 12-channel
(DPC12 MK1) 20
Direct Current
(DC) 190

E

Early design DD controller
(XPHS) 102
Electrical Fast Transient
(EFT) 76
Electrical/electronic sub-assemblies
(ESA) 79
Electromagnetic compatibility
(EMC) 76
Electromotive force
(EMF) 12
Electrostatic discharges
(ESD) 53

F

Fiberglass-reinforced epoxy-laminated sheets
(FR4) 59

G

H

I

L

M

N

O

P

Q

R

S

T

U

V

Chapter 1

Introduction

Artemis Intelligent Power Ltd (now Danfoss Scotland Ltd) has pioneered the development of Digital Displacement (DD) technology, which delivers a major improvement in the efficiency and controllability of fluid power machines and transmissions. The technology enables new applications such as hybrid vehicles and renewable energy. For instance, application of DD technology to all the world's excavators could save up to 40 MT of carbon dioxide per year [1].

These improvements are achieved by replacing the swash plate of conventional machines with digital control of each cylinder on a cycle-by-cycle basis using high-speed solenoid valves and allowing the DD device to operate as a pump or motor. Thus, the DD pump/motor allows not only to propel a fluid power machine but also to recover hydraulic energy by switching from pumping to the motoring mode of operation, which allows for fuel savings of more than 50% in diesel-powered excavators [2]. However, to achieve such efficiency, the precise control of the valves is crucial.

Artemis patented a technique for closed-loop calibration of DD motor [3] and demonstrated it for DD transmissions in large wind turbines (7 MW offshore wind turbine for Mitsubishi Power Systems Europe [4]).

Later Artemis developed a lower-cost, more compact solenoid valve design where only one shared coil is used for both low- and high-pressure valve actuation [5]. However, the existing closed-loop calibration techniques do not apply to this type of valves.

This project seeks to extend the closed-loop calibration technology of the DD motor to be applicable to the latest valve designs and to develop more advanced solenoid driver and valve control methods allowing improvement of the efficiency, reliability, and operational stability of the DD machine. The project embraces analogue and power electronic design, hardware and firmware design, synthesis, analysis, signal processing and real-time control.

1.1 Fundamentals of operation of Digital Displacement® Pump/Motor

The Digital Displacement Pump/Motor (DDPM) is a radial-type piston pump/motor of a positive displacement type, commutated by solenoid-actuated poppet valves on a stroke-by-stroke basis. A schematic diagram illustrating the basic concept of DDPM is shown in Figure 1.1. As can be seen, the cylinder of the DDPM is connected to the high- and low-pressure manifolds. The hydraulic fluid can be provided or absorbed from the high-pressure side; and from the low-pressure side, the manifold is connected to an atmospheric (or low-pressure fluid-boosted supply) tank [6].

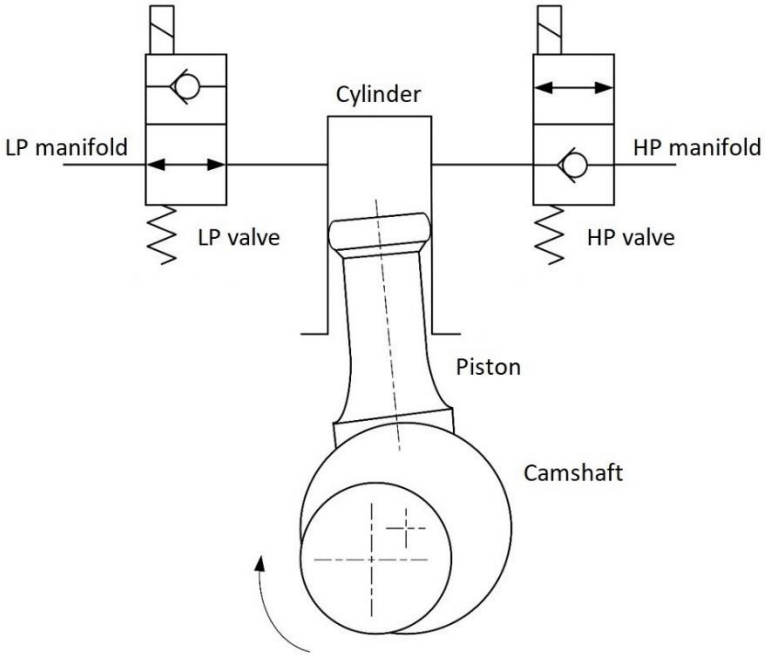

Figure 1.1. Schematic diagram of a single piston DDPM.

The new, more compact design Digital Displacement (DD) pumping/motoring modules (valves) have one shared coil for both the low-pressure valve (LPV) and the high-pressure valve (HPV). Figure 1.2 shows a schematic diagram of a single coil pumping/motoring DD module arrangement pointing to its principal components, taken from [5] and modified for easier interpretation.

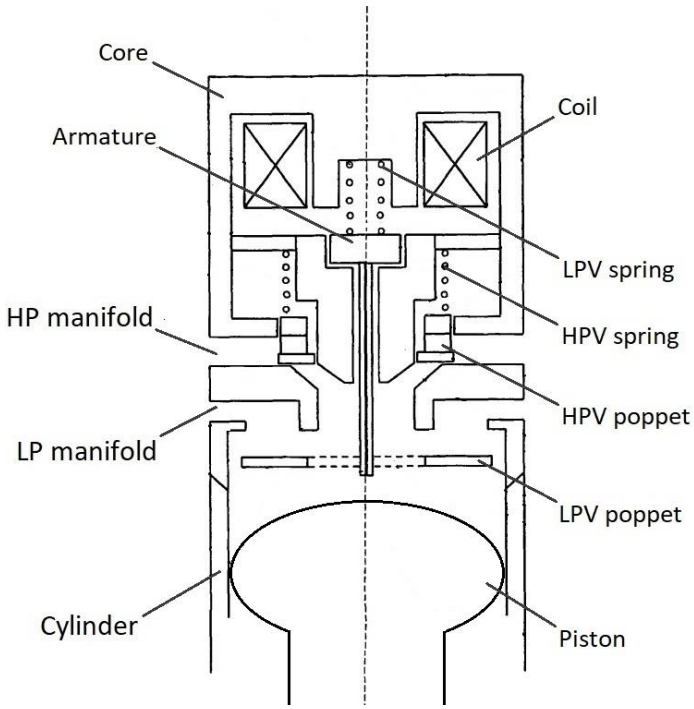

Figure 1.2. Schematic diagram of a single coil pumping/motoring DD module arrangement. [5].

A dedicated Digital Displacement Controller (DDC) actuates the valves on a stroke-by-stroke basis establishing a hydraulic connection between the moving piston and the appropriate manifold and determines the DD module configuration for pumping, motoring, or an idling mode of operation by modulation of the timing of commutating valve actuation.

Figure 1.3 shows schematic diagrams of the operation modes ((a) idling mode, (c) pumping mode, (d) motoring mode) of a pumping/motoring DD module including its transition state (b), which takes place when the DD module is changing the mode of operation at the energising stage. In the figure, the orange (dotted) line indicates the magnetic flux path at each state/mode of operation of the DD module, the blue line indicates the hydraulic oil flow direction, and the red line shows the piston motion direction.

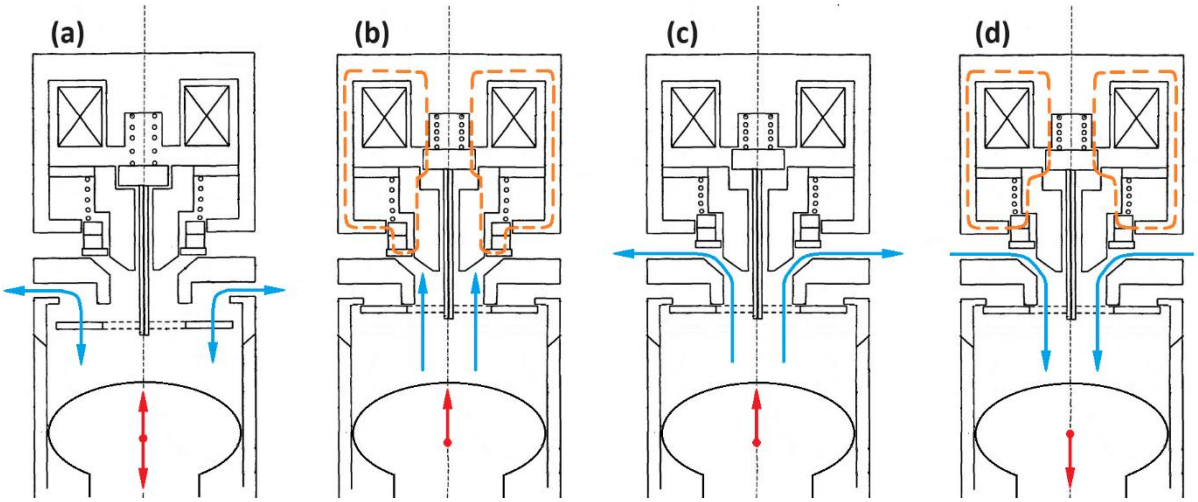

Figure 1.3. Schematic diagrams of the operation modes and the transition state of a pumping/motoring DD module. a) idling mode, b) transition state, c) pumping mode, d) motoring mode. (Orange (dotted) – magnetic flux path. Blue – oil flow direction. Red – piston motion direction.)

The LPV is a normally-open valve, and the HPV is a normally-closed valve. Thus, both valves must be de-energised to set the DD module in the idling mode of operation (Figure 1.3 (a)). During an idling cycle, the working chamber of the DD module is isolated from the high-pressure side, which keeps the working chamber mechanism unloaded, not causing any volumetric loss or pressure-related mechanical losses [6].

To start a pumping cycle, the controller closes the LPV just after the intake stroke when the piston is at the bottom dead centre (BDC) to provide the maximum displacement. When the piston initiates its motion towards the top dead centre (TDC) (Figure 1.3 (b)), the pressure in the working chamber starts to increase, reaching and exceeding the level of the high-pressure side and opening the high-pressure valve. Thus, connecting the working chamber with the high-pressure manifold during the next half-revolution of the shaft (Figure 1.3 (c)). At this point, the solenoid coil of the DD module can be de-energised since the LPV is held closed and the HPV held open by the pressure acting on the poppets, which is created by the fluid flow from the working chamber to the high-pressure manifold. When the piston reaches the TDC and starts moving towards the BDC, the working chamber will be de-pressurised, and both poppets will be returned to their initial position by means of the return springs, thus ending the pumping cycle. Figure 1.4 shows a schematic diagram that represents an ideal pumping cycle.

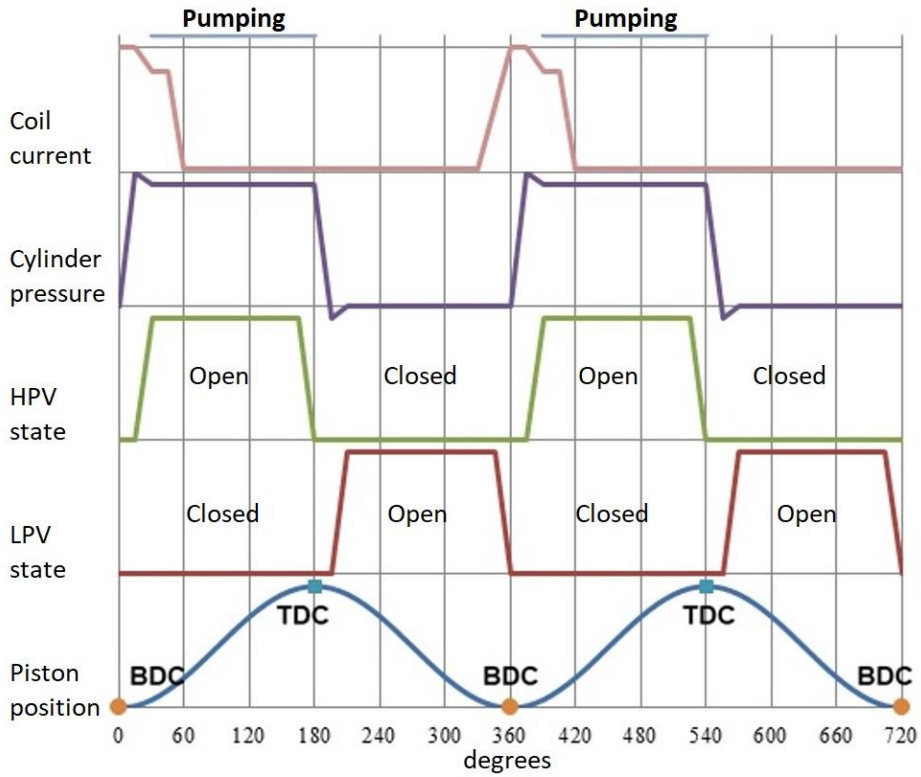

Figure 1.4. Schematic diagram to represent an ideal pumping cycle.

To begin a motoring cycle the controller energies the coil to close the LPV before the TDC. When LPV is closed (Figure 1.3 (b)), the pressure of the working chamber starts to increase, reaching and exceeding the level of the high-pressure side and opening the high-pressure valve just before the piston reaches the TDC. At this time, the magnetic flux changes its path latching the HPV poppet (Figure 1.3 (d)) since the latching path is shorter, i.e. its reluctance is lower. The controller decreases the coil current down to the value, which is enough to hold both valves activated. The hydraulic connection between the high-pressure side and the working chamber is established for the next half-revolution of the shaft. To end the motoring cycle, the controller de-energises the coil. When the solenoid magnetic force decays below the return spring force, the HPV closes, and the LPV reopens, the hydraulic fluid will be returned to the low-pressure tank over the next half-rotation of the shaft. Figure 1.5 shows a schematic diagram that represents an ideal motoring cycle.

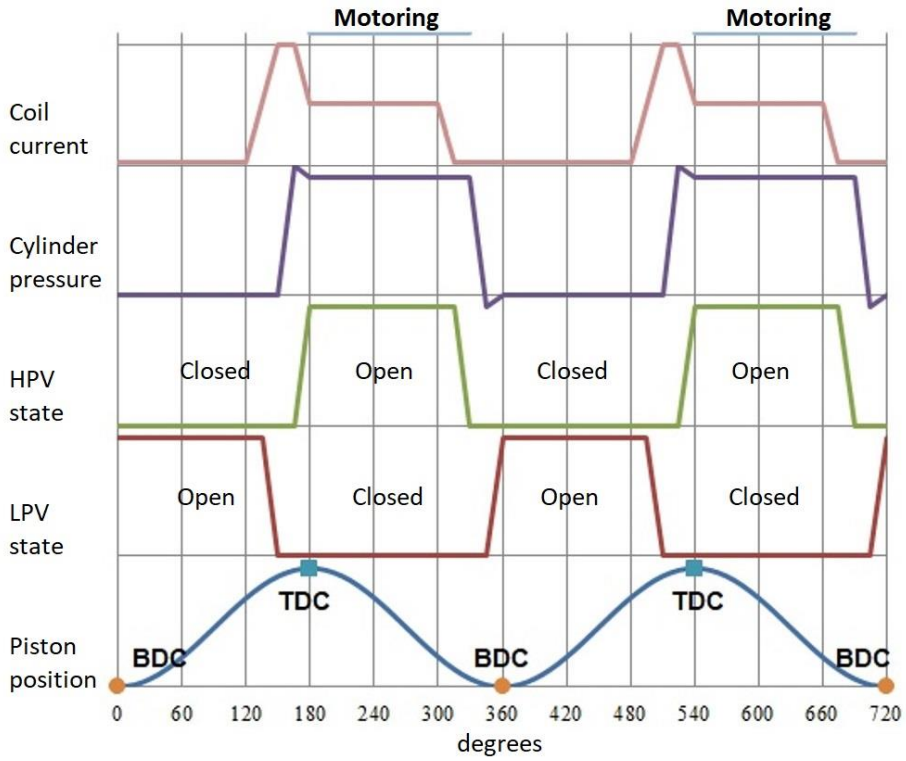

Figure 1.5. Schematic diagram to represent an ideal motoring cycle.

An accurate timing of the LPV closing and reopening events is crucial. If LPV closes too late the working chamber will not pressurize enough and the HPV will not open, and the machine will execute an idling cycle. However, if the LPV closes too early, the HPV will be open too far in advance, and the pumping cycle will take place before the piston reaches the TDC and the motoring cycle begins. Also, if the LPV will not be reopened before the piston passes the BDC, the working chamber will be commuted with the high-pressure side again when the piston starts its motion towards the TDC and an undesirable pumping cycle will be initiated, which causes a “juddering” of the DD machine, which in turn, may cause permanent damage to the mechanisms [6]. However, if LPV reopens too early, the motoring stroke will be reduced, thus, reducing displacement of the DD machine and, therefore, reducing the efficiency of the application.

1.2 Objectives

The overall goal of this thesis is to develop a next-generation solenoid valve actuation design for the new single-coil DD modules. The design must be more energy efficient, allow accurate control of the valve timing parameters, and enable self-calibration and self-diagnostic of the Digital Displacement Pump/Motor (DDPM). To achieve this goal, the following objectives were established.

1. To develop a more energy-efficient, cost-effective, and reliable solenoid coil driver compared to those coil drives that are used in the design of the present DD controllers.

2. To develop a reliable low-pressure valve (LPV) reopening detection method that will allow the closed-loop motoring technique to apply to the DDPMs based on the new single-coil design DD modules.

3. To develop a method that will improve precision in controlling the low-pressure valve closing angle applicable to the new single-coil DD module.

4. To investigate the possibility of the development of new self-diagnostics methods of the DDPM that will improve its reliability.

1.3 Rationale and motivation

The world's major problem that we are facing today is climate change caused by the increased generation of carbon dioxide (CO2) due to massive fossil fuel use and its accumulation in the atmosphere [7]. According to Intergovernmental Panel on Climate Change (IPCC), “climate change is a threat to human well-being and the health of the planet and any further delay in concerted global action will miss the brief, rapidly closing window to secure a liveable future” [8]. Therefore, the responsibility of every human being on earth is to contribute to the salvation of our home planet and to ensure the future for the next generations, and action must be taken today.

In order to avoid the ecological catastrophe, the Global Commission for Urgent Action on Energy Efficiency encountered that circa 32% of the CO2 emission reduction should be

contributed by switching to renewable energy and 37% must come from an improvement of efficiency worldwide [9]. Exhaust emissions of off-road mobile transport are not an exception. According to [10], 60% of the CO2 produced by off-road construction machinery are coming from fluid-powered excavators, which efficiency is less than 16%. Such low efficiency is due to a poor efficiency powertrain used in this kind of machinery, which is a combination of a 40% efficient diesel engine [11] and conventional hydraulic systems, which efficiency is between 30 and 40% [12].

Following the on-highway market electrification trend, the manufacturers of fluid-powered off-road machinery start offering battery-powered excavators (e.g., CAT 323). However, since most of the world's electricity comes from fossil fuels, electrification without improving efficiency does not do much in order to reduce CO2 emissions [13].

The Digital Displacement® technology can drastically increase the efficiency of hydraulic off-road machines due to its inherent energy efficiency and fast response time. Its implementation in the world's excavators can help to save up to 40 MT of CO2 per year [1].

Danfoss Power Solution already proposes a commercially available solution that delivers a 15% reduction in fuel consumption and CO2 emissions by swapping the excavator’s main hydraulic pump, which is a conventional swash plate pump, with a DD pump [14].

The project described in [15], demonstrates that simple replacement of the conventional pump with a 96 cc/rev DD pump in a 16-ton excavator gives a fuel saving between 16 and 21% and a productivity improvement of 28%.

According to [16], by replacing a swashplate pump with the DD pump in a 20-ton excavator, a 15-16% productivity improvement was reached by the faster response, faster time to steady state, faster individual cylinder cycle time, and DDP efficiency.

Also, a study was carried out by the Danfoss DD team to investigate the efficiency of electro-hydraulic systems for mobile applications in which a prime mover is an electric machine. The results show that a 16-ton electrical excavator requires a 24.8% lower capacity battery to complete a typical 8-hour shift if the DD pump is installed instead of a conventional swashplate pump [17].

Further improvement in the efficiency of hydraulic excavators is the reduction of throttling losses when operating multiple actuators simultaneously by a dynamic physical displacement allocation to services at different pressure levels allowed by a DD pump. The field results of

fuel reduction between 30 and 43% were demonstrated on a 16-ton excavator by installing a multi-service DD pump and a switching valve block [18].

Finally, the major improvement in the efficiency of fluid-powered excavators can be achieved by using the Digital Displacement pump/motor (DDPM) that enables energy recovery, storage or regeneration in the hydraulic system. According to [19] and [20], the simulation results show more than 50% of the fuel saving due to hydraulic energy regeneration from the boom and swing functions. The test results showed a regenerative efficiency of the 96cc/rev prototype DDPM between 63% and 87% over a dynamic range of operation [21].

The regenerative efficiency of the DDPM can be further improved by applying the closed-loop motoring technic [3], which was demonstrated for DD transmissions in large wind turbines of 2.4 MW and 7 MW [22]. However, closed-loop motoring is not applicable yet for the new more compact design DDPM that is intended to be used in fluid-powered off-road machines, which makes the search for a solution to this problem one of the main goals of this PhD work.

Therefore, there is an obvious motivation for me to contribute to the development of DD technology through this PhD project, the successful completion of which will lead to the energy efficiency improvement of fluid power systems and, thus, reduce carbon dioxide emissions.

1.4 Reading Guidance

Chapter 2 describes the developed coil driver design that offers efficiency, reliability, and cost improvements to the DD controller.

Chapter 3 describes a method that allows reliable detection of the low-pressure valve (LPV) reopening of the single coil DD modules during its pumping or motoring mode of operation. The method provides a reliable and stable signal indicating LPV reopening, which can be used as a feedback signal to enable the closed-loop motoring for the new-generation DD machines.

Chapter 4 describes an invention, which is the outcome of this PhD work. The invention proposes a method of stabilising the response time of a cyclically operating solenoid valve, thus, improving the prediction of the low-pressure valve (LPV) closing angle, the precision of which is crucial for the stable operation of a Digital Displacement (DD) machine. Also, this chapter describes the development and implementation of different coil current gradient control algorithms that allow this invention to be used practically for DD technology.

Chapter 5 describes another invention, which is the outcome of this PhD work. The invention proposes a sensorless method for determining the conditions/abnormality of the DD machine before the shaft rotation. Also, a based on the invention algorithm for determining the low hydraulic liquid level of the DD machine is proposed.

Chapter 6 describes the test results that demonstrate significant improvement of the DD technology achieved by implementing the developed next-generation valve actuation design in the 15-channel DD controller DDC15 designed to control a new DD pump/motor DDP1X0.

Chapter 7 presents the main conclusions along with a discussion of the work that lies ahead.

Chapter 2

Next-generation coil driver (NGCD) for Digital Displacement® solenoid valve

This chapter describes the developed coil driver design that enables efficiency, reliability, and cost improvements to the DD controller.

2.1 Introduction

Digital Displacement (DD) solenoid valve is a fast mechatronic valve which changes state by means of a solenoid actuator. The solenoid actuator is a device that converts electrical energy into mechanical energy, thus providing linear motion in a mechanical system such as solenoid valve. To operate the solenoid actuator a coil driver is required, which is a power electronic device, the main function of which is to connect and disconnect a power source from the solenoid coil. However, the fast-switching solenoid valves require more sophisticated coil drivers that can provide the fast build-up of the magnetic flux as well as its fast decay. Additionally, a coil driver must comply with the application requirements, which might demand features like energy regeneration during fast decay, current and voltage sensing, fast overcurrent protection, over and under voltage protection, etc.

Thus, it is fair to say that the coil driver is the key component in a valve actuation design. Therefore, it was decided that the new coil driver design development must be the first task in the next-generation valve actuation design development for DD machines. In addition, the coil driver prototype board will be used as a platform for further components' development of the next-generation valve actuation design.

2.2 Literature review on coil drivers

Figure 2.1 shows a schematic diagram of a basic electro-mechanical system that comprises a solenoid actuator and a coil driver circuit that allows energising and slow decay modes of operation and closed-loop current control of the solenoid coil. Coil driver comprises a MOSFET (2) that is used to connect and disconnect the power supply from solenoid coil (5), flyback diode (7) enables recirculation path for coil current when the MOSFET 2 is switched

off, current sense resistor (CSR) (10) is used to generate a feedback signal that is proportional to the coil current, control unit (1) generates the control signal for the MOSFET. The solenoid actuator itself comprises the coil (5) (usually made of copper), return spring (4), magnetic core (6), working air gap (9) and the magnetic armature (8) that is physically attached to the poppet (3) that is needed to be displaced.

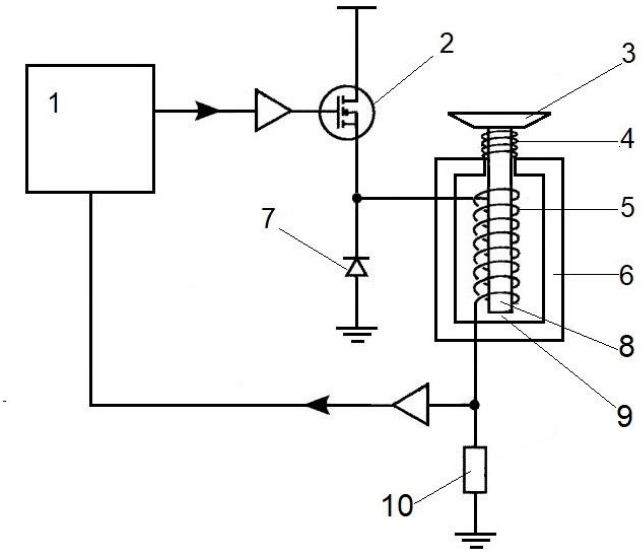

Figure 2.1. Schematic diagram of an electro-mechanical system that is comprised of a solenoid actuator and solenoid driving circuit that can provide closed-loop current control of the solenoid coil.

To set the coil driver in the energising mode the MOSFET is switched-on, the current begins to flow through the coil (also through the MOSFET and CSR). Because of the self-inductance of the coil, the current cannot build up instantly. According to the Faraday's Law, the current flow will induce an electromotive force (EMF) in the coil that can be calculated by equation (1).

$$E = -L\frac{di}{dt} \qquad (1)$$

Where E is the induced EMF in the coil, L - coil inductance, $\frac{di}{dt}$ - rate of change of coil current, the minus sign shows that the induced EMF is opposite to the change that is producing it [23].

The coil current will be changing according to the equation (2) [24].

$$i(t) = \frac{V}{R}(1 - e^{\frac{-tR}{L}}) \quad (2)$$

Where V is the supply voltage, R - circuit resistance, L - coil inductance, i - coil instant current, t - time, e - Euler's number.

The current flow creates a magnetic flux that flows through the core, armature, and air gap since the magnetic flux tends to flow through the path of higher magnetic permeability, which, according to [25], can be demonstrated with the Maxwell equation. The flux through the air gap will be approximately the same as through the magnetic material because the length of the air gap is much smaller than the total length of the flux path of the solenoid. The result is a uniform strong magnetic field across the air gap with opposite poles on the opposite sides of the gap [25]. Therefore, when the developed magnetic force will be above the return spring force the armature will be attracted to the core of the solenoid, thus, displacing the poppet (Figure 2.1).

According to [26], [27], [28], when the armature starts moving, it will induce a back-EMF in the coil, changing the rate of rise of the current. When the armature reaches the end stop, the current will continue to rise until it reaches a steady state and, from equation (2), it will be limited only by the circuit resistance.

After actuating the solenoid, the working air gap is much smaller, therefore, the reluctance of the magnetic path will be much smaller too. Therefore, the coil current that is needed to develop a sufficient magnetic force to keep armature at the end-stop position can be several times smaller. For this reason, the coil voltage can be decreased by applying a required pulse-width modulation (PWM) signal to the MOSFET gate. This, in turn, will reduce the power consumption, thus, significantly improving the efficiency of the system.

To set the coil driver in the slow decay mode, the MOSFET is switched-off, the coil will become a current source trying to maintain the current flow. If the path for the current flow is not provided the voltage across the MOSFET will increase to a very high value exceeding its maximum limit. This can be seen from equation (1).

The flyback diode provides the path for the current flow by shorting the coil, additionally providing safety measures for the driver circuit. Coil current will decay according to the equation (3) [29].

$$i(t) = I_0 e^{\frac{-tR}{L}} \quad (3)$$

Where I_0 represents the initial value of the current at the time the MOSFET was switched-off, R - flyback circuit resistance, L - coil inductance, i - coil instant current, t - time.

Since the magnetic force of the solenoid is proportional to the coil current [25], it will decrease with some lagging when the coil current decays. When the magnetic force is below the spring force, the armature will be returned to the initial position, inducing a back-EMF in the solenoid coil again [30].

Figure 2.2 reflects the switching cycle of the solenoid actuator and shows ideal waveforms of the armature position, MOSFET control signal, and the solenoid current profile that can be generated by means of the coil driver from Figure 2.1. The switching cycle comprises the turn-on phase (coil driver is set in energising mode), latching phase (coil driver is switching between energising and slow-decay modes) and turn-off phase (coil driver is set in slow-decay mode). The back-EMF signal that can be observed on the current waveform during turn-on and turn-off phases is induced in the coil due to the armature motion and can be used as feed-back signal of the armature position change.

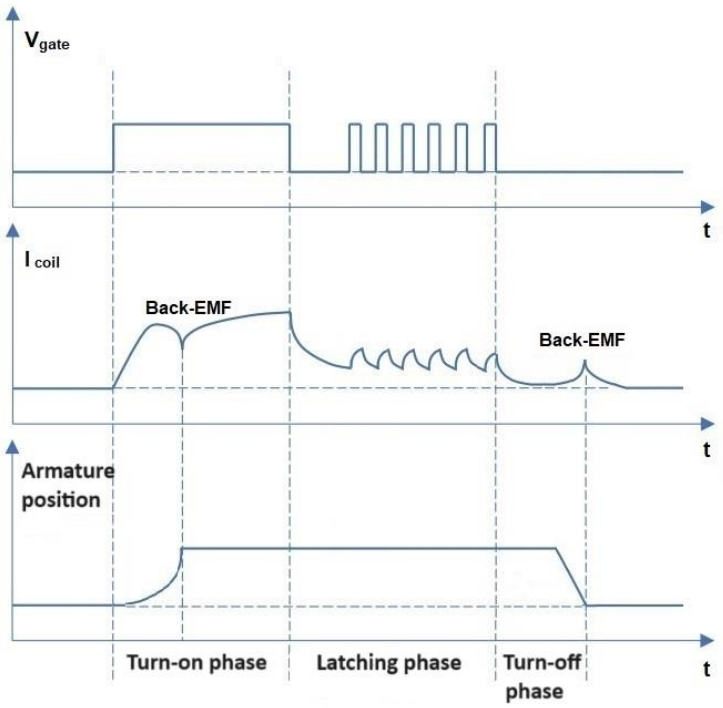

Figure 2.2. Idealised waveforms of a solenoid current, armature position, and the gate voltage of the MOSFET.

The current profile from Figure 2.2 is not suitable for solenoids that are used in fast switching applications as the turn-off phase is extended in time because the coil driver does not provide the fast-decay mode of operation.

Figure 2.3 shows a current waveform, known as the "peak-and-hold", that corresponds to a more recent approach to controlling solenoids where a fast cyclic operation is required in such applications as a fuel injector [27].

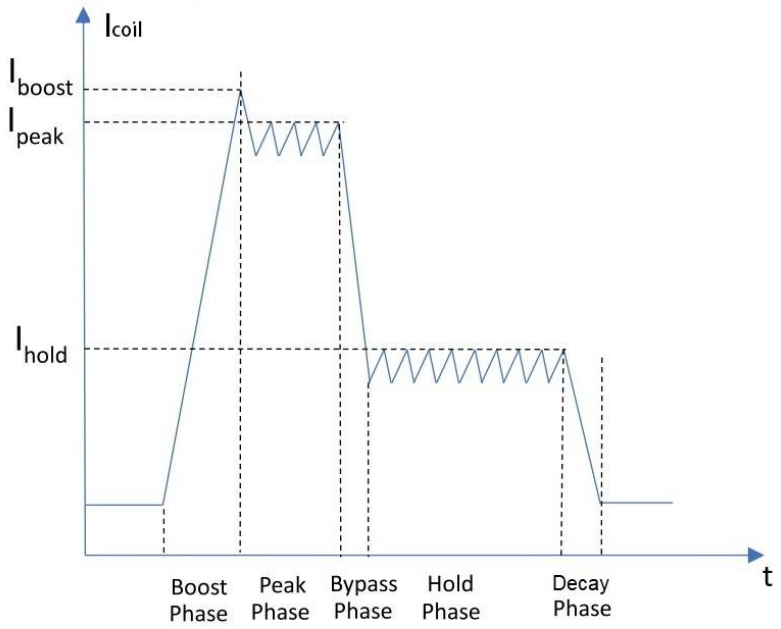

Figure 2.3.The "peak-and-hold" solenoid current profile of a fuel injector application [27].

During the Boost Phase, a maximum voltage is applied to ensure the steep gradient of the solenoid current. The rapidly increasing current provides a rapid increase of the magnetic force to initiate the armature motion as fast as possible.

During the Peak Phase, a certain current value is applied that will ensure a sufficient magnetic force is produced to keep the armature motion when traveling to the end stop position. To decrease the losses, during the Bypass Phase, the solenoid current is reduced up to the value at which enough force can be produced to hold the armature at the end stop position during the Hold Phase. During the Peak and Hold Phases coil current is controlled by means of the PWM technique switching a coil driver between energising and slow-decay modes of operation.

At last, the Decay Phase begins when the coil driver is set in the fast-decay mode of operation and the current is allowed to decay to zero fast, allowing the armature to be returned to the initial position by the return spring as fast as possible. The current decrease rate depends on the reverse voltage applied to the solenoid coil. According to [31], to estimate the approximate decay time can be used the finite time step equation (4) shown below can be used to estimate the approximate decay time.

$$\Delta t = L\frac{\Delta i}{V_c} \tag{4}$$

Where V_c is the voltage across the coil, L - coil inductance, the time Δt taken to decay current Δi.

Therefore, it can be concluded that for fast and efficient operation of a solenoid, the coil driver must be capable to provide the following modes of operation.

1. **Energising mode**: a mode during which the coil is being energised.
2. **Slow decay mode**: a mode during which the coil is shorted, thus, providing a low resistance path for the recirculating current.
3. **Fast decay mode**: a mode during which the coil current decreases rapidly to deenergise the coil.

The next subchapters review the most relevant topologies of the coil drivers that comprise three main modes of operation.

2.2.1 Coil driver with flyback diodes

According to [27], the solenoid driver with flyback diodes (Figure 2.4) provides the simplest and most efficient method to drive a solenoid. This topology is also known as a Full-bridge where a diagonal couple of MOSFETs is replaced by a couple of diodes. The energising current will flow through the coil when both MOSFETs are switched on. The slow decay can be performed on the high side or on the low side of the bridge when one of the MOSFETs is switched on and the other one is switched off. To implement the fast decay of the coil current, the power supply is reversed across the coil by switching off both MOSFETs. Therefore, the current flows through the flyback diodes, thus, discharging the stored energy in the coil back to the supply.

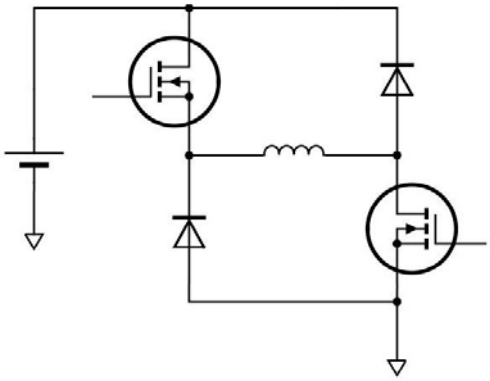

Figure 2.4. Schematic of the solenoid driver with flyback diodes.

The coil voltage during Decay Phase is

$$V_c = V_{supply} + 2V_{forward} + IR \quad (5)$$

Where V_c is the voltage across the coil during Decay Phase, V_{supply} is the battery voltage, $V_{forward}$ - flyback diode forward voltage, I - coil current, R circuit resistance.

2.2.2 Coil driver with MOSFET avalanching

The energising and slow decay modes of the solenoid driver with MOSFET avalanching (Figure 2.5) topology are similar to the Full-bridge topology except that the slow decay can be performed only on the low side when the high-side MOSFET is switched off and the low-side MOSFET is switched on. To initiate fast decay, both of the MOSFETs have to be switched off. The inductor current has no path to free-wheel or to fly back to the supply. This condition will lead to the increase of the coil voltage until the low-side MOSFET breaks down and will be driven into the avalanche mode, thus, dissipating the coil energy into heat [27]. The voltage across the coil is

$$V_c = V_{avalanche} + V_{forward} + IR \quad (6)$$

Where V_c is the voltage across the coil during Decay Phase, $V_{avalanche}$ is the avalanche voltage of the low-side MOSFET, $V_{forward}$ - flyback diode forward voltage, I - coil current, R - circuit resistance.

The drawback of this method is increased power loss at the fast-decay mode of operation compared with the flyback diode coil driver.

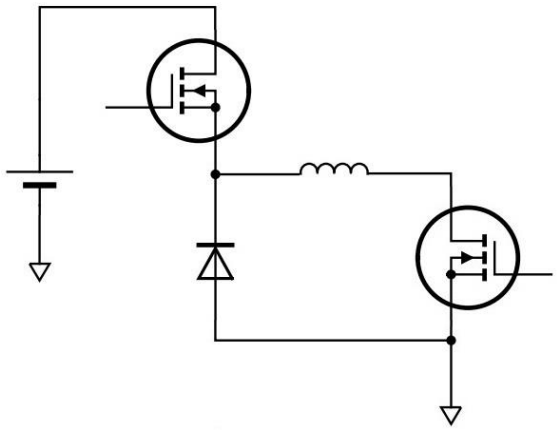

Figure 2.5. Schematic of the solenoid driver with avalanching MOSFET.

2.2.3 Solenoid driver with active clamp

The operation modes of the solenoid driver with active clamp (Figure 2.6) are similar to the operation modes of the driver with avalanching MOSFET. According to [27], at the Decay Phase, when both MOSFETs are switched off the coil voltage begins to rise, the Zener diode will start conducting before voltage will reach the low-side MOSFET V_{DS} breakdown, thus, pulling up the MOSFETS gate, which, in turn, will force the MOSFET into the linear region. The MOSFET then maintains the sum of the Zener diode breakdown voltage, the diode forward voltage, and the gate-source threshold voltage from drain to source.

Thus, the voltage across the coil during Decay Phase is

$$V_c = V_{MOSFET} + V_{forward} + IR \quad (7)$$

Where V_c is the voltage across the coil during Decay Phase, V_{MOSFET} is the voltage across the low-side MOSFET during Decay Phase, $V_{forward}$ - flyback diode forward voltage, I - coil current, R - circuit resistance.

The drawback of this method is increased power loss at the fast-decay mode of operation compared with the flyback diode coil driver.

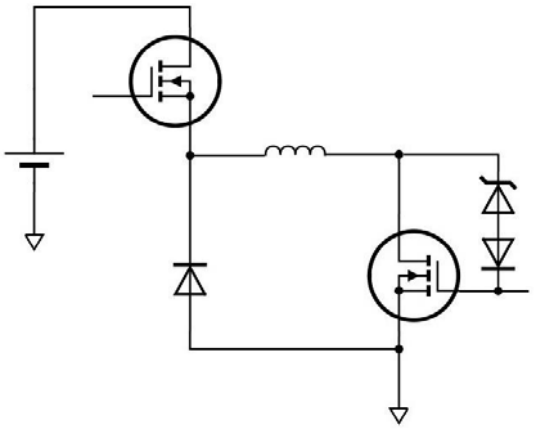

Figure 2.6. Schematic of the coil driver with active clamp.

2.2.4 Solenoid driver with Boost converter

According to [27], the solenoid driver with Boost converter topology (Figure 2.7) is the most complicated but provides the highest performance. The operation of this driver is very similar to the driver with flyback diodes. The only difference is that in this topology a voltage much higher than the battery voltage is used for the Boost and the Decay Phases, which is provided by a DC/DC converter. The higher supply voltage allows for faster toggling of the solenoid at the switch-on and switch-off stages. The coil voltage during the Decay Phase can be found from equation (5).

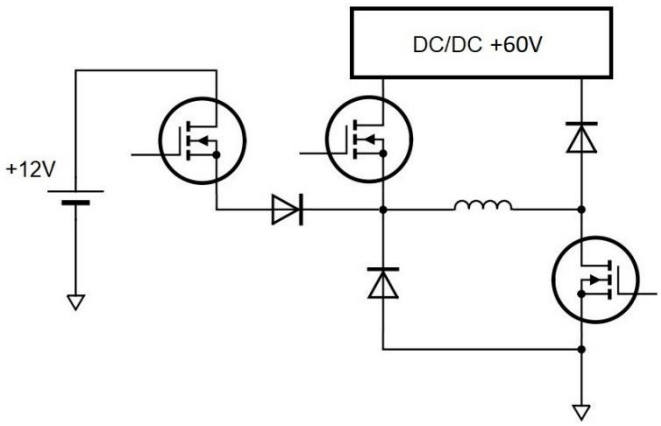

Figure 2.7. Schematic of the coil driver with Boost converter.

The drawback of this topology is increased components count and costs.

Table 2.1and Table 2.2 are compared the energy losses and performance of the reviewed above topologies (this data was taken from the source [27]).

Table 2.1. Energy losses comparison of the described above coil driver topologies (mJ) [27].

Topology	**Flyback**	**Avalanche**	**Active clamp**	**Boost**
Switching MOSFET (top)	0.3	0.3	0.3	0.3
Selector MOSFET (bottom)	1	5.1	3	4
Boost MOSFET	-	-	-	0.03
Flyback diode (bottom)	15.5	15.3	15.4	15.6
Flyback diode (top)	0.1	-	-	0.25
Switching diode	-	-	-	3.8
Zener diode	-	-	2	-
Total losses	17	20.7	20.7	26

Table 2.2. Performance comparison of the described above coil driver topologies [27].

Topology	**Flyback**	**Avalanche**	**Active clamp**	**Boost**
Cost	Low	Low	Low	High
Speed	Low	Medium	Medium	High
Efficiency	High	Low	Low	High
Reliability	Long term	Long term	Questionable	Long term

The other aspect that is worth mentioning is that none of these topologies offers synchronous rectification for the slow-decay mode of operation. Replacing the freewheeling diode with the MOSFET will decrease power losses when the PWM technique is used.

2.3 State of art on coil driver used in DD controllers.

This section gives a review of coil driver designs that are used in existing DD controllers.

2.3.1 Coil driver design of the early DD controllers.

Figure 2.8 shows the detailed schematic diagram of the coil driver used in early DD controllers, which are XPHS, AMC1, and AMC2 (AMC stands for Artemis Modular Controller). Figure 2.9 shows the simplified schematic diagram of this driver.

Coil driver of the early DD controllers allows three main operation modes that are required for a cyclically operated fast mechatronic DD valve. During the energising mode the high-side N-channel MOSFET is switched on, enabling current flows through the high-side MOSFET, fuse, and coil. The low-side P-channel MOSFET can be switched-on since the current path is blocked by the switching diode. During the slow decay mode, the high-side N-channel MOSFET is switched-off and the low-side P-channel MOSFET is switched-on, current recirculates through the low-side MOSFET, switching diode, fuse, and coil. During the fast decay mode, both MOSFETs are switched-off. Therefore, there is no path for the current flow, which makes the coil voltage increase until it reaches the avalanche voltage of the low-side P-channel MOSFET. The coil current starts flowing through the low-side loop, thus, dissipating the coil energy as heat across the MOSFET. The fuse provides left-side coil connector short-to-ground and short-to-supply protection, which is relatively slow (term of milliseconds).

A major benefit of this coil driver is that it requires only one control signal to enable all three modes of operations (energising, slow decay, and fast decay). This feature is achieved by implementing a low-side driver with a MOSFET switch-off delay, which is based on a Schmitt trigger with an RC circuit on its input. Thus, applying a high logic to the gate drivers will switch on the high-side and the low-side MOSFETs placing the coil driver in energising mode. After the energising mode, it is possible to place the coil driver in slow decay mode by applying a low logic for the time that is enough to discharge the high-side MOSFET gate but not enough to charge the capacitor of the RC circuit to the threshold voltage of the Schmitt trigger, thus keeping the low-side MOSFET switched on. Then, to continue keeping the coil driver in this mode, brief high logic pulses must be applied to keep the Schmitt trigger voltage below the upper limit and the gate voltage of the high-side MOSFET below the gate threshold voltage. A PWM signal of 5 kHz frequency and 0.001 duty cycle will set the coil driver (of the shown set-up) in slow-decay mode. Finally, if applying a low logic for the time that allows charging the capacitor of the RC circuit to a voltage of the Schmitt trigger tripping point will switch off both MOSFETs placing the coil driver in fast-decay mode.

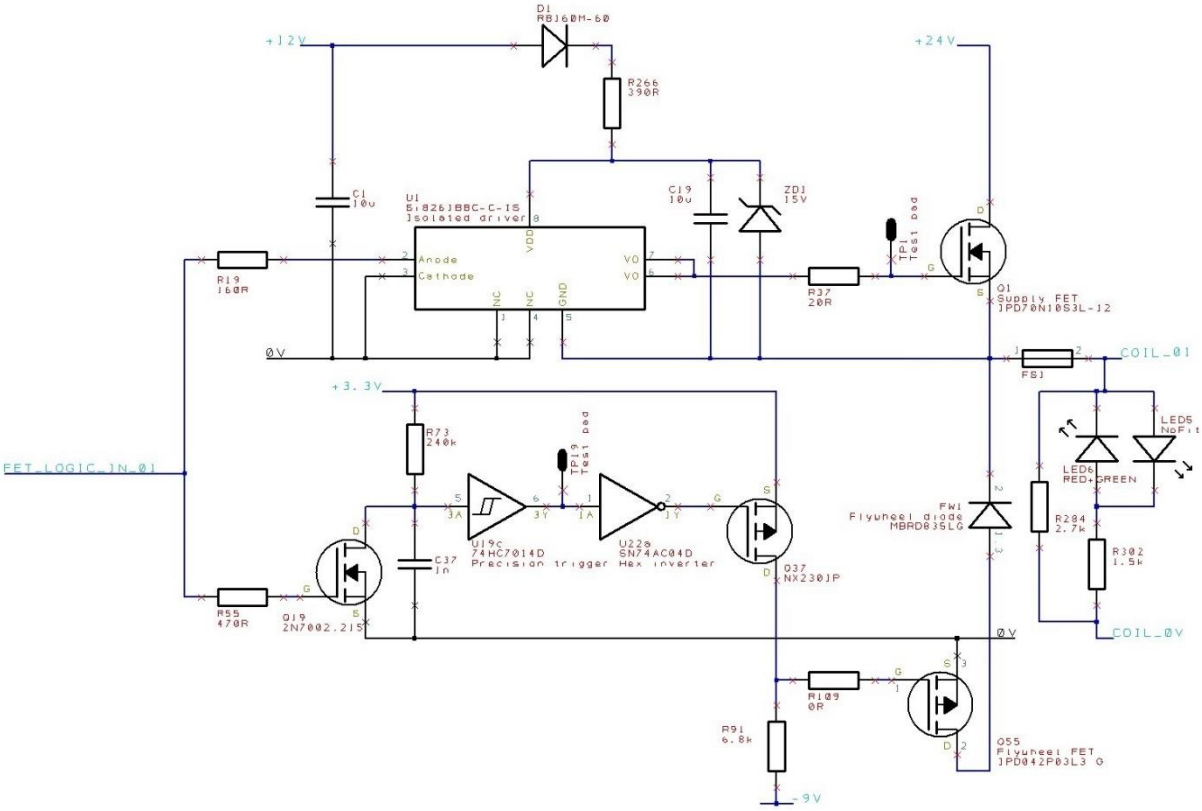

Figure 2.8. XPHS, AMC1, AMC2 coil driver schematic diagram.

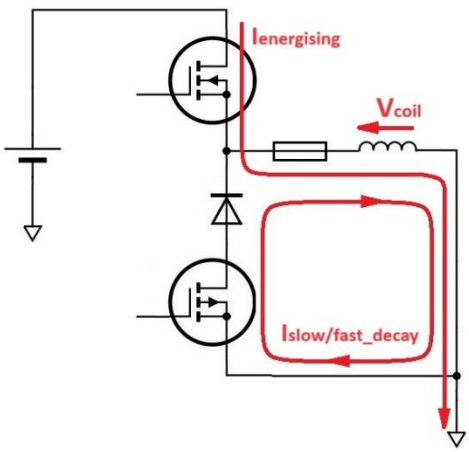

Figure 2.9. Simplified schematic diagram of XPHS, AMC1, AMC2 coil driver.

2.3.2 Coil driver design of the latest digital displacement controller.

Figure 2.10 shows the coil driver schematic diagram that is used in the DPC12 MK1, which was the most recent design of the Digital Pump Controller at the time this PhD research was initiated. Figure 2.11 shows the simplified schematic diagram of this driver.

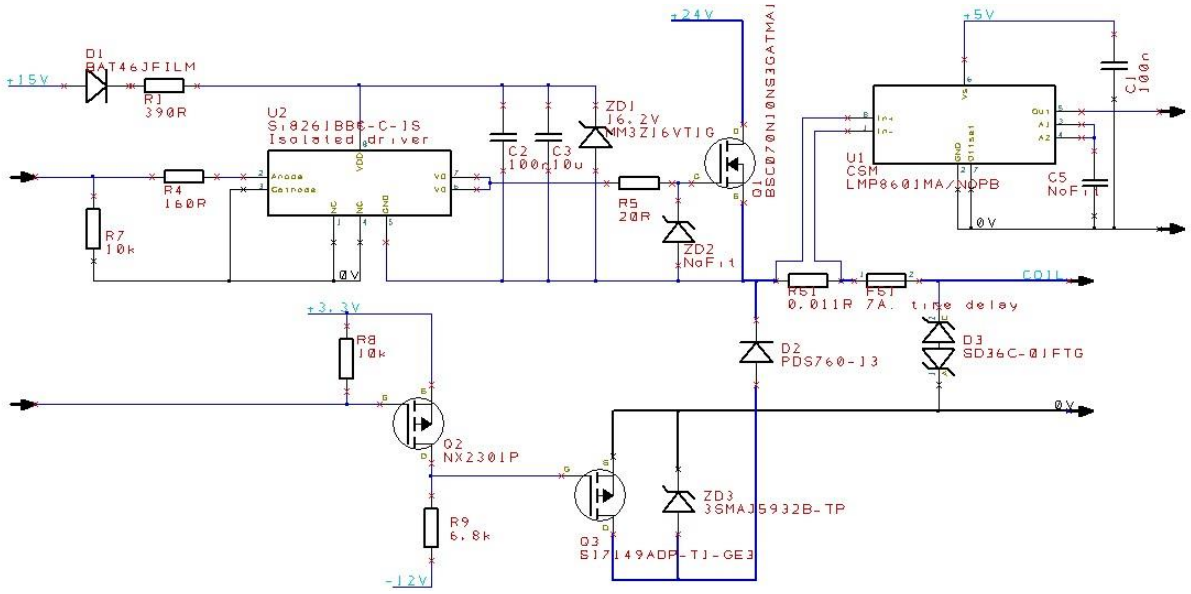

Figure 2.10. DPC12 coil driver schematic diagram.

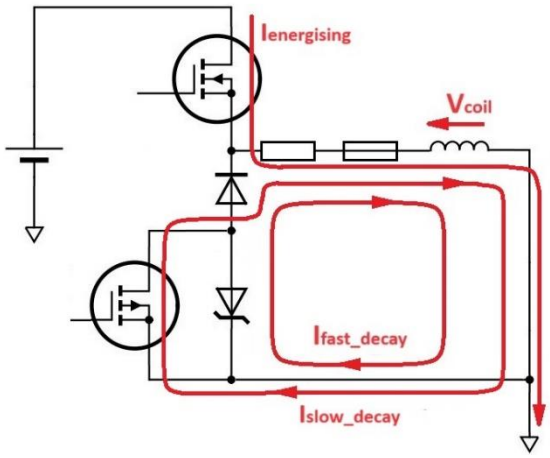

Figure 2.11. Simplified schematic diagram of DPC12 MK1 coil driver.

As can be seen from the diagram, the coil driver design of the recent DD controller is almost the same as the coil driver design of the early DD controllers. The main difference is that in the new coil driver design, a Zener diode is used to dissipate the coil energy during the fast-decay mode instead of avalanching the P-channel MOSFET. Additionally, this design provides a high-side coil current sensing and requires two control signals instead of one compared to the previous design.

Thus, analysing design of the coil drivers that are used in the DD controllers the following drawbacks can be highlighted.

1. To drive the gate of the low-side P-channel MOSFET a negative power supply is required. Increases components count, cost and footprint area.

2. The synchronous rectification at slow decay mode is not available. Increases energy losses and worsens thermal performance.

3. Energy recovery during fast decay is not available, stored coil energy dissipates as heat mostly across the Zener diode or P-channel MOSFET. Increases energy losses and worsens thermal performance.

4. High-side current sensing is much more expensive than low-side current sensing in the same range of precision. Increases cost.

5. The overcurrent protection is based on the fuse or the high-side current sensing that feeds the current signal into the ADC of the FPGA, the response time of which is slow and may not be capable of disconnecting the short circuit prior to component damage. Decreases reliability.

6. The one coil connector does not have short-to-battery protection. Decreases reliability.

Therefore, the coil driver improvement will consist in developing a design that will not possess the drawbacks listed above. Additionally, development should be focused on cost and footprint reduction of the circuit.

2.4 Results

2.4.1 NGCD design requirements

Table 2.3 gives the cornerstone requirements for the next-generation coil driver (NGCD) design, succeeding with which will lead to significant improvement of the DD controller.

Table 2.3. NGCD key design requirements and justifications.

	Requirement	Justification
1	Low-side coil current sensing.	Required for enabling the closed-loop control of the coil current. Offers lower cost compared to high-side sensing.

2	Energy regeneration at the fast-decay mode	Allows regeneration of the energy that is stored in the coil. Increases efficiency and improves the thermal performance of the system.
3	Synchronous rectification at slow-decay mode	Increases efficiency and improve the thermal performance of the system.
4	Fast overcurrent protection with recovery	Improves reliability of the system.
5	Maximum two control signals per channel	To match the available amount of the FPGA IOs for a 15-channel controller.
6	Low cost and small footprint area	Makes the DD controller more attractive in the market.
7	Average current up to 5 A, peak current up to 15 A.	Product development purposes. To allow testing of new prototypes of DD valves that might require higher testing currents.
8	Operating voltage range 9 to 36 V	To comply with the 24 V system automotive requirement.
9	Operating Ambient Temperature Range from -20°C to +75°C	To comply with automotive requirement.

2.4.2 Topology of the NGCD

From the previous section (Table 2.1) can be seen that the most efficient is the coil driver with flyback diodes (see Figure 2.4) because the energy stored in the coil is recovered back to supply during the Decay Phase. In, addition, most energy losses are due to not synchronous rectification at the slow decay mode. Therefore, replacing the low-side flyback diode with a MOSFET will allow the low-side synchronous rectification, which, in turn, improves the efficiency of the circuit. The high-side flyback diode, which enables the fast decay with energy regeneration, is not required to be replaced by a MOSFET as its average current and switching frequency will be low, therefore, its power losses will be quite low too (compared to the low-side diode). Another benefit of not replacing the high-side diode with a MOSFET is that the diode does not require a driving circuit or a driving signal.

Figure 2.12 shows a simplified schematic diagram of the NGCD, which is a pseudo-H-bridge topology with low-side current sensing and one of the high-side MOSFET replaced by a diode, which was proposed by me.

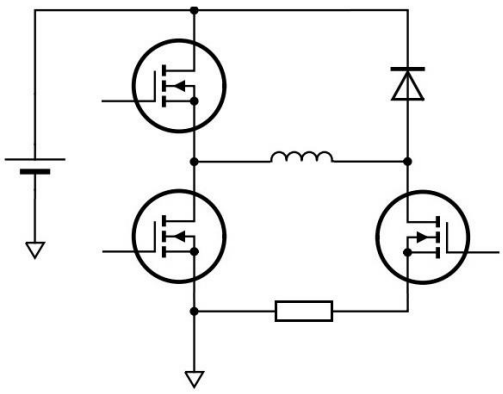

Figure 2.12. Simplified schematic of the NGCD.

To energise the coil, the diagonal high-side and low-side MOSFETs are switched on (Figure 2.13 a). Current flows through the coil and CSR, allowing the current to be monitored. To set the slow decay mode, both low-side MOSFETs are on, and the high side MOSFET is off (Figure 2.13 b). Coil current decays through CSR, allowing the current to be monitored. In fast decay mode (Figure 2.13 c), only the left low-side transistor is switched on. Coil current recirculates back to the supply (bulk caps), regenerating the energy that was stored in the coil. The flyback diode will become open circuit as soon as the current reaches 0 A, thus, isolating the coil from the supply. Therefore, current sensing is not required to control the fast-decay phase finalisation.

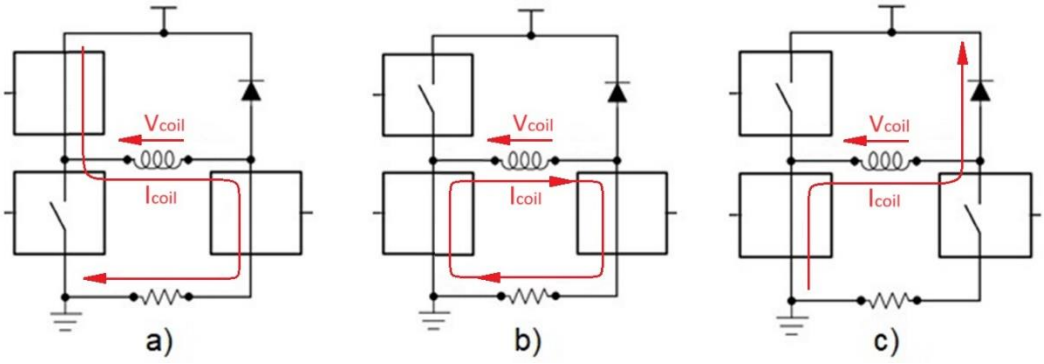

Figure 2.13. Modes of operation of NGCD: a) energising mode, b) slow decay mode, c) fast decay mode.

The coil voltage at fast decay mode V_c can be found by equation (8).

$$V_c = V_{supply} + V_{forward} + IR \tag{8}$$

Where $V_{forward}$ flyback diode forward voltage, I is average coil current during fast decay phase, R is resistance of the circuit at fast-decay mode.

Considering equation (4), the time of the decay phase will mostly depend on the supply voltage, which, according to Danfoss specifications, is expected to be 22-32 V at nominal operation. Therefore, the decay time of the NGCD will not be slower than the decay time of the coil driver used in the present design DD controllers.

2.4.3 Functional description of NGCD

2.4.3.1 Design overview

Figure 2.14 shows a functional block diagram of a 3-channel NGCD design.

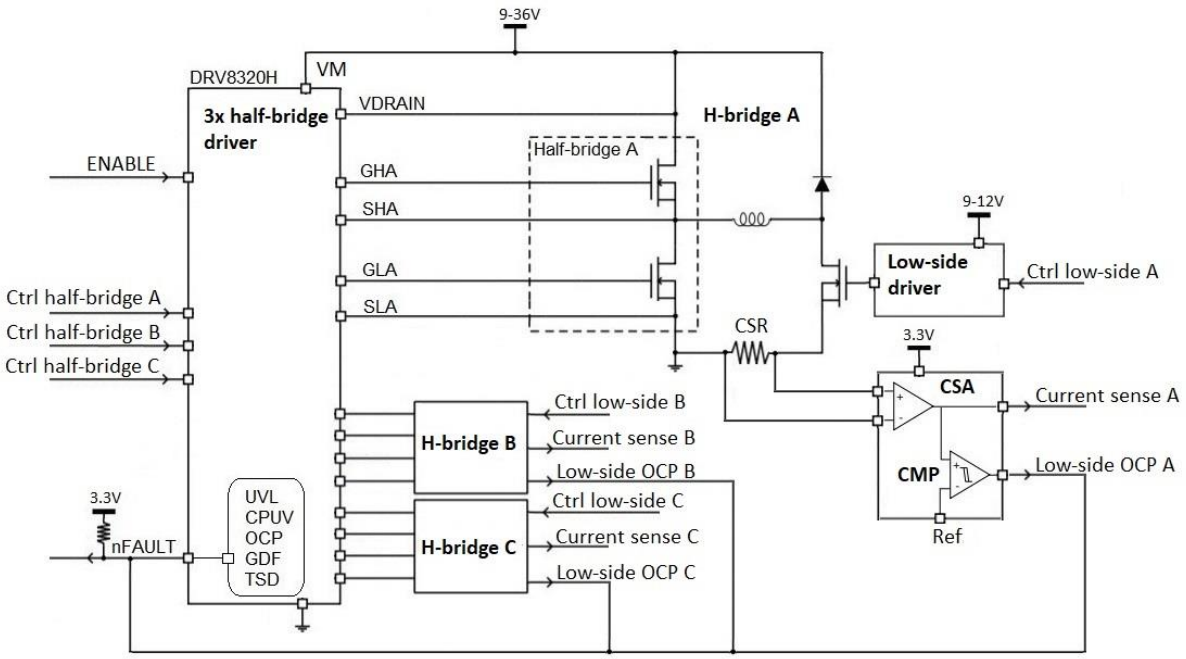

Figure 2.14. Functional block diagram of the NGCD.

As can be seen from the block diagram, each side of the H-bridge is controlled by a different gate driver circuit. A 6 to 60 V 3-phase gate driver IC DRV8320H was chosen to control the half-bridge, which is the left side of the H-bridge coil driver and will be used for PWM generation for coil current control purposes. The DRV8320 is set in 3x PWM Mode of operation according to the datasheet, to drive 3 half-bridges. After enabling the IC by setting high the ENABLE pin, each half-bridge requires only one control signal as it provides

automatic dead time control. The MOSFETs gate voltage is internally regulated by the low-dropout regulator (LDO) for the low-side and Charge pump for the high-side MOSFETs, which allows a 100% duty cycle. The MOSFET gate current is internally controlled too, the peak value of which is H/W configured according to MOSFETs requirements, therefore, a gate resistor is not required. In addition, DRV8320H provides a number of integrated protection features. These features include power supply undervoltage lockout (UVLO), charge pump undervoltage lockout (CPUV), gate driver fault detection (GDF), overtemperature shutdown (OTSD), and fast overcurrent protection (OCP) based on VDS monitoring of the MOSFETs. Any of the fault events will be indicated by the nFAULT pin.

The low-side MOSFET is used to enable current flow through the coil during its energising phase that occurs once per shaft revolution (i.e., toggle the valve at every revolution of the DD machine shaft). The over-current protection of this MOSFET is based on the low-side current sensing. When the output voltage of the CSA reaches the reference voltage of the comparator the output of which is connected to the nFAULT, which, is in turn connected to FPGA I/O, the OCP logic will pull down all control pins of the coil drivers connected to this nFAULT pin including the faulty one, thus halting the short circuit current.

The low-side CSA is used to sense voltage across CSR, which is proportional to coil current. The output of the CSA is connected to the ADC input of the FPGA, providing the coil current feedback signal for closed-loop current control and other purposes.

2.4.3.2 Main modes of operation

Table 2.4 describes the NGCD modes of operation. The DRV8320H ‘MODE’ pin should be connected to ground (GND) by 47 kOhm resistor to enable 3x PWM mode of operation (see DRV8320H datasheet).

Table 2.4. NGCD truth table

DRV Enable	Control half-bridge X	Control low-side X	Half-bridge HS gate X	Half-bridge LS gate X	Low-side gate X	Function
1	1	1	H	L	H	**Energizing Mode**
1	0	1	L	H	H	**Low-side Slow Decay Mode**

1	1	0	H	L	L	High side Slow Decay Mode
1	0	0	L	H	L	**Fast Decay/Standby Mode**
0	X	0	L	L	L	Standby/Reset Mode
0	X	1	L	L	H	Standby/Reset Mode

The main operating modes of NGCD are energizing, low-side slow-decay and fast-decay.

2.4.3.3 DRV8320H hardware interface

The DRV8320H has three resistor-configurable inputs which are IDRIVE, MODE, and VDS. This conversion lets the application designer configure the device settings. General fault information can be obtained through the nFAULT pin, which is the open-drain output and requires an external pullup resistor to function correctly.

- The IDRIVE pin configures the gate drive current strength.
- The MODE pin configures the PWM control mode.
- The VDS pin configures the voltage threshold of the VDS overcurrent monitors.
- The nFAULT pin becomes active at fault conditions described in Table 2.5.

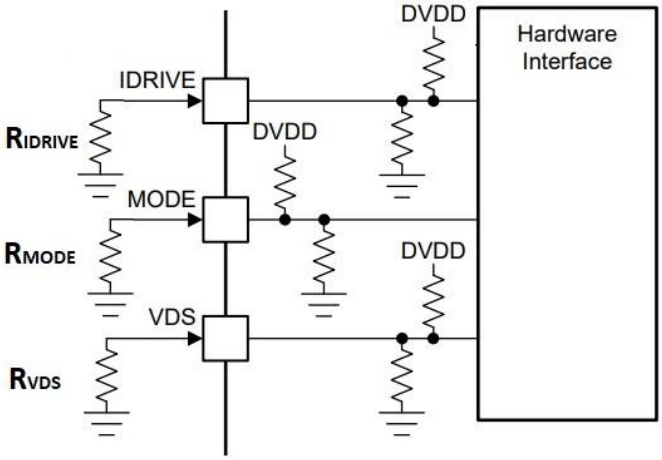

Figure 2.15. DRV8320H hardware interface [32].

2.4.3.4 NGCD fault actions and response

Table 2.5 describes the fault conditions and the fault response of the NGCD circuit.

Table 2.5. NGCD fault action and response.

Fault	Condition	Report	DRV8320 Gate Driver	Los-side Gate Driver	DRV8320H Recovery	NGCD Recovery
VM undervoltage (UVLO)	$V_{VM}<V_{UVLO}$	nFAULT	Hi-Z	Hi-Z	Automatic: $V_{VM}>V_{UVLO}$	Reset FPGA
DRV8320H Charge pump undervoltage (CPUV)	$V_{VCP}<V_{CPUV}$	nFAULT	Hi-Z	Hi-Z	Automatic: $V_{VCP}>V_{CPUV}$	Reset FPGA
DRV8320H VDS overcurrent (VDS_OCP)	$V_{DS}>V_{VDS\_OSP}$	nFAULT	Hi-Z	Hi-Z	Latched: ENABLE Pulse	Reset FPGA
DRV8320H Gate driver fault (GDF)	Gate voltage stuck>t_{DRIVE}	nFAULT	Hi-Z	Hi-Z	Latched: ENABLE Pulse	Reset FPGA
DRV8320H Thermal warning (OTW)	$T_J>T_{OTW}$	nFAULT	Active	Active	Automatic: $T_J<T_{OTW}$ - T_{HYS}	Reset FPGA
DRV8320H Thermal shutdown (OTSD)	$T_J>T_{OTSD}$	nFAULT	Hi-Z	Hi-Z	Automatic: $T_J<T_{OTSD}$ - T_{HYS}	Reset FPGA
Low-side overcurrent (LS_OCP)	$V_{CSA}>V_{LS\_OCP}$	nFAULT	Hi-Z	Hi-Z	-	Reset FPGA

2.4.3.5 Low-side gate driver operation

The switching frequency of the low-side MOSFET is determined by the shaft rotational speed of the DD machine. According to a DD machine specification, the maximum shaft rotation speed is 3000 rpm., which determines the maximum switching frequency of the low-side

MOSFET of 50 Hz. Due to the high inductance of the solenoid coil, the switch-on phase of the toggle MOSFET will occur at 0 A, which is lossless (known as soft switching). Therefore, low switching frequency and soft switching at the switch-on phase allow the use of a simple open-collector level-shifter circuit to drive the low-side MOSFET.

Figure 2.16 shows a block diagram of the proposed low-side gate driver (LSGD). This design provides a small propagation delay at the MOSFET turn-off event, lowering power dissipation when switching from on to off, and providing fast turn-off of the MOSFET during an overcurrent fault condition.

The driver is controlled by the FPGA, a logic low signal turns-on the MOSFET and logic high turns-off the MOSFET. The MOSFET must be defaulted to an off state at power-on to ensure a short-to-supply condition does not damage the device before the short circuit protection is activated. This is achieved by power sequencing the driver supply LDO, so it is not powered on until the 3.3 V power supply is on, which sets the BJT to operate in the saturation region, thus pulling the gate of the MOSFET to GND.

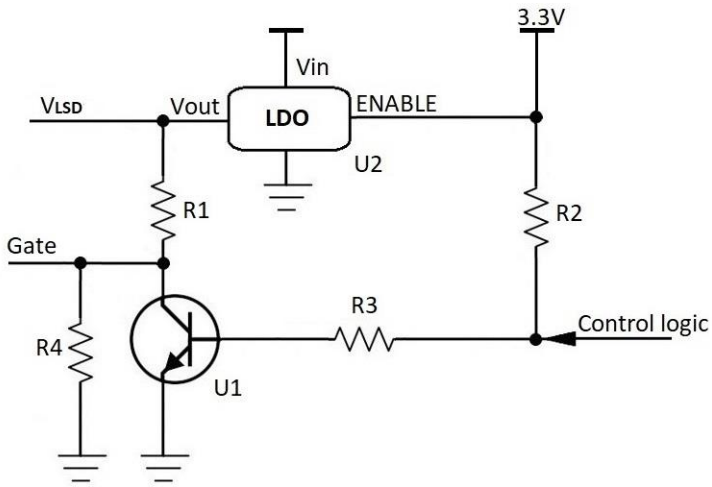

Figure 2.16. Low-side gate driver schematic diagram.

2.4.3.6 Current sensing

The NGCD current sensing is based on the low-side current sense amplifier (CSA) INA180. The CSA should be located as close as possible to the sense resistor to avoid input filtering, which introduces an error. The output of CSA is split in order to provide fast overcurrent protection and high precision current sensing.

To attenuate high-frequency disturbances, scale down and convert the CSA output into a differential signal, the signal conditioning circuit is used. The circuit schematic is shown in Figure 2.17.

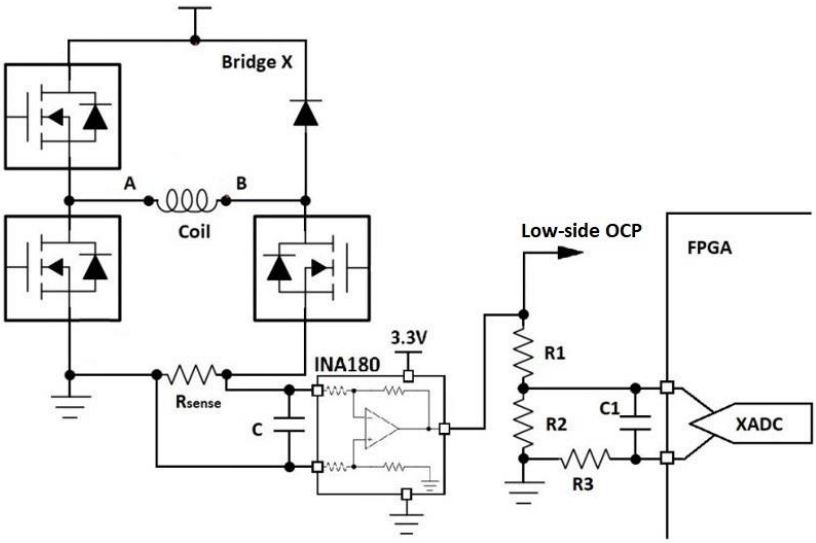

Figure 2.17. NGCD current sensing.

2.4.3.7 Low-side MOSFET overcurrent protection (OCP)

Figure 2.18 shows the circuit for the unidirectional overcurrent protection (OCP) solution. The response time is about 2.3 us from a fault occurring to the FPGA detecting the fault.

The INA180 has a maximum output of 3.3 V, which is equivalent to 23.6 A. The trip threshold is set by the reference voltage of voltage divider (R1 and R2) connected to the comparator's inverting input. When the voltage on the non-inverting input is larger than the reference voltage, the comparator output toggles low, and it is detected as a logic low on the FPGA input. R3 pulls FPGA input high at normal operation condition.

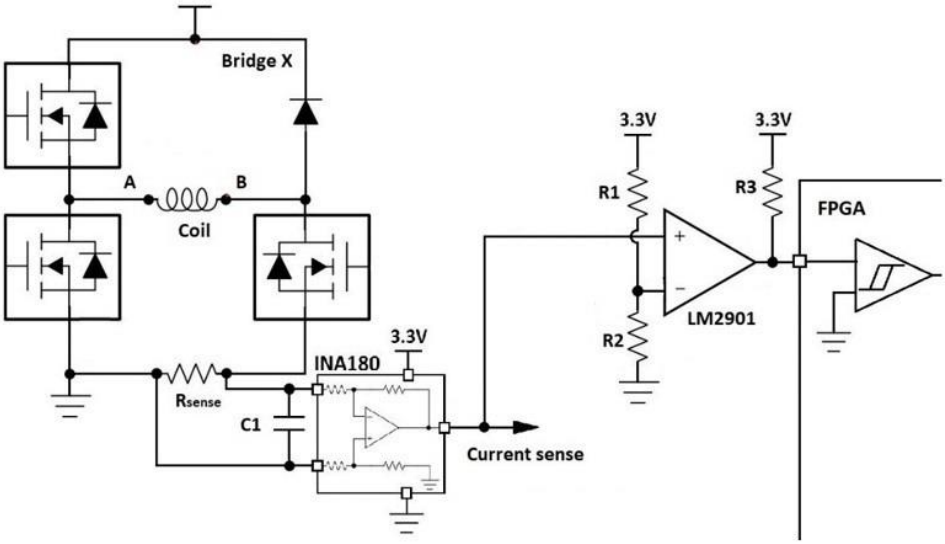

Figure 2.18. Fast-response overcurrent protection.

2.4.3.8 Fast over current protection (OCP)

A DD machine contains from 12 to 15 solenoid valves, which are connected by means of cables to the DD controller. Therefore, there is a possibility of short circuit (SC) scenarios such as coil lead short-to-ground, coil lead short-to-supply, and shorted load. According to Danfoss's requirements, the controller must possess SC protection with self-recovering after the SC conditions are gone. The NGCD possesses the following SC.

Short-to-supply protection half-bridge side

A short to supply from the half-bridge side (Figure 2.19) will be detected by low-side MOSFET VDS_OCP monitor feature. When overcurrent is detected the DRV8320H will turn-off the low-side MOSFET and activate the nFAULT output, which is connected to FPGA GPIO. The overcurrent threshold is determined by the pre-set value of the VDS_OCP threshold (see DRV832X datasheet).

The fault detection time is 4.23 us, consisting of VDS_OCP blanking time (4 us), driver propagation delay (150 ns) and MOSFET turn-off time (79 ns).

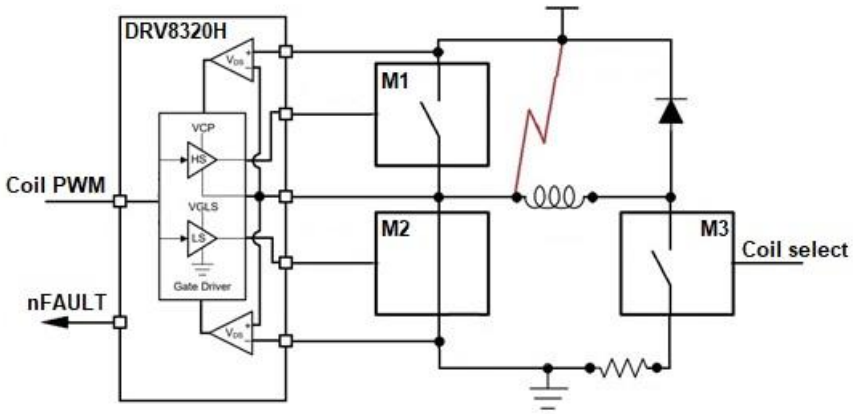

Figure 2.19. Short-to-supply protection from half-bridge side functional block diagram.

Short-to-ground protection half-bridge side

A short to ground from the half-bridge side (Figure 2.20) will be detected by high-side MOSFET VDS_OCP monitor. When overcurrent is detected the DRV8320H will turn-off the high-side MOSFET and activate the nFAULT output, which is connected to FPGA GPIO. The overcurrent threshold is determined by the pre-set value of the VDS_OCP threshold (see DRV832X datasheet).

The fault detection time is 4.23 us, consisting of VDS_OCP blanking time (4 us), driver propagation delay (150 ns) and MOSFET turn-off time (79 ns).

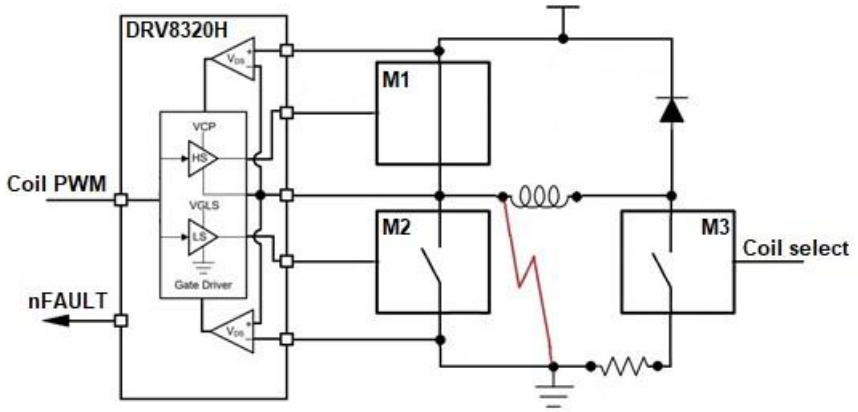

Figure 2.20. Short-to-ground protection from half-bridge side functional block diagram.

Short-to-supply protection low-side MOSFET (M3) side

A short to supply from coil connection side B (see Figure 2.21) will be detected by monitoring the voltage across the low-side current sense resistor. This gives a direct measurement of the current through the low-side MOSFET (M3). The voltage across the sense resistor is sensed by the low-side CSA, which is connected to the comparator's noninverting input, which in turn is connected to an FPGA GPIO.

Thus, when an overcurrent is detected, the FPGA will generate the appropriate signal to turn-off the low-side MOSFET.

The fault detection time of 4.481 us consists of the comparator prop delay (1.3 us), current sense amplifier prob delay (0.952 us), FPGA algorithm blanking time (2 us), low-side driver propagation delay (40 ns) and the MOSFET turn-off time (0.189 us).

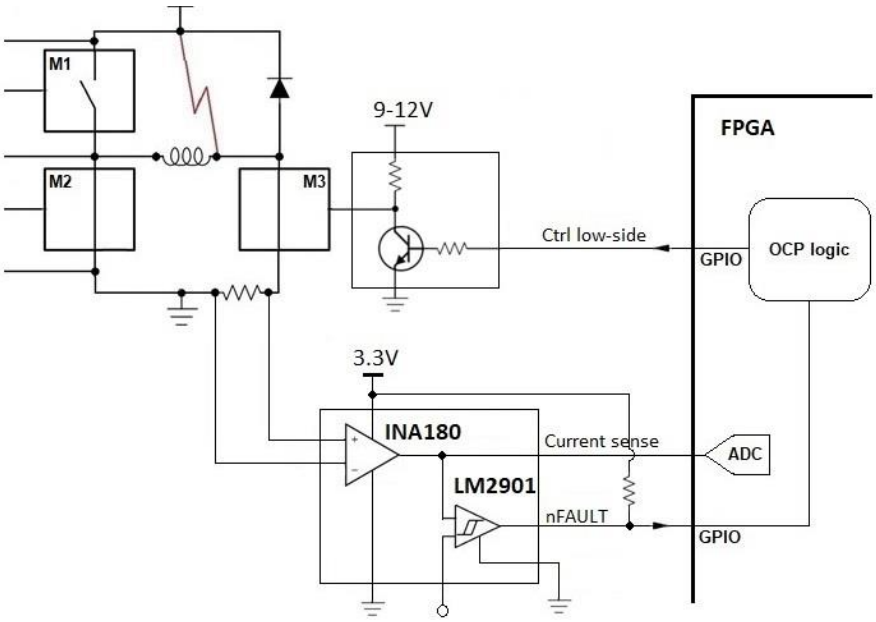

Figure 2.21. Short-to-supply protection from M3 side functional block diagram (M3 is switched on).

Another short-to-supply scenario from the MOSFET3 side is when the H-bridge is set in standby (also fast-decay) mode, when MOSFET3 is switched off and MOSFET2 is switched on (see Figure 2.22). In this case, the SC current will flow through the coil and the MOSFET2. The current will increase slowly due to coil inductance. When current reaches the VDS_OCP

threshold MOSFET2 will be switched off. However, the valve will be activated because VDS_OCP threshold must be larger than the solenoid pull-in current.

However, this SC scenario can be detected before the valve toggles, by the coil voltage sensing circuit (see Chapter 3), which senses voltage on the floating node between the diode and MOSFET3. The voltage on this node must be 0 V at the standby mode, when the SC takes place, this node will be pulled to supply, setting the output of the coil voltage sensing circuit high, thus indicating a fault.

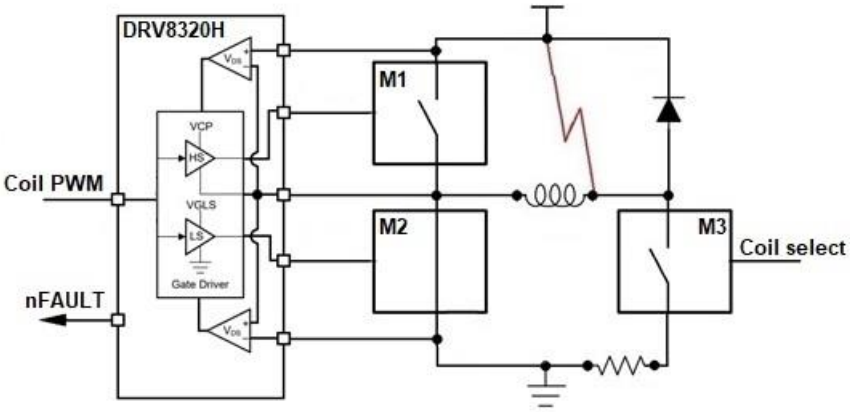

Figure 2.22. Short-to-supply protection from M3 side functional block diagram (M3 is switched off).

Shorted load protection

A shorted load (Figure 2.23) can be detected by the DRV8320H high-side VDS_OCP or by the low-side OCP (see Figure 2.20 and Figure 2.21).

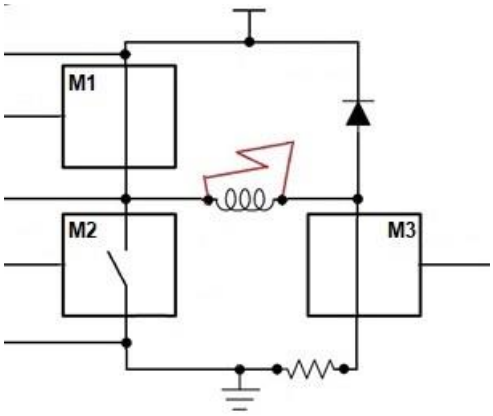

Figure 2.23. Shorted load schematic diagram.

2.4.4 NGCD prototype board design

This section describes the design of the "NGCD coil driver board 01A", which is the 3-channel coil driver prototype board based on NGCD design. Schematic and layout diagrams as well as components values calculation and design justification related to NGCD circuitry are given in this section. The description will be focused only on the NGCD circuit, the auxiliary circuitry such as power supplies, input protection or interface with the CPU boards will not be discussed. The design and manufacturing documentation is given in Appendix A.

2.4.4.1 DRV8320H setup

Table 2.6 shows the DRV8320H design parameters.

Table 2.6. DRV8320H design parameters

DESIGN PARAMETER		**REFERENCE**	**VALUE**
1	Nominal supply voltage	V_{VM}	24 V
2	Supply voltage range		9 V – 36 V
3	MOSFET part number	-	NVMFS6H824N
4	Target output rise time	t_r	< 150 ns
5	Target output fall time	t_f	< 100 ns
6	Maximum PWM Frequency	f_{PWM}	16 kHz
7	Peak current	I_{peak}	15 A
8	Operating ambient temperature	T_A	–20°C to +75°C

Figure 2.24 shows a schematic diagram of the DRV8320H setup. DRV8320H is set in 3x PWM Mode by connecting the MODE pin to the ground (GND) with a 47 kOhm resistor (R15). The INLx pins are tied to DVDD that provides +3.3 V, thus, pulling them high as required by the datasheet. The INHx pins are connected to FPGA that provides PWM logic to control the correspondent MOSFETs gates. The corresponding logic of the inputs and outputs state is listed in Table 2.7. Deadtime is controlled internally, which is set to 100 ns according to the datasheet.

Table 2.7. DRV8320H 3x PWM Mode Truth Table [32].

INLx	INHx	GLx	GHx	SHx
0	X	L	L	Hi-Z
1	0	H	L	L
1	1	L	H	H

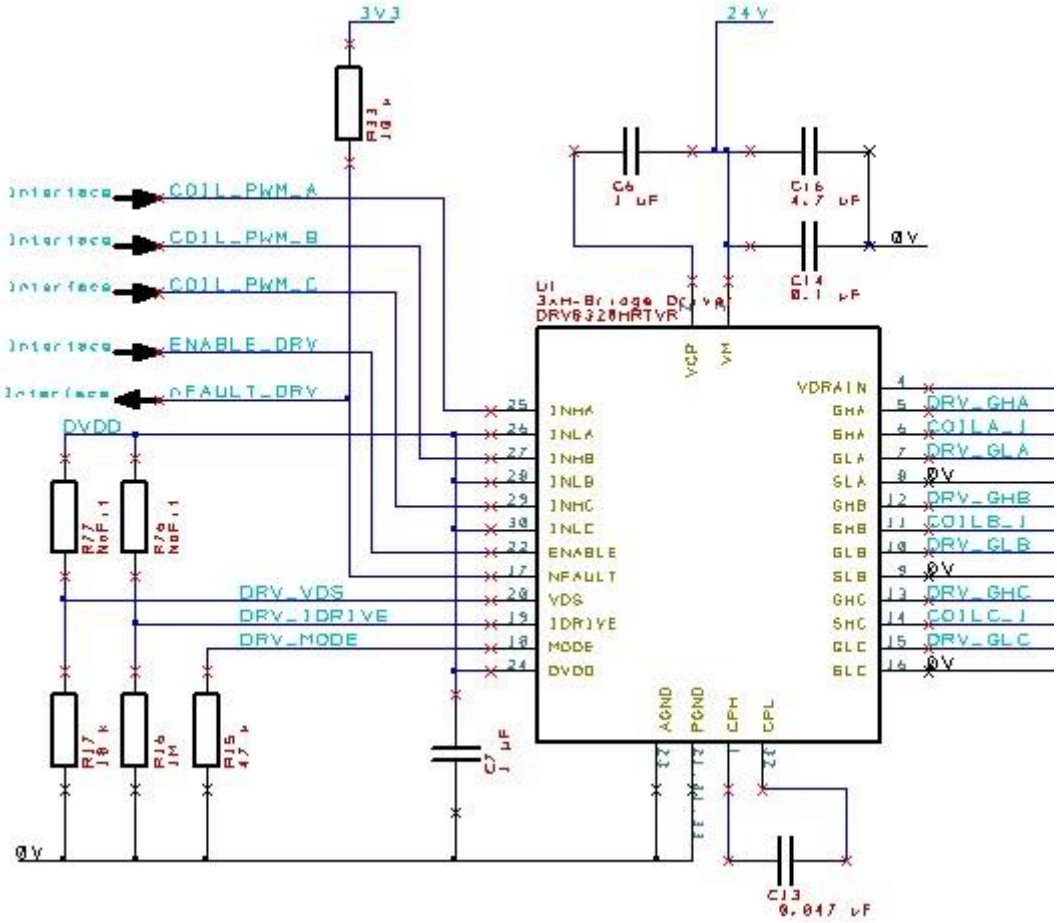

Figure 2.24. Schematic diagram of the DRV8320H circuit.

The MOSFETs over-current protection that is based on drain-to-source voltage monitoring (VDS_OCP). The VDS_OCP voltage threshold is set to 0.13- V by connecting the VDS pin to GND with an 18 kOhm resistor (R17). According to the datasheet, if drain-to-source voltage of the MOSFET exceeds the VDS_OCP threshold for longer than the blanking time (4 us), a VDS_OCP event is recognized and the correspondent MOSFET will be switched off and the NFAULT pin will be pulled down, which is connected to the FPGA. The DRV8320H does an automatic retry every 4 ms.

The VDS_OCP current threshold depend on drain-to-source resistance of the MOSFET. The drain-to-source resistance of a forward biased H-bridge MOSFET (NVMFS6H824N) is between 3 mOhm at -25°C and 6.3 mOhm at 75°C [33], which gives the VDS_OCP current threshold between 43 A and 21 A accordingly, which is above the maximum peak current established for the design.

The current MOSFETs gate is set to 120 mA (I_{Source}) for the turn-on and 240 mA (I_{Sink}) for the turn-off stage by connecting the IDRIVE pin to GND with a 1 MOhm resistor (R15). Therefore, according to [34], the MOSFET's rise time (t_r) and the fall time (t_f) can be approximated according to equations (9) and (10) respectively, using gate-to-drain charge (Q_{GD}) values form the datasheet.

$$t_r = \frac{Q_{GD}}{I_{Source}} = \frac{7 * 10^{-9}}{0.12} = 58ns \quad (9)$$

$$t_f = \frac{Q_{GD}}{I_{Sink}} = \frac{7 * 10^{-9}}{0.24} = 29ns \quad (10)$$

t_r and t_f will be used to estimate switching losses of the MOSFETs.

Both values of t_r and t_f are complies with the design parameter 4 and 5 from Table 2.6.

According to [34], the MOSFET3 propagation delay ($t_{d(off)}$) can be estimated according to equation (11)

$$t_{d(off)} = \frac{Q_{GS}}{I_{Sink}} = \frac{12 * 10^{-9}}{0.24} = 50\ ns \quad (11)$$

Where Q_{GS} is the gate−to−source charge and I_{Sink} is the turn-off peak current of the MOSFET.

The total turn-off time of the MOSFET can be found as the sum of t_f and $t_{d(off)}$, which is 79 ns. This value will be used for overcurrent protection (OCP) response time estimation.

Figure 2.25 illustrates a MOSFET switching time test circuit and the input and output waveforms.

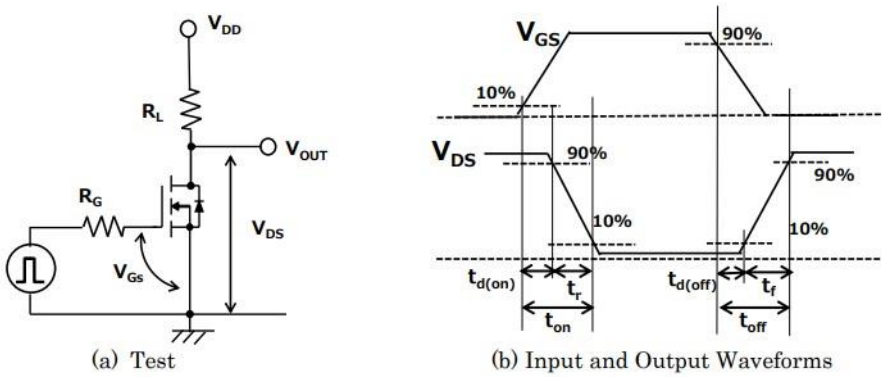

Figure 2.25. SMOSFET switching time test circuit and Input/Output waveforms [35].

The maximum PWM frequency of the application depend on the ADC sampling rate. This design is developing for Xilinx Artix-7 and ZYNQ-7000 FPGAs, the ADC maximum sampling rate of which is 1 MSPS. The worst-case scenario will be when the hysteresis coil current control is used because the PWM frequency is not constant. Therefore, maximum PWM frequency $f_{PWM(max)}$ can be found according to equation (12).

$$f_{PWM(max)} = \frac{ADC_{sampling\ rate}}{2 * N_{ADC\ channels}} = \frac{1 * 10^6}{2 * 16} = 31.25\ kHz \qquad (12)$$

However, when using hysteresis current control technique, the PWM frequency will never reach its maximum value of 31.25 kHz because of the large inductance of the DD valve solenoid coil (5-7 mH). Additionally, the maximum PWM frequency can be reduced by increasing the hysteresis threshold values. Therefore, the maximum that will be used for this design is 16 kHz, which is far below the maximum switching frequency (200 kHz) from the DRV8320H datasheet.

According to [32], for the supply voltage (V_{VM}) above 13 V, the maximum limit for the charge pump current (I_{VCP}) is 25 mA. From equation (13), the I_{VCP} = 1.82 mA, which is below the max limit.

$$I_{VCP} = 3 * Q_G * f_{PWM} = 3 * 38 * 10^{-9} * 16 * 10^3 = 1.82\ mA \qquad (13)$$

The same current of 1.82 mA will be taken by the low-side MOSFETs, which is below the maximum limit (75 mA) from the DRV8320H datasheet.

The internal 3.3 V LDO, which can supply a load up to 30 mA, is providing current for the following logic levels pins. Three INL pins with internal pull-down resistor of 100 kOhm, MODE pin with total voltage divider resistance of 97 kOhm, IDRIVE pin with total voltage divider resistance of 148 kOhm, and VDS pin with total voltage divider resistance of 91 kOhm. Therefore, the total current provided by the LDO will be 192 uA, which is below the maximum limit from the datasheet.

The 10k resistor (R33) pulls up the open drain NFAULT pin to the high logic voltage level (3.3 V). At 10 kOhm the NFAULT current will be 3.3 mA, which is below the input maximum limit of 5 mA.

Using calculated internal LDOs current values, the approximate power losses of the DRV8320H at the maximum supply voltage of 36 V (see Table 2.6) were estimated, which are 0.1 W (roughly). According to datasheet, the DRV8320H junction-to-ambient thermal resistance of the 32-pin WQFN package is 32.9°C /W. Therefore, the maximum junction temperature at the design maximum supply voltage and the maximum ambient temperature (see Table 2.6) will be 78.29°C, which is far below the operating junction temperature of 150°C from the datasheet.

Parameters of the charge pump and decoupling capacitors C6, C7, C13, C14, C16 are chosen according to the recommendations from the DRV8320H datasheet.

2.4.4.2 Low-side gate driver setup

Table 2.8 shows the target parameters of the Low-side gate driver design

Table 2.8. Low-side gate driver target design parameters.

DESIGN PARAMETER		**REFERENCE**	**VALUE**
1	Nominal supply voltage	V_{VM}	10 V
2	Supply voltage range		9 V – 12 V
3	MOSFET part number	-	NVMFS6H824N
4	Target turn-off delay time	$t_{d(off)}$	< 300 ns
5	Target fall time	t_f	<100 ns
6	Maximum PWM Frequency	f_{PWM}	50 Hz
7	Operating ambient temperature	T_A	–20°C to +75°C

Figure 2.26 shows a schematic diagram of the low-side driver, which is the open-collector level-shifter circuit based on the NPN bipolar junction transistor (BJT) Q11. The R73 resistor of 1.8 kOhm limits the collector current, and the R10 of 1.8 kOhm limits the base current of the BJT. The 4.7 Ohm resistor is placed to limit the MOSFET gate current during its turn-off. Resistor R55 of 51.1 kOhm pulls the gate to the ground (GND) to make sure the MOSFET is off at the start-up of the controller. The 10 kOhm resistor R29 connects the BJT base to the 3.3 V power supply, which is also used to enable the coil driver power supply of 10 V (see Figure 2.27), thus, the BJT will be placed to operate in the saturation region before the power supply of the gate driver switches on. This setup ensures the low-side MOSFET stays off until the FPGA is configured.

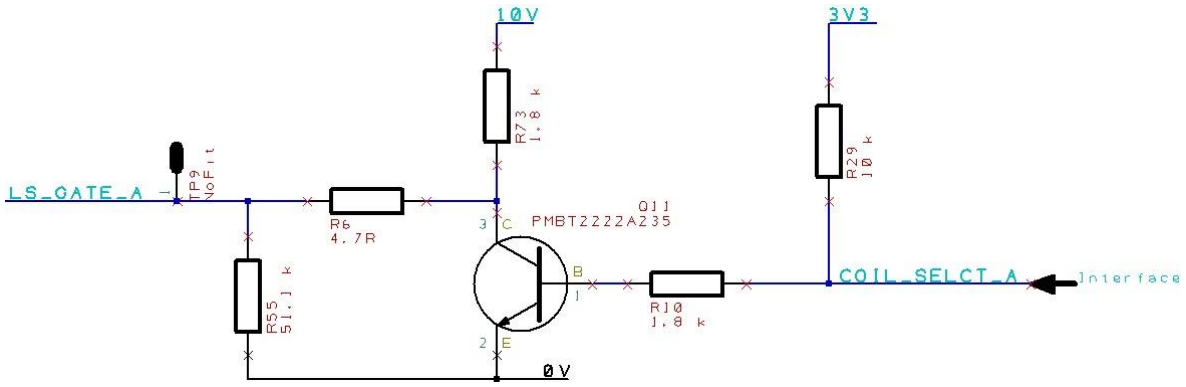

Figure 2.26. Schematic diagram of the low-side driver circuit.

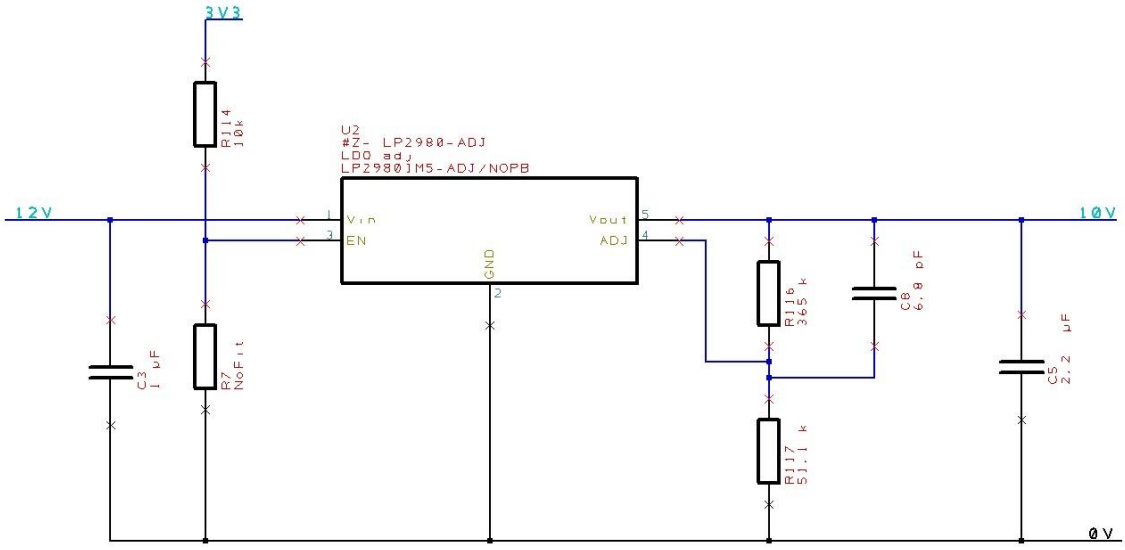

Figure 2.27. Schematic diagram of the low-side driver power supply circuit.

Figure 2.28 shows the LTspice model of the proposed low-side gate driver circuit. This model was used to prove the concept of the design and verify its parameters. The spice model of the NVMFS6H824N MOSFET was downloaded from the ONSEMI website [36].

As can be seen from the simulation results (Figure 2.29), during the turn-on event, the MOSFET current is close to 0 A due to the high inductance of the load. This ensures the lossless switching of the MOSFET at the turn-on. Therefore, an increased rise time (t_r) up to 2.31 us, due to the high value of the BJT collector current limiting resistor R2, will not affect the MOSFET thermal performance. However, decreasing the resistance of the R2 resistor to decrease the turn-on time of the MOSFET will lead to an excessive current through the BJT and increased power consumption of the gate driver.

During the turn-off stage, the current through the MOSFET is 12 A, which will generate switching losses. However, a small fall time (t_f) of 60ns and a switching frequency of 50 Hz make these losses negligible.

Figure 2.30 shows the MOSFET gate current, and Figure 2.31 shows the BJT collector, emitter, and gate currents, which are far below the maximum limits from the datasheet [37].

A summary of the low-side gate driver characteristics according to the simulation results is given in Table 2.9.

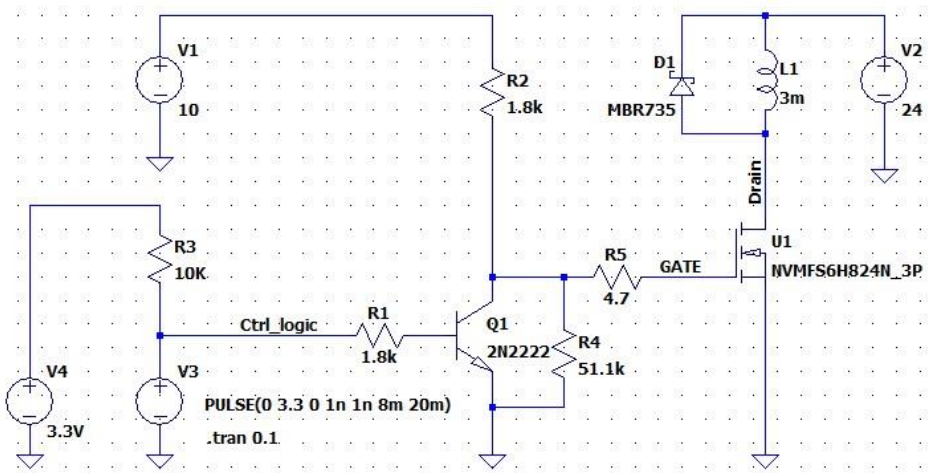

Figure 2.28 Low-side drive LTspice model.

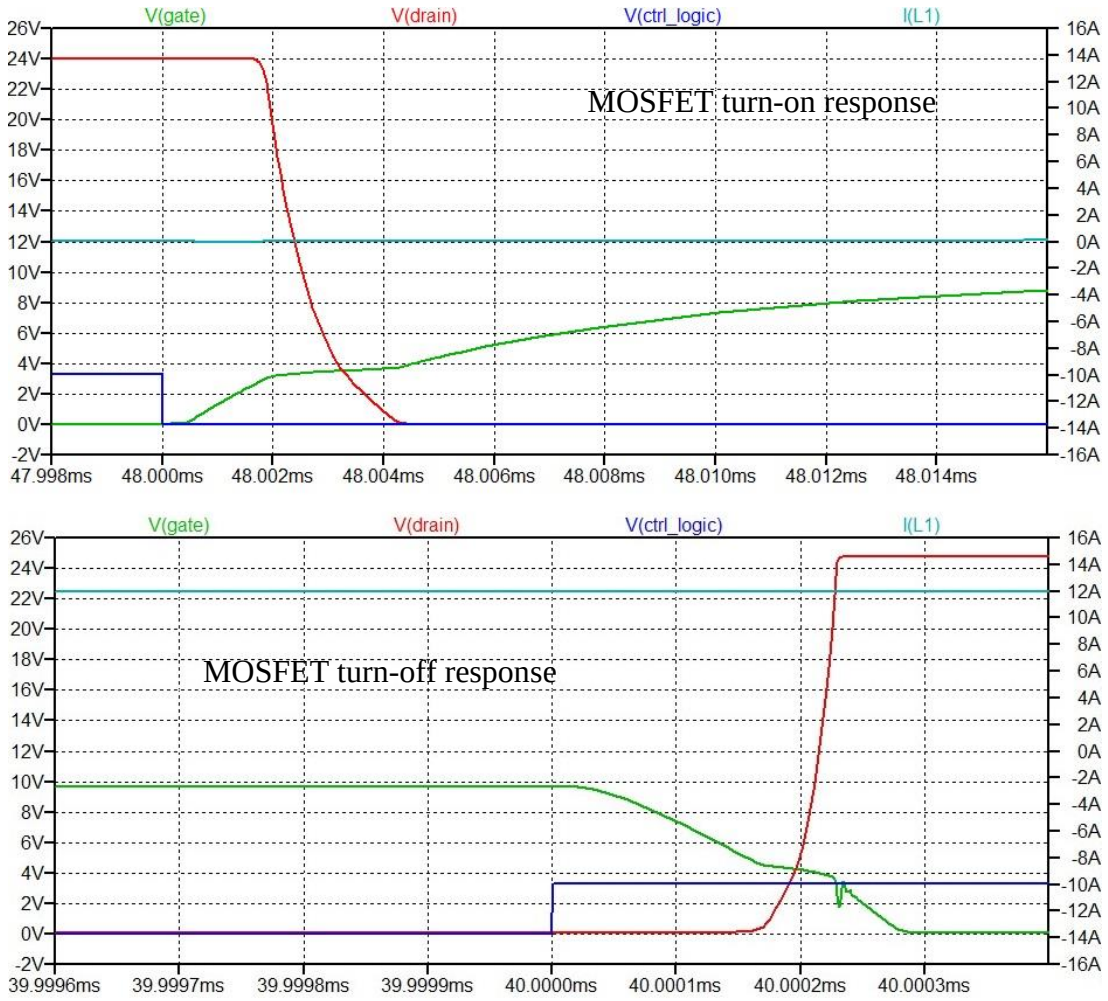

Figure 2.29. Low-side driver LTspice simulation results (MOSFET transients).

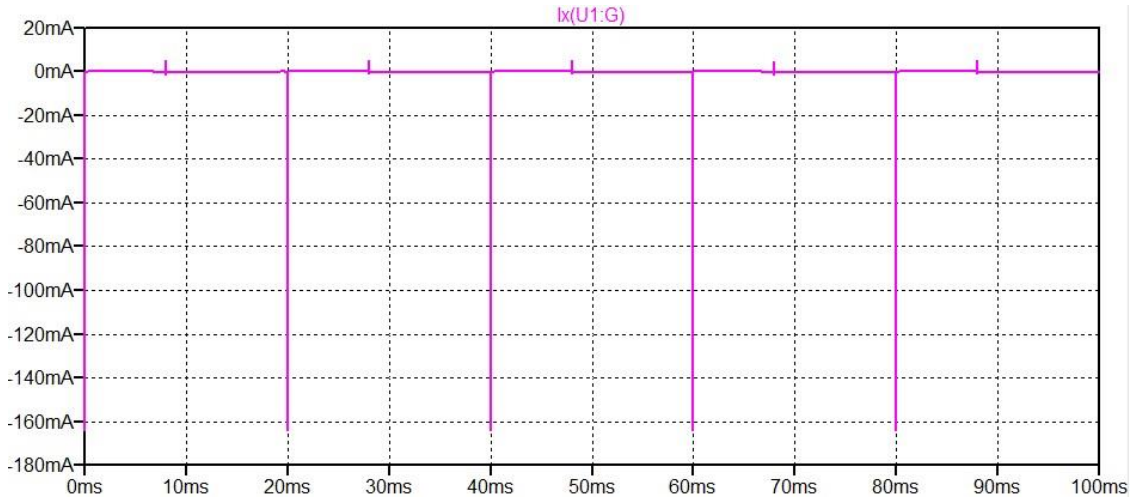

Figure 2.30. Low-side driver LTspice simulation results (MOSFET gate current).

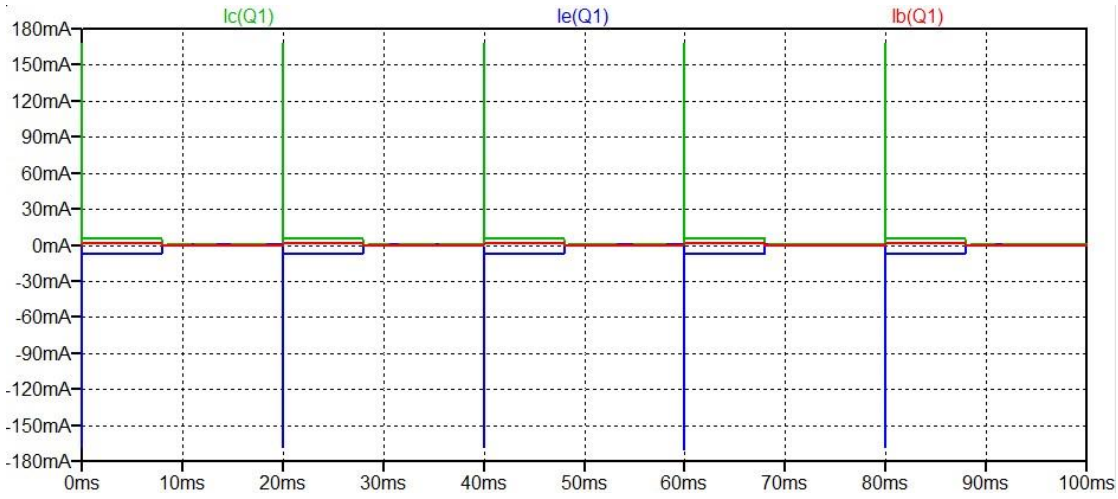

Figure 2.31. Low-side driver LTspice simulation results (BJT base, collector, emitter currents).

Table 2.9. Summary of the low-side gate driver characteristics.

PARAMETER	**REFERENCE**	**VALUE**
Nominal supply voltage	V_s	10 V
Supply voltage range		9 V – 12 V
MOSFET part number	-	NVMFS6H824N
Rise time	t_r	2.31 us
Fall time	t_f	60 ns
Delay turn-on time	$t_{d(on)}$	1.40 us
Delay turn-off time	$t_{d(off)}$	129 ns
Delay turn-on propagation delay	$t_{PD(on)}$	0.46 us
Delay turn-off of propagation delay	$t_{PD(off)}$	40 ns
Source current	I_{source}	< 7.5 mA
Sink current	I_{sink}	< 600 mA
Standby current at nominal supply voltage	I_{idle}	5.6 mA
Maximum switching frequency	f_{sw}	50 Hz
Operating ambient temperature	T_A	–20°C to +75°C

2.4.4.3 Current sensing setup

Table 2.10 shows the target design parameters of the current sensing circuit of the NGCD prototype board.

Table 2.10. Current sensing target design parameters.

DESIGN PARAMETER		REFERENCE	VALUE
1	Power-supply voltage	V_{supply}	3.3 V
2	Low-side current sensing	-	VCM = 0 V
3	Mode of operation	-	Unidirectional
4	Maximum sense current	I_{max}	15 A
5	Maximum sense current	I_{min}	0.1 A
6	Nominal sense current range		3-12 A
7	Small-signal bandwidth	-	> 120 kHz
8	CSR maximum power dissipation	PD_{max}	< 1.5 W
9	CSR package – (in)	$Case\ Code$	1206
10	Maximum operating temperature	$T_{A\,max}$	–20°C to +75°C
11	Current sensing total error	$Total\ Error$	< 2.5% at the nominal current range, TJ = 75°C

Figure 2.32 shows the schematic diagram of the current sensing circuit of the NGCD prototype board, where U3 is the current sense amplifier (CSA), R1 is the current sense resistor (CSR), and C29 is a decoupling capacitor that ensure the CSA supply is stable. Due to the low cost and small package, the INA180 was chosen as the CSA for the NGCD design. According to [38], the accuracy of the CSA is better for larger values of the CSR. However, to keep the cost and the footprint of the circuit as small as possible the size and the dissipation power of the CSR were limited by the parameters 8 and 9 from Table 2.10. Therefore, using values from the design parameters table, the maximum value of the CSR was found from equation (14).

$$R_{sense} < \frac{PD_{max}}{I_{max}^2} = \frac{1.5}{15^2} \cong 0.007\ Ohm \tag{14}$$

The CSR TLR2BPDTD7L00F75 of 0.007 Ohm, 1.5 W, and 75 ppm/C was chosen for this application.

Next step was to choose the GAIN of the CSA, which was from equation (15)

$$GAIN < \frac{V_{supply}}{I_{max} * R_{sense}} = \frac{3.3}{15 * 0.007} \cong 31 \tag{15}$$

The CSA INA180A1IDBVR of GAIN 20 and bandwidth of 350 kHz was chosen for this design.

According to [39], the positive and negative output swing limitations must be examined to make sure that the current-sense signal is properly passed to the output. Equations (16) and (17) examine the positive and negative output swing limitations accordingly.

$$V_{SP} > I_{max} * R_{sense} * GAIN \rightarrow \ 3.27 > \ 15 * 0.007 * 20 = 2.1 \qquad (16)$$

$$V_{SN} < I_{max} * R_{sense} * GAIN \ \rightarrow 0.0005 < 0.1 * 0.007 * 20 = 0.014 \qquad (17)$$

Where V_{SP} and V_{SN} are the positive and negative output swings from the datasheet.

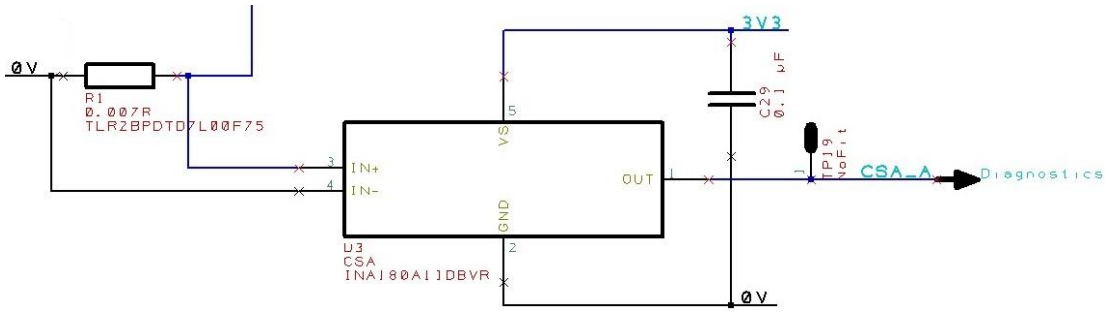

Figure 2.32. Schematic diagram of the current sensing circuit.

Current sensing circuit error analysis

The CSA error tool from Texas Instruments was used to analyse the total current sense error of the circuit. The tool is based on equation (18), it takes into account a range of the parameters of the analysed CSA and system operating condition inputs from users, the output is the error curve across an adjustable current range.

$$e_{RSS} = \sqrt{(e_{Vos} + e_{CMRR} + e_{PSRR})^2 + e_{Ibias}^2 + E_{GAIN}^2 + e_{CSR}^2} \ ; \ (\%) \qquad (18)$$

Figure 2.33 shows the input values of the designed system and Figure 2.34 shows the input parameters specified by the tool according to the datasheet of the selected device, which is INA180. Figure 2.35 shows the error analysis results of the current design.

System Operating Conditions	
Supply Voltage (V)	3.3
Common Mode Voltage (V)	0
Room Temp Calibration	No
Desired Temperature (°C)	75
System Current Conditions	
Maximum Measured Current (A):	15
Nominal Measured Current (A):	7
Minimum Measured Current (A):	0.5
Use Maximum Calculated Shunt?	No
Shunt Resistor Specifications	
Shunt Resistor (mΩ)	7
Resistor Tolerance (%)	1.00%
Resistor Drift (ppm/C)	75.0

Figure 2.33. System operation conditions inputs according to the design parameters.

Parameter	INA180x1 (Low side)
Operational V_{CM} Range	-0.2 V to 26 V
Surviving V_{CM} Range	-0.3 V to 26 V
Gain (V/V)	20
Gain Error @ 25°C (max)	0.80%
Gain Error Drift (ppm/°C)	20
Gain Error @ 75°C (max)	0.90%
V_{OS} @ 25°C (max µV)	150
V_{OS} Drift (max µV/°C)	1
VOS @ 75°C (max µV)	200
CMRR (min dB)	84
PSRR (min dB)	88
Supply Voltage Range	2.7 V to 5.5 V
I_Q (max mA)	0.3
I_B (typ µA)	80
I_{SD} (max µA)	N/A
Analog Output Specifications	
Bandwidth (kHz)	350
Slew Rate (V/µs)	2
Swing To Ground (mV)	5
Digital Output Specifications	
Number of ADC Bits	N/A
Fastest Conversion Time	N/A
Digital Interface Options	N/A
Additional Information	
Low-Side capable	✓
Bi-directional Capable	
ALERT Function Included	
Other Special Feature(s)	
Additional Qualified Options:	AEC-Q100 Grd 1
Operating Temp Range (°C)	-40°C to 125°C
Package(s)	SOT-23 (5)

Figure 2.34. INA180 parameters inputs according to the datasheet.

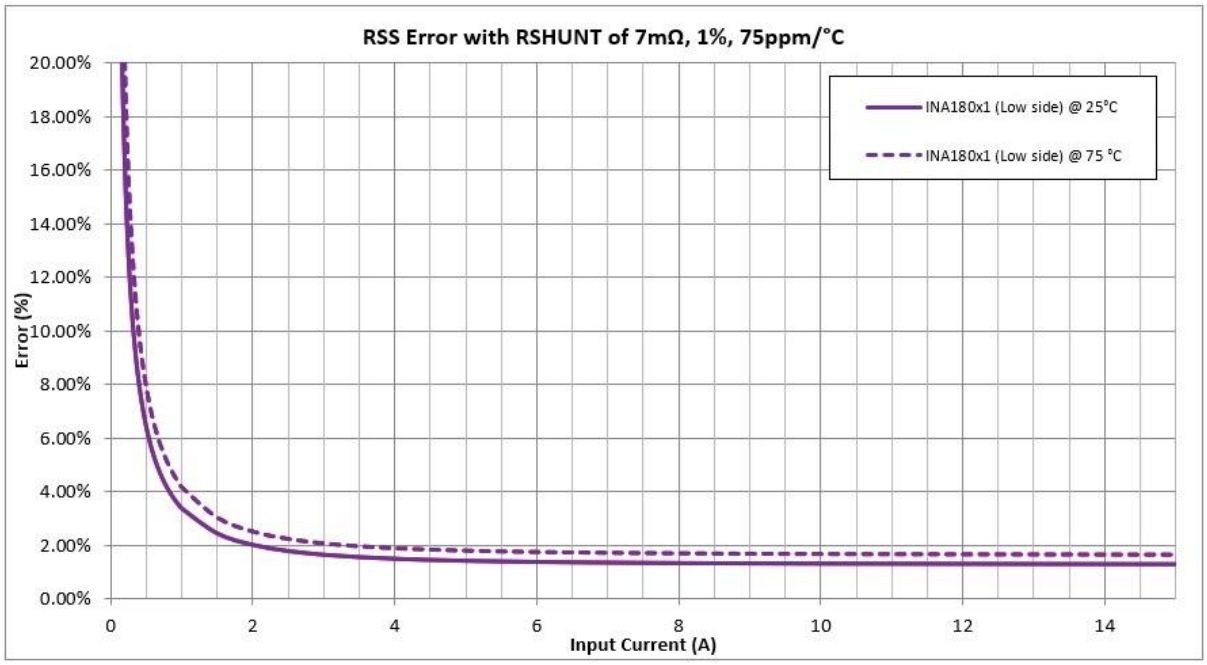

Figure 2.35. Error analysis results of the NGCD prototype board current sensing circuit.

From the error analysis results can be seen that the total current sense error at the nominal current range from 3 A to 15 A and at the temperature of 75°C is below the established limit of 2.5%, established by the design parameters. This will allow precise closed-loop coil current control.

High-side current sensing vs low-side current sensing

To illustrate the benefits of the proposed low-side current sensing circuit against the high-side current sensing circuit that is used in the present DD controller (DPC12 MK1), the error comparison between a low-cost CSA that is used in the proposed design INA180 and a CSA of higher cost and higher precision CSA INA185 was carried out. The comparison results are shown in Figure 2.36.

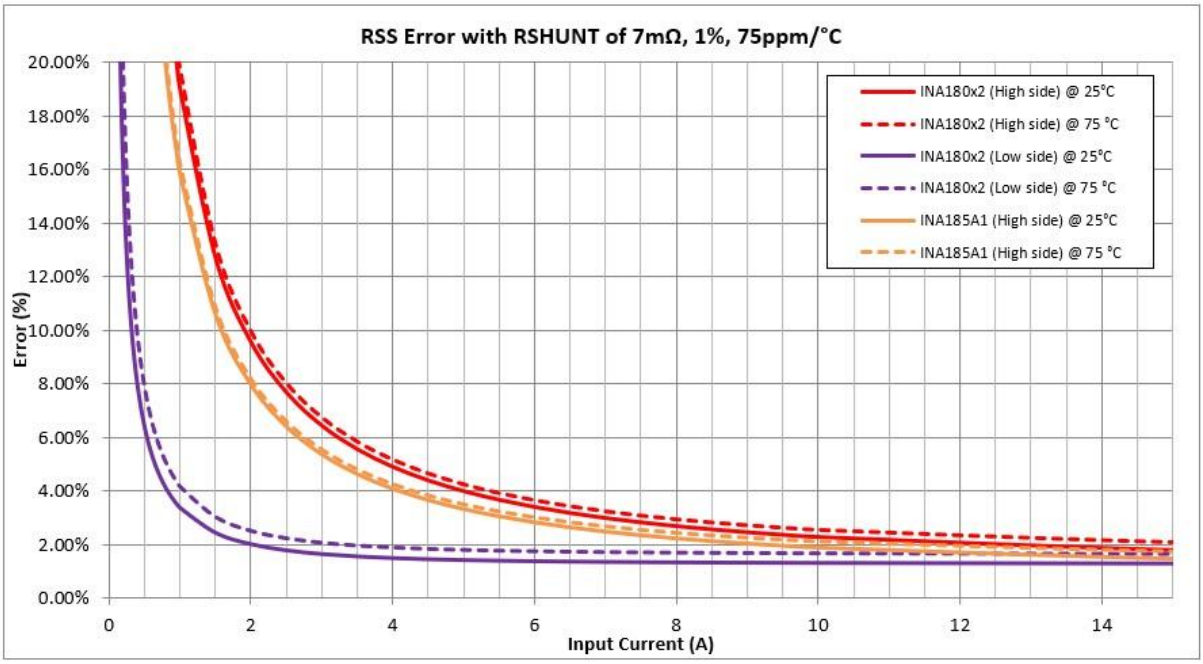

Figure 2.36. Current sensing error comparison between the low-side the high-side current sensing methods.

As can be seen from the comparison results, for the current range up to 10 A, the precision of the low-side current sensing is much higher than the precision of the high-side current sensing, even using more expensive current sense amplifiers.

For instance, the peak current of the PAV8 and MAV10 pumping current profiles is 5 A. Taking into account that the response time stabilisation of a cyclically operated valve requires the coil current profile at each switching cycle to be as close as possible to the reference (see Chapter 4), the illustrated increase of the current sensing error may lead to a decrement of the operation stability of the DD machine or will require additional measures for compensation of the timing error. Also, it will significantly affect valve diagnostics, such as coil temperature estimation by coil resistance, which requires precise current measurement in the range below the solenoid actuation point (2-3 A).

2.4.4.4 Low-side overcurrent protection (OCP) setup

Table 2.11 shows the target design parameters for the low-side fast overcurrent protection (OCP).

Table 2.11. Low-side overcurrent protection design parameters.

Input	Overcurrent Conditions		Output	Supply
CSA	I_{OC_TH}	t_{resp_OCP}	OCP_{out}	V_{supply}
INA180A1	15 A	< 2.5 us	Open collector	5 V

Figure 2.37 shows a schematic diagram of the low-side overcurrent protection circuit designed for NGCD prototype board, where resistors R97 and R98 forms a voltage divider that provides the reference voltage equal to the CSA threshold voltage CSA (V_{th}), resistor R96 connects open collector of the comparator to 3.3 V supply to provide high logic signal at normal operation condition, capacitors C29 and C9 ensure that comparator supply and reference voltages are stable.

According to [40], the OCP design calculation should include the following aspects.

At first, the output voltage of the chosen CSA (V_{th}) at the threshold current was determined from equation (19), which is 2.1 V.

$$V_{th} = I_{OC\_TH} * R_{sense} * GAIN_{CSA} = 15 * 0.007 * 20 = 2.1\ V \quad (19)$$

Next, the response time of the CSA was determined from equation (20), which is 952 ns.

$$t_{resp\_CSA} = \frac{V_{out}}{SR_{CSA}} = \frac{2.1}{2} = 952\ ns \quad (20)$$

Where SR_{CSA} is the slew rate of current sense amplifier from the datasheet.

Finally, an open collector output comparator with a response time smaller or equal 1.548 us ($t_{resp\_OCP} - t_{resp\_CSA}$) and of a 5 V supply voltage must be chosen. The 4-channel comparator LM2901DR2G of the supply voltage range 3 – 36 V and the response time of 1.3 us match the established design requirements.

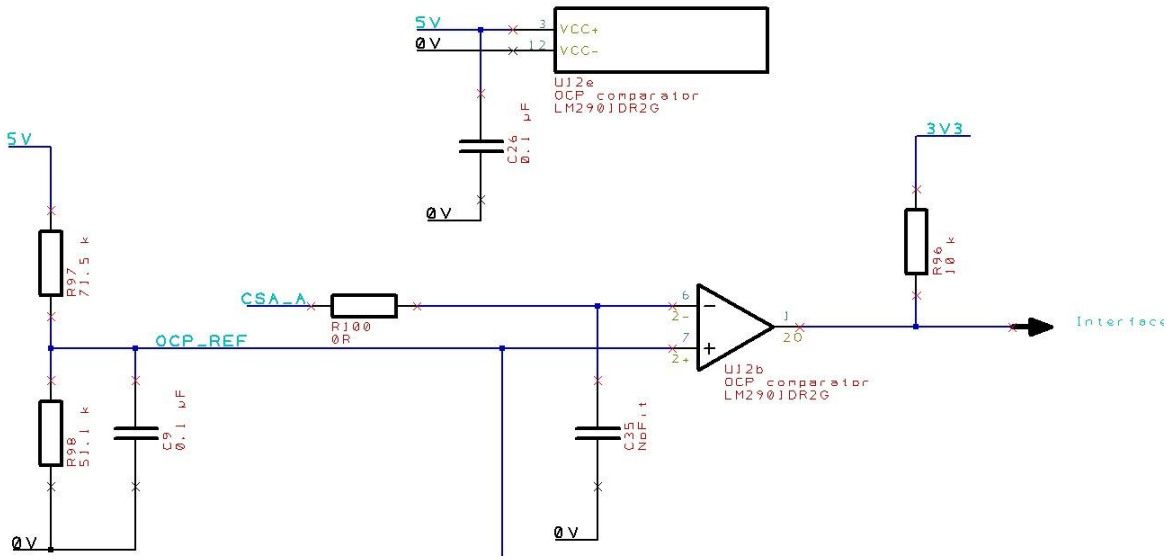

Figure 2.37. Schematic diagram of the low-side overcurrent protection (OCP) circuit.

Taking into account the low-side driver propagation delay of 40 ns, the MOSFET turn-off time of 189ns (see 2.4.3.5) and 2 us blanking time of the developed firmware (see Appendix B), the total response time of the low-side overcurrent protection response time is 4.481 us, which is nearly the same as the DRV8320H OCP response time (4.229 us).

2.4.4.5 H-bridge setup

Table 2.12 shows the NGCD prototype board H-bridge target design parameters.

Table 2.12. H-bridge design parameters.

DESIGN PARAMETER		**REFERENCE**	**VALUE**
1	Nominal supply voltage	V_{VM}	24 V
2	Supply voltage range		9 V – 36 V
3	MOSFET part number	-	NVMFS6H824N
4	ESD protection clamping voltage	V_{CL}	< 65 V
5	Short circuit current	I_{SC}	< 450 A
6	Peak current	I_{peak}	15 A
7	Average current	I_{DC}	5 A
8	Maximum switching frequency	f_{sw}	16 kHz
9	Operating ambient temperature	T_A	–20°C to +75°C

Figure 2.38 shows a schematic diagram of the H-bridge circuit of the NGCD prototype boards where bridge MOSFETs Q1, Q2, Q8 and bridge diode D16 are switching the voltage or its polarity applied to the solenoid coil. A clamping diode of working voltage 38 V and 58 V clamping voltage D19 is used to protect the circuit against electrostatic discharges (ESD). Decoupling capacitor C1 of 0.01 uF is used to supply high-frequency currents. Parameters calculation of the H-bridge main components is given below.

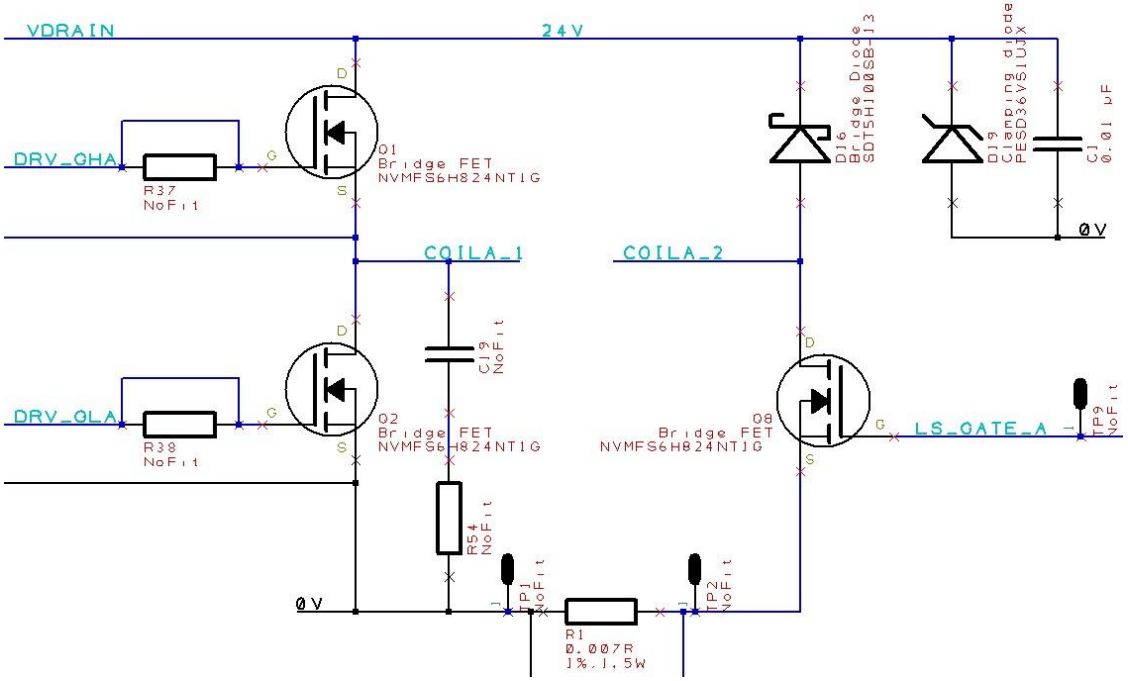

Figure 2.38. Schematic diagram of the H-bridge circuit.

Bridge MOSFETs short circuit (SC) compliance calculation

Because the final controller design is intended to be automotive, the parameters of the automotive setup were used to model a short circuit (SC) scenario.

According to [41], in automotive systems, SC to the battery has a low probability and applies an additional impedance of the conductors that connect controller to the battery, which will limit the fault current. The most severe SC scenario is that which is supplied from the local bulk capacitance.

In our case, the worst-case SC scenario is the coil lead to ground (GND), which is affecting the high-side MOSFET and should be neutralised by the DRV8320H overcurrent protection (OCP) within 4.3 us.

Figure 2.39 shows the LTspice model of the short circuit (SC) worst-case scenario for the NGCD prototype board. The assumption is made the controller should be connected to the power supply by a 5 AWG cable of a minimum length of 1m (L2), and the short circuit (SC) is caused by a 14 AWG cable of a minimum length of 0.02 m (L1). The minimum on-state resistance ($R_{DS\text{-}on}$) of the MOSFET (R1) is the minimum resistance at -25°C from the datasheet. The NGCD prototype board bulk capacitance is 720 uF (C1, C2, C3). Switch SW1 connects the circuit to the ground for 4.3 us, thus, imitating the short-circuit (SC).

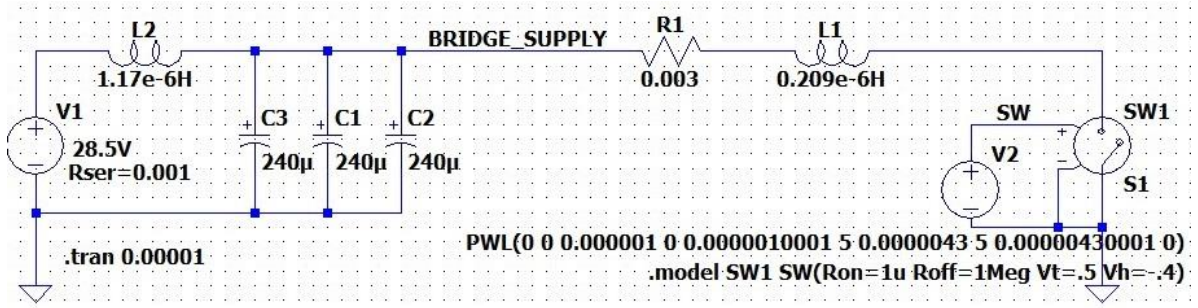

Figure 2.39. LTspice model of the short-circuit (SC) worst-case scenario for the NGCD prototype board.

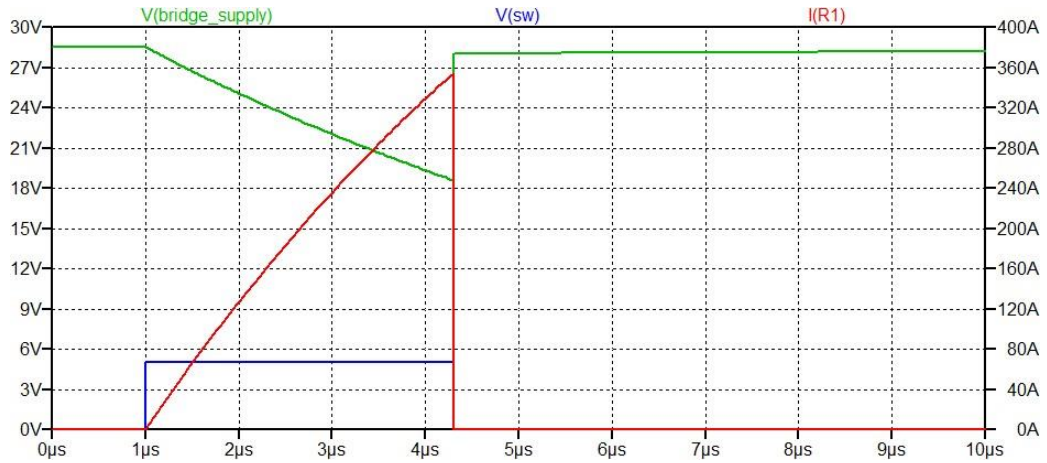

Figure 2.40. Simulation results for the short-circuit (SC) worst-case scenario for the NGCD prototype board.

From the simulation results (Figure 2.40), the worst-case scenario short-circuits (SC) current I_{SC} for the NGCD prototype board is 350 A, which mostly depends on the bulk capacitance (at constant R1, L1, and L2). However, for the 15-channel DD controller, the bulk capacitance is

expected to be 1500-2000 uF. Therefore, a short-circuit current I_{SC} of 450 A will be used for further calculation. From Figure 2.41 can be seen that the bridge MOSFET (NVMFS6H824N) can withstand the current of 450 A at drain-to-source voltage 28.5 V during 10 us, which is far above the overcurrent protection (OCP) response time of 4.3 us.

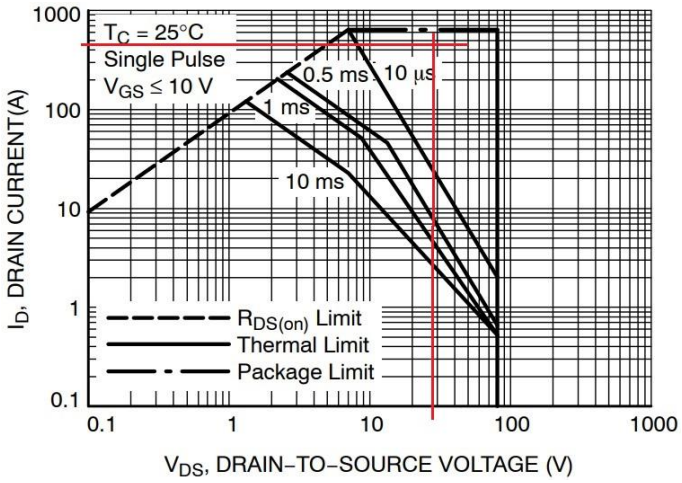

Figure 2.41. Maximum rated forward biased safe operating area of the bridge MOSFET NVMFS6H824N [36].

According to [42], the next step is to calculate the MOSFET junction temperature during the short-circuit (SC) conditions $T_{j(SC)}$ from equation (21).

$$T_{j(SC)} = T_{A(max)} + I_{SC}^2 * R_{DSon(max)} * R_{\theta jc} = 75 + 450^2 * 0.0063 * 0.022 = 103°C \quad (21)$$

Where $R_{DS(on)}$ is the MOSFET's maximum on-state drain-to-source resistance from the datasheet at the application maximum temperature $T_{A(max)}$ (see Table 2.12), $R_{\theta jc}$ is transient thermal resistance that corresponds to a square single pulse of the fault duration (4.3 us in this case) from the datasheet (see Figure 2.42).

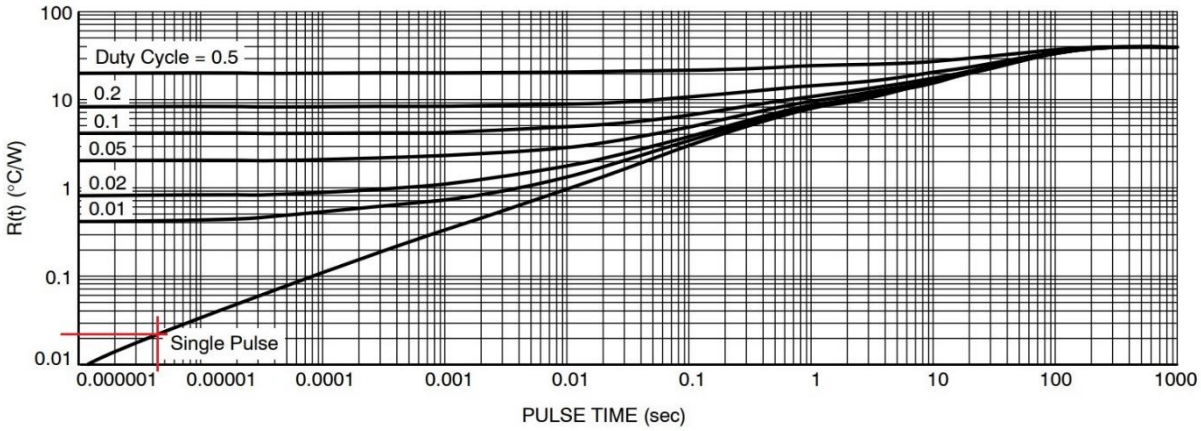

Figure 2.42. Thermal characteristics of the bridge MOSFET NVMFS6H824N [36].

Thus, the bridge MOSFET temperature at the worst-case short-circuit (SC) scenario will be below 103°C, which is far below the MOSFET's maximum operating junction temperature of 175°C from the datasheet.

Bridge MOSFETs average current compliance calculation

At first, the average current of the maximum expected load must be defined.

At present, the prototype DD motoring valve MAV10 during motoring at 3000 rpm provides the maximum load. A generic motoring current profile for a single coil DD valve is shown in Figure 2.43. Table 2.13 shows the current profile parameters of the prototype DD motoring valve MAV10 at 3000 rpm, which were established experimentally.

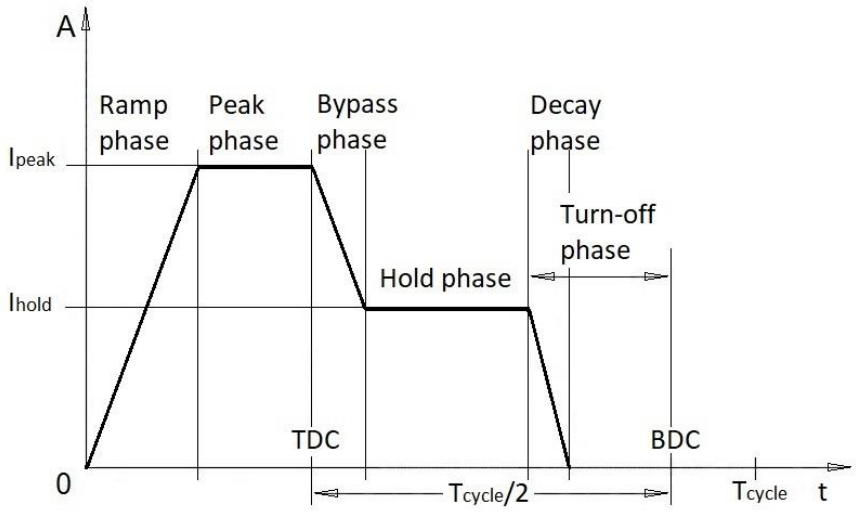

Figure 2.43. Motoring current profile of a single coil DD solenoid valve.

Table 2.13. Current profile parameters of the prototype DD motoring valve MAV10 at 3000rpm.

PARAMETER	REFERENCE	VALUE
Peak current	I_{peak}	10 A
Hold current	I_{hold}	5 A
Ramp phase time	t_{ramp}	4 ms
Peak phase time	t_{peak}	4 ms
Bypass phase time	t_{bypass}	1.5 ms
Hold phase time	t_{hold}	1.5 ms
Decay phase time	t_{decay}	1 ms
Turn-off time	$t_{turn-off}$	7 ms
Switching cycle period at 3000rpm	T_{cycle}	20- ms

From Figure 2.43 can be derived equation (22) to be used for the calculation of the average current of the coil.

$$I_{coil_{DC}} = \frac{(\frac{I_{peak}}{2} * t_{ramp} + I_{peak} * t_{peak} + (\frac{I_{peak}-I_{hold}}{2} + I_{hold}) * t_{baypass} + I_{hold} * t_{hold} + \frac{I_{decay}}{2} * t_{decay})}{T_{cycle}} \quad (22)$$

Therefore, using current profile parameters from Table 2.13, from equation (22) the average coil current at the maximum expected load is 4.56 A, which will be rounded to 5 A for further calculation.

The next step is to calculate the average current of each MOSFET of the bridge in a worst-case scenario.

The assumption is made that the worst-case scenario for bridge MOSFETs is when operating at the maximum PWM frequency of 16 kHz at 75°C ambient temperature. Also, it can be assumed that the PWM duty cycle is equal to 0.5, because due to the high initial inductance of the solenoid coil most of the load current will flow through the high-side PWM-MOSFET and during the bypass and decay the load current flows through the low-side PWM-MOSFET. Due

to a small difference between the load and Select-MOSFET currents, it can be assumed that they are equal.

Therefore, the average current I_{avr} of the bridge MOSFETs for the worst-case scenario are as follows.

- High-side PWM-MOSFET (Q1): 2.5 A.
- Low-side PWM-MOSFET (Q2): 2.5 A.
- Select MOSFET (Q8): 5.0 A.

Next step

According to [42], the MOSFET copper and switching losses can be estimated from equations (23) and (24) accordingly.

$$P_c = I_{avr}^2 * R_{DS(on)} \tag{23}$$

Where P_c – MOSFET conduction losses, $R_{DS(on)}$ – MOSFET on-state drain-to-source resistance from the datasheet, I_{avr} – MOSFET average current

$$P_{sw} \cong f_{sw}(V_{DD} * I_{peak} * (t_r + t_f) + Q_{rr} * V_{DD}) \tag{24}$$

Where P_{sw} – MOSFET switching losses, I_{peak} – MOSFET peak current, f_{sw} – MOSFET switching frequency, V_{DD} – supply voltage, Q_{rr} – reverse recovery charge of the body diode from the datasheet, t_r and t_f – MOSFET rise and fall time.

The average conduction or switching losses of the MOSFET per valve switching cycle can be found from the equation (25).

$$P_{avr} = \frac{\sum_n (P_n * t_n)}{T_{cycle}} \tag{25}$$

Where P_{avr} are the average (conduction or switching) losses of the MOSFET per cycle, P_n and t_n are the (conduction or switching) losses of the MOSFET and the time of the corresponding current profile, T_{cycle} is a period of the valve switching cycle.

Table 2.14 summarises losses calculation for each MOSFET of the bridge in the worst-case scenario.

Table 2.14. Bridge MOSFETs power losses in the worst-case scenario.

FET	f_{sw}	V_{DD}	t_r	t_f	Q_{rr}	$R_{DS(on)}$	$P_{c(avr)}$	$P_{sw(avr)}$	P_{tot}
Q1	16kHz	28.5V	59ns	29ns	67nC	4.5mOhm	39mW	150mW	189mW
Q2	16kHZ	28.5V	59ns	29ns	67nC	4.5mOhm	39mW	150mW	189mW
Q8	50Hz	28.5V	-	60ns	67nC	4.5mOhm	158mW	1mW	159mW

According to the datasheet, the maximum junction temperature of the NVMFS6H824N MOSFET used for the H-bridge design is 175°C. Therefore, allowing maximum T_J = 100°C at T_A = 75°C for the bridge MOSFET at the worst-case scenario power losses P_{tot} from Table 2.14, the highest junction-to-ambient thermal resistance $R_{\theta JA(max)}$ can be calculated from equation (26). The results, which can be used as a reference for PCB design, are given in Table 2.15.

$$R_{\theta JA(max)} = \frac{T_J - T_A}{P_{tot}} \tag{26}$$

Table 2.15. MOSFET's maximum junction-to-ambient thermal resistance allowed for H-bridge MOSFETS of the next-generation coil driver design (NGCD) design.

Bridge MOSFET		$R_{\theta JA(max)}$
Q1	High-side PWM-MOSFET	132°C/W
Q2	Low-side PWM-MOSFET	132°C/W
Q8	Select MOSFET	157°C/W

According to the datasheet, the NVMFS6H824N junction-to-ambient thermal resistance is 39.8°C/W when the MOSFET is surface-mounted on an FR4 board using a 650 mm^2 2 oz copper pad. The maximum junction-to-ambient thermal resistance allowed for the bridge PWM-MOSFET is 132°C/W, which is 3.3 times smaller than from the datasheet, which, in turn, indicates that developing a layout design that will comply with the next-generation coil driver (NGCD) established design parameters is feasible.

Bridge diode compliance calculation

The 100 V, 5 A Schottky diode SDT5H100SB was chosen for this design. According to the datasheet [43], his diode can withstand a non-repetitive peak forward surge current of 120 A, 8.3 ms single half sine-wave superimposed on the rated load, which is far above the 15 A peak current established by the design parameters.

To make sure that SDT5H100SB complies with design requirements the following calculation was done.

The bridge diode worst-case scenario can be produced when operating MAV10 at pumping mode and the shaft rotation speed of 3000 rpm. The approximate current profile is shown in Figure 2.44, where the decay phase was calculated from the equation (4) using approximate MAV10 initial inductance of 5mH, system voltage of 24 V and 10 A current for the peak phase of the MAV10 current profile.

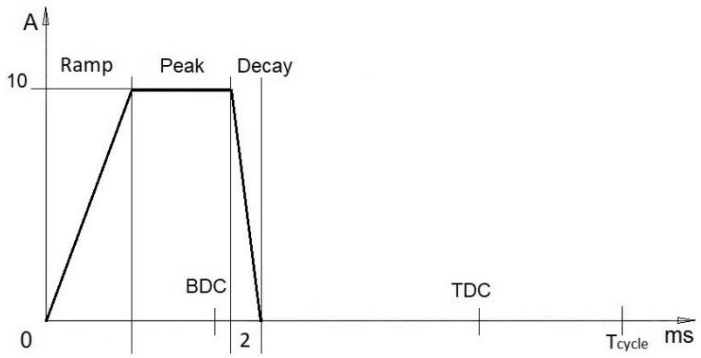

Figure 2.44. MAV10 current profile when DD machine operates as a pump.

According to [42], the diode conduction and switching losses can be calculated from equations (27) and (28) accordingly. However, for this application switching losses can be neglected due to a low switching frequency of the diode (50 Hz).

$$P_c = I_{avr} * V_F \tag{27}$$

$$P_{sw} \cong \frac{1}{4} Q_{rr} V_{DD} f_{sw} \tag{28}$$

Where P_c – diode conduction losses, P_{sw} – diode switching losses, V_F – diode forward voltage, I_{avr} – diode average current, f_{sw} – diode switching frequency, V_{DD} – supply voltage, Q_{rr} – diode reverse recovery charge.

According to the current profile from Figure 2.44, the average diode current at the worst-case scenario can be found from equation (29), which is 0.5 A.

$$I_{avr} = \frac{\frac{I_{peak}}{2} * T_{decay}}{T_{cycle}} = \frac{\frac{10}{2} * 0.002}{0.02} = 0.5\ A \qquad (29)$$

Thus, from equation (27), the thermal losses of the bridge diode in the worst-case scenario are 0.31 W, which gives a 7.75°C temperature rise, applying the junction-to-ambient thermal resistance value of 25°C/W from the datasheet. Therefore, at the maximum ambient temperature of 75°C (established by the design parameters), the diode junction temperature will be equal to 82.75°C in the worst-case scenario, which is far below the value from the datasheet of 175°C.

2.4.4.6 NGCD prototype board layout design

The NGCD prototype board PCB design was developed using Easy-PC software.

Figure 2.45 shows the top and bottom layers of the 6-layer printed circuit board (PCB) of the next-generation coil driver (NGCD) prototype board. The inner layers consist of two ground and two power planes. The complete set of the PCB-layers drawings is given in Appendix A.

The top layer contains the following circuits. The input protection circuit, which provides overvoltage, overcurrent, and reverse polarity protection; bulk capacitance of 720 uF; three H-bridges with low-side current sensing circuits; analogue switches that switch the output supplied to the ADC of the FPGA between current sensing and voltage sensing circuits; 12 V, 10 V, 5 V power supply circuits and the chip-KIT shield connectors providing an interface for the Arty-A7 FPGA board and the DDC15 logic board, which is the next-generation DD processor prototype board.

The circuits that are located on the bottom layer of the PCB are the 3.3 V power supply, low-side gate drivers, low-side overcurrent detection circuit, and the solenoid coil voltage sensing circuit that is described in Chapter 2 .

All inputs and outputs of the board are electrostatic discharge (ESD) protected by adding a series resistance of 100 Ohm and a transient-voltage-suppression (TVS) diode of corresponding working peak reverse voltage (V_{RWM}) (see schematics in Appendix A).

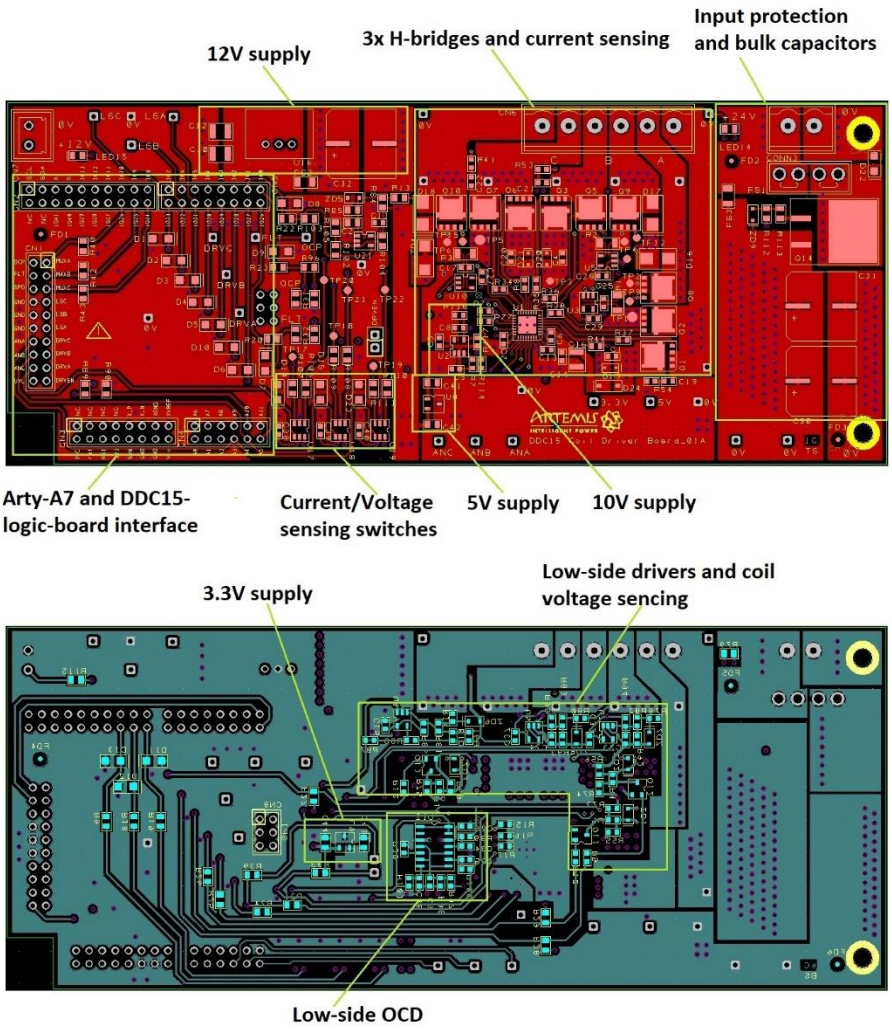

Figure 2.45. PCB's top (red) and bottom (blue) layers of the of the NGCD prototype board.

The layout of the NGCD prototype board was developed following the general practice and rules of the PCB design, considering EMI radiation, heat sinking, proper grounding, and current capability of traces and vias. Additionally, the layout recommendation from the component's datasheets were taken into account, as well as the recommendation's documentation for the switching power supplies layout design, such as [44], [45], [46], [47], [48], [49].

Thermal performance estimation of the NGCD prototype board

As it was mentioned before, one of the main purposes of the NGCD prototype board is to evaluate the coil driver circuit, which is a power electronic circuit that is expected to generate heat during operation. Therefore, it is important to predict the board's thermal performance to

make sure it is compatible with the design requirements and that the required evaluation testing will be possible to complete.

A COMSOL model was developed to estimate the temperature of the power MOSFETs of the coil driver and the input protection circuits of the NGCD prototype board for the worst-case scenario.

Figure 2.46 shows the COMSOL model geometry, which is an approximate 3D design of the NGCD prototype board created in AutoCAD using the 2D DXF files of the PCB design extracted from the Easy-PC. It comprises MOSFETs of the input protection and coil driver circuits that will generate most of the heat; inner copper planes and dielectric layers that participate in heat distribution within the board; Top and bottom thermal planes, tracks, pads, and thermal vias that are enhancing heat transfer from the power components to the bottom copper layer and within the board. Vias of the high-side MOSFETs are also connected to the inner power plain, according to the PCB design.

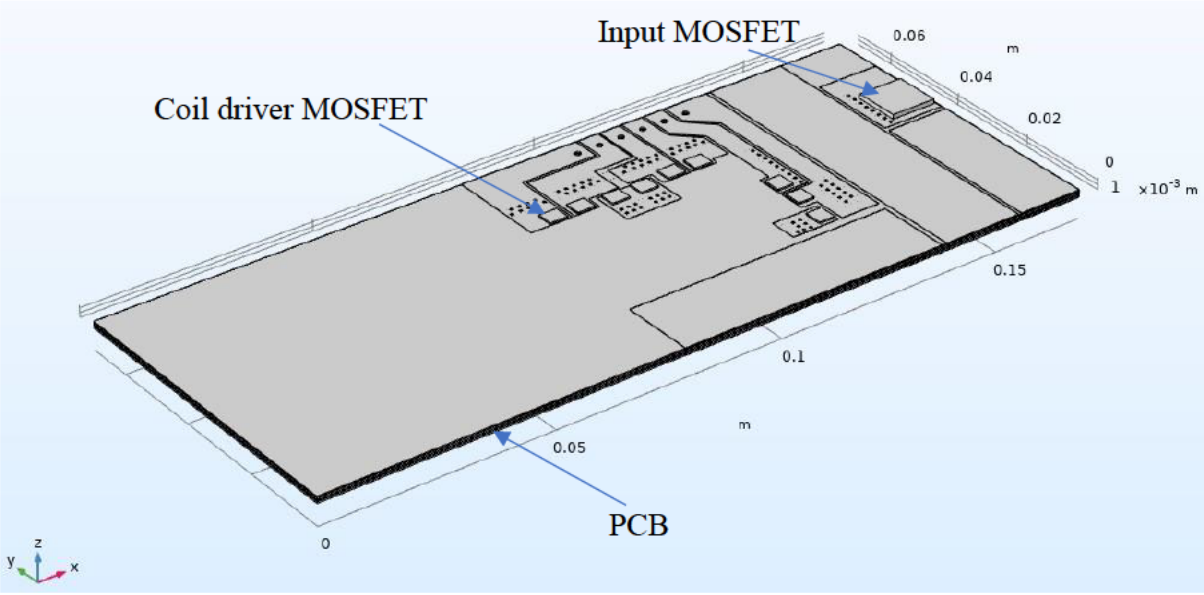

Figure 2.46. Geometry of the NGCD prototype board used for COMSOL thermal analysis.

Figure 2.47 shows the material and their properties that were used in the COMSOL model, from which the FR4 material was assigned to the dielectric layers, Copper was assigned to MOSFETs and other copper components of the board, and Air was assigned to all boundaries of the model.

Air *(mat11)*

	Property	Variable	Value	Unit	Property group
☑	Thermal conductivity	k_iso ; kii...	k(T)	W/(m·K)	Basic
☑	Surface emissivity	epsilon_rad	0.8	1	Basic
	Coefficient of thermal expansion	alpha_iso...	alpha_p(pA,T)	1/K	Basic
	Mean molar mass	Mn	0.02897	kg/mol	Basic
	Bulk viscosity	muB	muB(T)	Pa·s	Basic
	Relative permeability	mur_iso ;...	1	1	Basic
	Relative permittivity	epsilonr_i...	1	1	Basic
	Dynamic viscosity	mu	eta(T)	Pa·s	Basic
	Ratio of specific heats	gamma	1.4	1	Basic
	Electrical conductivity	sigma_iso...	0[S/m]	S/m	Basic
	Heat capacity at constant pressure	Cp	Cp(T)	J/(kg·K)	Basic
	Density	rho	rho(pA,T)	kg/m^3	Basic
	Speed of sound	c	cs(T)	m/s	Basic
	Refractive index, real part	n_iso ; nii...	1	1	Refractive index
	Refractive index, imaginary part	ki_iso ; kiii...	0	1	Refractive index
	Parameter of nonlinearity	BA	(def.gamma...	1	Nonlinear model

FR4 (Circuit Board) *(mat12)*

	Property	Variable	Value	Unit	Property group
☑	Heat capacity at constant pressure	Cp	1369[J/(kg*K)]	J/(kg·K)	Basic
☑	Density	rho	1900[kg/m^3]	kg/m^3	Basic
☑	Thermal conductivity	k_iso ; kii...	0.3[W/(m*K)]	W/(m·K)	Basic
	Relative permeability	mur_iso ;...	1	1	Basic
	Electrical conductivity	sigma_iso...	0.004[S/m]	S/m	Basic
	Relative permittivity	epsilonr_i...	4.5	1	Basic
	Coefficient of thermal expansion	alpha_iso...	18e-6[1/K]	1/K	Basic
	Young's modulus	E	22e9[Pa]	Pa	Young's modulus and Poisson's ratio
	Poisson's ratio	nu	0.15	1	Young's modulus and Poisson's ratio

Copper *(mat13)*

	Property	Variable	Value	Unit	Property group
☑	Heat capacity at constant pressure	Cp	385[J/(kg*K)]	J/(kg·K)	Basic
☑	Density	rho	8960[kg/m^3]	kg/m^3	Basic
☑	Thermal conductivity	k_iso ; kii...	400[W/(m*K)]	W/(m·K)	Basic
	Relative permeability	mur_iso ;...	1	1	Basic
	Electrical conductivity	sigma_iso...	5.998e7[S/m]	S/m	Basic
	Coefficient of thermal expansion	alpha_iso...	17e-6[1/K]	1/K	Basic
	Relative permittivity	epsilonr_i...	1	1	Basic
	Young's modulus	E	110e9[Pa]	Pa	Young's modulus and Poisson's ratio
	Poisson's ratio	nu	0.35	1	Young's modulus and Poisson's ratio
	Reference resistivity	rho0	1.72e-8[ohm...	Ω·m	Linearized resistivity
	Resistivity temperature coefficient	alpha	0.0039[1/K]	1/K	Linearized resistivity
	Reference temperature	Tref	298[K]	K	Linearized resistivity

Figure 2.47. Materials and their properties that were used in the COMSOL thermal model.

Figure 2.48 shows the COMSOL model builder window as well as surface-to-ambient radiation and heat flux boundary conditions and settings. From the model builder tree, can be seen that to study the board's thermal performance Heat Transfer in Solid physics was applied. It contains

the solid domain that was applied to all domains of the model. Thermal contact was applied automatically to the boundary between MOSFETs and thermal pads. Heat sources were applied to the MOSFETs according to Table 2.14. Surface-to-ambient radiation boundary was applied to all surface boundaries. Heat flux 1, which uses the external natural convection correlation for the upside of a horizontal plate, is applied to the top surface of the board. Heat flux 2, which uses the external natural convection correlation for the downside of a horizontal plate, is applied to the bottom surface of the board. Heat flux 3, which uses the external natural convection correlation for a vertical wall, is applied to the lateral surface of the board. The thermal insulation boundary is not applicable in this model.

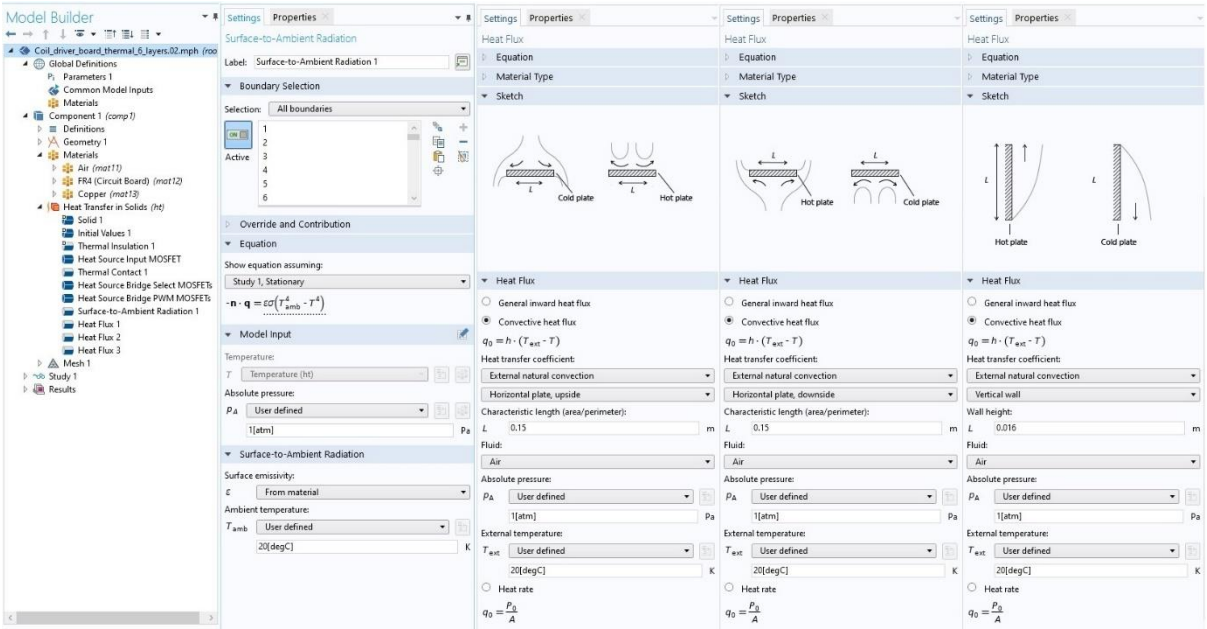

Figure 2.48. COMSOL model builder, surface-to-ambient radiation and heat flux boundary conditions and settings.

Figure 2.49 shows the results of the NGCD prototype board COMSOL thermal model simulation. According to the results, the steady-state temperature of the board's power components at the worst-case scenario load and ambient temperature of 20°C are as follows.

- Coil driver PWM-MOSFET: 73-75°C, which is 100°C below the maximum allowed temperature from the datasheet.
- Coil driver Select-MOSFET: 65-67°C, which is 108°C below the maximum allowed temperature from the datasheet.

– Input protection MOSFET: 52°C, which is 123°C below the maximum allowed temperature from the datasheet.

The model does not include the temperature increase of the copper conductors due to the joule heat or generated heat of the other components. However, during the PCB design, the power tracks characteristics were calculated to keep the temperature rise within 1-2°C, and the heat of the other components does not expect to be significant.

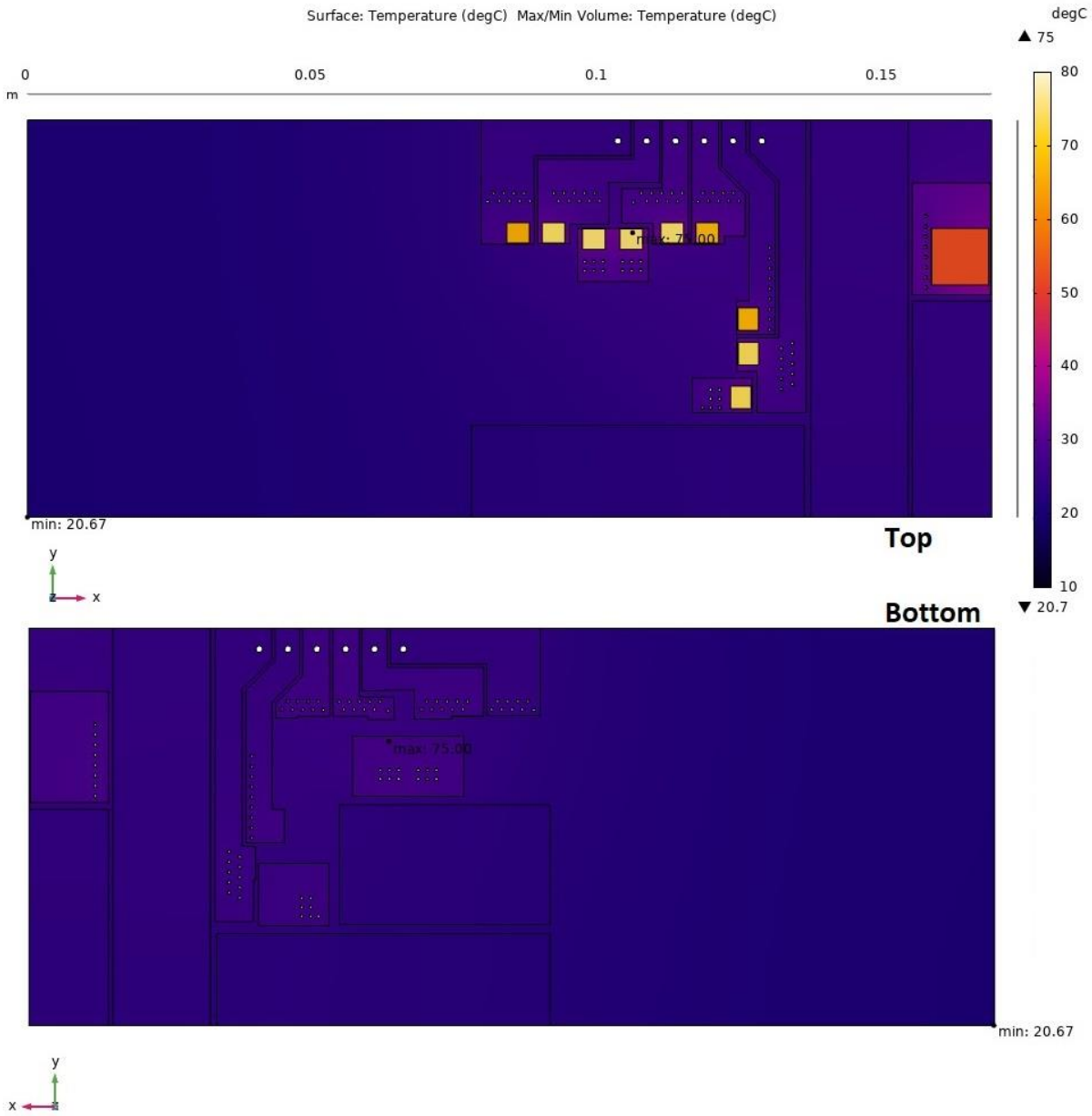

Figure 2.49. NGCD prototype board COMSOL thermal model simulation results.

Therefore, it can be concluded that the thermal characteristics of the board are compatible with the design requirements allowing the required evaluation testing to be accomplished.

2.4.5 Low-side synchronous vs non-synchronous rectification

One of the main requirements for the next-generation coil driver (NGCD) design is to enable synchronous rectification (also known as active rectification) for the slow decay mode of operation. This will improve the coil driver's efficiency and thermal performance.

Table 2.16 compares the heat losses and temperature of the NGCD power components with and without synchronous rectification. Where for the non-synchronous rectification example, the PDS760 diode from the DPC12 MK1 controller design is used as a low-side flyback diode instead of low-side MOSFET that enables low-side synchronous rectification in NGCD design. The temperature of the components was estimated by simulation using the CMOSOL model for 20°C ambient temperature.

Table 2.16. Heat losses and components temperature estimation for the NGCD design with and without synchronous rectification.

Bridge component	f_{sw}	V_s	P_c	P_{sw}	P_{tot}	T_c **at** T_A**20**°C
Synchronous rectification at slow decay mode						
High-side PWM-MOSFET	16kHz	28.5V	39mW	150mW	189mW	73-75°C
Low-side PWM-MOSFET	16kHz	28.5V	39mW	150mW	189mW	73-75°C
High-side Flyback-Diode	50Hz	28.5V	54mW	-	54mW	28-30°C
Low-side Select-MOSFET	50Hz	28.5V	158mW	1mW	159mW	65-67°C
Per bride losses					**591mW**	
Non-synchronous rectification at slow decay mode						
High-side PWM-MOSFET	16kHz	28.5V	39mW	150mW	189mW	80-84°C
Low-side Flyback-Diode	16kHz	28.5V	1550mW	-	1550mW	320-323°C
High-side Flyback-Diode	50Hz	28.5V	54mW	-	54mW	39-42°C
Low-side Select-MOSFET	50Hz	28.5V	158mW	1mW	159mW	73-77°C
Per H-bride losses					**1952mW**	

As can be seen from the results, the heat losses of the NGCD are more than three times larger when non-synchronous rectification is used instead of synchronous rectification during slow-decay mode. Also, the temperature analysis shows that the temperature of the flyback diode that replaces the low-side PWM-MOSFET will be 320°C larger, which is 145°C more than its maximum operating temperature from the datasheet. This will cause permanent damage to the component. Otherwise, the footprint must be significantly increased, which would increase the size and cost of the design.

2.4.6 NGCD cost estimation

Table 7 is a per channel costing for the NGCD design components without the voltage sensing circuit (see Chapter 2), saving approximately 40% on the existing design (DPC12 MK1).

Table 2.17. NGCD cost per unit based on 1k units from Mouser on 27/03/2020.

Component	£
DRV8320H /3	0.44
NVMFS6H824N ×3	1.542
SDT5A100SB	0.125
MM3Z15VST1G	0.021
PMBT2222A	0.019
TLV76701DRVR /12	0.035
ULR1S-R007FT2	0.174
Resistors	0.15
Capacitors	0.25
INA180(A1)	0.183
PESD36VS1UJ	0.085
LM2901	0.028
Total:	**3.06**

The estimated cost of adding the voltage monitoring components, including the analogue switch (SN74LVC2G66), is approximately £0.30 per channel.

2.4.7 NGCD prototype board test results

Figure 2.50 shows a photograph of the manufactured NGCD prototype board. A complete test has been carried out according to a previously developed test plan, which includes such tasks as visual inspection, continuity and short circuits test, power-on test, supply voltages test, detailed testing of each module of the NGCD circuit as well as verification of the main parameters established by the design requirements of the NGCD as a whole design. The equipment used for NGCD prototype board testing is given in Table 2.18.

This chapter will not describe the entire testing of the prototype board as all the modules worked according to the datasheet and the design parameters at the first power-on. Only the test results that were used to verify the simulation models and the results that point to the design issues will be described in this chapter.

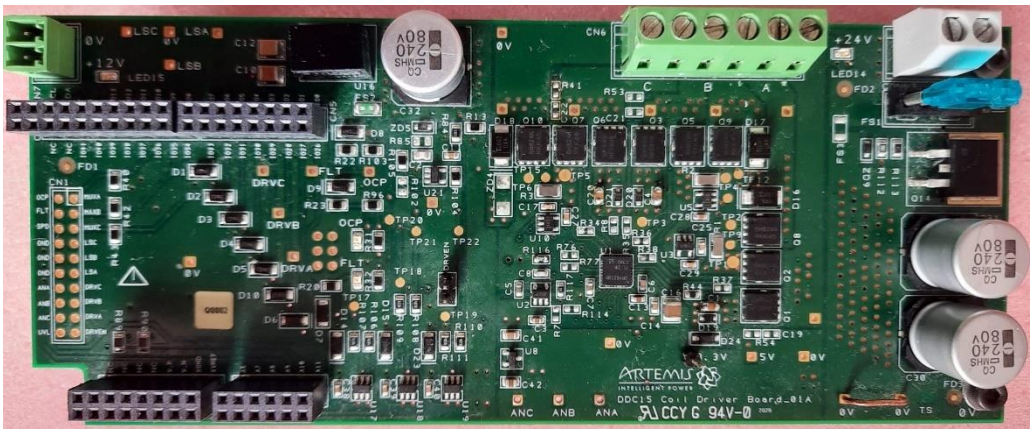

Figure 2.50. Photograph of the next-generation coil driver (NGCD) prototype board.

Table 2.18. Test equipment used for NGCD prototype board testing.

Multimeter	TENMA 72-7730A
Oscilloscope	Agilent DSO-X-2014A / KEYSIGHT MS0-X 2024A
Variable power supply	EA-PS 9080-60 T
Clamp current meter	FLUKE i310s
Thermal camera	FLIR C5
Spectrum analyser	Rohde&Schwarz FPC1000
TEM cell	TekBox TBTC3
FPGA board	ARTY-A7 100T
Load	PAV8 / DDP96

2.4.7.1 Fast overcurrent protection (OCP) testing

To test the overcurrent protection (OCP) of the NGCD board, the following short circuit (SC) conditions were created: coil-lead-short-to-ground and coil-lead-short-to-supply from the DRV8320H OCP side and coil-lead-short-to-supply from the low-side OCP side. As was specified in the SC condition of the LTspice simulation model (see 2.4.4.5), the NGCD board was connected to the 28.5 V power supply by the 5 AWG cable of 1 meter length and the coil connector input was shorted to GND or supply by a 14 AWG cable of 0.02 m length. The SC current was measured using a clamp current meter clamped across the SC cable. Also, outputs of the current sensing, nFAULT of the DRV8320H or of the low-side OCP, and DRV8320H ENABLE input were monitored using oscilloscope.

As can be seen from the short-to-ground scenario test results Figure 2.51, it is the most severe SC fault, reaching the SC current of 370 A within 6us disconnection time provided by DRV8320H OCP, which is 1.5 us more than the estimated total delay time using datasheet specifications. The SC current reached within 4.5 us is about 350 A, which is the same as from the simulation result.

The short-to-supply scenario test results (Figure 2.52) show that fault conditions are less severe, developing a SC current of 350 A within 6us disconnection time provided by the DRV8320H OCP. This is due to the large inductance of the SC caused by the power supply cables. Again, the test delay time is 1 us larger than the estimated delay time from the datasheet specifications.

The short-to-supply scenario from the low-side OCP side (Figure 2.53) was disconnected within 4 us reaching the SC current value of 240 A, which is 0.5 us less than the estimated total delay time from the datasheet specifications.

Figure 2.51. Short-to- GND test (DRV8320H OCP). Yellow waveform – DRV_ENABLE pin voltage, red waveform – short circuit current, green waveform – nFAULT pin voltage, blue waveform – CSA output voltage.

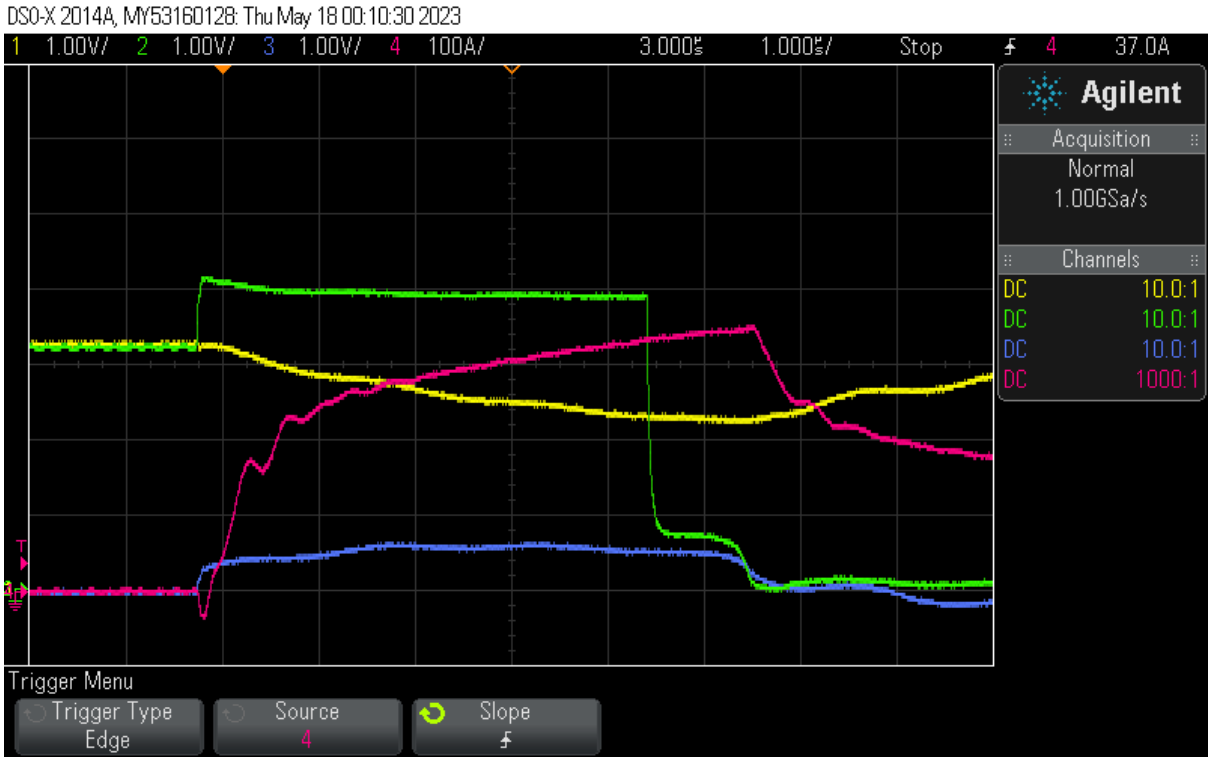

Figure 2.52. Short-to-supply test (DRV8320H OCP). Yellow waveform – DRV_ENABLE pin voltage, red waveform – short circuit current, green waveform – nFAULT pin voltage, blue waveform – CSA output voltage.

Figure 2.53. Short-to-supply test (Low-side OCP). Yellow waveform – DRV_ENABLE pin voltage, red waveform – short circuit current, green waveform – nFAULT pin voltage, blue waveform – CSA output voltage.

The following can be concluded from the test results.

The LTspice model, developed for defining the short circuit (SC) current during the fault condition, gives a fair result, which can be used for overcurrent protection (OCP) design calculation.

The design of the low-side OCP gives a very fast and stable SC disconnection time of 4us, including 2 us blanking time. If required, the blanking time can be decreased down to 1 us, thus making the SC current lower (from 240 A to 200 A in this example).

The OCP of the DRV2380H, which is based on MPSFET's drain-to-source voltage monitoring, gives a stable 6-6.5 us disconnection time, which is 1-1.5 us more than expected. This extra delay is increasing the SC current, which might require additional measures for the 15-channel controller design that is expected to have significantly larger bulk capacitance. For MOSFETs

of a lower pulsed drain current rating, an additional inductance (e.g., ferrite beads) between the half-bridge source node and coil connector can be recommended.

The Fluke i310s current clamp probe was used for the CS test (see Table 2.18). The probe bandwidth is 20 kHz, which implies a di/dt limit of around 40 A/us. Since the di/dt of the SC current is around 200 A/us at the start and the end of the pulse, the probe di/dt limitation will introduce a significant error in the displayed value on the oscilloscope at these stages. However, this limitation of the test equipment does not impede measuring the peak and length of the SC current pulse with acceptable precision, which was the goal of this experiment.

2.4.7.2 H-bridge negative transients and ringing test

To test the gate and the H-bridge for an undesirable transient during MOSFETs switching, the coil driver was loaded to allow 10 A current through MOSFETs at 24 V, which are the nominal parameters at the motoring mode of the DD machine. During the test, the CSA output, MOSFET's gate and drain-to-source voltages were monitored using oscilloscope. The tip-and-barrel technique was used to achieve accrued measurements.

Half-bridge test results

From the test results (Figure 2.54 and Figure 2.55) oscillations (ringing) of 20-25 MHz and 90-126 MHz can be seen, which are superimposed on the gate and source node voltages and the coil current. Also, an undershot below the ground can be seen on the gate and source node voltages.

Several negative consequences can be caused by the oscillations on the gate or the source node. According to [50], the principal problems that can be caused by the superimposed ringing on the source node are exceeding the MOSFET breakdown voltage margin, which can be caused by the first peak of the ringing waveform, and the excess of conducted or radiated noise produced by the ringing waveform. According to [51] and [52], synchronous buck converters, which is the NGCD in the coil current control mode of operation, generate broadband noise in 50-300 MHz range.

Also, according to [53], due to the fast-rising drain-to-source voltage transient of one MOSFET, a current is injected towards the gate by the Miller capacitance of the other MOSFET

of the half-bridge, thus, causing a voltage spike on the MOSFET's gate. If this spike is larger than the gate threshold voltage, the MOSFET will turn on causing the short through across the half-bridge.

According to [50], [51] and [52], this ringing is caused by a resonant of the series RLC loop created by the loop parasitic inductance, the loop resistance, and the low-side MOSFET output capacitance (when the low-side MOSFET is turned off and high-side MOSFET is turned on. The loop is closed by the decoupling capacitor of the half-bridge.

Various methods can be used to shift the resonant frequency of the RLC loop in order to mitigate the oscillations. The most common methods are changing the dV/dt of the drain-to-source slew rate, changing decoupling capacitance, decreasing parasitic inductance, adding a snubber circuit and gate-source capacitor, etc.

Further, an attempt will be described to tune the half-bridge design by changing the decoupling capacitance and the MOSFET's slew rate.

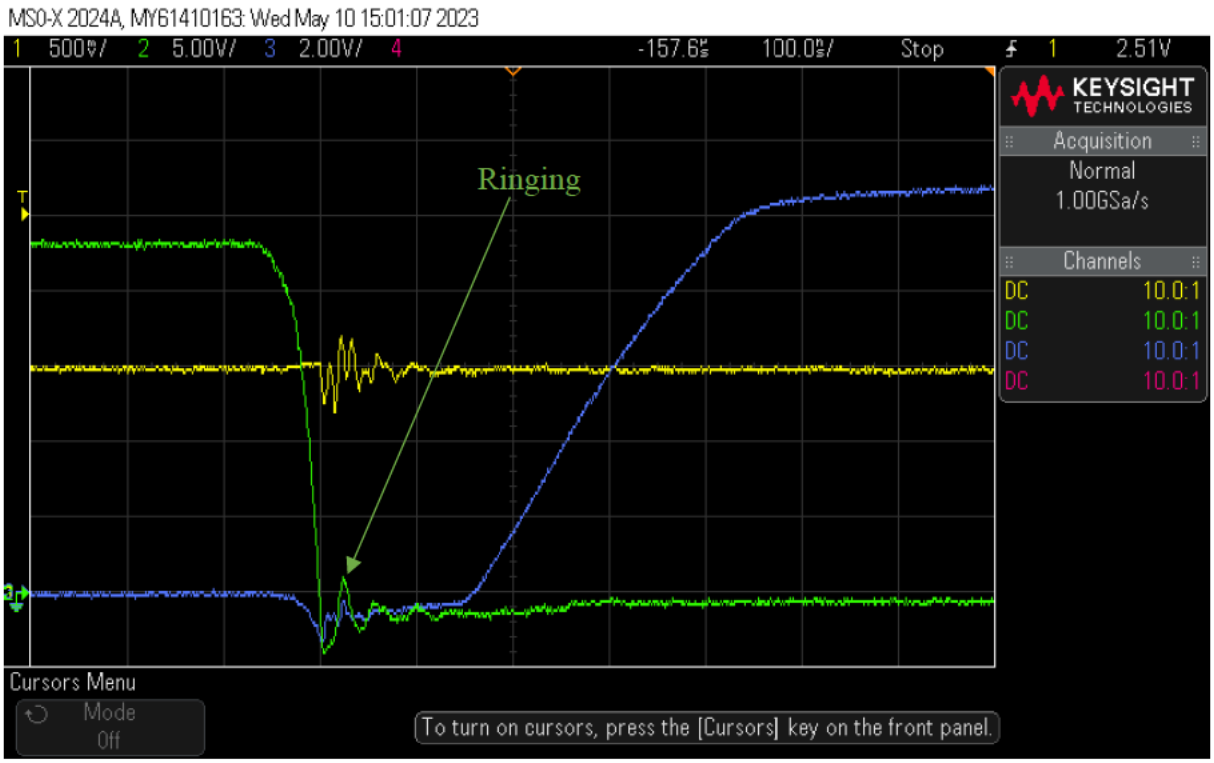

Figure 2.54. Gate and source node negative transients and ringing test at MOSFET turn-on (half-bridge low-side). Yellow trace – load current, green trace – MOSFET drain-to-source voltage, blue – MOSFET's gate voltage. (MOSFET current is about 10 A)

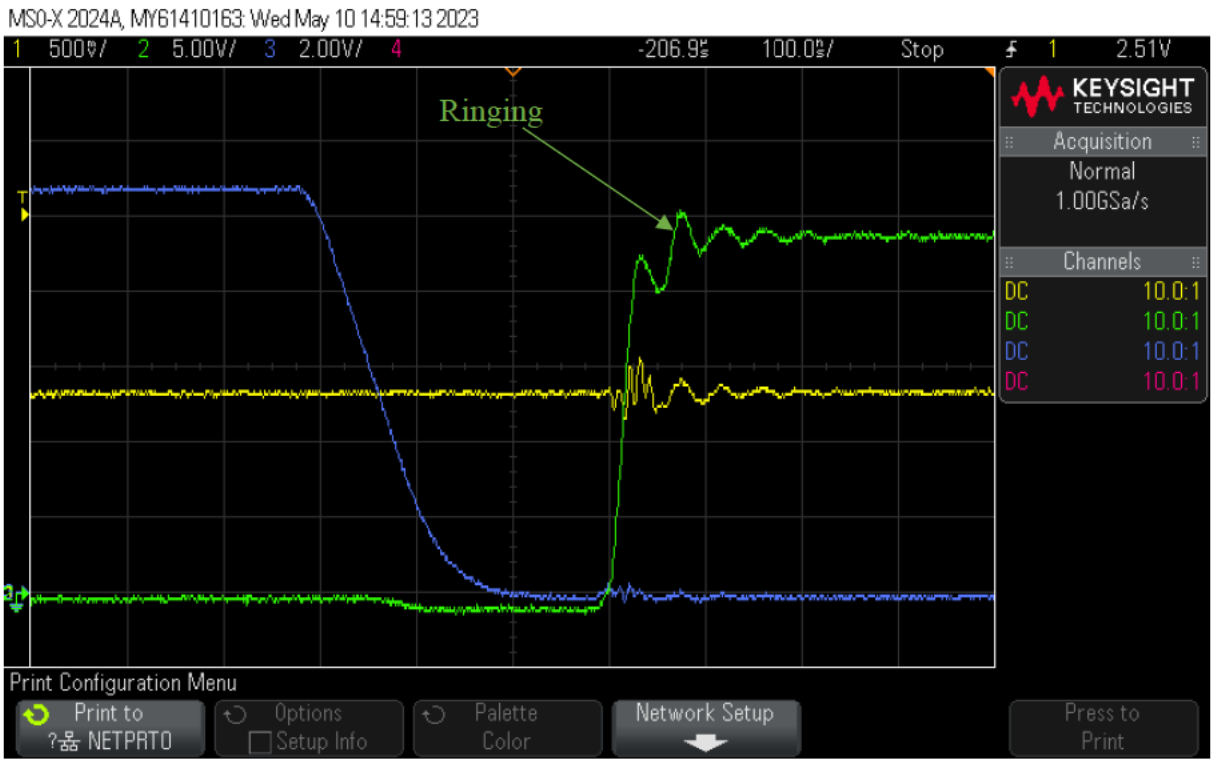

Figure 2.55. Gate and source node negative transients and ringing test at MOSFET turn-off (half-bridge low-side). Yellow trace – load current, green trace – MOSFET drain-to-source voltage, blue – MOSFET's gate voltage. (MOSFET current is about 10 A)

Low-side MOSFET test results

From the test results (Figure 2.56), the oscillations (ringing) of 20-25 MHz and 90-126 MHz can be seen on the voltage and current trace. Also, on the MOSFET's drain-to-source voltage an overshot above the supply voltage can be seen. The amplitude of the overshoot is within the margin, which by general practice must be 80% of the MOSFET breakdown voltage specified in the datasheet. Also, there is no risk of the short-rough due to the high-side diode if the overshot peak voltage is below the bridge supply voltage. However, similarly to the half-bridge, the ringing of 90-126 MHz will generate a broadband noise. Therefore, an attempt will be taken to mitigate this ringing by decreasing the MOSFET's slew rate (see Section 2.4.8.).

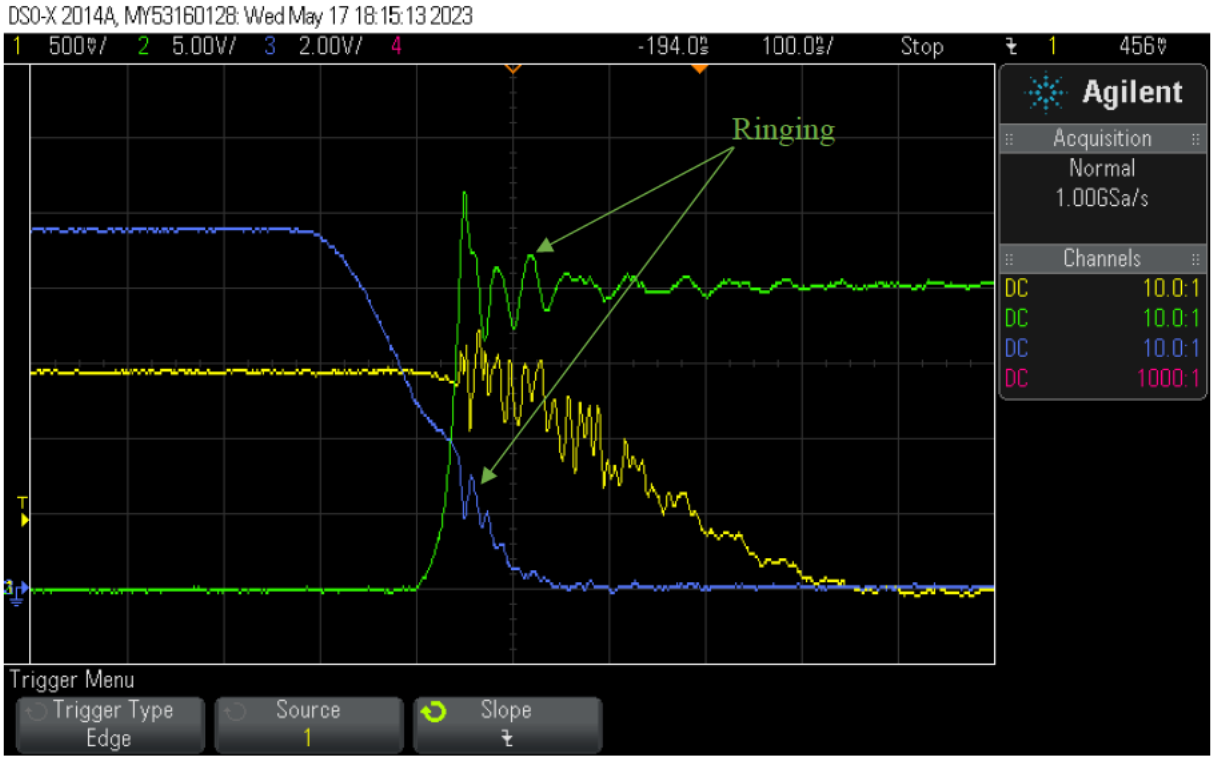

Figure 2.56. Source node negative transients and ringing test at MOSFET turn-off. Yellow waveform – low-side MOSFET current, green waveform – low-side MOSFET drain-to-source voltage, blue – MOSFET's gate voltage. (MOSFET current is about 10 A)

2.4.7.3 Radiated emissions testing

According to [54] and [49], almost any product that contains electronics must pass the electromagnetic compatibility (EMC) test before accessing the market. This testing ensures that the product does not emit a large amount of electromagnetic interference (known as radiated and conducted emissions) as well as its operation will not be affected by the surrounding electromagnetic disturbances. The EMC testing can be classified as follows.

Emissions testing:

- Radiated emissions testing
- Conducted emissions testing
- Flicker & harmonic testing

Immunity testing:

- Transient tests (ESD, EFT, Surges, Power Quality)
- Continuous Tests (Conducted, Radiated and Magnetic field)

At this stage of the next-generation coil driver development, it is relevant to evaluate the design for radiated emissions and immunity to the surrounding electromagnetic emissions.

In this section, the radiated emissions test and its results will be described. The required immunity testing will be described in Chapter 3 section 3.3.5.

Figure 2.57 shows a schematic diagram, and Figure 2.58 shows a photograph of the electromagnetic emissions test bench. During the test, the NGCD board was placed on the dielectric pad inside the transverse electromagnetic (TEM) cell that is used for the detection of electromagnetic field radiated by the tested board. The TEM cell is connected to the spectrum analyser that is set to measure the field strength peak values with a 100 kHz resolution bandwidth (which the max in this case) in range of 1-1000 MHz over the sweep of 10. Then the average peak value within 10 samples of the sweep in dB(uV/m) is outputted. The tested board was controlled by the FPGA board Arty-A7, powered by a 24 V power supply, and loaded by the digital displacement pump DDP96. The experiment was executed inside a grounded steel container.

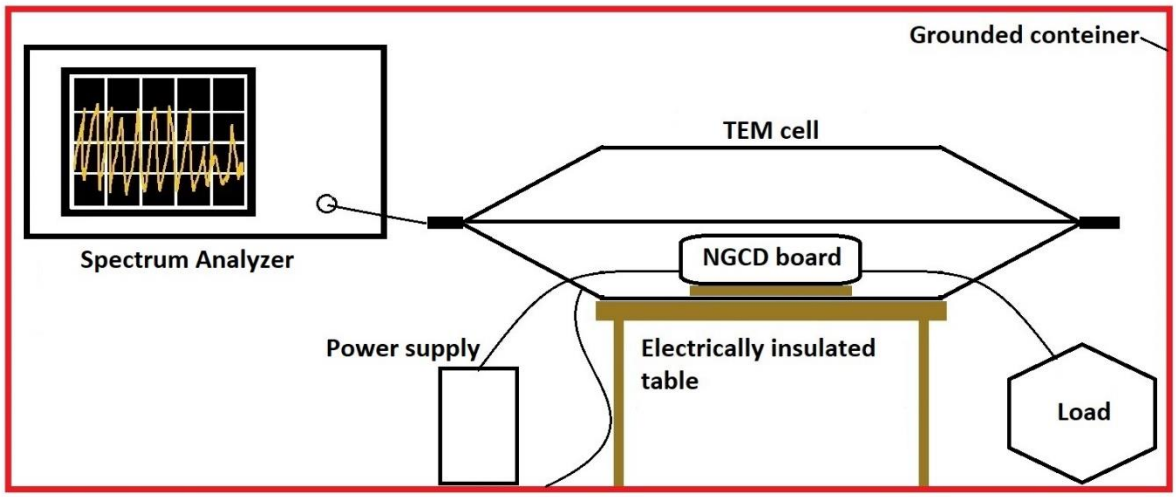

Figure 2.57. Schematic diagram of the electromagnetic emissions test bench.

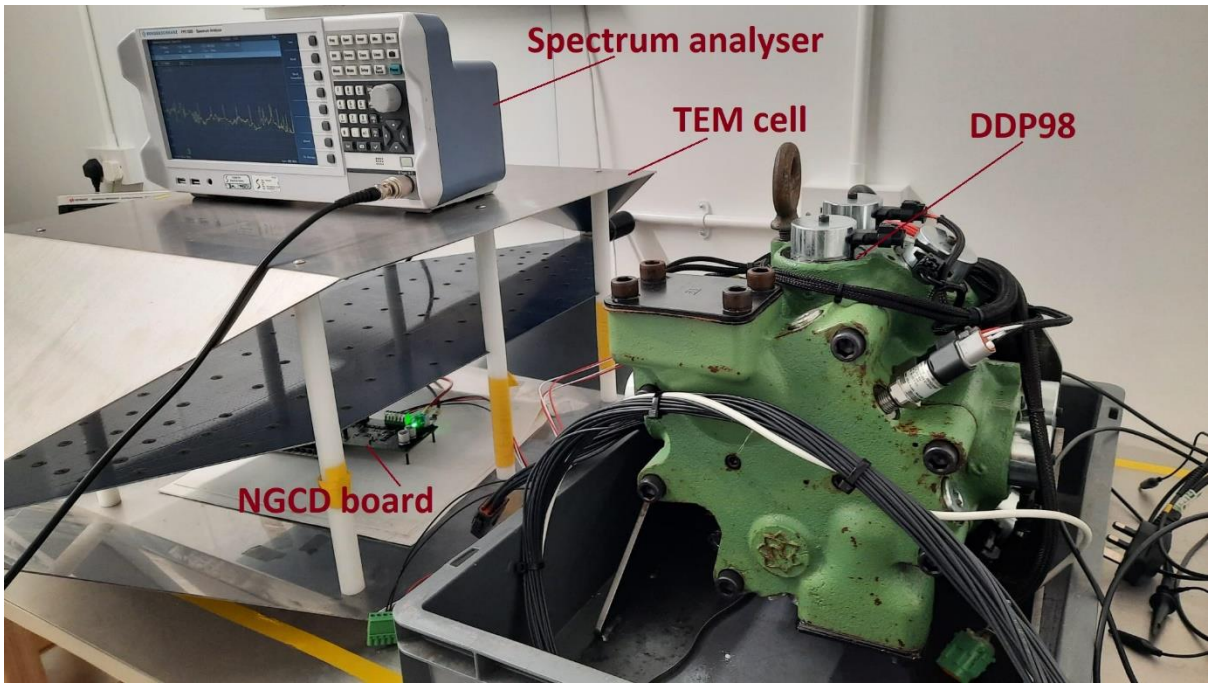

Figure 2.58. Photograph of the emission test setup for the NGCD prototype board.

Figure 2.59 shows the emissions test results where the red waveform is the measured electromagnetic field strength of the emissions generated by the FPGA control board Arty-A7. This noise is defined as the background noise for this test, also, it contains the surrounding noise. The yellow waveform is the measured electromagnetic field strength of the emissions, that were generated when the NGCD prototype board ran three valves in motoring mode (worst-case current profile) at a switching cycle equivalent to 3000 rpm.

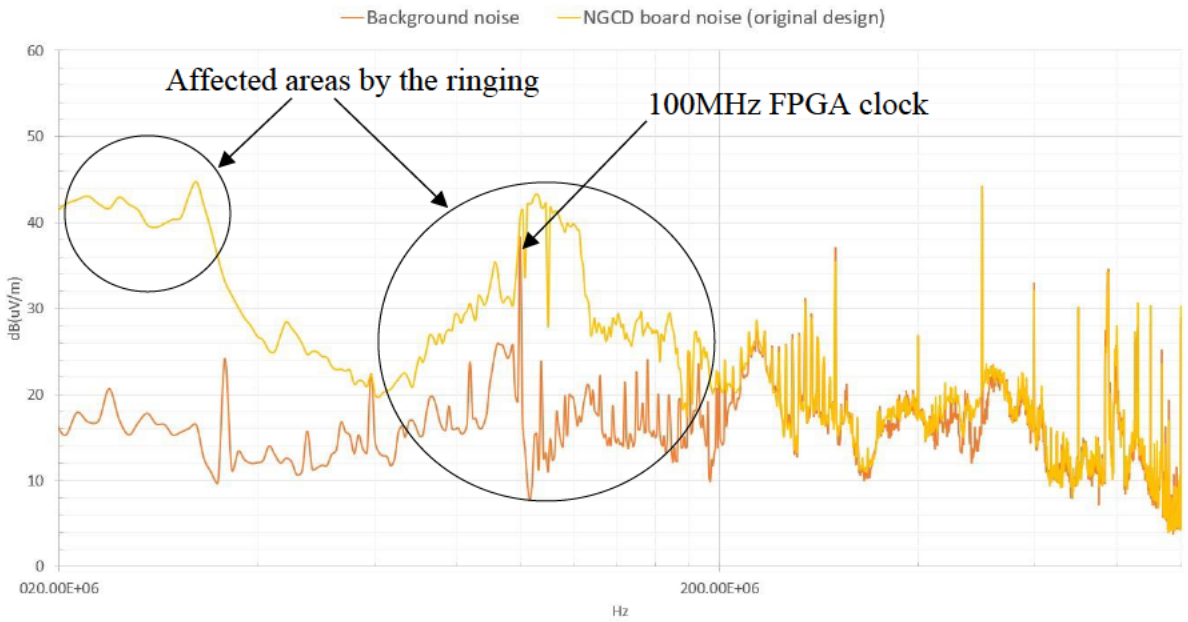

Figure 2.59. NGCD prototype board emissions test results. Red waveform – background noise (Arty-A7 board is on), yellow waveform – NGCD boar noise (operating three channels at the worst-case scenario).

As can be seen from the test results, there is a significant increase of the electromagnetic field strength in ranges of 20-30 MHz and 70-200 Mhz, which correspond to the MOSFET's S-node ringing frequency and to typical synchronous buck converters noise of 50-300 MHz discussed in [53].

Therefore, it is expected that the noise in the affected areas will be reduced after the reduction of the S-node ringing.

The next question is how critical this noise is and how it will affect the electromagnetic compliance (EMC) test of the controller. To answer those questions, first, we have to look at the limits. Since the NGCD will be driving the DD machines targeting the automotive market, the EMI limits established for vehicles will be used as the reference.

Figure 2.60 shows limits for broadband (BB) and narrowband (NB) radiated emissions over the applicable frequency range of 30MHz to 1GHz when measured using quasi-peak (QPK) and average (AVG) detectors, respectively, as defined by "Comité International Spécial des Perturbations Radioélectriques" (CISPR). The correlation factor between QPK and AVG measurements is 10 dB at 120 kHz resolution bandwidth (RBW). The measuring antenna distance is 10 meters for vehicles and 1 meter for electrical/electronic sub-assemblies (ESA). An additional 10 dB is allowed if the antenna is positioned at 3 meters for vehicle testing [55].

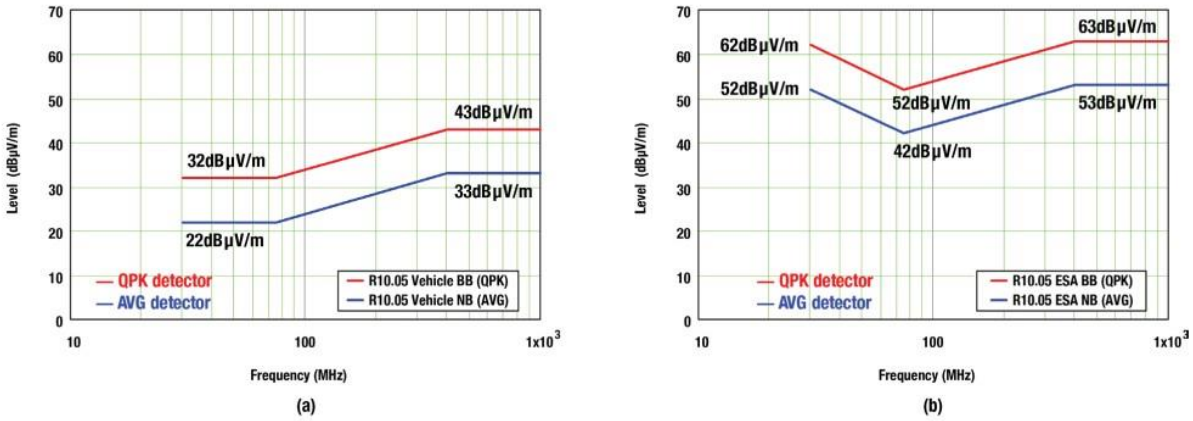

Figure 2.60. UNECE Regulation 10, radiated EMI limits for vehicles at 10 meters (a); and ESAs at 1 meter (b) [55].

Since our device is tested separately from the vehicle, the limits established for ESAs must be considered. The NGCD board emission test was done to get the average values, which allows identifying continuous and repetitive waves, thus, finding frequency regions affected by the ringing. The average values of the continuous waves are equal to peak and quasi-peak values. The average values of the repetitive waves are slightly smaller than their peak or quasi-peak values, and the average values of the random waves are much smaller than their peak or quasi-peak values. The limits that are provided by regulations are for the test where the ESA is placed 1m from the antenna. The NGCD prototype board was placed inside the TEM cell, which is 0.1 meter from the antenna, thus, providing larger measurements due to shorter distance to the source of the electromagnetic field. Also, the prototype board contains three channels only, when the digital displacement controller will have 15-channels.

Therefore, only a relative comparison of the NGCD board emissions results to the broadband limit can be made. Thus, considering the test worst values of 44 dB at 32 MHz and 43 dB at 106MHz, it can be seen that these values are below the AVG limit values by about 7 dB and 2dB respectively. According to [54], the safe result is when the actual emissions are lower than the limits by 5-6 dB since the uncertainty between different labs is up to 5 dB. Considering the larger antenna-to-device distance of the regulation limits test, it can be assumed that NGCD board emissions are in the safe region.

Therefore, it can be concluded that the radiated emission test described in this chapter is useful for troubleshooting, however, to predict the EMC test lab results for the digital displacement

controller by using the TEM cell emission testing results, the following procedure should be done.

- A 15-channel controller with 1.5 meters cables must be tested.
- A quasi-peak and average values/measurements must be acquired.
- Using specialised software (e.g., EMCview), the acquired measurements must be converted into equivalent values that correspond to the provided limits test conditions (antenna is placed 1 meter from the ESA).

2.4.7.4 Thermal performance test and COMSOL model verification

For the thermal performance test, all three channels of the NGCD prototype board were loaded using the DDP96 machine until the board temperature was stabilised. The board temperature was monitored using a thermal camera, and the ambient temperature - using a thermal couple.

A motoring current profile with a switching cycle that corresponds to 3000 rpm was used. A closed-loop controller was used to control the current of the peak and hold phases. The waveform of the test coil current profile is shown in Figure 2.61 and PWM frequency measurement results are shown in Figure 2.62 and Figure 2.63. Table 2.19 summarises the load parameters of the thermal performance test of the NGCD prototype board.

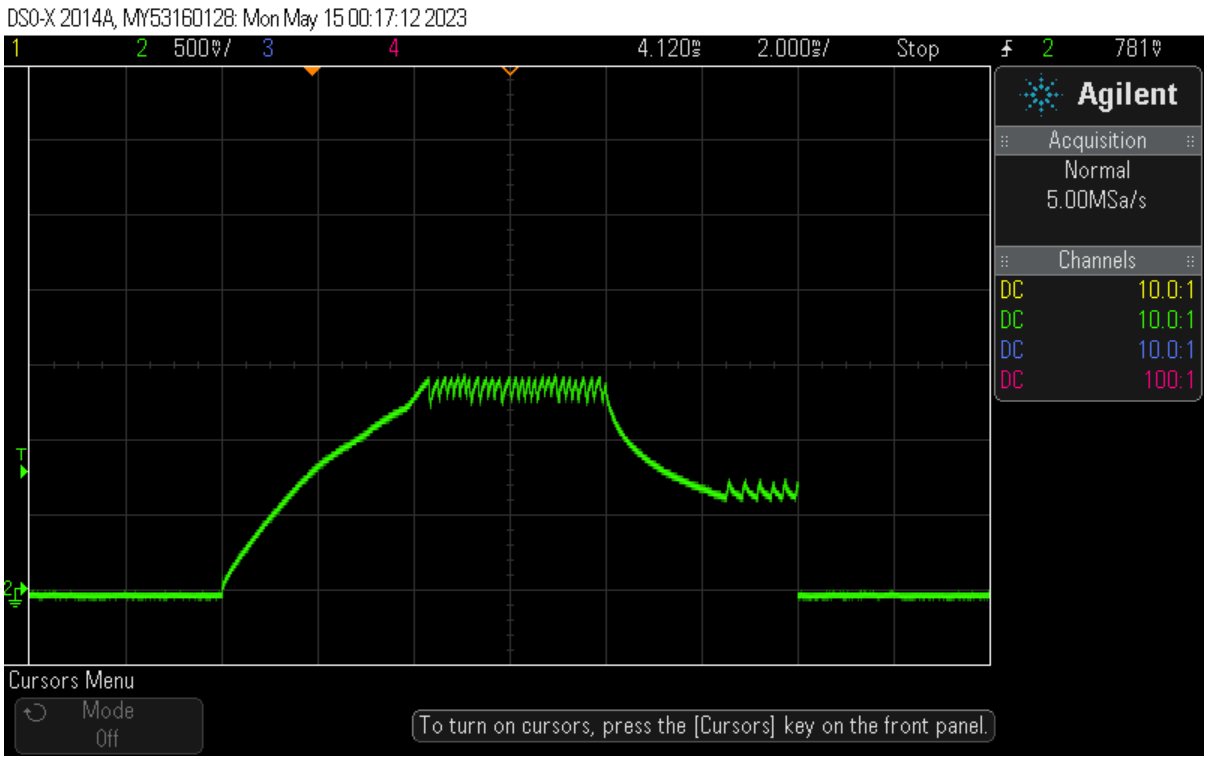

Figure 2.61. A current profile that was used fot the NGCD board thermal performance testing.

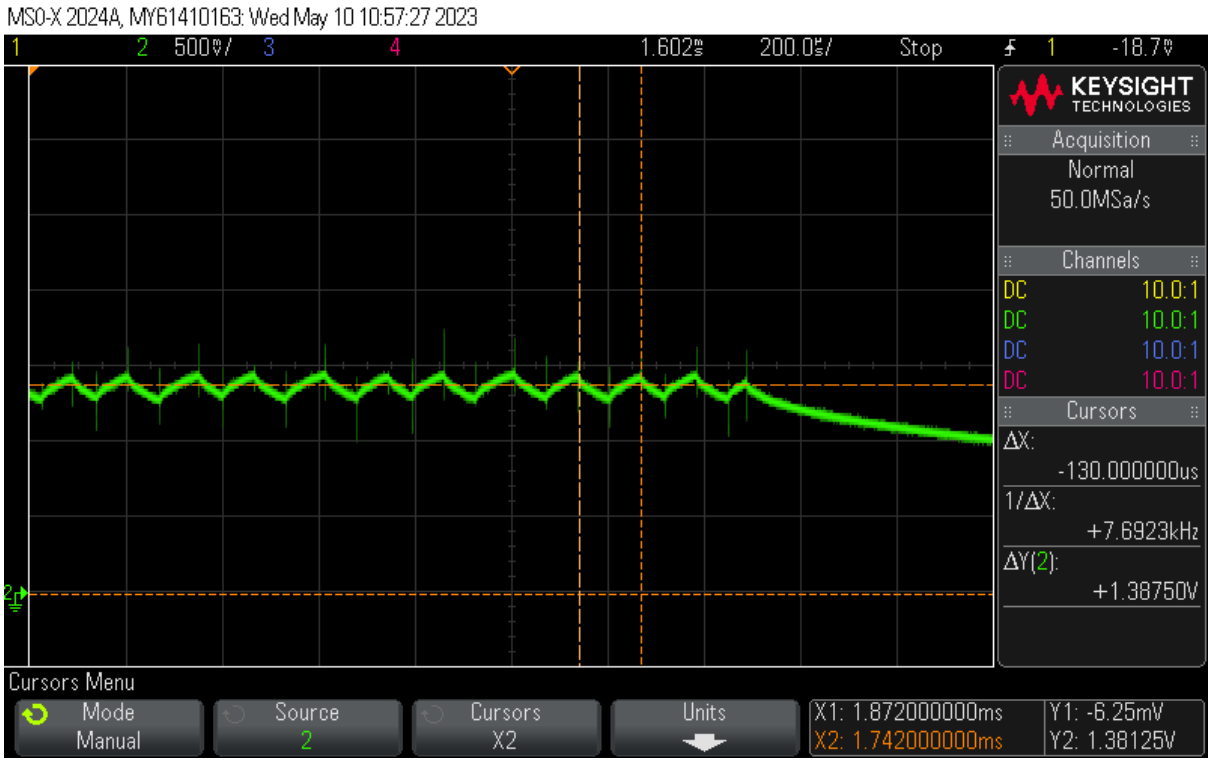

Figure 2.62. PWM frequency measuremnt at the peak phase of the coil current profile.

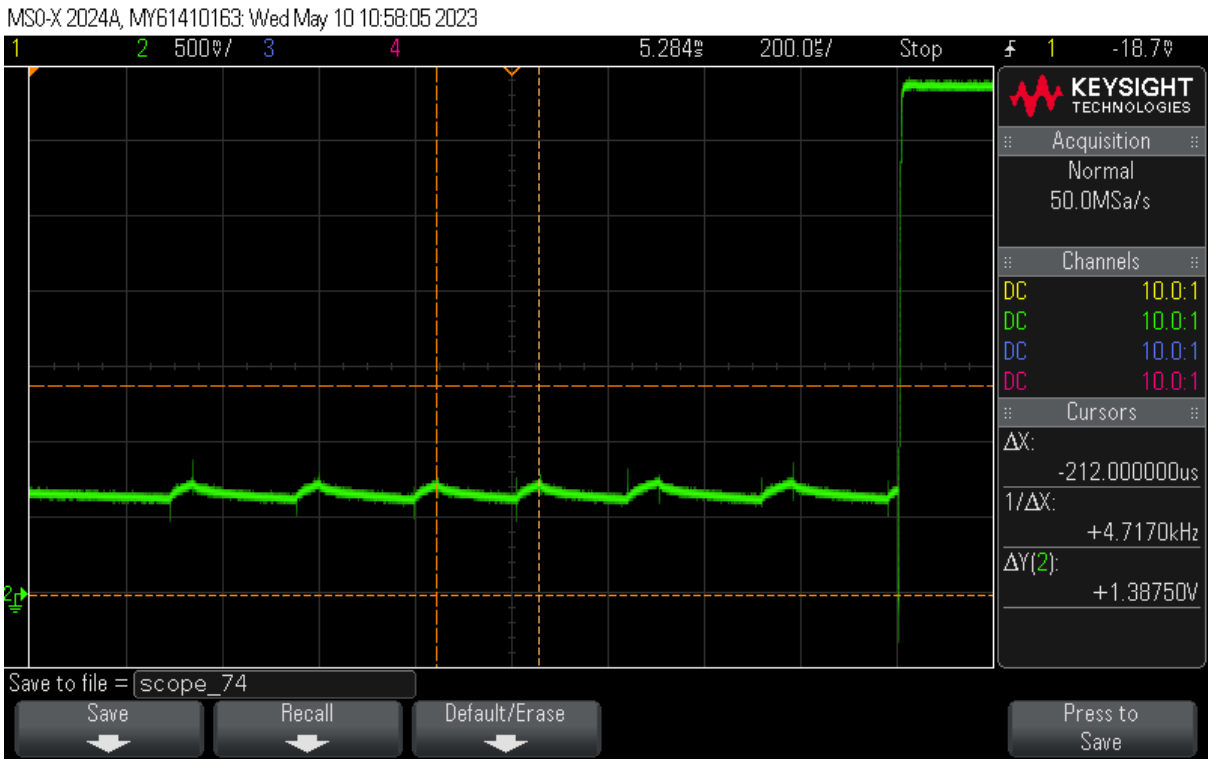

Figure 2.63. PWM frequency measuremnt at the hold phase of the coil current profile.

Table 2.19. Prameters of the coil current profile used for the thermal performance testing.

PARAMETER	**REFERENCE**	**VALUE**
Peak current	I_{peak}	10 A
Hold current	I_{hold}	5 A
Ramp phase time	t_{ramp}	4 ms
Peak phase time	t_{peak}	4 ms
Bypass phase time	t_{bypass}	2.5 ms
Hold phase time	t_{hold}	1.5 ms
Decay phase time	t_{decay}	1 ms
Turn-off time	$t_{turn-off}$	4 ms
Switching cycle period at 3000rpm	T_{cycle}	20 ms
Load	-	PAV8

Using the load parameters from Table 2.19, the input and the bridge MOSFETs average current values were calculated, which are as follows.

– High-side PWM-MOSFET (Q1): 2.22 A.
– Low-side PWM-MOSFET (Q2): 2.22 A.
– Select MOSFET (Q8): 4.31 A.
– Input MOSFET (Q14): 6.66 A.

Finally, the power losses of each MOSFET were calculated (see Table 2.20), which were used in COMSOL simulation model.

Table 2.20. Calculation results of the bridge MOSFETs power losses at the NGCD thermal performance test.

FET	f_{sw_peak}	f_{sw_hold}	V_{DD}	t_r	t_f	Q_{rr}	$R_{DS(on)}$	P_c	P_{sw}	P_{tot}
Q1	7.7kHz	4.7kHz	24V	59ns	29ns	67nC	4.5mOhm	22mW	43mW	65mW
Q2	7.7kHZ	4.7kHZ	24V	59ns	29ns	67nC	4.5mOhm	22mW	43mW	65mW
Q8	50Hz		24V	-	60ns	67nC	4.5mOhm	83mW	1mW	84mW
Q14	-		24V	-	-	-	10mOhm	443mW	-	443mW

Figure 2.64 shows the CMOSOL simulation results aquired using parameters from Table 2.20 and Figure 2.66 shows the thermal camera readings at the NGCD thermal performance test.

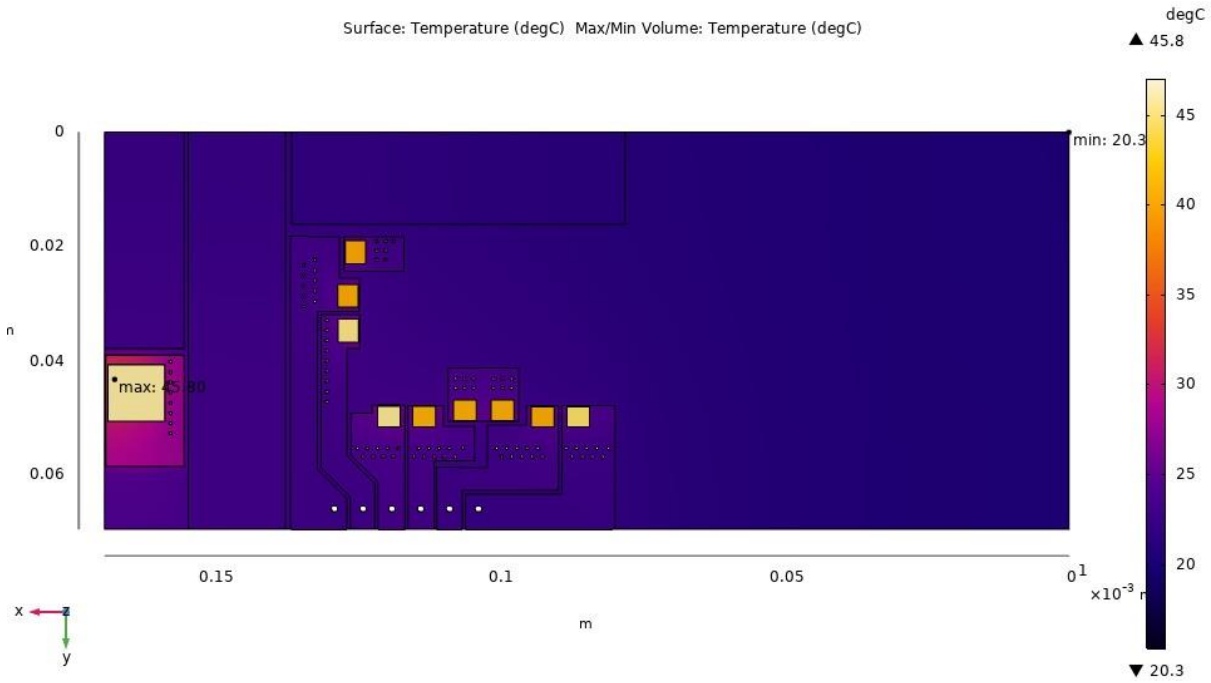

Figure 2.64. CMOSOL simulation results using parameters of the NGCD thermal performance test.

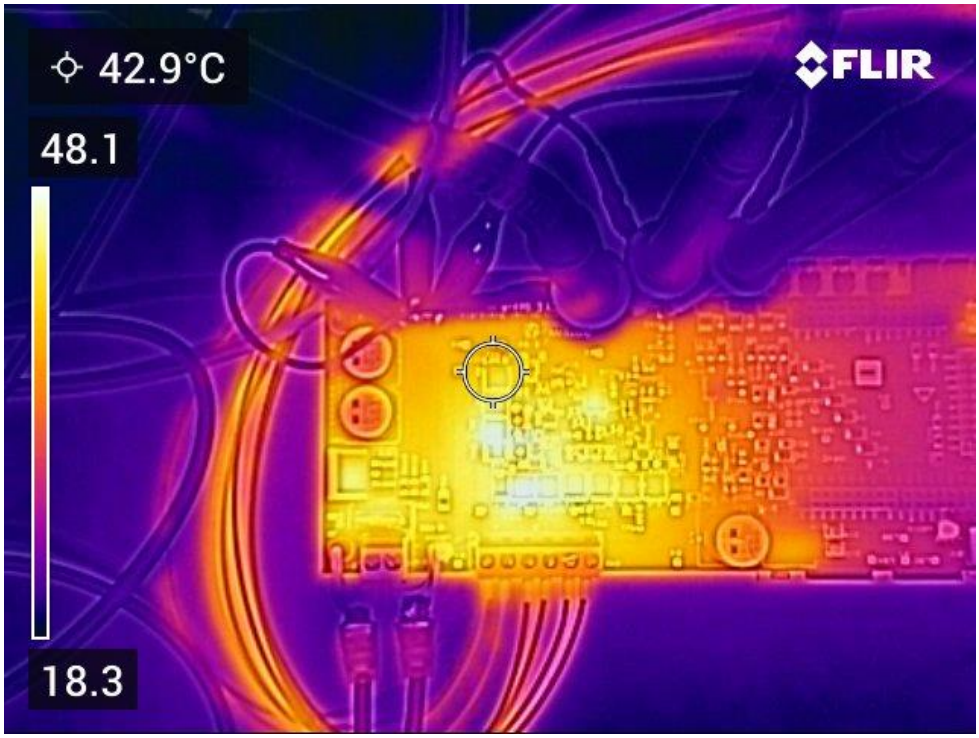

Figure 2.65. Thermal camera readings at the NGCD thermal performance test.

Table 2.21 gives a comparison between the thermal performance simulation and the test of the NGAD prototype board results.

Table 2.21. Comparison of the MOSFETs temperature between the simulation and test results.

MOSFET	T(°C) test at T_A 20°C	T(°C) simulation at T_A 20°C	Error (%)
Q1	43-48	40-41	6.98-14.58
Q2	43-48	40-41	6.98-14.58
Q8	45-48	44-46	2.22-4.44
Q14	46	45	2.22

As can be seen from Table 3, there is some discrepancy between the simulation and test results, which produces an error of the simulation results between 2.22% and 14.58%. Analysing the hot spots of the prototype board from the thermal camera reading, can be seen that the hottest area is where most of the current circulates (power_supply-coil_driver and coil_driver-coil_connector loops). Also, the largest discrepancy between simulation and test results belongs to MOSFETs that are placed over the overlapping current loops.

Therefore, the difference between the simulation and test results can be explained by that the simulation model does not take into account the joule heat generated by the current flow through the PCB copper components.

Thus, the error of the simulation results can be reduced by creating a Multiphysics model of the prototype board, which will include the heat transfer in solid and the electric currents physics, which considers joule heating.

Another approach to reducing the simulation error is creating a PCB design that will allow an even current flow distribution within the board, thus avoiding the multiple heat sources being overlapped at one point of the PCB. This will lead to an even distribution of the Joule heat over the PCB, thus equally splitting the simulation error within analysed components. The "source star" or "source single point" power distribution technique can be used for that purpose, which will benefit the PCB design in different aspects (see [56]).

Regarding the COMSOL model, it can be concluded that the developed thermal model gives fair results that can be used for orientation when designing power electronics.

Regarding the thermal performance of the NGCD, from the test results can be seen that at the full load, the maximum temperature rise of a power MOSFET is 28 degrees when a large volume of air is provided for heat exchange around the board. The MOSFET junction temperature will be around 102 degrees at the maximum ambient temperature of 75 degrees specified by the design requirements. This is 73 degrees below the MOSFET's maximum operating temperature specified in the datasheet, which provides a safe operation of the MOSFET. However, for the controller designed to operate inside an IP67-rated (water and dustproof) enclosure, the use of a heatsink is required.

2.4.7.5 Solenoid valve residual energy regeneration test

This test shows that the Next Generation Coil Driver can provide up to 12.25% of energy recovery during the fast decay.

Figure 2.66 shows the coil current profile and the PWM signal samples captured when actuating the DD valve MAV8 in the air during the energy regenerating test. The turn-on phase of the solenoid lasts first 3 ms, at this phase the energy is being consumed. Then solenoid is

switched into the fast-decay mode (the turn-off phase) to allow the regeneration of the remaining energy.

The data acquired during the test were used to estimate the average currents at each stage of the current profile and the average duty cycle of the peak stage. Then using calculated average values, phase duration time and supply voltage value, the spent and the regenerated energy values were calculated. All values of the energy regeneration calculation are given in Table 2.22.

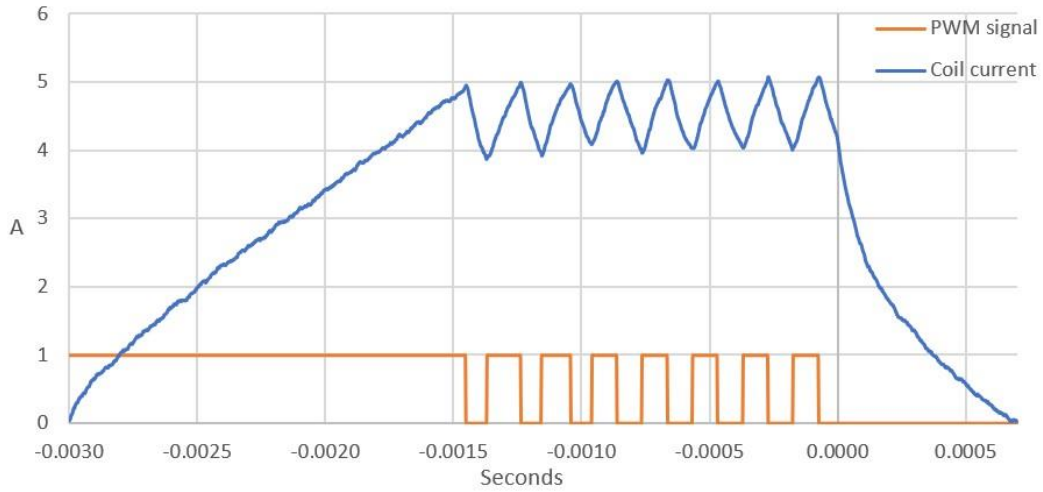

Figure 2.66. Samples of the coil current profile and PWM signal captured during energy regeneration test.

Table 2.22. Energy regeneration test calculation results.

Supply voltage	24 V
Ramp phase average current	2.72 A
Peak phase average current	4.51 A
Decay phase average current	1.35 A
Peak phase average duty cycle	0.51
Ramp phase time	1.55 ms
Peak phase time	1.45 ms
Decay phase time	0.7 ms
Used energy at ramp phase	0.10 J
Used energy at hold phase	0.08 J
Total used energy	0.18 J

Regenerated energy	0.02 J
	12.25%

2.4.8 Tuning of the NGCD design.

As can be seen from the test results described previously, a ringing was observed on the S-node of the half-bridge and the drain of the low-side MOSFET. Additionally, the ringing was causing undershoots and overshot as well as an increase of radiated emissions in the frequency range of the oscillations. As it was mentioned previously, these ringing are caused by a resonant of the series RLC loops created by the circuit parasitic inductance and capacitance.

According to [48], [49]. [50], [51], [52] and [57] various methods can be used in order to mitigate the oscillations. The most common methods are changing the MOSFETs drain-to-source slew rate, changing decoupling capacitance, decreasing parasitic inductance, adding a snubber circuit and gate-source capacitor, etc.

The tuning results of the H-bridge design by changing the decoupling capacitance and the dV/dt of the MOSFET's slew rate are described in this chapter.

Half-bridge tuning

First, the slew rate of the half-bridge MOSFETs was decreased by two times by replacing the 1MOhm IDRIVE resistor of the DRV8320H setup with 75 kOhm. According to the datasheet, this decreases the gate current of all MOSFETs by two times.

Figure 2.67 and Figure 2.68 show the half-bridge negative transients and ringing test results at MOSFET turn-off and turn-on events, respectively, with a decreased slew rate. As can be spotted, the slew rate of the MOSFET has decreased by two times. The ringing of the higher frequency (106-125 MHz) is significantly mitigated when the ringing of the lower frequency (20-25 MHz) does not reduce much.

Next, the H-bridge ceramic decoupling capacitor of 0.01 uF was replaced by the 1 uF capacitor, thus, providing more current for fast switching (eliminating ESL).

Figure 2.69 and Figure 2.70 show the test results of the modified H-bridge circuit. As can be seen, the lower frequency ringing of 20-25 MHz cannot be observed anymore, and the frequency oscillations are significantly mitigated.

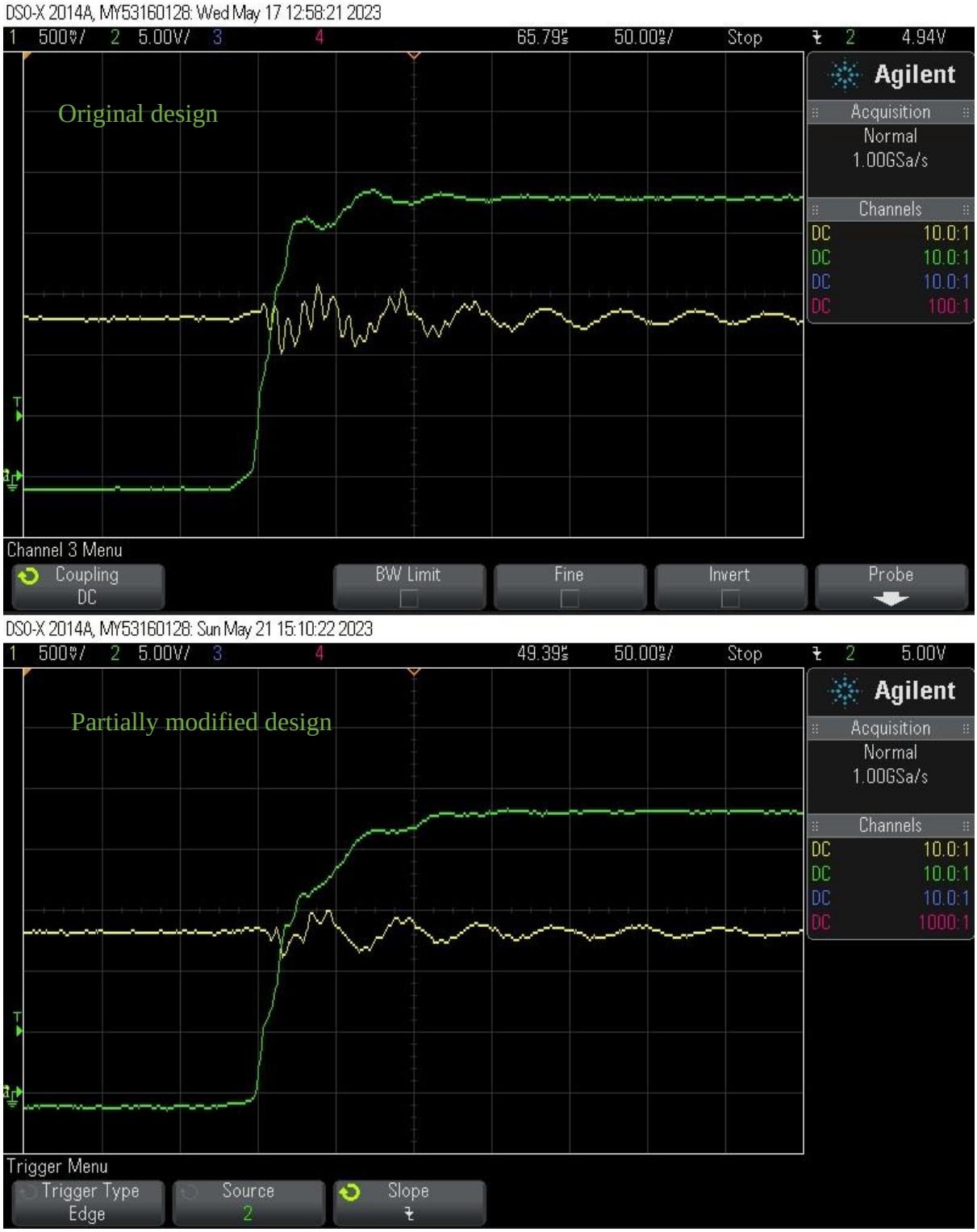

Figure 2.67. Half-bridge negative transients and ringing test at MOSFET turn-off. Top - original design, bottom - partially modified design by decreasing the slew rate by two times. Yellow trace – load current, green trace – MOSFET drain-to-source voltage (MOSFET current is about 10 A).

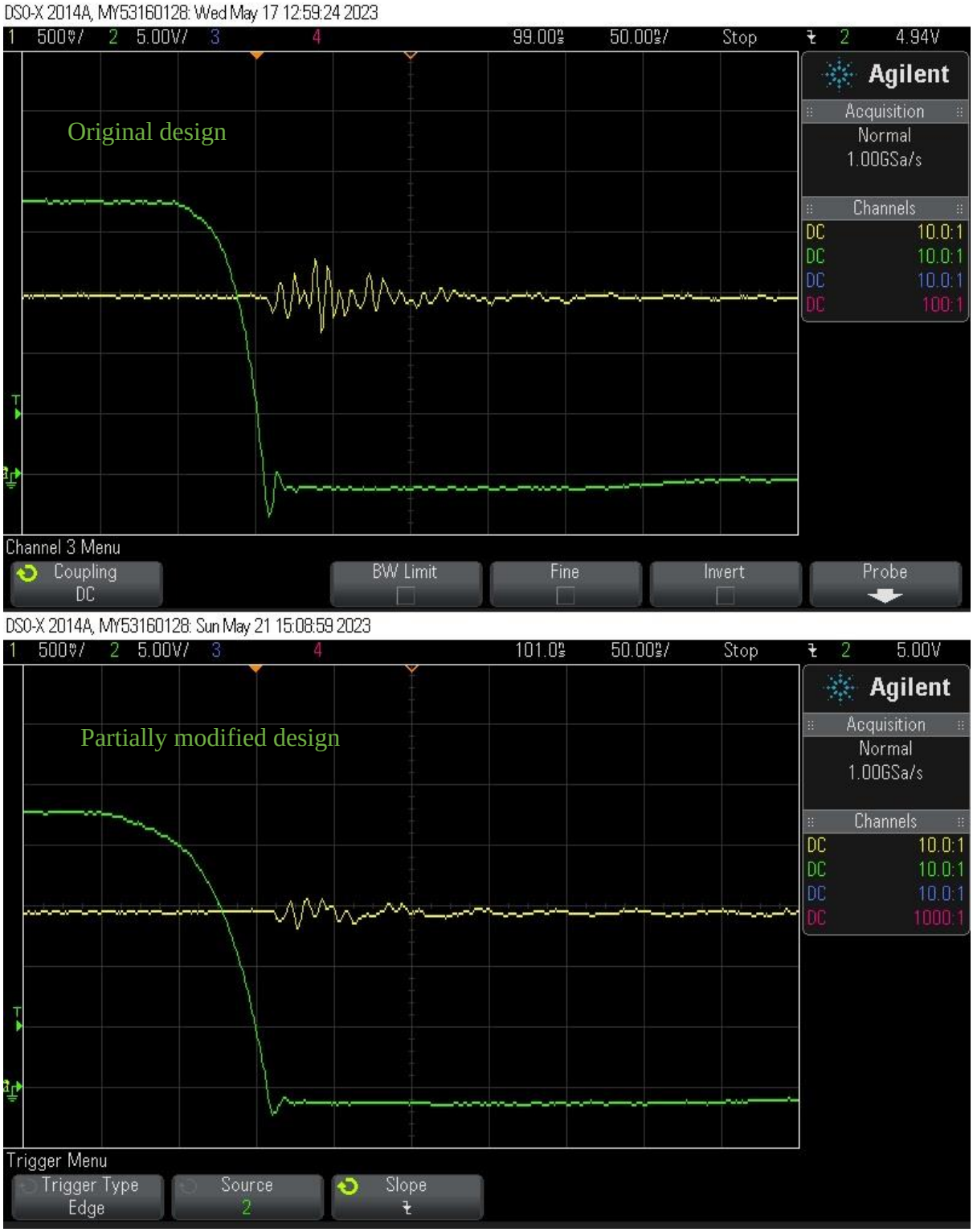

Figure 2.68. Half-bridge negative transients and ringing test at MOSFET turn-on. Top - original design, bottom - partially modified design by decreasing the slew rate by two times. Yellow trace – load current, green trace – MOSFET drain-to-source voltage (MOSFET current is about 10 A).

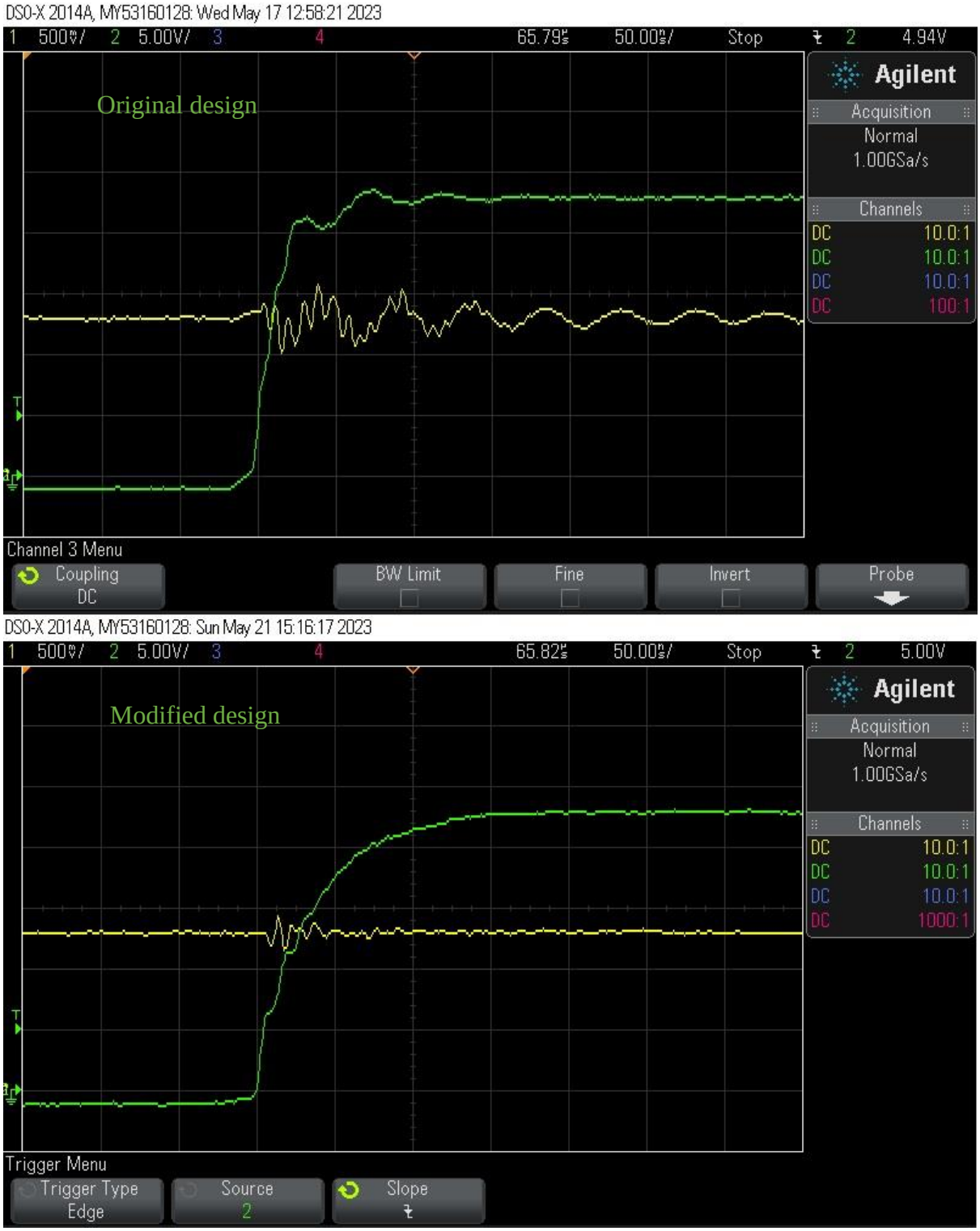

Figure 2.69. Half-bridge negative transients and ringing test at MOSFET turn-off. Top - original design, bottom – modified design by decreasing the slew rate by two times and replacing 0.01uF bridge decoupling capacitor by 1uF. Yellow trace – load current, green trace – MOSFET drain-to-source voltage (MOSFET current is about 10 A).

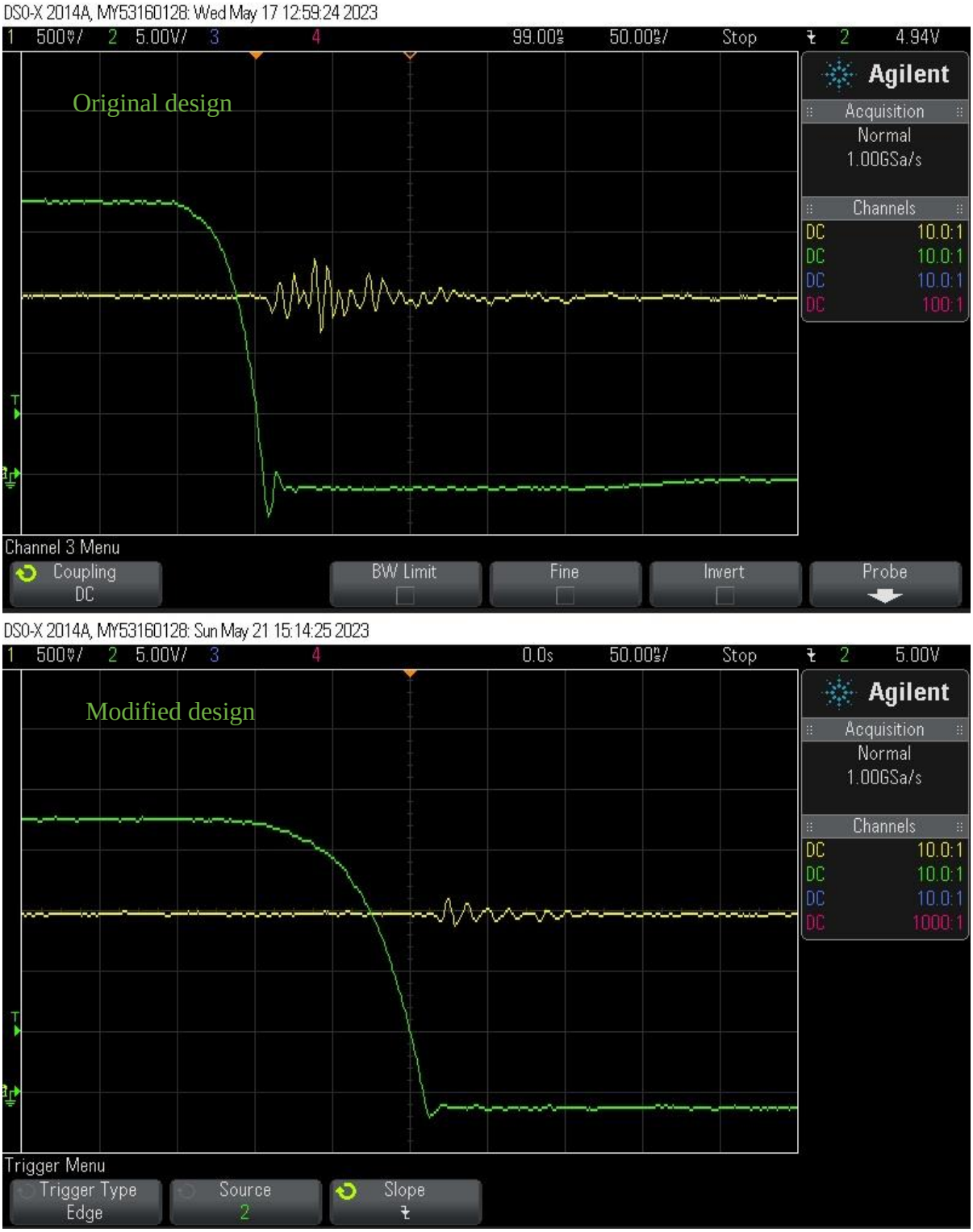

Figure 2.70. Half-bridge negative transients and ringing test at MOSFET turn-on. Top - original design, bottom – modified design by decreasing the slew rate by two times and replacing 0.01uF bridge decoupling capacitor by 1uF. Yellow trace – load current, green trace – MOSFET drain-to-source voltage (MOSFET current is about 10 A).

Low-side driver tuning

In order to mitigate the ringing of the drain node of the low-side MOSFET the voltage slew rate was decreased by three times approximately by replacing the 4.7 Ohm gate resistor with a resistor of 68 Ohm.

Such a solution will increase the response time of the low-side overcurrent protection (OCP) by around 100 ns, which is not significant for this application. The effect on the thermal performance of the low-side MOSFET will be negligible due to its low switching frequency (50 Hz max).

Figure 2.71 shows the test results of the modified circuit, comparing it to the original one. As can be seen, the ringing was successfully mitigated, and the peak voltage of the drain voltage spike was decreased from 9 V up to 2 V, which can be considered a very good result.

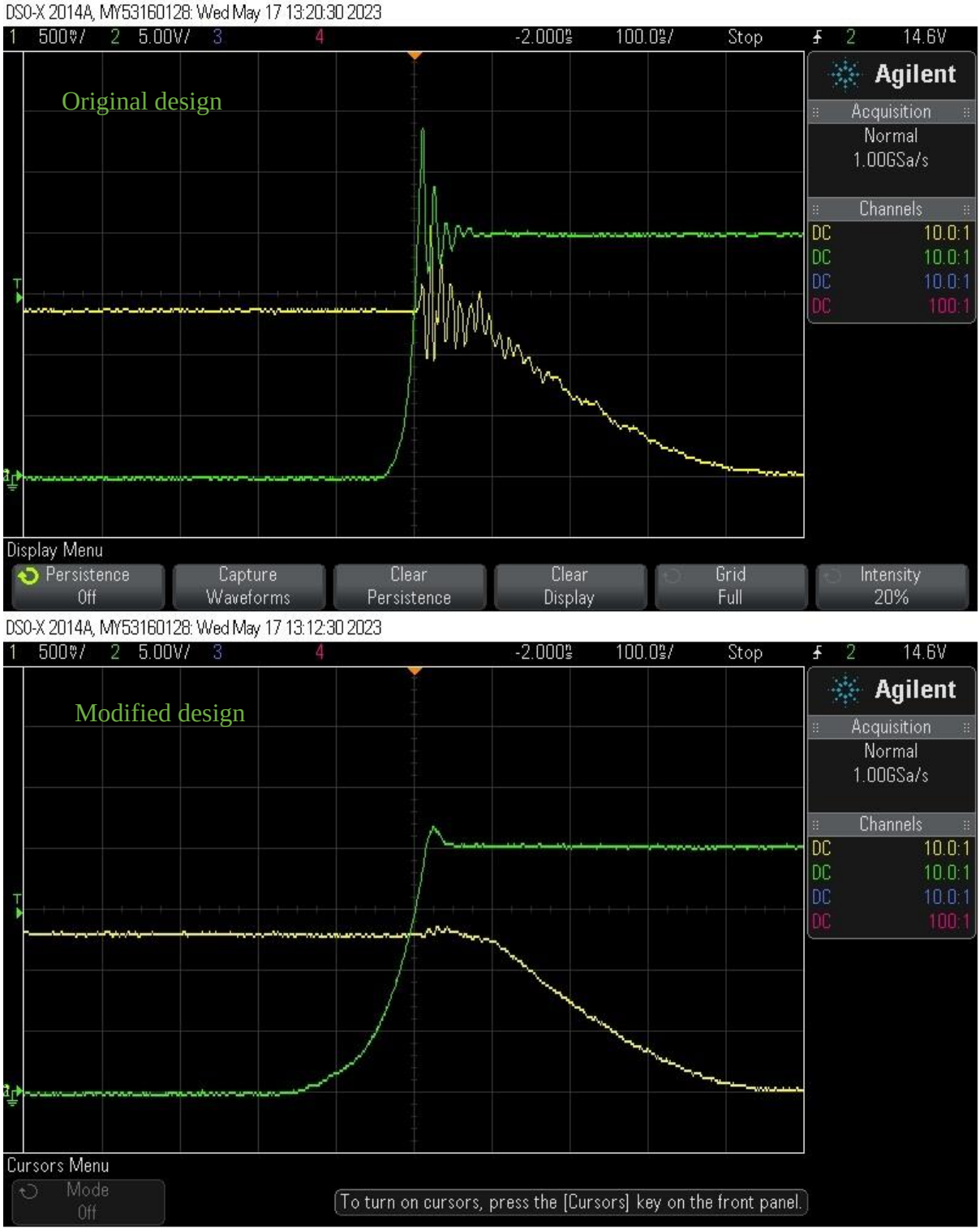

Figure 2.71. Drain node negative transients and ringing test at MOSFET turn-off. Top - original design, bottom - modified design by decreasing the slew rate by three times. Yellow waveform – low-side MOSFET current, green waveform – low-side MOSFET drain-to-source voltage. (MOSFET current is about 10 A)

Radiated emissions results

After mitigating the ringing of the H-bridge nodes, the radiated emission test was carried out again. Figure 2.72 shows the NGCD prototype board emissions test results of the modified design, and Figure 2.73 shows the comparison of the radiated emissions test results between the original and modified designs.

As can be seen from the results, a significant reduction of the radiated emissions was achieved by mitigating the H-bridge ringing. A reduction of 9-8 dB can be observed in the range between 20 MHz and 25 MHz a, 5-6 dB in the range of 30-32 MHz, 10-15 dB in the range of 106-126 MHz, and 8-15 dB in the range of 130-200 MHz. Thus, the margin between the regulation limit and the board's actual emissions was brought down from 2 dB up to 9 dB at the closest point.

Thus, considering the previously mentioned statement that the emissions secure margin is 5-6 dB and the fact that the regulation limit is given for the test when the antenna is placed 1 meter from the tested device, it can be stated that the 15-channel DD controller based on the NGCD design of the modified setup will highly likely pass the EMC test.

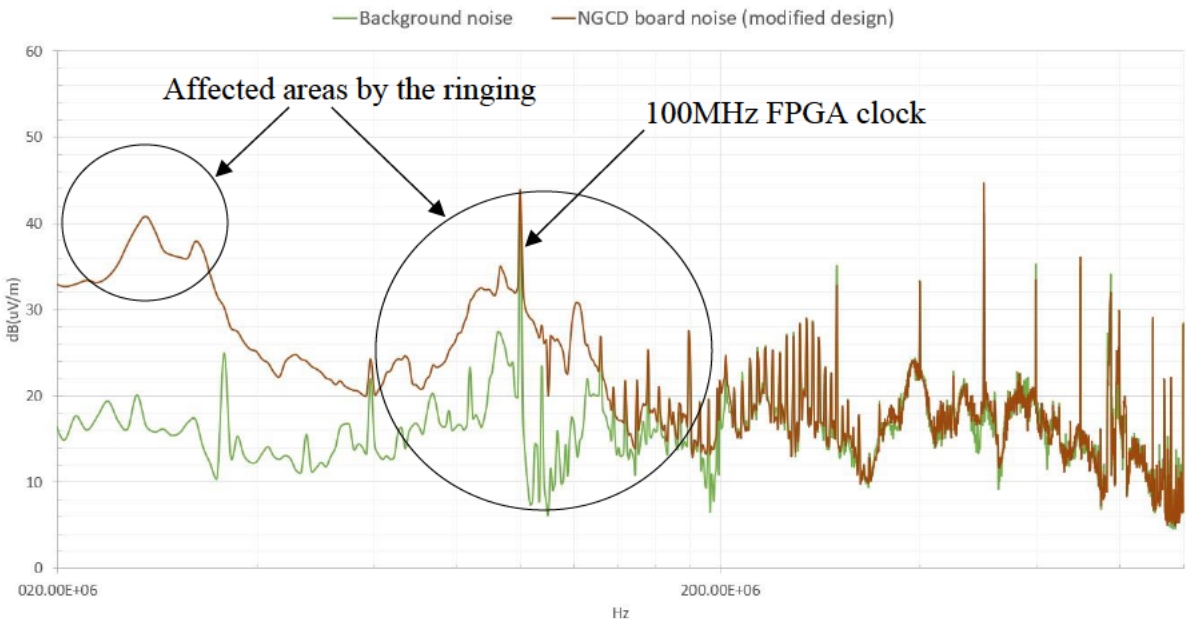

Figure 2.72. NGCD prototype board emissions test results of the modified design. Green waveform – background noise (Arty-A7 board is on), brown waveform – NGCD boar noise (operating three channels at the worst-case scenario).

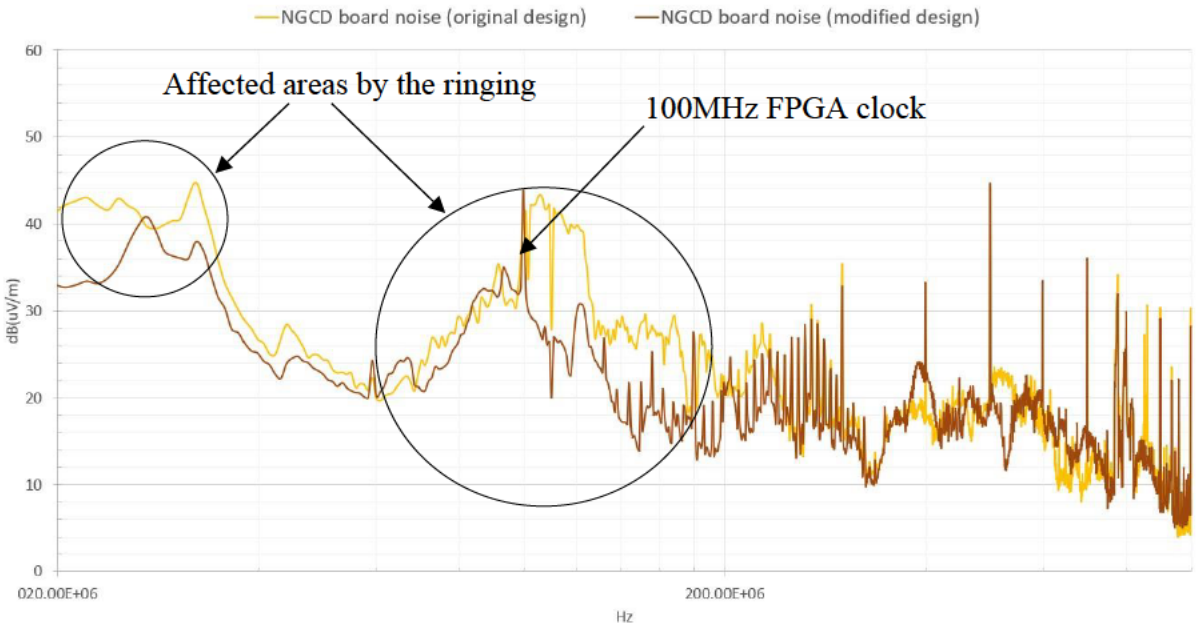

Figure 2.73. Comparison of the radiated emissions test results of the NGCD prototype board, original design vs modified design. Yellow waveform – original design, brown waveform – modified design.

Thermal performance check

However, decreasing of the slew rate proportionally increases the switching losses of the MOSFETs. Table 2.23 gives a summary of the power losses estimation of the H-bridge MOSFETs. As can be seen, the switching losses of the half-bridge MOSFETs Q1 and Q2 doubled. According to COMSOL simulation, this will increase the temperature rise of the MOSFETs from 20-21°C to 31-32°C, which is by 35%. The increase in the temperature rise will require to decrease the thermal resistance of the design in order to keep the MOSFETs junction temperature around 100°C.

Table 2.23. Bridge MOSFETs losses estimation of the NGCD prototype board modified design.

FET	f_{sw_peak}	f_{sw_hold}	V_{DD}	t_r	t_f	Q_{rr}	$R_{DS(on)}$	P_c	P_{sw}	P_{tot}
Q1	7.7kHz	4.7kHz	24V	117ns	58ns	67nC	4.5mOhm	22mW	83mW	105mW
Q2	7.7kHZ	4.7kHZ	24V	117ns	58ns	67nC	6.3mOhm	22mW	83mW	105mW
Q8	50Hz		24V	-	150ns	67nC	6.3mOhm	83mW	2mW	85mW

Therefore, it can be concluded that decreasing the slew rate of voltage across the MOSFETs to improve the radiated emission results, caused by S-node ringing, can be not always suitable for fast-switching applications or applications that require enhanced thermal performance.

Alternative solutions such as snubbers or the use of the drain-to-source capacitor should be considered in future development.

2.5 Summary and conclusions of the chapter

This chapter established the next-generation coil driver (NGCD) design for Digital Displacement® (DD) solenoid valves. That allows for a major improvement in efficiency, reliability, and cost compared to the present design of the coil drivers used in DD controllers. Thus, reaching the first goal of this thesis.

Simulation and test results demonstrate that the DD controller will significantly benefit from integrating the NGCD design due to the following features.

- Reduction of heat dissipation at fast-decay mode with energy regeneration up to 12.25%.
- Reduction of heat dissipation at slow-decay mode more than three times.
- A fast overcurrent protection of a maximum response time of less than 6.5 us.
- Low-side coil current sensing.
- Two control signals per channel to enable three modes of operation.
- 5 A average current capability at up to 15 A peak current.
- Operating voltage 9 to 36 V.
- Operating ambient temperature from -20°C to +75°C.
- Footprint and cost reduction up to 40%.

The development of the next iteration of the NGCD will be focused on decreasing the footprint and component count by using a 3.3x3.3 mm power MOSFETS instead of a 5x6 mm, integration of one-chip solutions for the low-side current singing and overcurrent detection circuits (e.g., INA381A2), and for low-side gate drivers (e.g., DRV8300). Also, the power rating of the current sense resistor (CSR) will be decreased from 1.5 W to 1 W by using a current sense amplifier (CSA) of higher gain and CSR of lower resistance (e.g., CSA GAIN 20, CSR 3 mOhm), which will benefit the design from a wider choice for CSR, reduction of power dissipation and cost.

Finally, the NGCD design was approved for use in the 15-channel controller DDC15, which is successfully operating the new design Digital Displacement pump/motor machine DDP10X.

Chapter 3

Low-pressure valve reopening detection

This chapter describes a method that allows reliable detection of the low-pressure valve (LPV) reopening of the single coil DD modules during its pumping or motoring mode of operation. The method provides a reliable and stable signal indicating LPV reopening, which can be used as the feedback signal to enable the closed-loop motoring of the new-generation DD machines.

3.1 Introduction

As mentioned previously, a pump/motor DD machine can provide both pumping and motoring. The low-pressure valve LPV and the high-pressure valve HPV have a shared magnetic circuit and so one solenoid coil. During the pumping cycle, after the solenoid is actuated, the LPV is held closed, and the HPV is held open by the pressure that is applied on the low-pressure poppet (LPP) and the high-pressure poppet (HPP) surfaces in the direction against the return spring. This pressure is created by the hydraulic oil flow created due to the piston motion toward top dead centre (TDC). Therefore, the solenoid is not required to be energised during the pumping cycle, and the power supply can be disconnected just after the LPV closes. As soon as the piston reaches TDC, the piston starts moving towards the bottom dead centre (BDC) the pressure will drop and both valves (LPV and HPV) will change their state to the opposite by means of the return spring. Therefore, the pumping cycle will last until the end of the piston stroke, and both valves will be toggled by themselves at the ideal timing without any control signal being required. Thus, the end of the pumping cycle is self-controlled, providing the maximum displacement and safe operation of the machine (there is no risk of starting the undesired motoring cycle when the piston is moving toward BDC).

However, during the motoring cycle, the situation is different. After the solenoid is energised and both poppets (LPP and HPP) are shifted initiating the motoring cycle the solenoid has to continue to be energised in order to keep providing the electromagnetic force to hold LPV closed, and HPV opened while the piston is moving towards the BDC. Both valves require to be toggled to the stand-by position by means of the control signal before the piston reaches BDC, otherwise, an undesired pumping cycle will be initiated as soon as the piston starts moving toward TDC.

The maximum displacement of the DD machine at the motoring mode of operation can be achieved when the full stroke of the piston is used. Therefore, to reach maximum displacement, the LPV must be reopened when the piston is as close as possible to BDC, which is very difficult to achieve without controlling the LPV reopening timing, which, in turn, requires an LPV reopening feedback signal.

In 2010-2011 Artemis Intelligent Power Ltd has developed and patented a technique for closed-loop control of DD motors, which is described in patent [3]. The back-EMF signal, induced in the solenoid coil by the armature motion, which is physically attached to the LPP, was used as the LPV reopening feedback signal name as 'reopening signal'. Therefore, the reopening signal indicates the angle at which the LPV reopens. Also, the reopening signal (or lack of one) can be used to diagnose faulty valves, which can then be disabled by the controller.

Later, Artemis Intelligent Power Ltd has developed and patented a lower-cost, more compact solenoid valve design, the concept of which is described in patent [58]. However, the existing closed-loop techniques were not applicable because the back-EMF signal was not detectable by the available methods.

Figure 3.1 shows a schematic diagram of the early design DD module that has two valves (LPV and HPV) with two separate coils, and a new more compact DD module that has one common coil for both LPV and HPV.

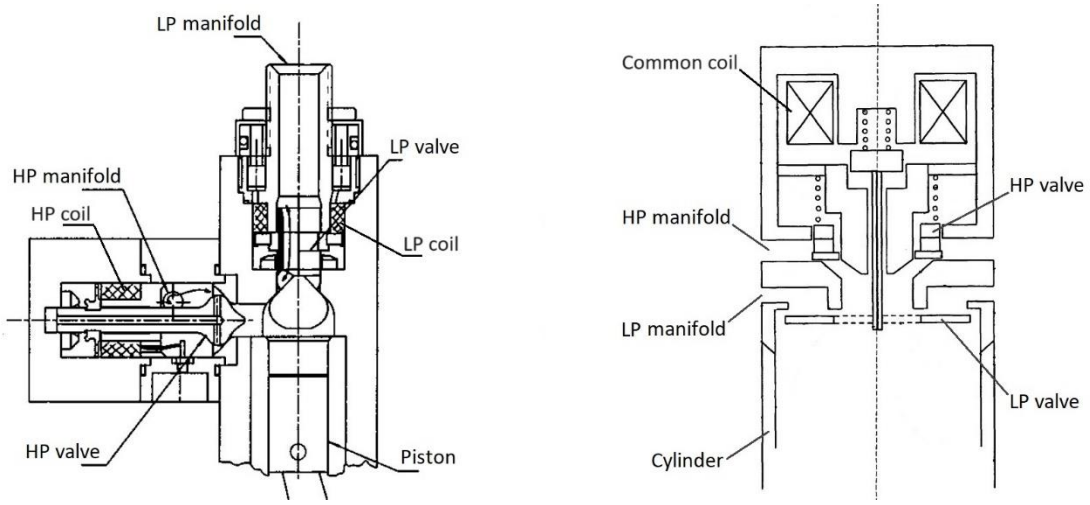

Figure 3.1. Left – schematic diagram of a DD module that has a separate coil for each valve, LPV and HPV [59]. Right – schematic diagram of a DD module that has one common coil for LPV and HPV [5]. (Not to scale)

In machines that have physically separate LPVs and HPVs, each coil energises separately by applying a PWM signal. The LPV energises at the start of the motoring cycle, to shunt the LPV, and de-energises soon after. The HPV energising starts at a similar time, but continues, albeit with a lower duty cycle, until the end of the motoring cycle. In this case, the reopening signal is easy to detect, since it occurs long after the LPV current has decayed, and the reopening signal is superimposed against the coil 0 V or 0 A. The early design controllers contain circuitry which detects the reopening signal as a small voltage dip (Figure 3.2, a) and sends this information to the controller as a digital signal. By measuring the time of this signal relative to the shaft position signal, the controller can thus calculate the angle at which the LPV was reopened.

However, the new DD modules have one shared coil for both LPV and HPV. Therefore, the reopening signal is superimposed with the decay voltage (Figure 3.2, b) of the decay phase. This makes it much harder to detect.

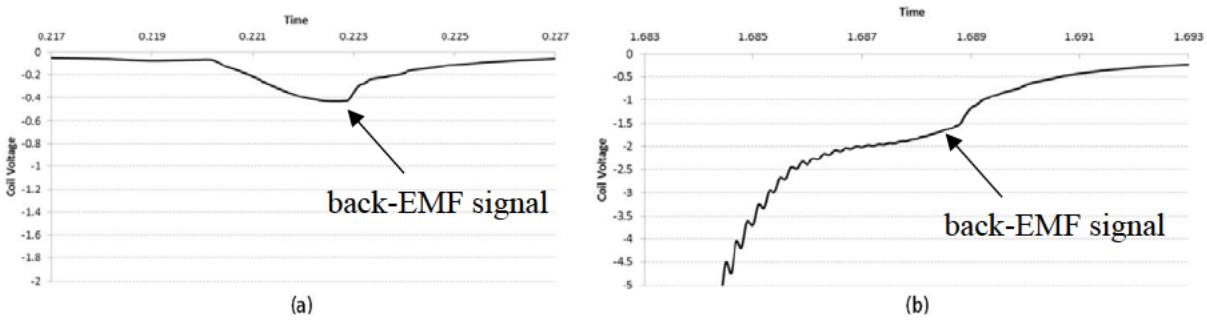

Figure 3.2. a) Voltage drop at reopening in the valve with the separate coil. b) Voltage drop at reopening in the MAV valve with the shared coil. (Samples provided by Daniil Dumnov)

3.2 State of art on back-EMF detection at LPV reopening

This section gives an overview of methods that were used for LPV reopening detections of the DD modules with separate solenoid coils for LPV and HPV and prior investigation work that was undertaken by the DD department to enable the LPV reopening detection in the new more compact design of the DD modules with a shared solenoid coil.

3.2.1 Back-EMF detection in early design DD valves

The patent [3] describes a circuit that allows detecting a back-EMF signal induced by the coil armature motion at the de-energising stage of a solenoid DD valve. This circuit was used in the

early DD controllers (XPHS/AMC1/AMC2) to detect the reopening of the early design LPV that has the magnetic circuit separated from the HPV magnetic circuit and has its own coil (Figure 3.1, b).

According to the patent [3], the circuit shown in Figure 3.3 comprises a coil driver and a back-EMF detection circuit (64). The coil driver circuit consists of a P-channel MOSFET 54 that is connecting a power supply across the solenoid coil (52), a flywheel diode (60), and a Zener-diode (optional) (62) for current-dumping. The MOSFET (54) is controlled by means of a controller (not shown), which is connected to gate (56). The back-EMF detection circuit consists of a level-shifting Zener-diode (68) that is connected to the sensed node (58), an inverting Schmitt trigger (66), a bias resistor (72), and a protection resistor (70). Diodes (74) and (76) that are protecting the input of the Schmitt trigger as well as capacitor (78) that forms a low-pass filter together with the protection resistor (70) are optional. The output of the Schmitt trigger is connected to the controller (not shown).

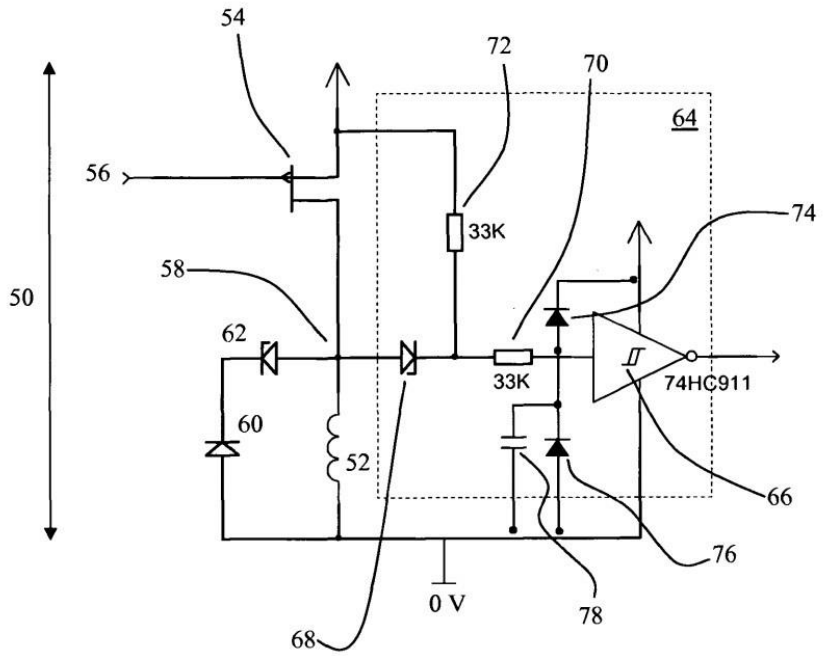

Figure 3.3. Block diagram of the back-EMF detection circuit used in AMC/AMC2 [3]

During the operation, when the MOSFET is switched off, the voltage of the sensed node is 0 V and the Schmitt trigger's input is driven by the bias resistor to the voltage of the level-shifting Zener-diode of 3 V, which set the Schmitt trigger output low. When the MOSFET is switched on, the sensed node is pulled to the supply voltage, the coil is energising. Protecting resistor

protects the Schmitt trigger input the output of which continues to be low. When the solenoid needs to be de-energised, the controller switches off the MOSFET, and the coil decay current flows through the flywheel circuit. The voltage of the sensed node becomes negative, the magnitude of which is equal to the value of the current-dumping Zener-diode clamping voltage. The Schmitt trigger's output is set high. When the coil current falls to 0 A, the flywheel circuit becomes an open circuit, and the sensed node voltage is pulled to 0 V. The Schmitt trigger's output is set low. At this stage, the solenoid coil is being de-energised, and the magnetic force falls below the return spring force, which initiates the motion of the armature. The motion of the armature through the coil induces a back-EMF, which sets a negative voltage at the sensed node, which in turn, sets the output of the Schmitt trigger high. This signal is detectable by the controller and used as the feedback signal of the LPV reopening.

Figure 3.4 shows oscilloscope diagrams acquired during the back-EMF detection circuit testing, which was implemented in the previous models DD controller (XPHS). In the back-EMF detection circuit of this controller, the non-inverting Schmitt trigger is used instead of the inverting one, which differs from what is shown in Figure 3.3. Where the blue waveform is the analogue coil signal measured at the sensed node, and the red waveform is the digital signal measured at the output of the back-EMF detection circuit. The output signal is compatible with the FPGA GPIO.

Figure 3.4. Test results of the beck-EMF detection circuit that is proposed in the patent (The figure is taken from [60]).

As can be seen from the test results the reopening signal generated in machines with the physically separated LPVs and HPVs has quite a pronounced amplitude of about 5 V, which allows its reliable detection on the hardware level.

3.2.2 Amplifying back-EMF signal by applying a boost coil

In March 2016, Artemis Intelligent Power investigated the possibility of amplifying the back-EMF signal during LPV reopening in the single coil motoring valve MAV8 (stands for 8th generation motoring annular valve). Fergus McIntyre conducted the research and the experiment. The idea was to use an additional "boost" coil with a significantly larger number of turns to amplify the back-EMF signal. The experimental multi-coil consisted of a power coil of 150 turns and a boost coil of 1000 turns. A series of experiments with different configurations of coils connection were conducted to verify the back-EMF improvement and the impact of the boost circuit on the overall performance of the valve.

Figure 3.5 shows schematic diagrams of the experimental configurations of the boost circuit. The back-EMF signal was sensed by measuring the voltage at the output of the boost circuit, which is connected to the controller, with respect to the ground.

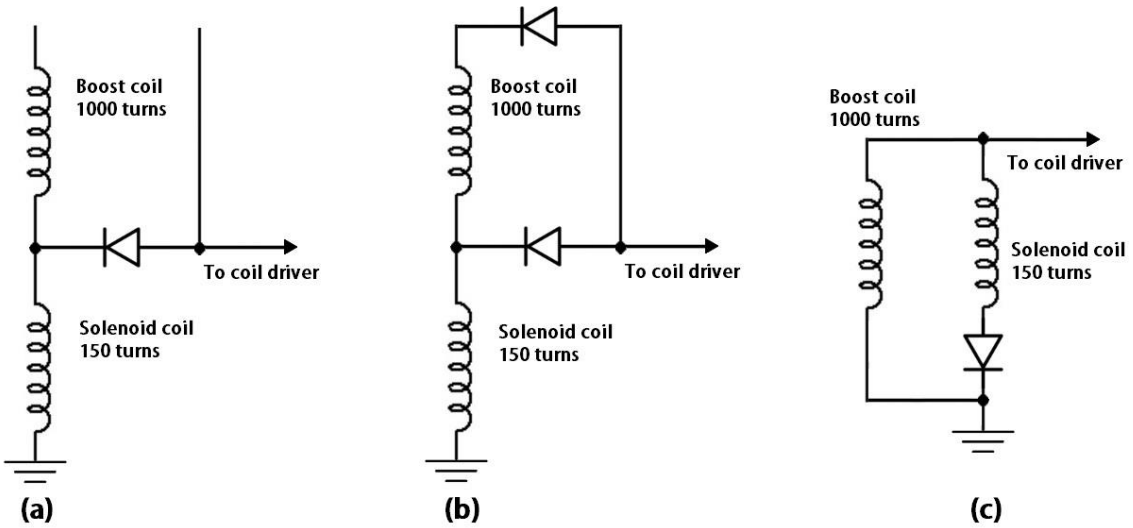

Figure 3.5. Schematic diagrams of the boost circuit during the testing: a) boost coil is disconnected, b) series connection of the boost coil, c) parallel connection of the boost coil.

The results of the tests are as follows.

a) No improvement of the reopening signal (the amplitude was not measured), the LPV closing time is 5.4 ms.

b) The amplitude of the reopening signal is 1.6 V, and the LPV closing time is 6.2 ms.

c) The amplitude of the reopening signal is 1.2 V, the LPV closing time is 7.0 ms.

Figure 3.6 shows the frontal cut of a fragment of the single-coil MAV8 valve against the MAV8 with a boost coil. As can be seen from the figure, the boost coil was integrated into the MAV design without increasing the length of the magnetic path. However, the thickness of the still part of the magnetic path was reduced, thus reducing its cross-section area. Nevertheless, the cross-section of the still part of the magnetic path is 2.6 times larger than the cross-section area of the armature.

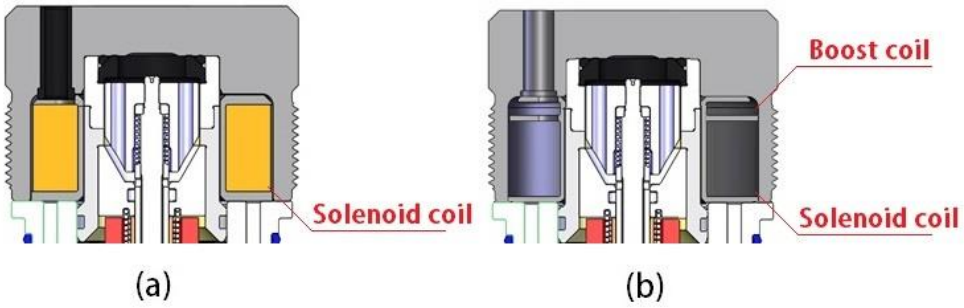

Figure 3.6. Frontal cut of the MAV8 valve: a) single coil design, b) double coil design.

Summarising the experiment results, the following conclusions were made:

1. The boost coil slows down the closing time of the LPV.

2. At the series and parallel connection of the boost coil, significant enhancement of the back-EMF signal was achieved. However, the industrial application of such a solution would require three wires from the coil to the controller and the implementation of additional sensing circuity, which makes the system commercially less attractive.

3. The amplified signal continues to be overlapped by the fast decay voltage, which requires the development of new detection methods.

4. The diode that is placed in series with the solenoid coil will increase the overall power loss of the system.

3.2.3 Developing a more sophisticated back-EMF detection algorithm

Following F. McIntyre's experiments, Artemis Intelligent Power investigated the possibility of detecting the signal by using a more sophisticated detection algorithm. This research was conducted by Daniil Dumnov.

The focus of this work was to assess the feasibility of using different methods to detect the reopening signal reliably and accurately for the single-coil MAV valve. This was done by importing test data (coil voltage, coil current, poppet position etc.) into MATLAB software, which allowed the different methods to be quickly developed and tested. It was found that by using a complex processing logic (see Figure 3.7), it was possible to accurately detect the reopening signal based on the coil voltage.

Figure 3.7 shows the logic developed by Daniil Dumnov in the Simulink/MATLAB environment in order to detect the MAV reopening signal.

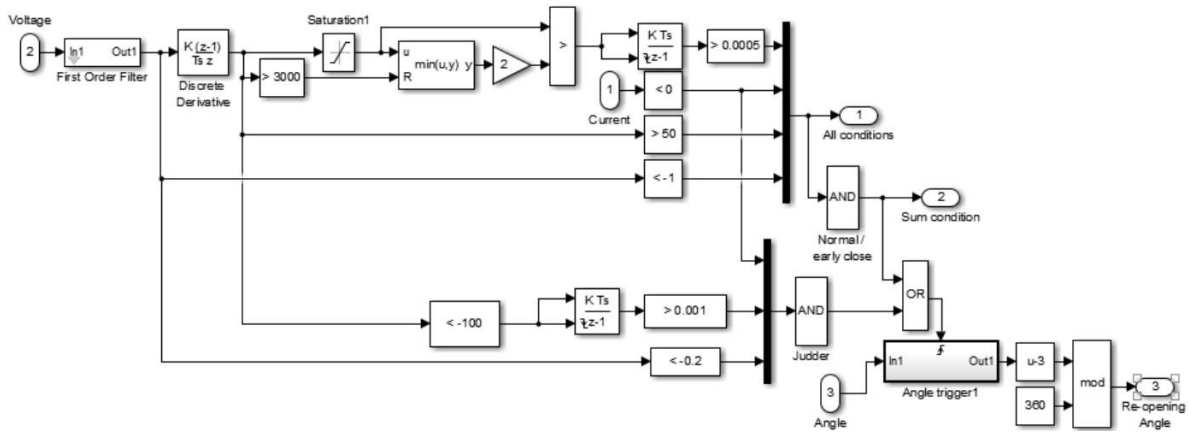

Figure 3.7. Logic developed in Simulink/MATLAB to detect the MAV reopening signal by Daniil Dumnov.

According to Daniil Dumnov, the logic was essentially the following conditions:

– Since the valve has been switched off, the value of dV/dt (low pass filtered) has increased by a factor of 2 AND [A <= 0] AND [-dV/dt > 50] AND [V < -1]

The voltage waveform containing the MAV reopening signal that is superimposed with the fast decay voltage of the decay phase as well as the output of the developed algorithm detecting the signal are shown in Figure 3.8.

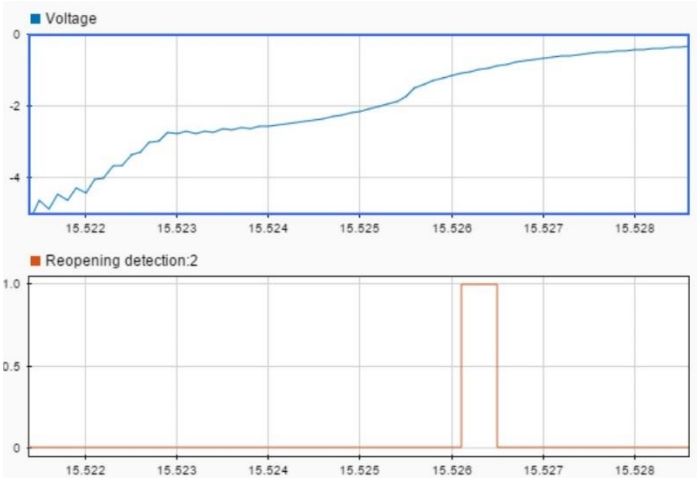

Figure 3.8. The output of an algorithm developed to detect a reopening signal from the MAV coil voltage. (Provided by Daniil Dumnov)

In summary, it was found that by using complex processing logic, it was possible to accurately detect the reopening signal (within MATLAB), based on the coil voltage measurements. However, if the processing logic was limited to those functions that would be feasible to implement in an electronic circuit, or on the controller software, it was found to be not possible to develop an accurate detection method. The major hurdle was that since the voltage dip was superimposed upon the latching decay, the usual method of a simple comparator (is voltage < x?) did not work, and differentiation was required. Unfortunately, the coil voltage is too noisy for differentiation to give a reliable indication of the reopening signal, even with other simple logic conditions added to the processing.

3.2.4 Back-EMF sensing in DPC12

Since the back-EMF detection circuit described in 3.2.1 did not work for the new MAV design, there was no reason to include it in the DPC12 design. The Artemis engineers opted for current sensing in order to detect the back-EMF signal during LPV reopening. In addition, the current sensing circuit also will be used for closed-loop current control, over-current detection, etc.

Figure 3.9 shows a simplified schematic diagram of the DPC12 MK1 current sensing design, which is the high-side current sensing circuit feeding the output into the FPGA's ADC for further processing of the current signal.

Mark Brett has developed two methods in order to detect the LPV reopening signal. One of the methods was based on detecting a sudden increase of the coil current amplitude due to the back-EMF, generated by the LPV reopening when the coil driver is set in the slow-decay mode (high-side MOSFET is off and the low-side MOSFET is on). Detection of the solenoid valve state change by analysing coil current profile during turn-off transition is described in [30].

The other method was based on injecting a small amount of current into the coil using the closed-loop current control, the output of which (duty cycle, frequency, etc.) will be monitored in order to detect its variation caused by the back-EMF induced during LPV reopening. Detection of the solenoid valve state change by analysing the output of the coil current controller is described in [61].

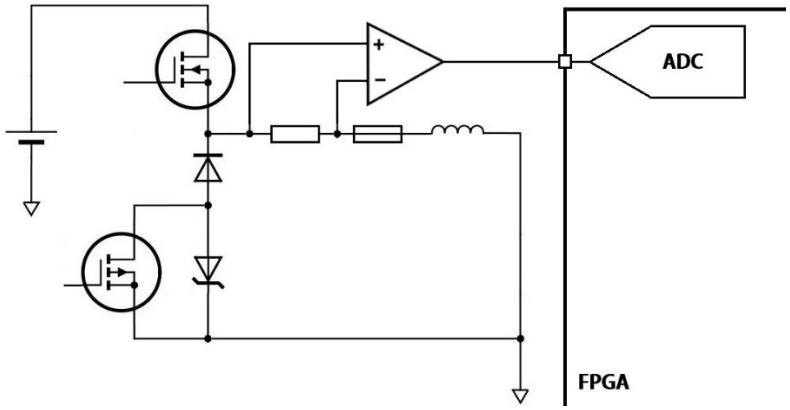

Figure 3.9. Schematic diagram of the DPC12 current sensing circuit that is used for detecting back-EMF generated by the LPV reopening.

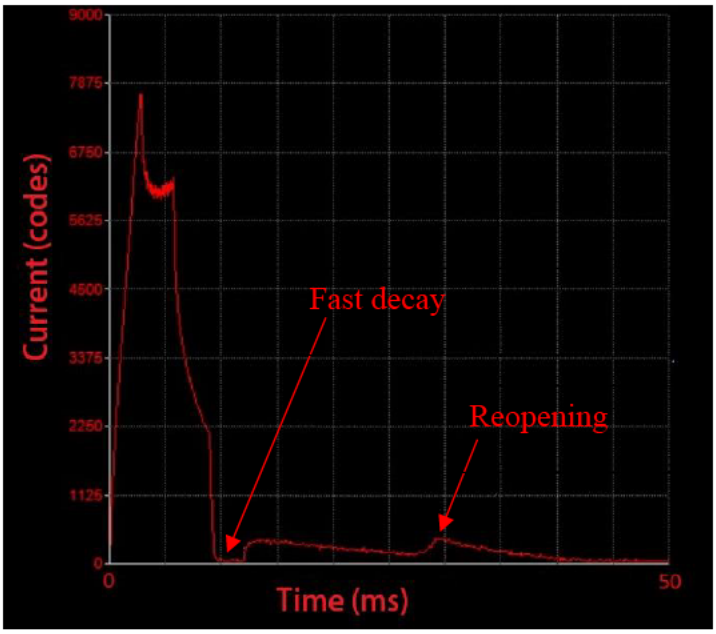

Figure 3.10.Coil current signature generated during PAV8 reopening detection test (sample provided by Mark Brett).

Both methods work well for only pumping valve PAV8, however, none of them was capable to detect the LPV reopening event in the single-coil MAV valves because the back-EMF signal was completely shadowed by the coil residual current.

3.3 Results

This section describes the developed method that allows the detection of the LPV reopening applicable to the single-coil motoring or pumping-only DD modules at any mode of operation.

3.3.1 Concept of the proposed back-EMF sensing method

Figure 3.11 shows the next-generation coil driver (NGCD) pseudo-H-bridge circuit set in fast-decay mode in order to provide coil voltage sensing at the H-bridge floating node during the LPV reopening. When H-bridge is set in fast decay mode the stored coil energy will discharge back to supply through diode D1. When D1 is conducting, the floating node voltage will be pulled to the supply through D1. When the coil current decays to 0 A, D1 opens and the coil becomes an open circuit, with one side pulled to the system ground by M2. The RDS of M2 and power cable resistance can be neglected due to low resistance. Therefore, it can be assumed that the floating node voltage (VF) will equal the coil voltage (VC). Due to the high impedance

of the coil voltage sensing circuit, the voltage amplitude of the reopening signal at the floating node is expected to be much larger than its voltage across the current sense resistor (Rsense) when current sensing is used instead by setting the H-bridge in slow-decay mode, thus, shorting the coil by M2 and M3.

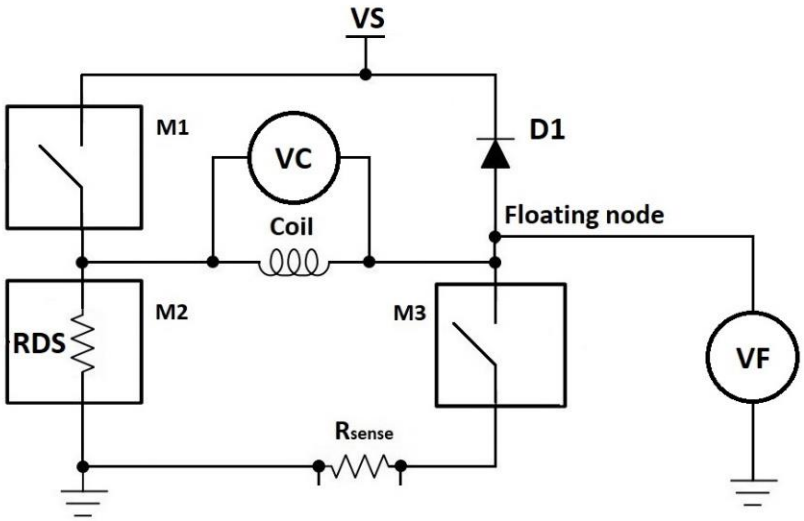

Figure 3.11. Schematic diagram of the NGCD H-bridge in fast decay mode.

Figure 3.12 shows the setup of the test bench used to prove the concept described above and Figure 3.13 shows its schematic diagram. The circuit consists of the 3x Half-bridge evaluating board BOOSTXL-DRV8323RH controlled by Arty A7 FPGA board, the low-pass filter (R1 of 10 kOhm and C2 of 1 nF) and decoupling capacitor C1 of 0.1 uF. The valve MAV8 was used as the load. The current sensing circuit of the 3x Half-bridge board was modified in order to sense the coil current during fast decay (see Figure 3.13), and the DRV8323H was set in independent PWM Mode according to the datasheet [32].

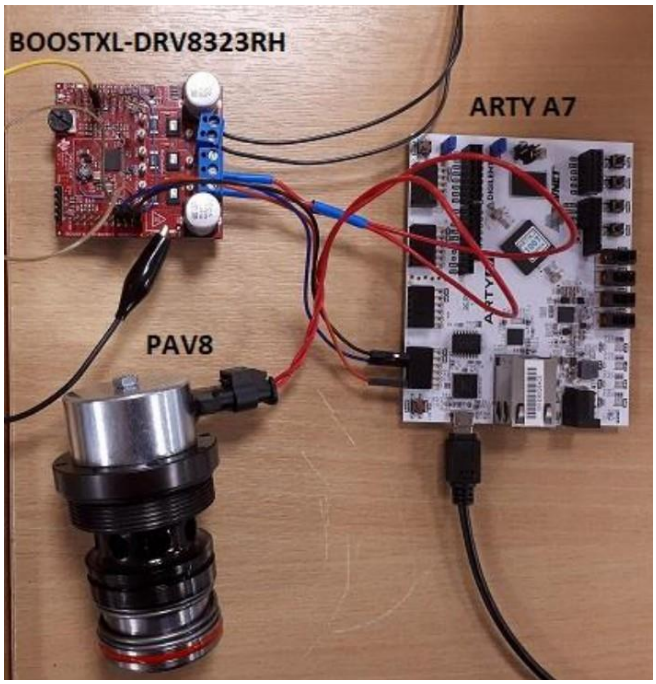

Figure 3.12. Back-EMF sensing experiment sutup.

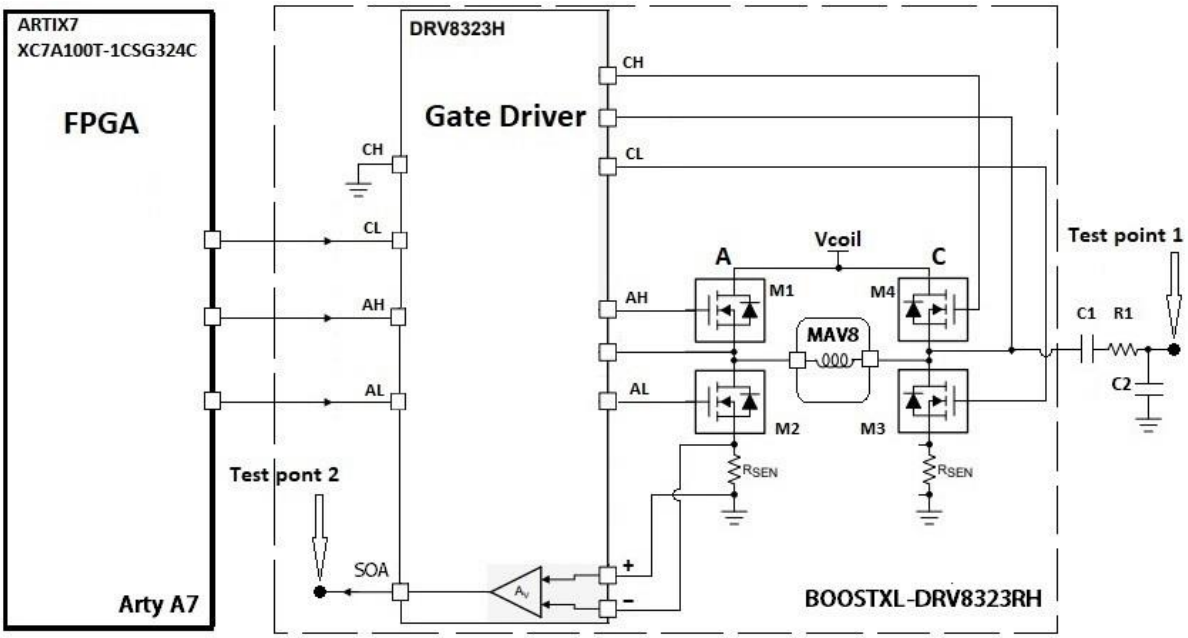

Figure 3.13. Schematik diagram of the back-EMF sensing experiment sutup.

The MAV8 was energised in three stages:

- Stage 1: coil energised for 5 ms.
- Stage 2: coil in slow decay for 1 ms.
- Stage 3: coil in fast decay for 994 ms.

Figure 3.14 shows scope plots from test points 1 and 2 (see Figure 3.13), captured during the experiment, and H-bridge timing diagrams. The experiment consists of two phases:

- Phase 1: the LPP is unblocked (Figure 3.14, a)
- Phase 2: the LPP is blocked (Figure 3.14, b)

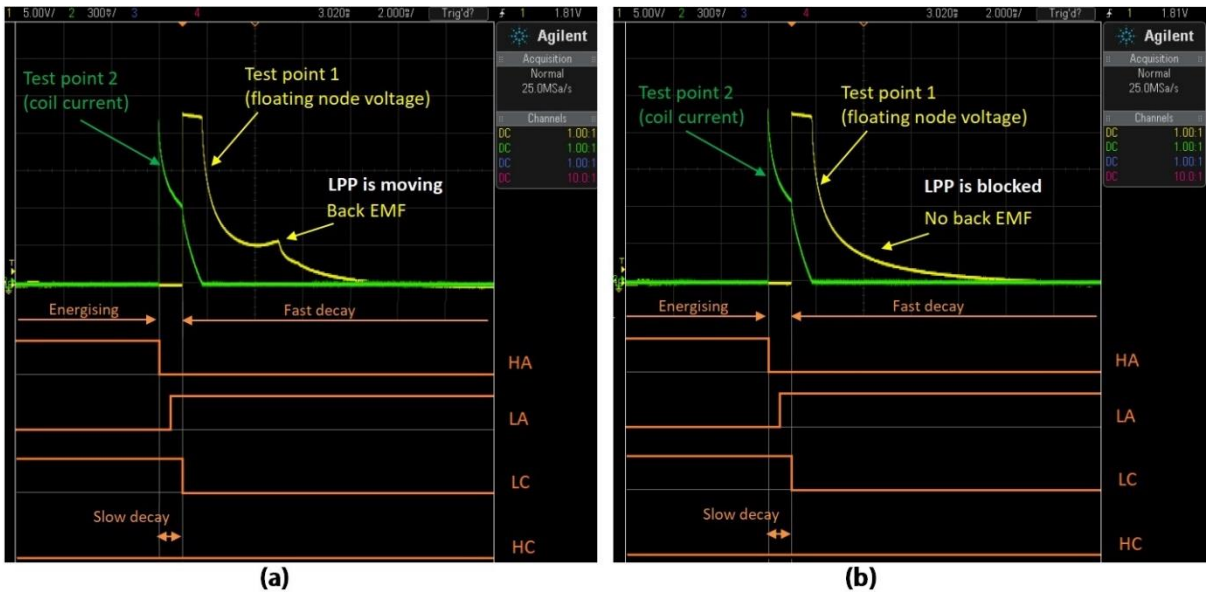

Figure 3.14. Back-EMF sensing experiment results: a) the LPP of MAV8 is unblocked; b) the LPP of MAV8 is blocked.

From the plot, it can be seen that the floating node (FN) voltage is 0V when the bridge is in energising or slow decay mode. When the bridge is in fast-decay mode the FN is pulled to supply through the body diode of M4. When the coil current reaches 0 A, the FN voltage slowly decays due to the residual currents in the solenoid. Comparing the voltage plots (Figure 3.14 a and b), it is very clear to see the back-EMF voltage superimposed on the decaying voltage when LPP is moving.

For reliable detection of the reopening back-EMF signal, the FN voltage must be sent to the FPGA ADC input for further processing. However, the number of ADC inputs provided by the

FPGA is limited, allowing 1 input per valve. The same inputs also must be used for processing the coil current signal.

Therefore, a circuit that provides sensing of the coil voltage and current using only one ADC channel of the FPGA was developed, which is described in the next section.

3.3.2 Coil voltage and current monitor circuit for solenoid DD valves

Figure 3.15 shows a schematic diagram of the coil voltage and current monitor circuit (VCMC). The circuit comprises the coil voltage sensing circuit and the coil current sensing circuits, bilateral analogue switch, and output conditioning circuit that comprises voltage divider and anti-aliasing filter (AAF).

The voltage sensing circuit comprises of clamping and ESD protection (R1 & D2), voltage divider (R1, R2 & R4), snubber (R2 & C1), buffer (op-amp).

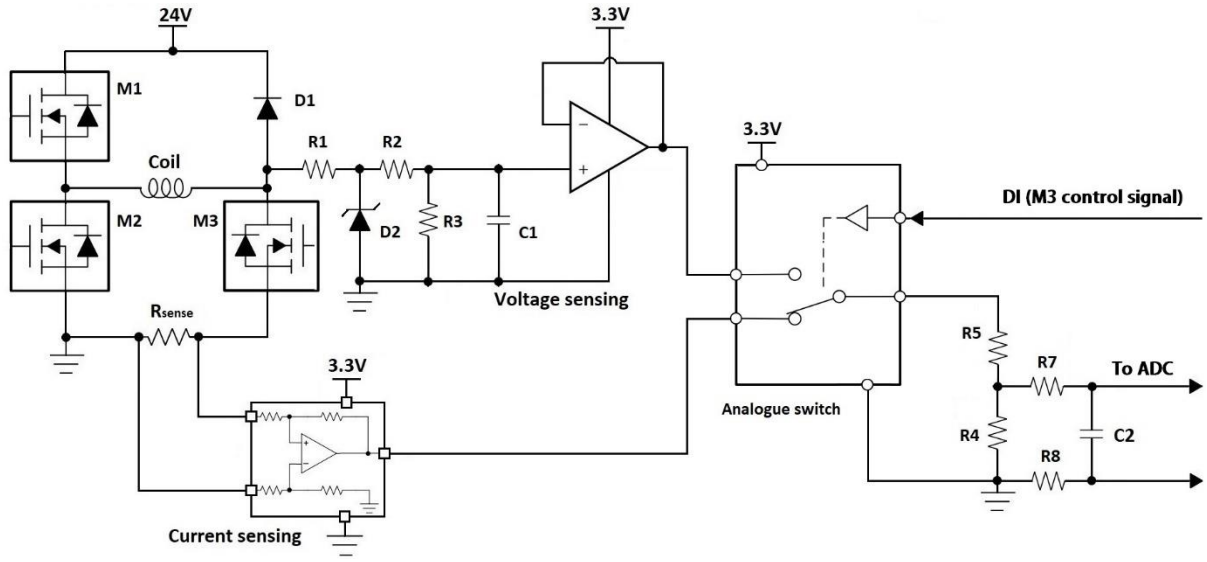

Figure 3.15. Block diagram of the coil voltage and current monitor circuit (VCM).

The circuit holds the op-amp's non-inverting input at 0V when the coil is de-energized. Positive back-EMF signals imposed on op-amps input are buffered and directed to the analogue switch inputs.

Figure 3.16 illustrates principle of operation of the VCMC circuit. The same ADC channel can be shared between normal current regulation and back-EMF sensing. Since the reopening event is expected to happen when the coil is de-energised (H-bridge is in fast-decay mode), and coil current regulation is required while the coil is energised (H-bridge is in energising or in slow-decay mode).

The analogue switch passes signals from the op-amp to the FPGA ADC input when the bridge is in fast-decay mode (Figure 3.16, c) and passes signal from the CSA to the FPGA ADC when the bridge is in energising mode or slow-decay mode (Figure 3.16, a & b).

The signal used to select the switch path is the same signal that controls the low-side gate driver of the MOSFET M3, therefore, one GPIO of the FPGA can be used to control M3 and the analogue switch.

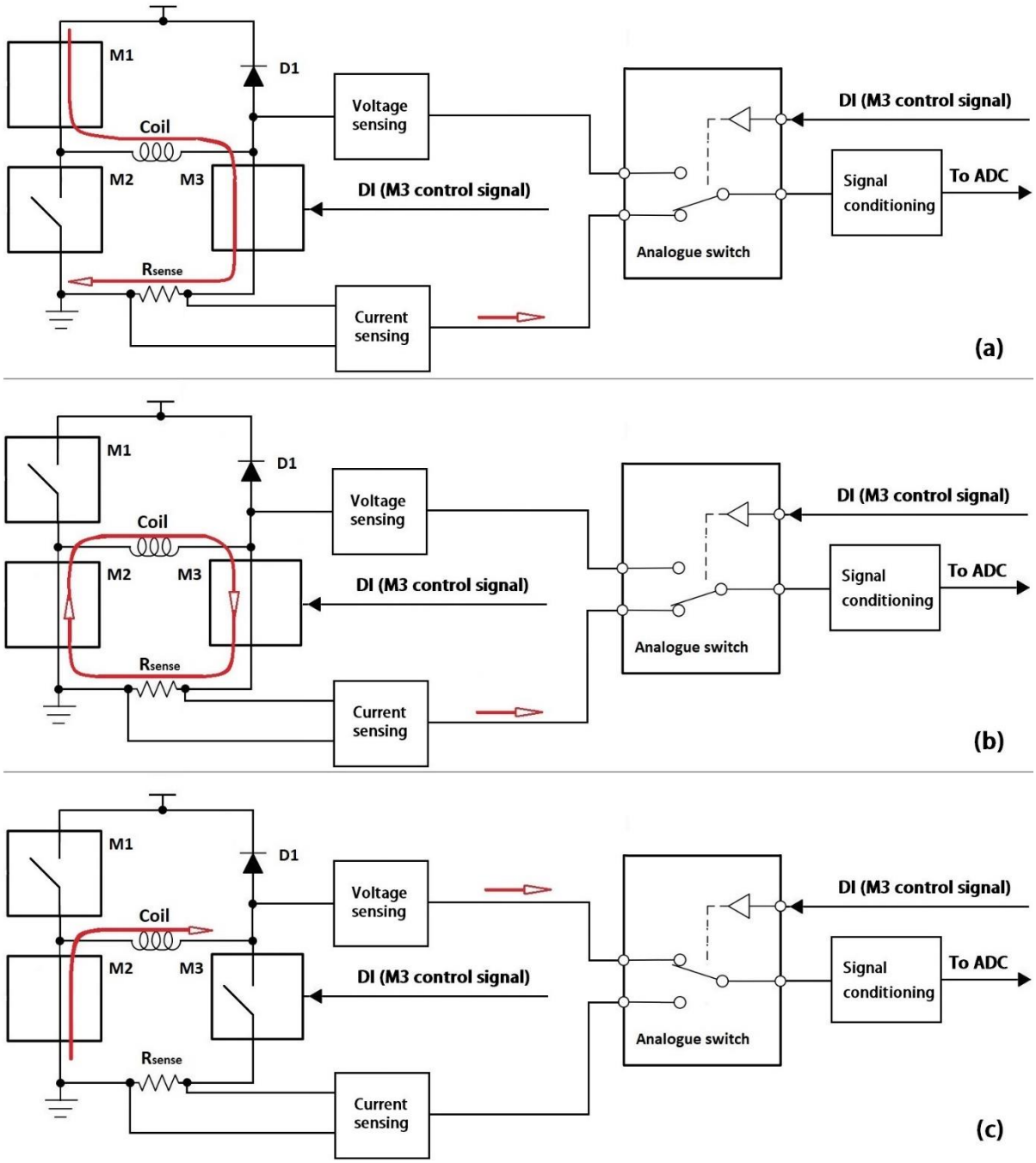

Figure 3.16. Block diagrams to illustrate principle of operation of VCMC circuit: a) coil current sensing at energising mode, b) coil current sensing at slow decay mode, c) coil voltage sensing at fast decay mode.

3.3.3 LTspice simulation results of the coil voltage sensing circuit

Two model analyses of the voltage sensing circuit were performed in LTspice: the transient and the AC analysis. The purpose of the simulation is to prove the functionality and interference immunity of the circuit since the harness delivering power from the controller to the DD valves

will be exposed to the surrounding electromagnetic noise generated within an automotive or industrial environment.

Figure 3.17 shows LTspice model of the coil driver H-bridge in fast-decay mode and coil voltage sensing circuit developed to do the AC analysis. Type of sweep is decade, number of points pre decade is 100, start frequency is 1 Hz, stop frequency is 1 GHz. From the result (Figure 3.18) can be seen that the cut-off frequency is around 5.4 kHz and the slope is around -50 dB/Decade.

Experimentally was established that the average back-EMF signal frequency of MAV8 is around 1 kHz, which is below the cut-off frequency of the circuit. Therefore, the useful signal will not be attenuated by the circuit.

According to [62] the lowest noise frequency of the bulk current injection (BCI) immunity test is 100 kHz (see Table 3.1), which, according to Figure 3.18, will be attenuated approximately down to 1%.

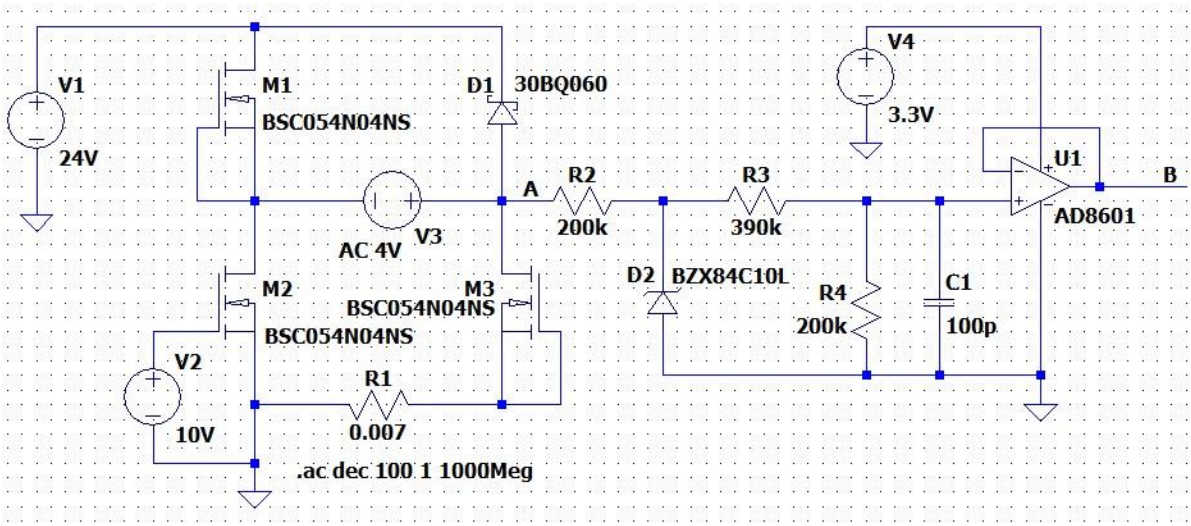

Figure 3.17. LTspice model of the voltage sensing circuit for AC analysis.

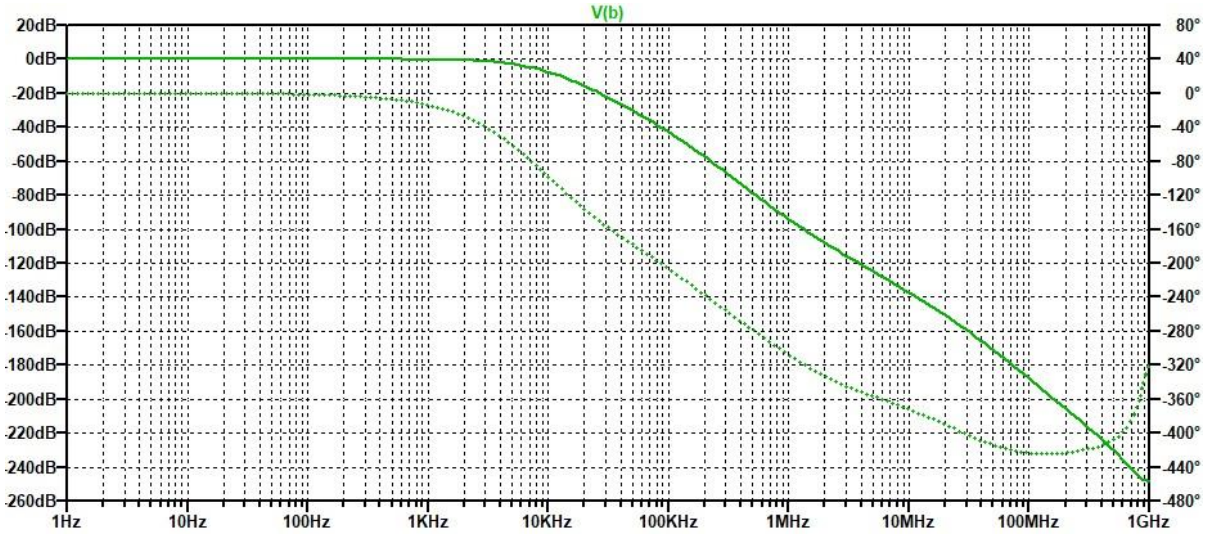

Figure 3.18. Simulation results of LTspice model of the voltage sensing circuit for AC analysis. The bold line is the Bode magnitude plot, the dotted line is Bode phase plot.

Table 3.1. Example of BCI test severity levels, according to ISO 11452-44 [62].

Frequency band (MHz)	**Test level I (mA)**	**Test level II (mA)**	**Test level III (mA)**	**Test level IV (mA)**	**Test level V (mA)**
0.1 to 1	20	33	50	66	Specific values agreed between the users of this document.
1 to 3	60 * f^a / 3	100 * f^a / 3	150 * f^a / 3	200 * f^a / 3	
3 to 200	60	100	150	200	
200 to 400	60 * 200 / f^a	100 * 200 / f^a	150 * 200 / f^a	200 * 200 / f^a	
[a] In the formulae, f is in MHz					

Figure 3.19 shows the model for the transient analysis. The V3 source simulates the coil voltage during LPV reopening when H-bridge is set in fast-decay mode (see Figure 3.20). It contains a "motoring" back-EMF superimposed on the decaying voltage and a "pumping" back-EMF superimposed over 0 V. As can be seen from Figure 3.23, the maximum voltages at node B and C are kept slightly below 3.3 V and both back-EMF signals are divided according to the voltage divider setup. This proves the correct operation of the circuit.

The coil power cables that connect the coil driver and the solenoid valve will be exposed to electromagnetic interference generated by external sources, which can affect the operation of the coil voltage sensing circuit.

Therefore, to illustrate the radiated interference immunity of the circuit, an approximate simulation of a BCI immunity test was made. For this example, was used a modulated noise of

a frequency 0.1 MHz at an injected current of 200 mA, which according to [62] (see Table 3.1) is the most severe level; the carrier frequency is 1 kHz. Inductors L1 and L2 simulate the coil power cables of 1.8 meter and inductor L3 simulates the BCI probe that is inducing modulated noise into the coil cables, which is shown in Figure 3.21. Therefore, L3 is the primary winding and L1, and L2 are the secondary windings of a transformer with a 1:1 turn ratio. The coupling coefficient of 0.45 is such to induce noise of an RMS current of approximately 200 mA in L1 and L2. The noise is generated by V5 and V6 sources.

The coil voltage with superimposed noise is shown in Figure 3.22. As can be seen from the simulation results Figure 3.23, the noise was effectively attenuated and the useful signal stays pretty much the same, where both beck-EMF signals are clear. This proves the immunity of the circuit to surrounding radiated emissions.

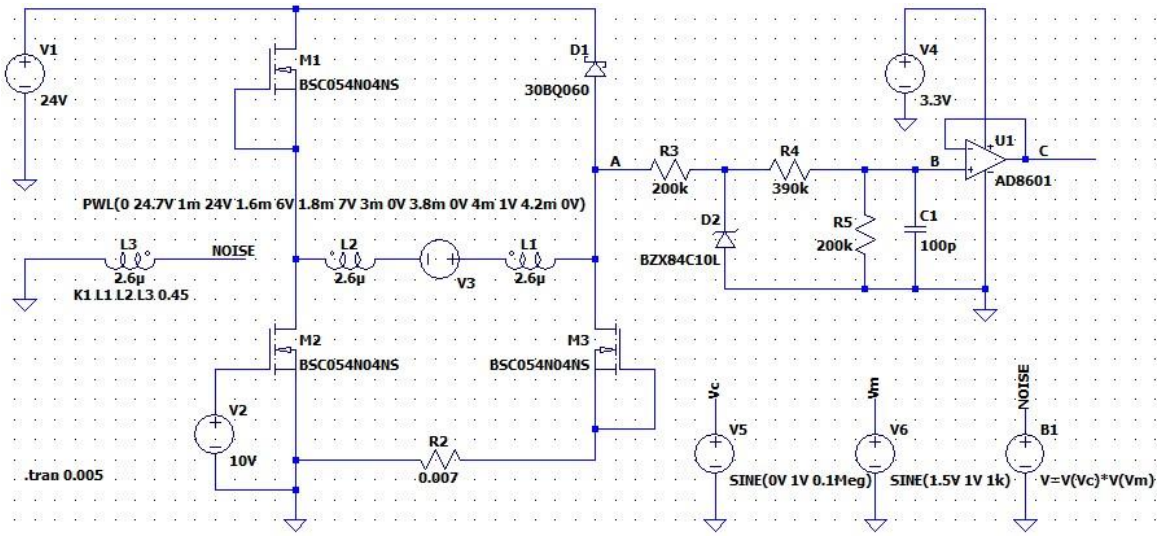

Figure 3.19. LTspice model of the voltage sensing circuit for transient analysis.

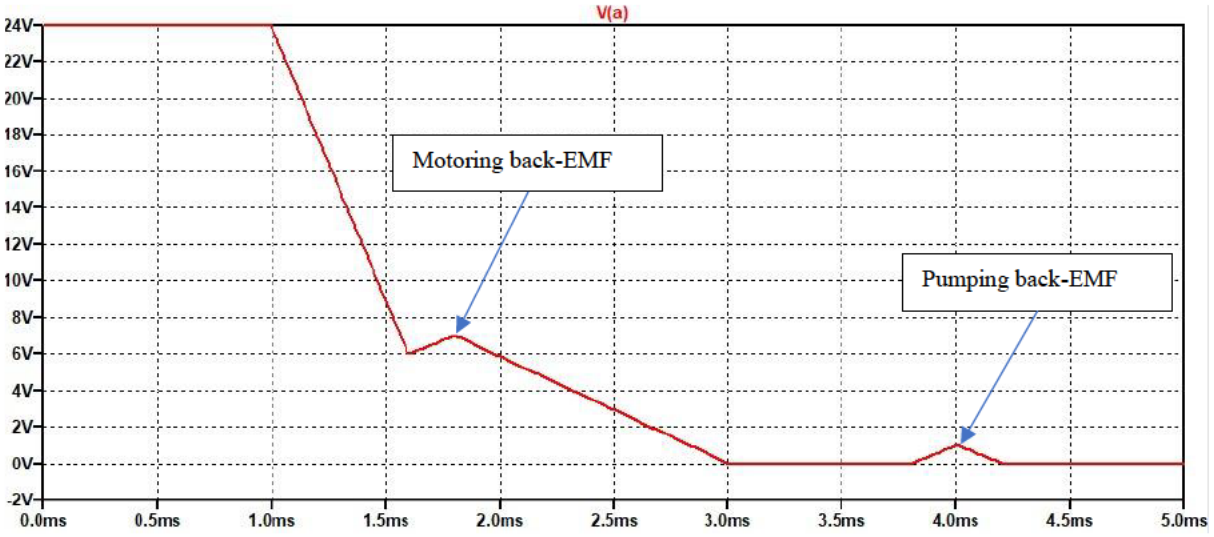

Figure 3.20. The voltage on the S-node A developed by the V3 source that simulates the coil voltage during LPV reopening when H-bridge is set in fast-decay mode (noise is not applied).

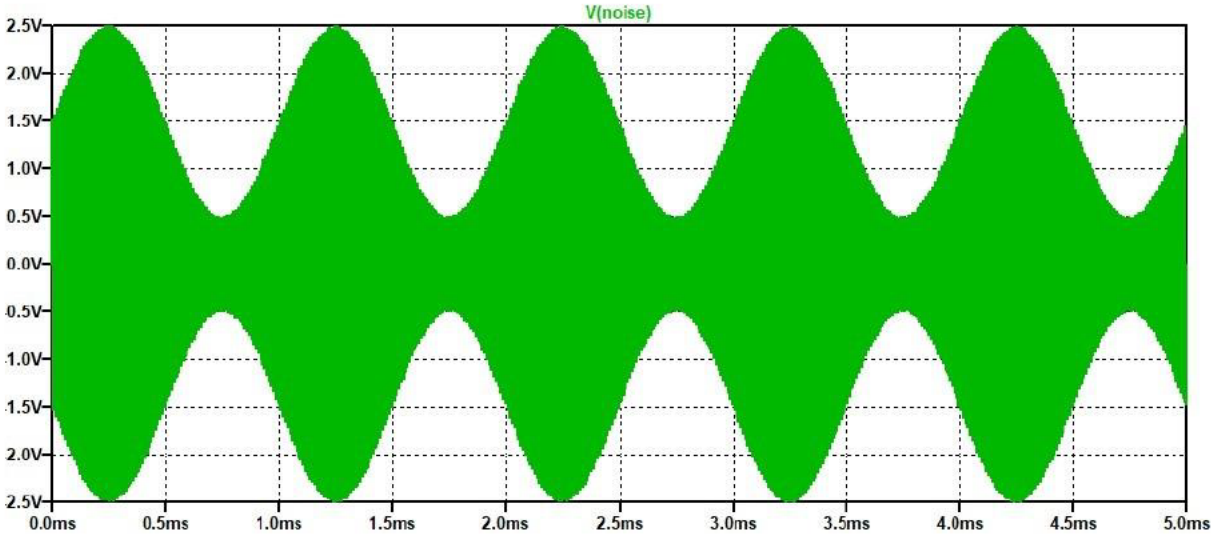

Figure 3.21. Modulated noise of 1 kHz and 0.1 MHz developed by V5 and V6 sources.

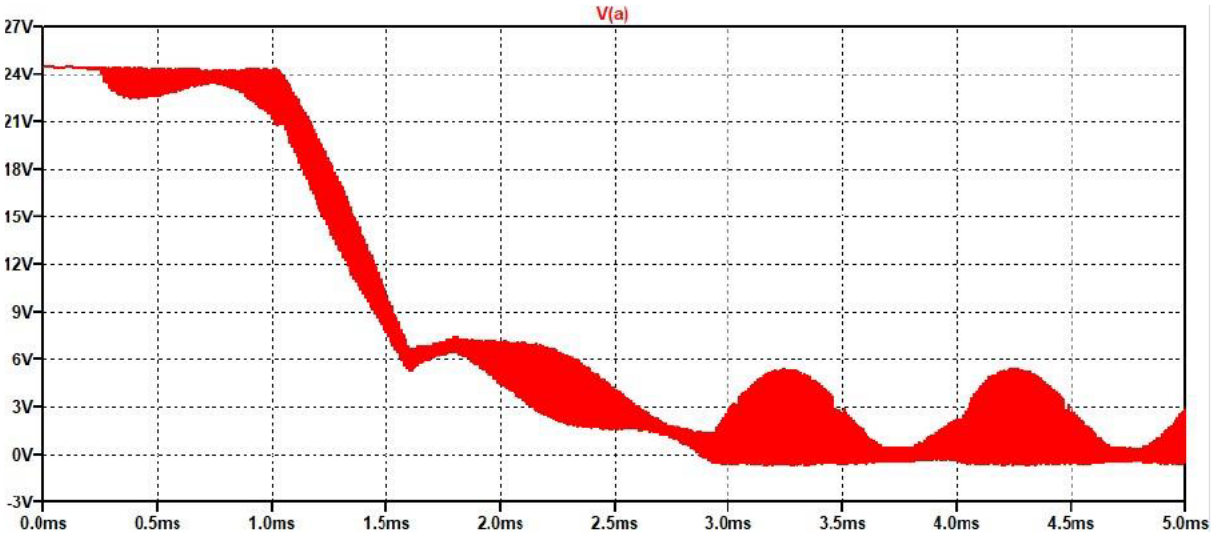

Figure 3.22. The voltage on the S-node A developed by the V3 source and with the noise being applied.

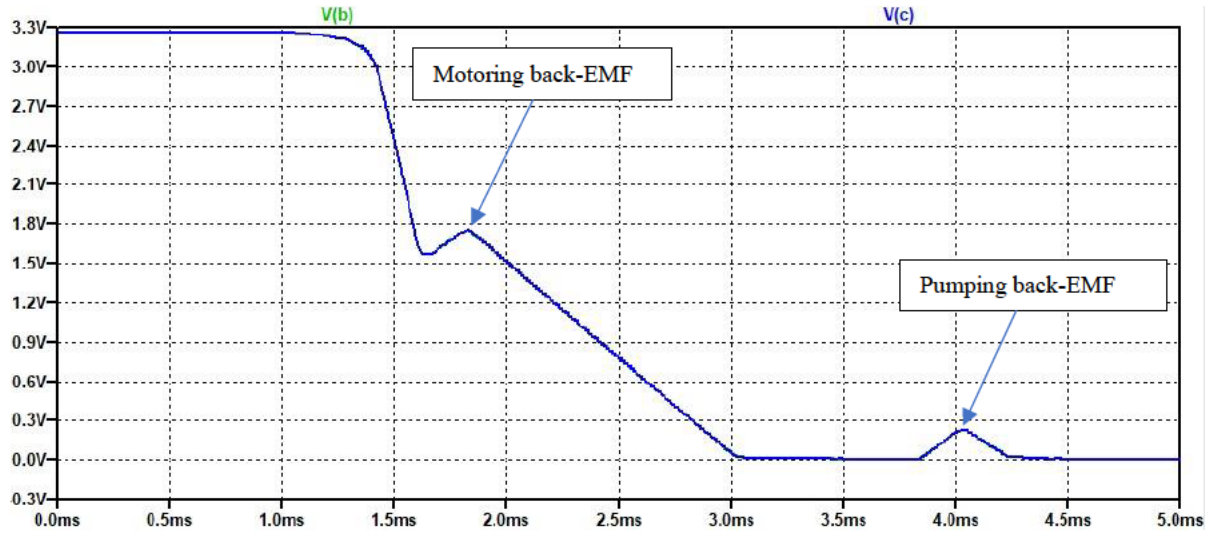

Figure 3.23. The output of the voltage sensing circuit (the S-node voltage was filtered and divided). The noise is successfully attenuated, and both back-EMF signals are clear.

3.3.4 Reopening detection algorithm

MATLAB/Simulink software was used for LPV reopening detection algorithm development using. The coil voltage samples that contain LPV reopening back-EMF voltage superimposed over the decay voltage were obtained by operating PAV8 at the test bench using the next-generation coil driver (NGCD) prototype board and imported into MATLAB.

Figure 3.24 shows a sample of the coil voltage trace that contains the LPV reopening back-EMF voltage, which was obtained by operating a PAV8 valve in the air. This voltage profile

is similar to the one that is generated during the fast-decay phase of the motoring cycle of a DD pump/motor machine when operating on the test rig. Therefore, this sample can be used for the development of the reopening detection algorithm.

During the algorithm development, it was aimed to detect the back-EMF voltage as close as possible to the peak value because it corresponds to the end of the LPV reopening event.

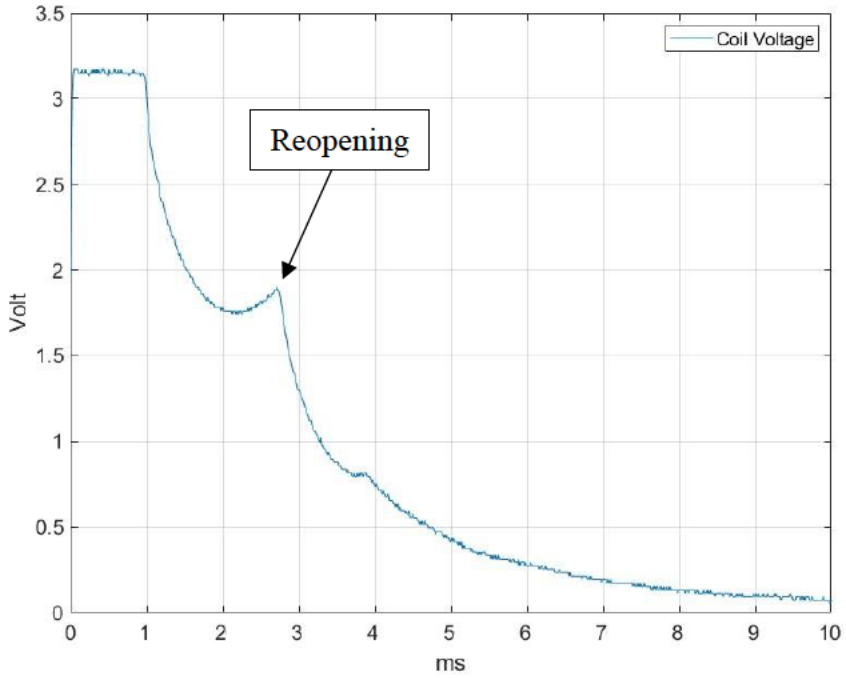

Figure 3.24. Sample of coil voltage trace containing LPV reopening back-EMF, captured during operating PAV8 at the bench test.

Figure 3.25 shows a block diagram of the Simulink model that consists of the first-order low-pass filter algorithm (see Figure 3.26) and the LPV reopening detection algorithm (see Figure 3.27).

The low-pass filter block contains two inputs: the coil voltage sample imported from MATLAB and the time constant value (T_const) that defines the attenuation rate of the filter. The output of this block is the filtered coil voltage, which is fed into the reopening detection block for further processing. Additionally, into the reopening detection block, two threshold constants are fed, which define the setup of the algorithm. The output of this block is a Boolean signal multiplied by three for better illustration purposes, the high level of which indicates the LPV reopening is being detected.

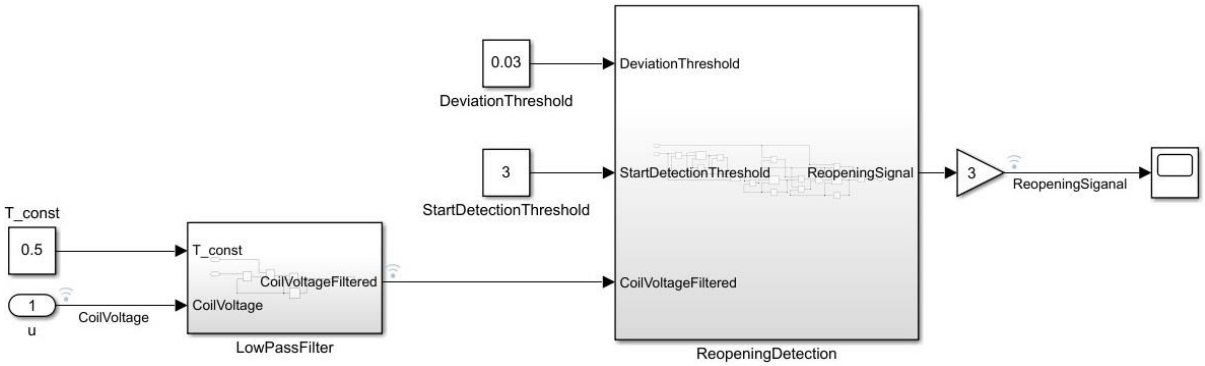

Figure 3.25. Simulink model of the LPV reopening detection algorithm,

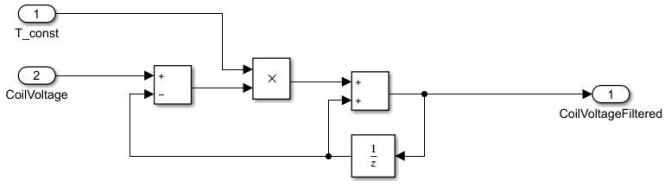

Figure 3.26. First order low-pass filter algorithm.

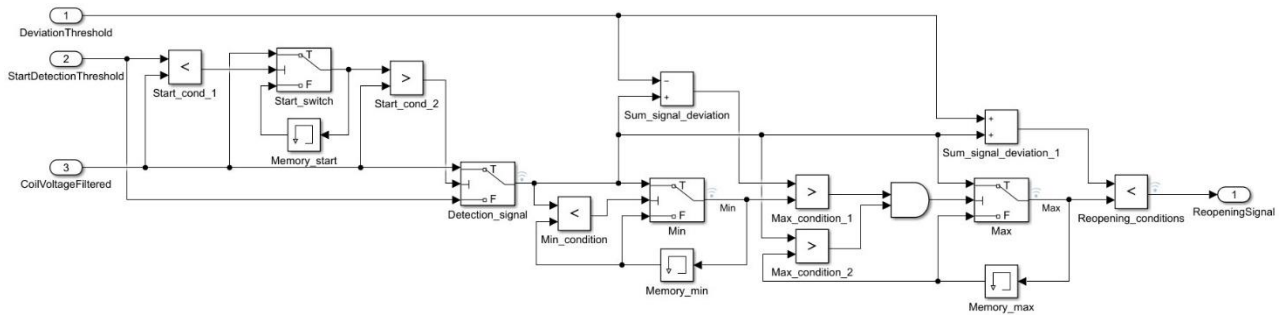

Figure 3.27. LPV reopening detection algorithm.

The reopening algorithm logic is as follows.

1. Detect the conditions that define initiation of the reopening detection, which are detecting the coil voltage reaches a value above the Start Detection Threshold and then the value below. The Start Detection Threshold value should be slightly below the Zener diode break-down voltage divided by the voltage divider of the coil voltage sensing circuit (see Figure 3.17). In this example, the Start Detection Threshold value is 3 V.

2. Determine the minimum value of the coil voltage.

3. Determine the maximum value of the coil voltage, applying a Deviation Threshold for additional filtering, which in this example equals 0.03 V.

4. Flag reopening if the current value of the coil voltage is below the maximum value by the Deviation Threshold value.

Figure 3.28 shows the response of the reopening detection algorithm on input data, which is the coil voltage sample trace; and Figure 3.29 shows the coil voltage trace against the reopening signal, which was generated by the reopening detection algorithm. As can be seen, the reopening signal is set high just after the peak of the back-EMF voltage, which is what was intended to achieve.

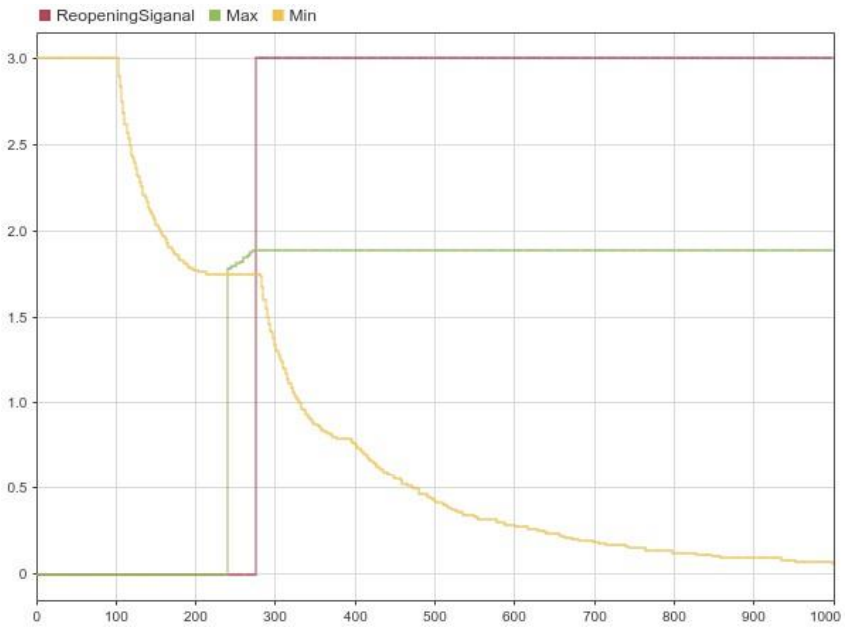

Figure 3.28. Maximum and minimum traces of the filtered coil voltage trace and the reopening signal generated by the reopening detection algorithm.

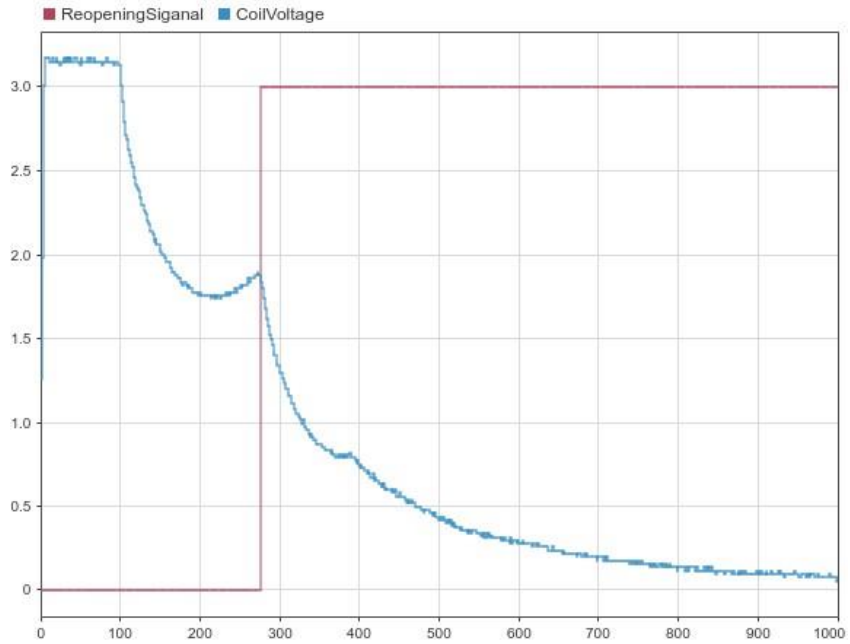

Figure 3.29. Coil voltage trace against the reopening signal generated by the reopening detection algorithm.

The LPV reopening detection algorithm was implemented in VHDL. The VHDL code (see Appendix A) was integrated into the NGCD prototype board testing firmware, developed for the ARTYA7 FPGA board.

3.3.5 LPV reopening detection testing

The NGCD prototype board (see Chapter 2), which includes the coil voltage and current monitor circuit (VCMC), controlled by the ARTYA7 FPGA board, was used for testing the LPV reopening detection method proposed in this chapter.

Figure 3.30 shows the schematic of the substitution loop method BCI test setup used for the interference immunity testing of the coil voltage sensing circuit when Figure 3.31 shows a picture of it. The setup was done according to ISO 11452-4. This test also demonstrates the correct functionality and reliability of the circuit and reopening detection algorithm implemented in VHDL.

Before the test, the NSG 4070 system was calibrated to adjust the power needed to induce 200 mA current with a 50 Ohm impedance over the 0.1 - 400 MHz frequency range. The same power level associated with the 50 Ohm impedance was used during the test, at which the DDC15 coil driver board was operating PAV8 valves of the unfilled DDP96. The oscilloscope

probes were connected to the H-bridge voltage sensing node, to the output of the VCMC and to the FPGA board debug pin that will set high when the LPV reopening is detected.

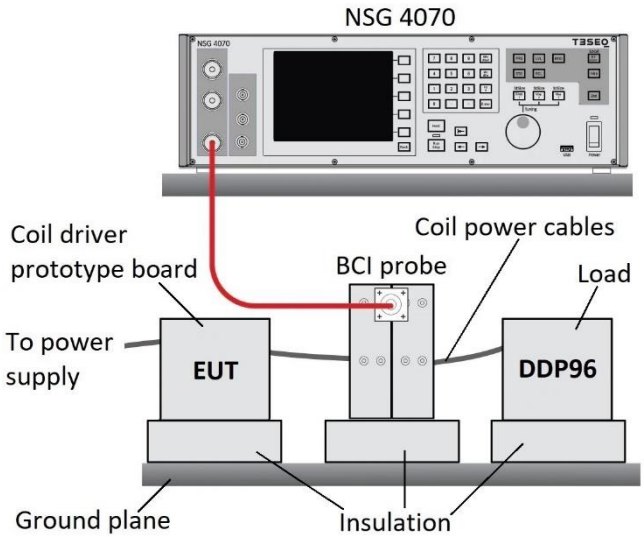

Figure 3.30. Schematic of the substitution loop method BCI test setup used for the RF immunity testing of the coil voltage sensing circuit.

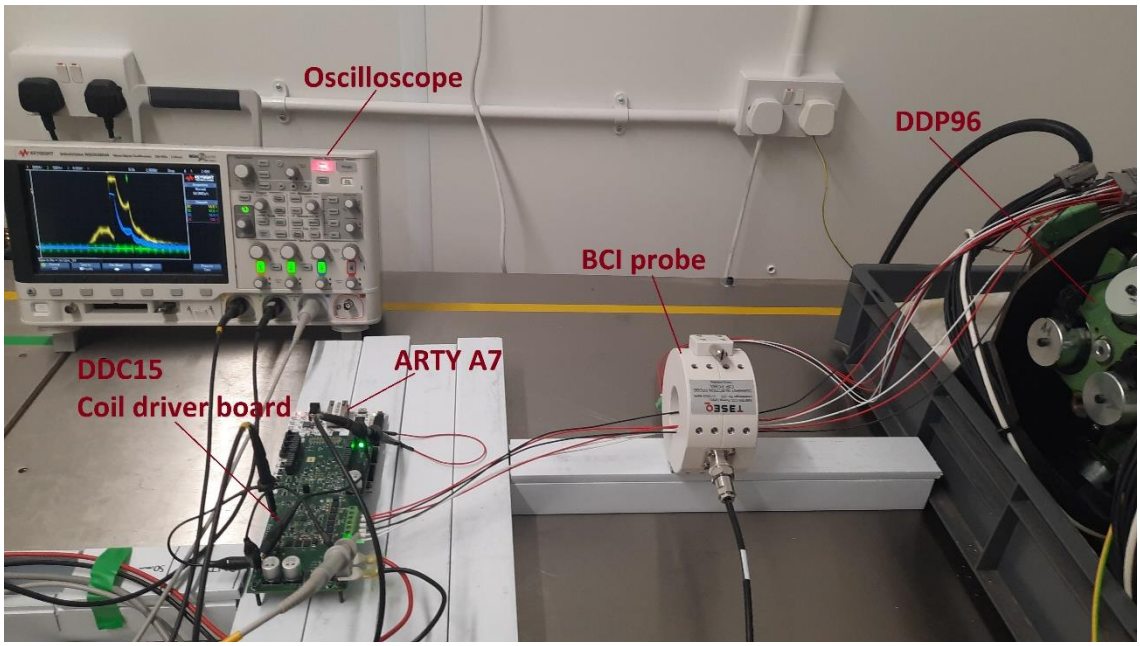

Figure 3.31. Picture of the substitution loop method BCI test setup used for the RF immunity testing of the coil voltage sensing circuit.

Figure 3.32 shows the test results of the LPV reopening detection circuit when the BCI equipment is switched off and the NGCD board drives the PAV8 load. The yellow trace illustrates the VCMC output, which shows the coil current when the solenoid valve turns on and the coil voltage when it turns off. The coil current is closed loop controlled with the current reference set to 5.5 A, which is enough to activate the valve. When H-bridge is set to the fast-decay mode, the VCMC has switched to sense the coil voltage, the output of which is equivalent to the H-bridge sense node voltage (blue trace). The LPV reopening back-EMF voltage is clear to see, and it is being detected correctly, which is indicated by the debug pin set high (green trace) just after the peak. Therefore, the VCMC and the LPV reopening detection method operate correctly.

Figure 3.33 and Figure 3.34 show the BCI immunity test results at 100 kHz and 200 kHz, accordingly. It can be seen that the LPV reopening detection is not affected by the distortions. The noise injected into the coil cables is being effectively attenuated by the low-pass filter of the circuit, the VCMC circuit continues to operate as normal, and the LPV reopening is detected.

The BCI immunity test was accomplished over all frequency ranges mentioned in ISO 11452-4 (see Table 3.1), and no anomalies in the operation of the VCMC or the LPV reopening detection were observed.

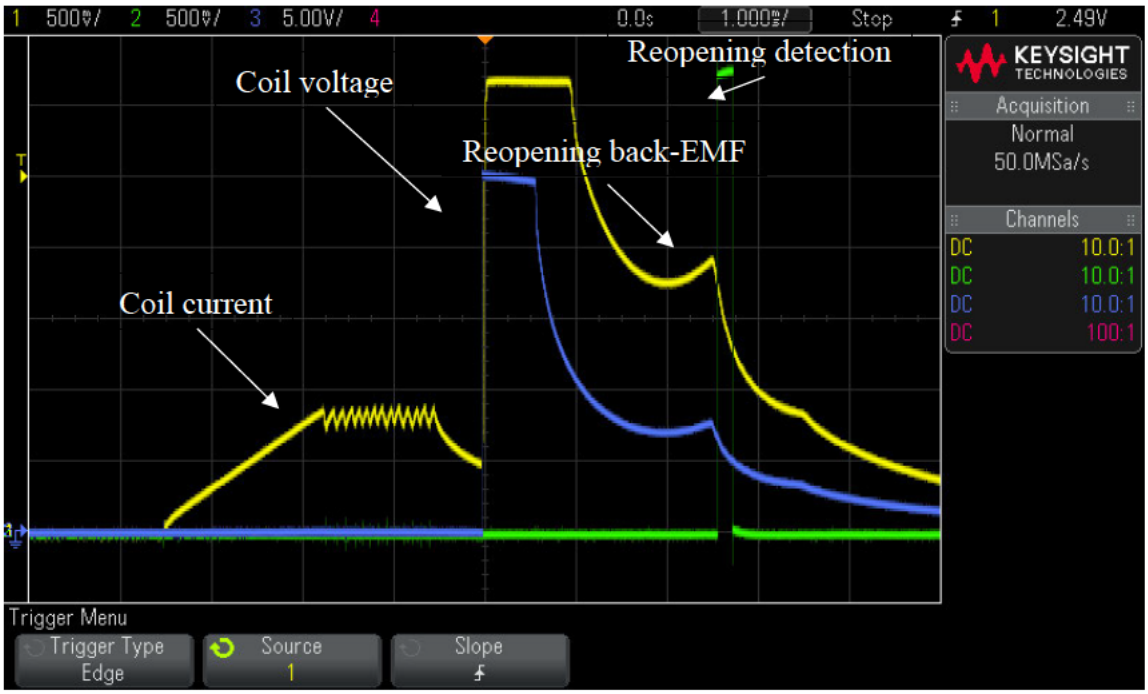

Figure 3.32. Performance test results of the LPV reopening detection circuit (BCI equipment is off). Yellow – VCMC output (coil current/voltage); blue – H-bridge "sensing" node voltage; green – LPV reopening debug pin voltage.

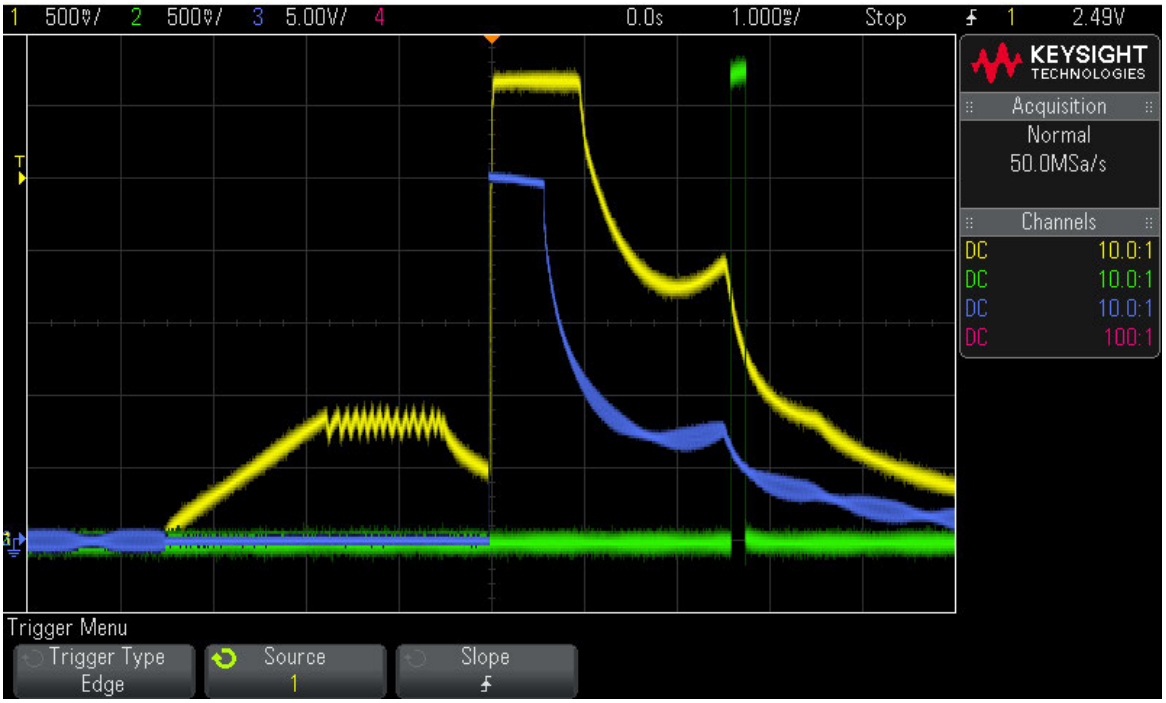

Figure 3.33. BCI immunity test results at 100 kHz. Yellow – VCMC output (coil current/voltage); blue – H-bridge "sensing" node voltage; green – LPV reopening debug pin voltage.

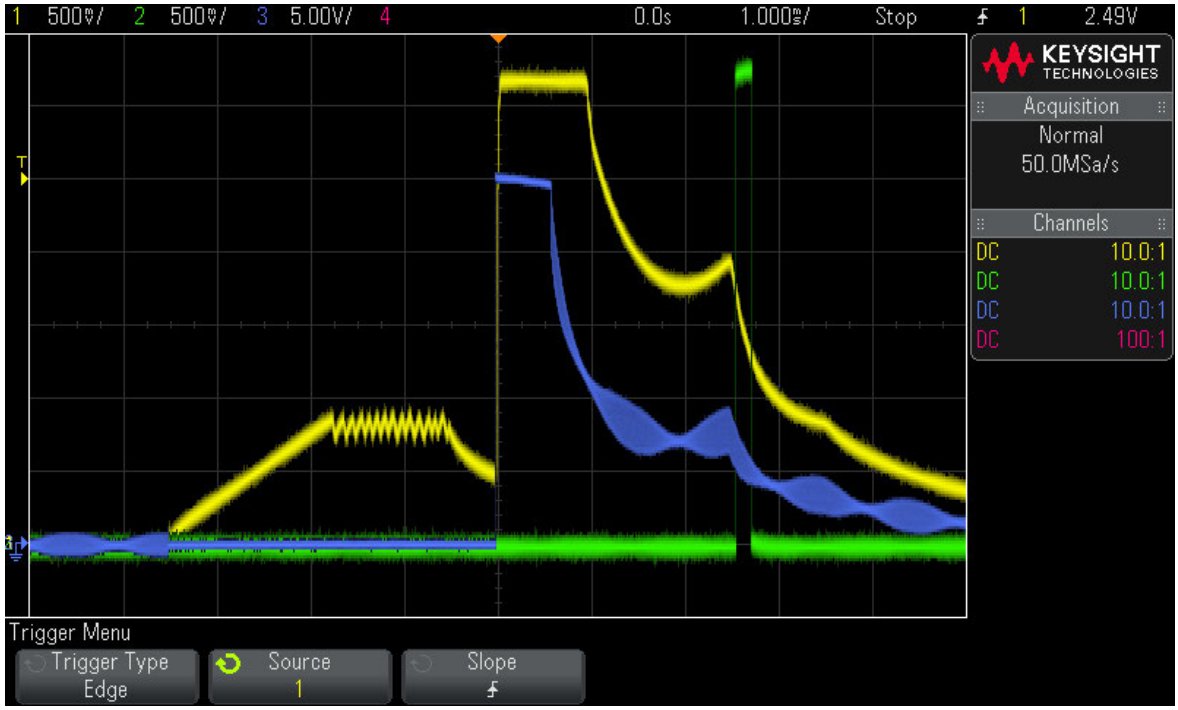

Figure 3.34. BCI immunity test results at 200 kHz. Yellow – VCMC output (coil current/voltage); blue – H-bridge "sensing" node voltage; green – LPV reopening debug pin voltage.

3.3.6 Voltage sensing vs current sensing for the reopening back-EMF detection

A bench test was carried out to compare the LPV reopening back-EMF signals obtained by voltage sensing and current sensing circuits. The test was done by operating in the air the PAV8 valve using the NGCD prototype board (see Chapter 2). This circuit board contains coil voltage and current monitor circuits (VCMC). During the test, the same valve was energised by the same coil driver using the same current profile and at the same conditions.

During voltage sensing, the valve was placed in fast-decay mode after it was energised, and VCMC was set in the voltage sensing mode. The VCMC output was monitored by oscilloscope.

During current sensing, the valve was placed in the fast-decay mode for 1.4 ms to allow complete de-energising of the solenoid coil (VCMC is set in voltage sensing mode). After the valve was de-energised, it was placed in the slow-decay mode to allow the current generated by the LPV reopening back-EMF to flow through the current sense resistor, and the VCMC was set in the current sensing mode. The VCMC output was monitored by oscilloscope.

As can be seen from the test result (Figure 3.35), the amplitude of the reopening back-EMF signal, sensed by the coil voltage sensing circuit (red waveform), is about 10 times larger than the amplitude of the signal that was sensed by the coil current sensing circuit (blue waveform), which is 750 mV vs 75 mV. Also, it is worth mentioning that the voltage signal is 4 times divided by the circuit voltage divider when the current signal is 20 times amplified by the Current-Sense Amplifier IC.

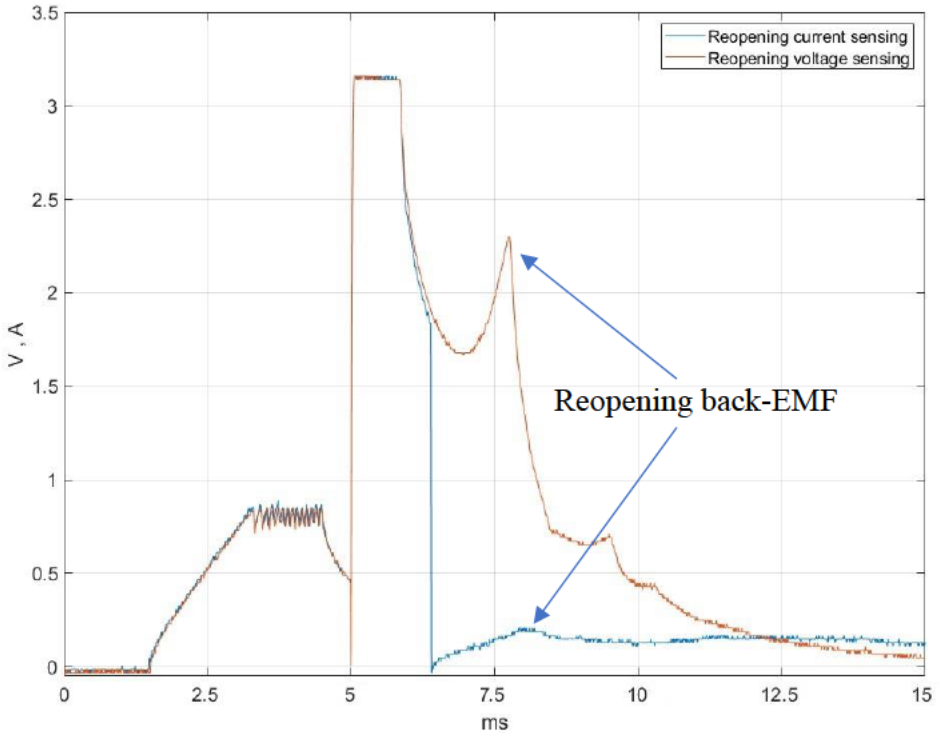

Figure 3.35. Comparison of LPV reopening back-EMF sensing using voltage sensing circuit (red waveform) and current sensing circuit (blue waveform), PAV8 bench test.

The small amplitude of the current-sensing-based signal can cause problems with its detection. In particular, it makes detection not reliable or not possible when operating the valve in oil instead of air. The oil reduces the speed of the plunger motion, therefore, further reducing the amplitude of the induced back-EMF signal based on current sensing.

Another drawback of the current signal is that it lags the voltage signal (therefore, it lags the LPV reopening event) and its peak is more extended, which will reflect on the precision of the reopening detection.

Thus, it can be concluded that the voltage sensing method for the LPV reopening back-EMF detection has several benefits over the current sensing method for the same purpose.

3.4 Summary and conclusions of the chapter

The method of LPV reopening detection has been established in this chapter, thus reaching the second goal of this thesis.

Firstly, a circuit that allows sensing of the coil voltage during the solenoid de-energising stage when the coil driver is set in the fast-decay mode was developed. It was demonstrated experimentally that the amplitude of the back-EMF signal that is detected by the coil voltage sensing circuit is several times larger than the amplitude of the signal that is detected by the coil current sensing circuit, when both signals were generated at the same condition.

The results of the LTspice simulation and the bench testing prove that the circuit operates correctly, and it is immune to the full range of surrounding radiated noise specified in ISO 11452-4. Therefore, the circuit can be used for automotive or industrial applications.

Also, the LPV reopening detection algorithm was developed, which was implemented using VHDL. The firmware with integrated reopening detection VHDL code was successfully tested on the bench using the NGCD prototype board.

Finally, the developed hardware and firmware were approved to use in the design of the DDC15 controller, which allows the successful operation of DDPM DDP1X0 using closed-loop reopening control in motoring mode of operation (see Chapter 6).

Chapter 4

Response time stabilisation of cyclically operated solenoid valves

This chapter describes an invention (inventors: Christian Norgaard, **Andriy Tkachuk Volodymyrovych**), which is the outcome of this PhD work. The invention proposes a method of stabilising the response time of a cyclically operating solenoid valve, thus, improving the prediction of the low-pressure valve (LPV) closing angle, the precision of which is crucial for the stable operation of a Digital Displacement (DD) machine. Also, this chapter describes the development and implementation of different coil current gradient control algorithms that allow this invention to be used practically for DD technology.

The original idea of the Response time stabilisation of cyclically operated solenoid valves (RTS) invention belongs to Christian Norgaard. My input to this invention consists in the development of practical methods of the RTS invention, its implementation and demonstration of its feasibility. Also, I was investigating the novelty of the invention and generating the invention report.

4.1 Introduction

The RTS invention solves the problem of the solenoid valve response time variation that takes place due to the solenoid circuit resistance or supply voltage change. The resistance change is owing to the temperature change of current conductors of the solenoid circuitry, such as solenoid coil or power cables, which are usually made from copper. Also, the resistance of the solenoid circuit can vary when power cables with different lengths or cross-section areas (CSA) are used to power the valves of a DD machine in different applications.

Currently, an open-loop valve control method is used, which doesn't provide a constant closure time of the valve. To ensure the correct timing of valve closure, solenoid valves need to be triggered (fired, powered) more in advance (early) to compensate for the valve response time variation due to the mentioned factors. Triggering valves earlier, decreases the piston useful stroke of a fluid working machine, thus, decreasing its displacement (cc/rev).

Therefore, aspects of the invention aim to increase the performance of the fluid working machine employing electronically controlled solenoid valves by making the solenoid valve response time unsusceptible to the solenoid circuit resistance change.

4.1.1 Background of the invention

The present invention relates to a method for stabilising the response time of cyclically operated solenoid valves that are used to regulate the flow of fluid in a DD hydraulic machine.

In prior art DD machines, (e.g. EP2775144A2, Artemis), the timing of closure of high and low-pressure valves must always be conservative (i.e. early), to ensure that correct operation is achieved over the full range of fluid properties. However, this reduces the efficiency and capability of the machine because less fluid is displaced than would be the case were the timing less conservative. Also, the closure of high and low-pressure valves at times of higher flow creates more noise and could reduce the life of the valves and can create undesirable torque and pressure ripple in the flow output of the fluid working machine.

Closed- or open-loop control is possible (i.e., the timing of valves closure can be closed-loop controlled when a property of the valve or a signal generated by a detector (sensor) that detects valves closure is used as a feedback signal. Also, the timing of valves closure can be open-loop controlled when the prediction (knowing) of the valve response time is crucial. Table 4.1 gives key factors that affect the response time of a solenoid valve, thus making its prediction very complex. Description of the factors is as follows.

Characteristic 3 changes dynamically with the operation of the pump/motor. Characteristic 4 is fixed for each respective installation (more specifically likely to vary between installations). Characteristic 1 can vary dynamically, but also with time/environmental influence. Characteristic 2 typically increases with the cumulative (lifetime) number of hours of machine operation. Characteristic 5 varies between installations (24 V for industrial installations, 9 V to 36 V for automotive installations).

Table 4.1. List of factors affecting the response time of a solenoid valve.

	Factors affecting the response time of a solenoid valve
1	Fluid properties of the working fluid
2	Degree of wear of the machine components
3	Resistance due to the temperature of the solenoid coil or cables
4	Resistance due to the CSA or length of the cables
5	Application supply voltage.

The temperature of the coil and cables is an important factor, as they are commonly made of copper that changes resistance with temperature. The heating effect of both arises from electrically driving the solenoid and by the ambient conditions. The temperature of the coil is also influenced by the oil temperature, which depends on the operation condition of the hydraulic machine.

During the normal cyclic valve operation, the resistance of the coil and cables changes within each cycle. This is because each cycle has an associated current flow through the solenoid coil that causes joule heating, thus causing a brief heating period within the cycle. Considered on a per-cycle basis, the marginal heating effect, and thus resistance change is very small, however, multiplied up (with a high frequency of valve operation) these effects soon become significant in their effect on the response time of the valve in question and thus the overall operation of the DD pump/motor.

Another important factor that significantly influences the DD valve response time is the coil driver supply voltage, the nominal value of which is different from application to application or can be of a wide range within one application (e.g. automotive applications). A DC-DC converter can be used to ensure the coil driver supply voltage is constant when operating a DD machine in an automotive application (e.g. DPC12 MK1). However, this solution substantially increases the controller's cost, size, and heat losses. Additionally, a fast-switching DC-DC converter can be a primary source of electromagnetic emissions, which can hinder the controller from passing the EMC test.

Figure 4.1 shows two traces of a coil current of the same solenoid valve at different resistances of the solenoid coil circuit (R_{max} and R_{min}) and/or different supply voltages of the application. In both cases, the valve is energised in open-loop mode. The solenoid with maximum resistance and the solenoid with minimum resistance established for the application. T1 and T1n is the time required for the coil current, to reach pull-in value at a certain resistance. ΔT1 represents the difference between T1 and T1n. T2 and T2n are the response times of the same valve at different resistances (the time when the armature finishes its motion). ΔT2 represents the difference between T2 and T2n. ‘a’ is the nominal angle/gradient of the rising edge of the coil current during the energising phase.

Figure 4.2 shows an experiment results of an open-loop energising test of an experimental DD valve PAV8 (the valve design was modified to increase the back-EMF signal at closing) at

different supply voltages of 28 V and 18 V. As can be seen, the difference in response time (ΔTresponse) of the valve caused by the drop of the supply voltage by 10 V is about 1.4 ms.

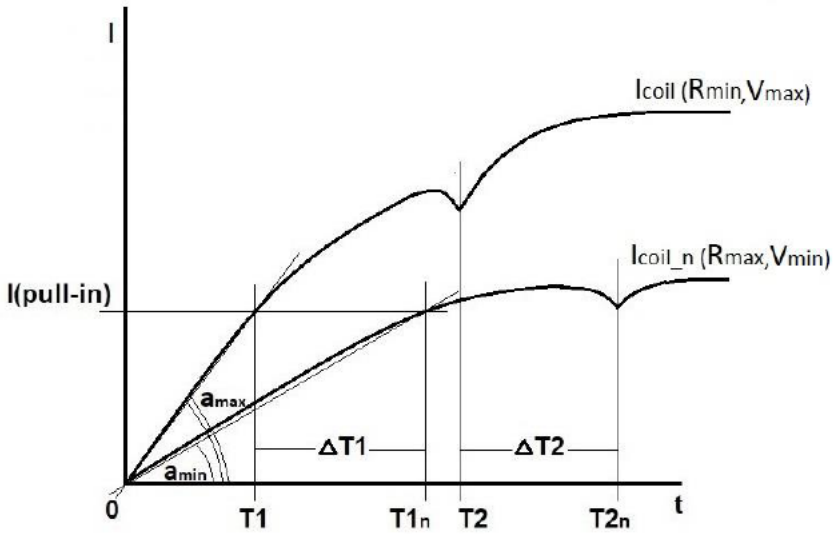

Figure 4.1. Illustration of coil current of the same solenoid valve at different resistances and/or voltages of the solenoid coil circuit when the RTS method is not applied.

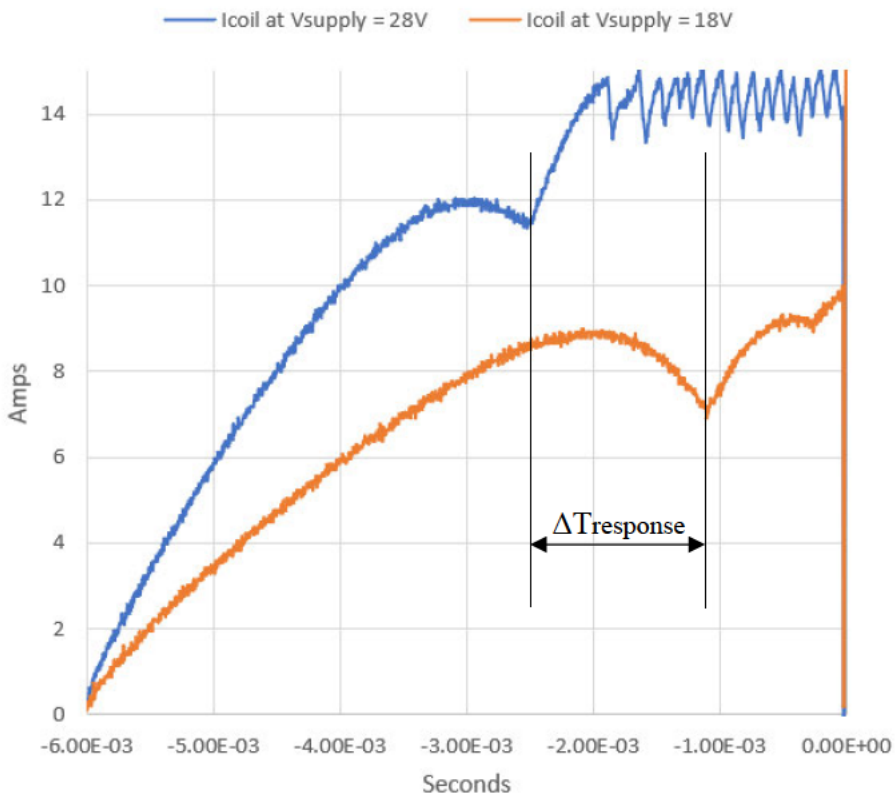

Figure 4.2. Current traces of an experimental DD valve open-loop energising test at supply voltages 28 V (blue) and 18 V (orange).

4.2 Prior Art related to the invention

This section gives a list with a brief description of known engineering practice that relates to the 'Response time stabilisation (RTS) of cyclically operated valves' invention, the investigation of which was required for the invention report.

The patent [63] from Deutsches Elektronen-Synchrotron describes a device for determining the strength of the magnetic field of an electromagnet and discloses temperature compensation/mitigation in the form of "…a temperature calculation circuit is provided to account for temperature changes in the magnet. This enables the magnetic field intensity signal determined by the low-pass element based on the detected magnetic voltage to be corrected according to the heat-related resistance change of the magnet.".

However, there is no suggestion of using the corrected determined field strength for another purpose. Rather than controlling a current in order to correctly control a solenoid valve, as per the present invention, this document doesn't disclose control of a solenoid valve. Neither does it suggest that the heat-related change in resistance of the magnet is an aspect that could be applied in the area of solenoid control.

The patent [64] from Hanon Systems Corp offers a solution for adjusting the resistance of the solenoid circuit by adding into the circuit that of passive electronic devices (i.e. hardware) with an opposite temperature coefficient to the solenoid current conductor, which aims to compensate for the solenoid coil resistance change over the temperature change. Therefore, this is simply a hardware invention addition (insertion of hardware with counteracting thermal response etc), and thus is different to the present invention.

The patent [65] from Bosch discloses current measurement in the energisation phase of solenoid movement. This method for operating the solenoid valve of a fuel injection system for a diesel engine involves calculating the derivative of the current gradient and identifying activation time based on the point of occurrence of maximum value and calculated derivative.

Our method does not involve calculating the derivative of the current gradient, nor identifying activation time based on the point of occurrence of maximum value and calculated derivative. Our method involves controlling the gradient of the solenoid current according to a predefined reference.

Patent "Medical fluid machine having solenoid control system with temperature compensation" [66], discloses determining a voltage drop across the coil by determining a voltage drop between the first and second voltage signals and dividing the voltage drop by the electrical current amount to determine the resistance of the coil.

In one embodiment, this document provides a solenoid system, which uses the solenoid coil current sensing to detect Solenoid armature motion, and provides feedback to a solenoid control circuit, which uses the feedback information to reduce power dissipation and operating noise in a solenoid. The present invention does not detect Solenoid armature motion.

In another primary embodiment, this document provides a system that uses solenoid coil voltage and current sensing along with knowledge of coil resistance at a known temperature to derive coil temperature. The present invention does not require knowing (deriving) a coil temperature for any reason.

A patent from Nikon "Compensating temperature effects in magnetic actuators" [67], discloses identifying a gain and adjusting the current provided to the actuator using the gain.

This invention differs from ours because it uses temperature measurement of the magnet as the feedback signal for the current controller. It does not aim to control or stabilise the response time of a solenoid valve, it aims to adjust the current to maintain a correct or desired force in light of temperature-induced variations to a force constant.

Mitsubishi Denki Kabushiki Kaisha patent discloses a slope (gradient) control of a current through an electromagnet; “In FIG. 10, a suction force control section 303 is provided with a slope restriction section 500 between a command generation section 400 and a current control section 401. The slope limiter 500 converts the suction force command value 407 into a command value 501 that is equal to or less than a fixed rate of change, that is, has a predetermined slope at the rise and fall of the current. It controls the current of the electromagnet 301 based on the command value 501.” [68].

An object of this invention is to provide an electromagnetic contactor for suppressing a shock occurring in the case of throwing and opening. An object of our invention is to provide a repeatable response time of a cyclically operating solenoid valve at each switching cycle.

Raytheon patent "Method of controlling solenoid" discloses taking into account changes in conditions “...by increasing voltage and current to maintain the desired response time of the solenoid valve” [69].

This invention doesn’t disclose that the response time of a cyclically operated valve can be stabilised (kept repeatable) by controlling the gradient of the rising edge of the current profile up to or above the pull-in current of a solenoid valve, thus, ensuring that the pull-in current will be reached over the same period (time) and the current waveform will be kept constant (unchanged) over this period (time) at each switching cycle.

The patent [70] "Method for actuating a solenoid valve and associated device" discloses supplying an actuating current, maintaining the actuating current at a holding level, and reducing the actuating current in a reduction phase.

The idea of this document is to control the switch-on time of a solenoid by increasing the coil current during a “pre-charge phase” to a level at which still no actuation of the valve takes place and the valve is in a preloaded condition. In a peak phase, the actuating current is briefly set to a high value in order to ensure the actuation of the solenoid valve in the shortest possible time. Our method proposes to control the gradient of the rising edge of the coil current profile until or above the current reaches the pull-in value, thus, controlling the switch-on time of the solenoid valve.

The Danfoss patent [61] "Method and device for determining the state of an electrically controlled valve" discloses changing the frequency of PWM, control algorithms, a time-varying control signal, electrically controlled actuator.

The invention relates to a method for determining the state of a solenoid valve, whether it is opened or closed. Our invention relates to a method for stabilising the response time of a solenoid valve at energising without any detection of the state of the valve.

Patent [71] "Method and circuit for detecting the armature position of an electromagnet" (Magnet Schultz, from 2001) discloses determining the position of the solenoid core, by comparing induced EMF to a reference voltage.

This invention relates to a method and to a circuit for detecting the armature position of an electromagnet. Our invention relates to a method for stabilising the response time of a solenoid valve at energising without any detection of the armature position.

Patent [72] "Modified electrical actuation of an actuator for determining the time at which an armature strikes a stop" (from Vitesco Technologies GmbH) claims a method, device, and computer program for the electrical control of an actuator for determining the time of an anchor stop.

In this patent, a method is disclosed for operating an actuator having a coil and a displaceable mounted armature driven by a magnetic field generated by the coil, in a measurement operating mode for ascertaining a time at which the armature reaches its stop position after activation of the actuator. In our invention, the coil voltage or coil current measurements are not used for determining the time at which an armature strikes a stop, nor do we intend to determine the time at which an armature strikes a stop at all.

The patent [73] from Thomas Magnete GmbH "Method for controlling a cyclically operated electromagnet" discloses a measure of the voltage and current curves of the coil, determining a minimum pull current, determining max current, determination of a time to stop the armature, regulating the level of control voltage depending on the time difference compared to the predetermined time difference.

According to claim 1, this invention proposes a method for the cyclical control of an electromagnet at the energising stage using the time difference T2 - T1 to monitor the intended function of the electromagnet by exceeding a predetermined limit value for the time difference T2 - T1 to an electrical error message from the electrical control to a higher-level electrical control or leads to a reporting facility. No gradient control of the electromagnet current is mentioned. In addition, no T2 or difference between T2 and T1 is used in our invention.

Methods described in other claims of this invention use T3, T4, and the difference between T4 and T3 to provide the cyclical control of an electromagnet. Our method does not use T3, T4 or the difference T4 -T3 for any purpose.

4.3 Results

4.3.1 Invention description

As shown in Figure 4.3, each solenoid valve comprises at least an electromagnetically inductive coil (6) wound around a movable armature (7), a resetting/return spring (5), and a low- or a high-pressure poppet (4) that is physically attached to the armature, wherein the coil is electrically connected to an electronic controller that actively controls one or more said valves to determine the net displacement of fluid by the working chamber on a cycle-by-cycle basis.

The controller comprises at least a coil driver circuit (2), a sensing circuit (3) that provides a feedback signal of coil current or voltage (or both), a CPU (1) that can be programmed to

generate a required PWM used to control MOSFETs of the coil driver circuit in order to control gradient of the rising edge of the solenoid current profile during its energising.

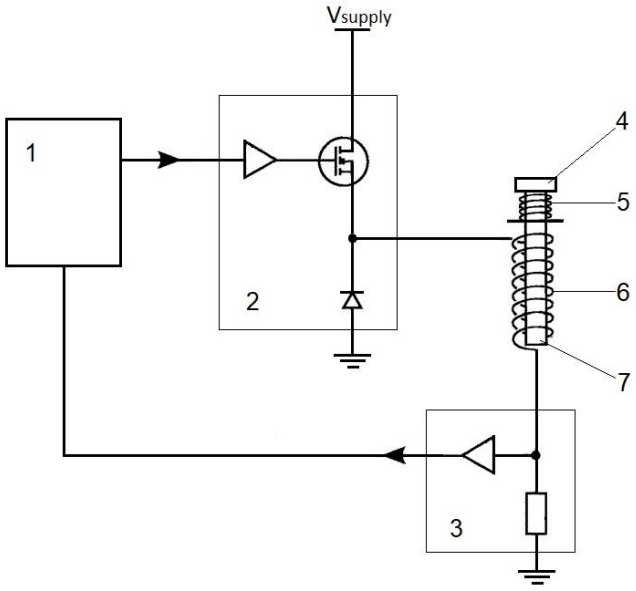

Figure 4.3. Circuit diagram of a basic solenoid drive system.

The invention consists of controlling the gradient of the solenoid current profile during each energising cycle (i.e., keeping the gradient constant according to the current profile reference at every switching cycle) at least up to reaching pull-in current when the current reference gradient I_{ref} is defined by the equation (30) for the maximum coil circuit resistance and the minimum supply voltage established for the application. Thus, ensuring that the solenoid pull-in current will be reached in the same period/time ($\Delta T1 \rightarrow 0$) at every switching cycle regardless of the solenoid coil circuitry resistance (or voltage) change which occurs between cycles. Before the armature starts its motion, the electromagnetic force developed by the solenoid is primarily correlated to (dependent on) the coil current. Therefore, during this motionless stage, the time required for the electromagnetic force to reach the 'attracting force' value will remain constant from cycle to cycle, regardless of the resistance change. Because it is the electromagnetic force reaching the attracting force, that marks the beginning of motion, thus the armature will start its motion at the same time within each switching cycle.

If the motion time is small, and thus insignificant in respect of the overall response time, and thus such changes can be ignored in the control to achieve a constant response time. Thus, the overall response time is significantly, and effectively stabilised, by the control of the solenoid

current for at least part of the motionless stage of the armature. However, if the motion time is significant, the current gradient must be controlled until the end of the plunger motion to achieve maximum precision of the response time.

$$I_{ref} = i(t) = \frac{V_{min}}{R_{max}}(1 - e^{\frac{-tR_{max}}{L_{coil}}}) \quad (30)$$

Where V_{min} is the minimum supply voltage established for the application, R_{max} - maximum coil circuit resistance established for application, L_{coil} – solenoid coil inductance, i - coil instant current, t – time of the energising phase, e - Euler's number.

Figure 4.4 shows an example of the reference current profile calculated by the empiric coil current equation using coil inductance of the solenoid valve and minimum voltage and maximum resistance established for the application.

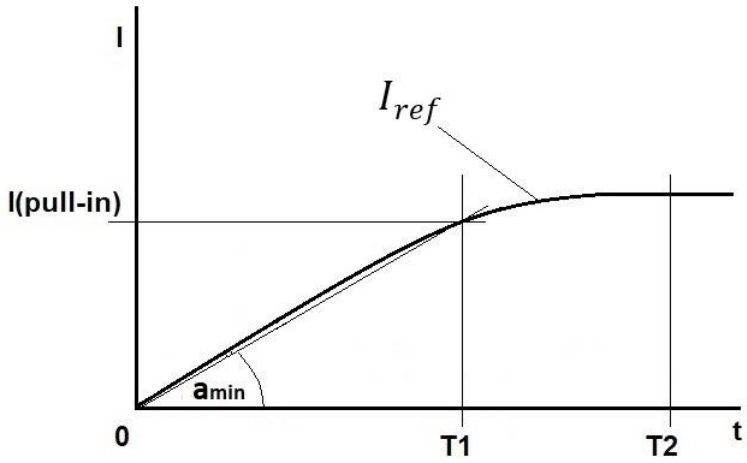

Figure 4.4. Example of the reference current profile calculated by the empiric coil current equation using coil inductance of the solenoid valve and minimum voltage and maximum resistance established for the application.

Thus, by controlling coil current gradient during the energizing stage, the overall time required to change valve state from open to closed (or vice versa) will be kept unchanged from cycle to cycle ($\Delta T2 \rightarrow 0$, see Figure 4.5) regardless of the solenoid coil circuit resistance.

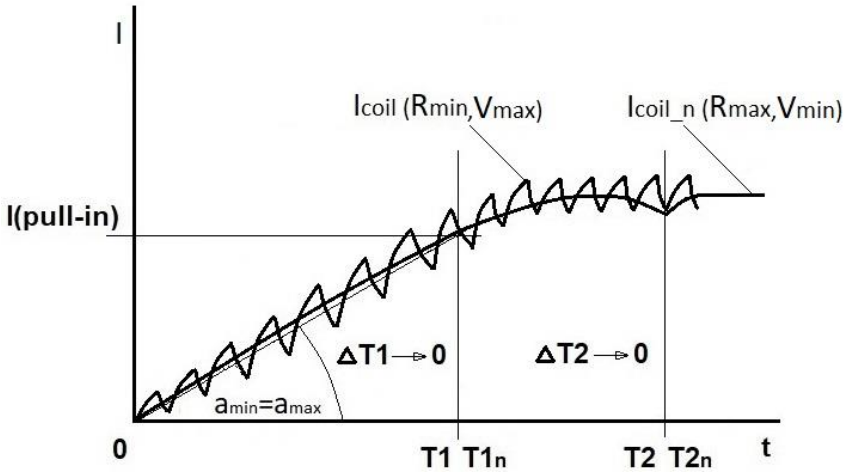

Figure 4.5. Illustration of coil current of the same solenoid valve at different resistances and/or voltages of the solenoid coil circuit coil current when RTS method is applied.

In this example, the current profile reference is equal to the coil current, which makes the current controller saturate when coil resistance reaches Rmax and supply voltage reaches Vmin that were established for the application. For most applications, the Rmax and Vmin values can be chosen that will not allow controller saturation. Therefore, the current reference above the saturation point can be approximated by linear equations as show Figure 4.6, or a combination of linear and power-law equations (see Figure 4.7).

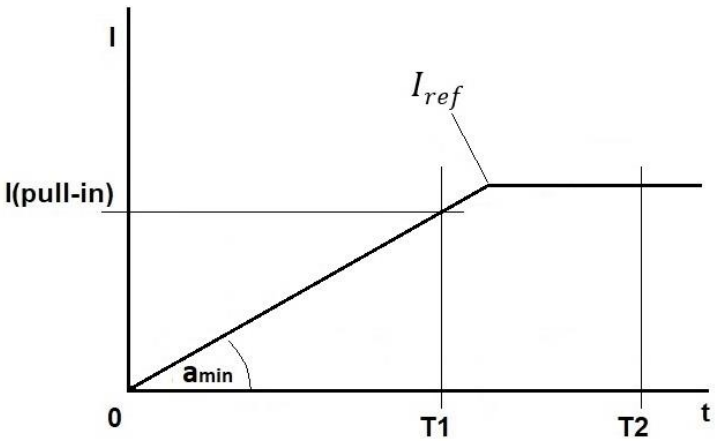

Figure 4.6. Example of a current profile reference generated by applying linear equations.

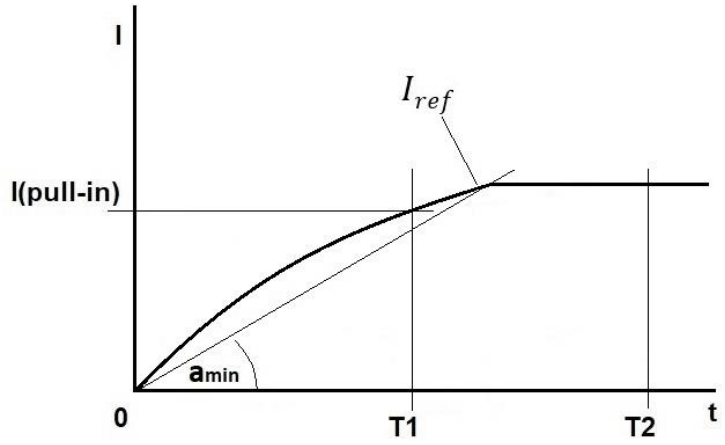

Figure 4.7. Example of a current profile reference generated by applying power-law and linear equations.

Therefore, ensuring the coil current gradient during the energising phase is the same (repeatable) and, at the same time, the electromagnetic force will reach the same values (including the solenoid attracting force value) over the same time at each switching cycle of the solenoid valve will make its response time repeatable (constant from cycle to cycle) independently on coil resistance or/and supply voltage. This makes the LPV closing angle prediction more precise and allows for decreasing the compensation time margin, thus, increasing the piston's useful stroke in turn.

4.3.2 Development and implementation of the current gradient control algorithms

As it was mentioned previously, parallel and independent control of multiple solenoid valves is required for the proper operation of a DD machine (12-15 valves per DD machine). To provide a precise operation of each valve an FPGA (Artix-7/ZYNQ-7000) is used in DD controllers. Therefore, the coil current gradient control algorithm must be implementable in hardware description languages (HDL). The VHDL language is used in the Danfoss DD department.

According to my research, the equation (30) that is shown in previous section and best describes the coil current gradient reference for a solenoid valve is not feasible to implement in VHDL as it requires a floating-point implementation for the power-law expression. Therefore, the algorithm development was focused on an approximation of the coil current gradient (current

profile) reference, which consists of the functions that describes the ramp and the peak phases of the coil current profile (see Figure 4.8). When the peak phase is described by equation (31).

$$I_{ref} = I_{peak} \tag{31}$$

Where I_{ref} is an ongoing reference value and I_{peak} is the current value of the coil current profile peak phase.

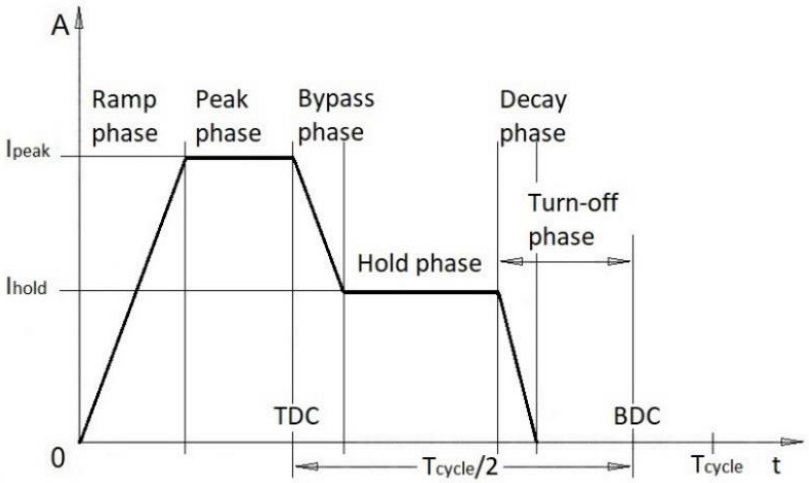

Figure 4.8. Coil current profile of a DD valve at motoring mode of operation.

The next step of the development was to verify the correct operation of the developed coil current gradient control algorithms by simulation before proceeding with the VHDL implementation.

The simulation must prove that the algorithm provides response time stabilisation (RTS) of the solenoid valve within a supply voltage and coil circuit resistance ranges established to be appropriate for a DD automotive application.

The international standard ISO 16750-2 provides a table of established voltage ranges for supply voltage for system devices with 24 V nominal voltage, which is used as a reference for the direct current supply voltage test to verify equipment functionality at a minimum and maximum supply voltage. The 22-32 V supply voltage range (see Table 4.2, code G) was assumed to be appropriate for DD automotive application at nominal operation conditions.

Table 4.2. ISO 16750-2 supply voltage test ranges for system devices with 24 V nominal voltage [74].

Code	Minimum supply voltage (V)	Maximum supply voltage (V)
E	10	32
F	16	32
G	22	32
H	18	32

The temperature range from -20°C to +120°C for the solenoid coil was assumed to be appropriate for nominal operation conditions of a DD machine, which, according to equation (32), gives 0.4Ohm variation of the solenoid coil resistance for the DD valve MAV8.

$$R = R_{ref}(1 + \alpha(T - T_{ref})) \quad (32)$$

Where R is the resistance of the conductor at temperature T, R_{ref} is the reference resistance of the conductor at temperature T_{ref}, and α is the temperature coefficient of resistance for conductor material.

Thus, allowing 0.1 Ohm for the resistance variation of the solenoid coil cable (due to different application requirements and temperature variation), the maximum variation of the resistance for the solenoid coil circuit was assumed to be 0.5 Ohm at nominal operation conditions of a DD machine.

Figure 4.9 shows the Simulink model that was created to be used for the current gradient control algorithm development. The Simulink model of a solenoid valve setup is approximate to the DD valve PAV8 characteristics, and it is operated by a basic coil driver circuit with a low-side current sensing, which in turn, is controlled by the controller that is based on the developed coil current gradient control algorithm. The resistor, which is in series with the solenoid coil is used to change the coil circuit's series resistance. Supply voltage, control signal, solenoid coil current, solenoid plunger (armature) displacement and velocity are monitored. The solenoid coil current is used as the feedback signal for the controller.

The controller provides closed-loop coil current gradient control using the hysteresis current control technic, where the hysteresis lover and upper limits are set to 30 mA and -30 mA accordingly. The coil current reference is generated from the equations that describe the required gradient of the current profile ramp and peak phases.

The hysteresis current control technique was chosen due to its low requirements for the computation power of a CPU, which will be very beneficial when implementing the algorithm for low-cost FPGAs. Also, it does not require any tuning, unlike when using P, PI, or PID controllers, which allows for saving human hours.

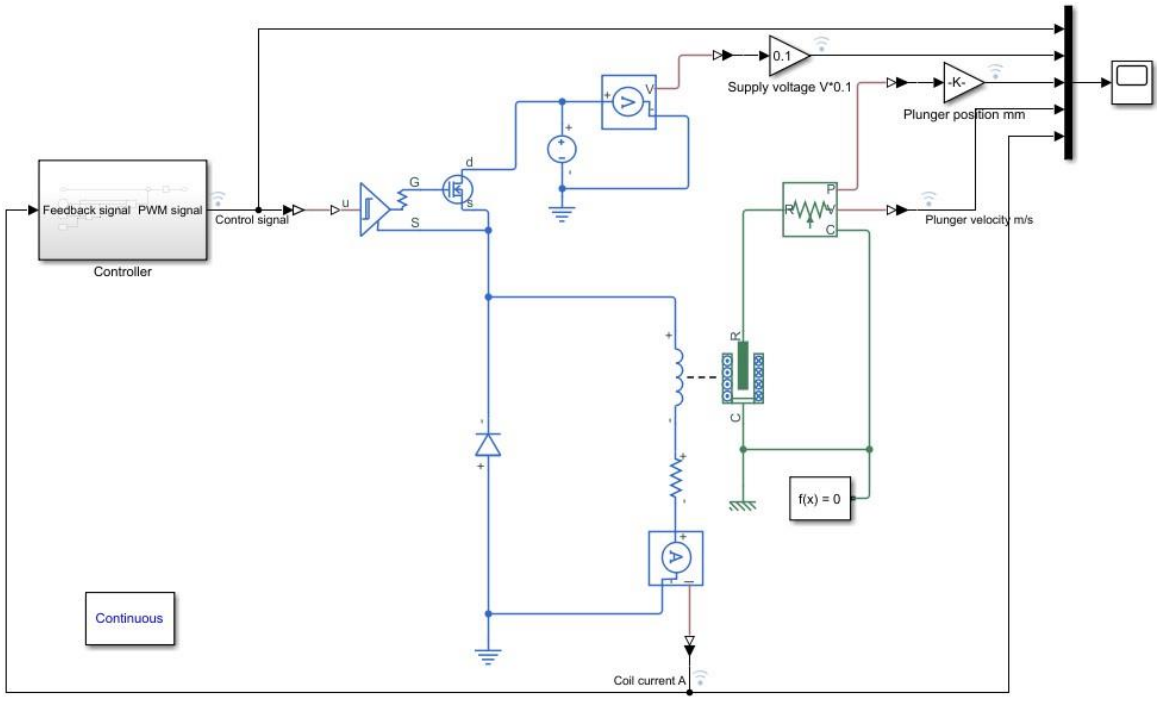

Figure 4.9. Simulink model used for current gradient control algorithm development.

4.3.2.1 Linear current gradient control

The first approach to provide a current gradient control of the coil current profile ramp stage was accomplished by generating an ongoing current reference value by using a linear equation (33). Figure 4.10 shows a graph generated by the linear equation using random values for I_{peak} and T_{ramp}.

$$I_{ref} = i(t) = \frac{I_{peak}}{T_{ramp}} * t \tag{33}$$

Where I_{peak} is the current value of the peak phase, T_{ramp} is the period (time duration) of the ramp phase of the current coil current profile, and t is a time (counter value) at the correspondent current reference value I_{ref}.

For the VHDL implementation, the equation (33) can be simplified if replacing the division operation with a single constant, which in turn, is multiplied by a scaling constant to keep all the values within the integer range. The scaling constant should be a power of two number (2^n) to enable the substitution of the multiplying operation by the binary shift operation. The developed VHDL code can be found in Appendix B.

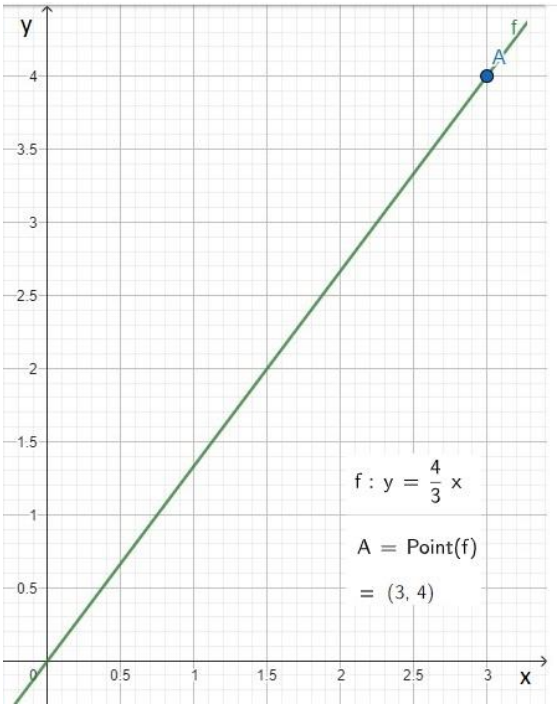

Figure 4.10. A graph generated by equation (33) for $I_{peak} = 4$ and $T_{ramp} = 3$.

Figure 4.11 shows the coil current gradient control algorithm based on liner equations (31) and (33) developed in Simulink. The simulation lasts for 5 ms. During the first 2.5 ms, the current reference is generated using equation (33) and the next 2.5 ms using equation (31), where the T_{ramp} is set to 2.5 ms and the I_{peak} is set to 4 A. The error between reference and feedback values is continuously compared to the hysteresis limits. If the error is larger than the upper hysteresis limit, the control signal turns low. Or, if the difference is smaller than the lower hysteresis limit, the control signal turns high.

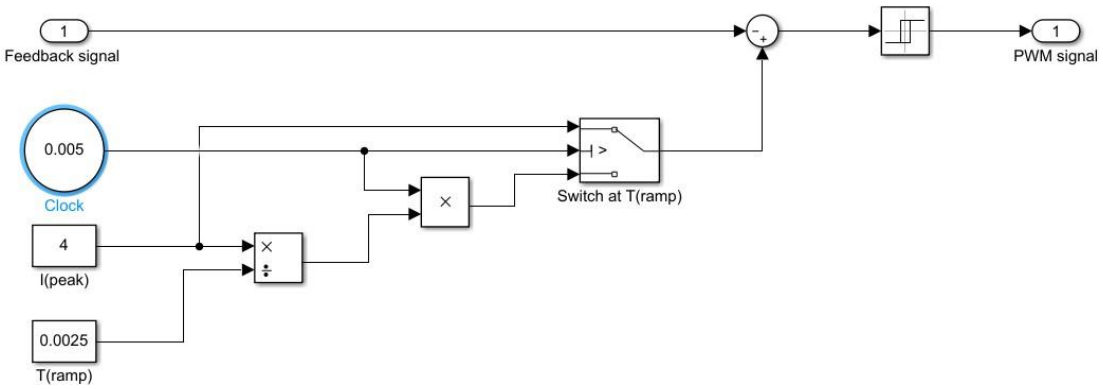

Figure 4.11. Linear current gradient control algorithm.

The simulation was run for the maximum and minimum supply voltage and coil circuit resistance values established previously.

Figure 4.12 shows the simulation results at the maximum supply voltage of 32 V and the minimum coil series resistance 0.1 Ohm of the DD application. Figure 4.13 shows the simulation results at the minimum supply voltage of 32 V and the maximum coil series resistance 0.1 Ohm of the DD application.

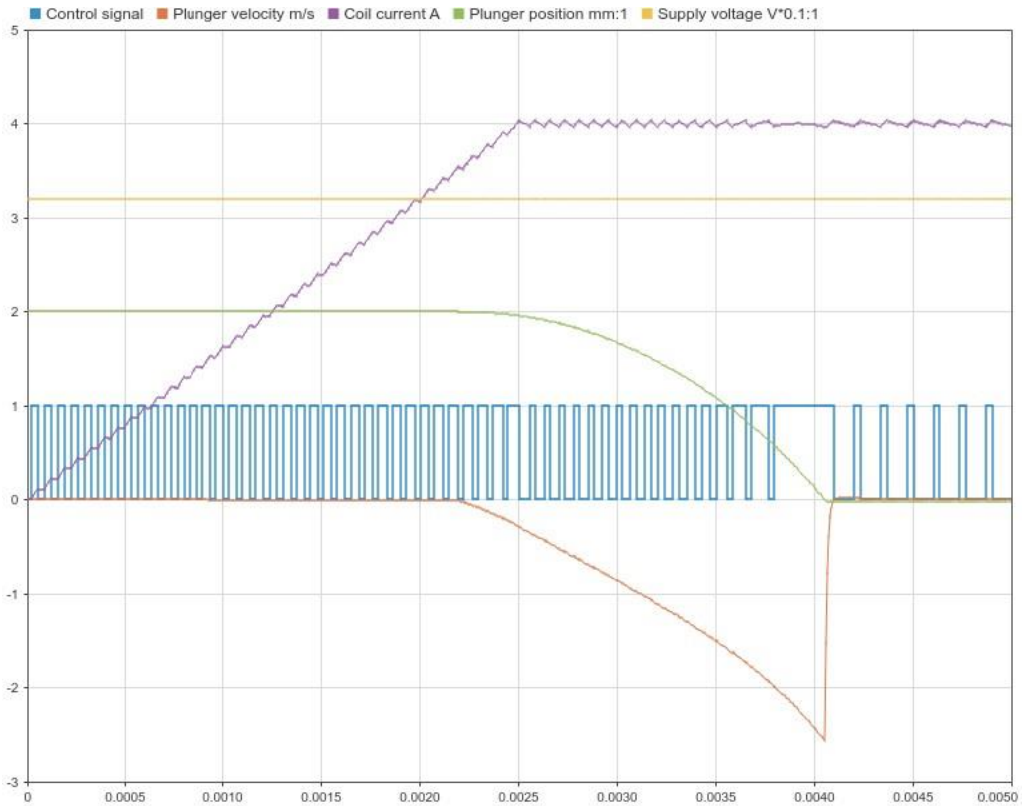

Figure 4.12. Linear current gradient control simulation results at supply voltage of 32 V and added coil series resistance of 0.1 Ohm.

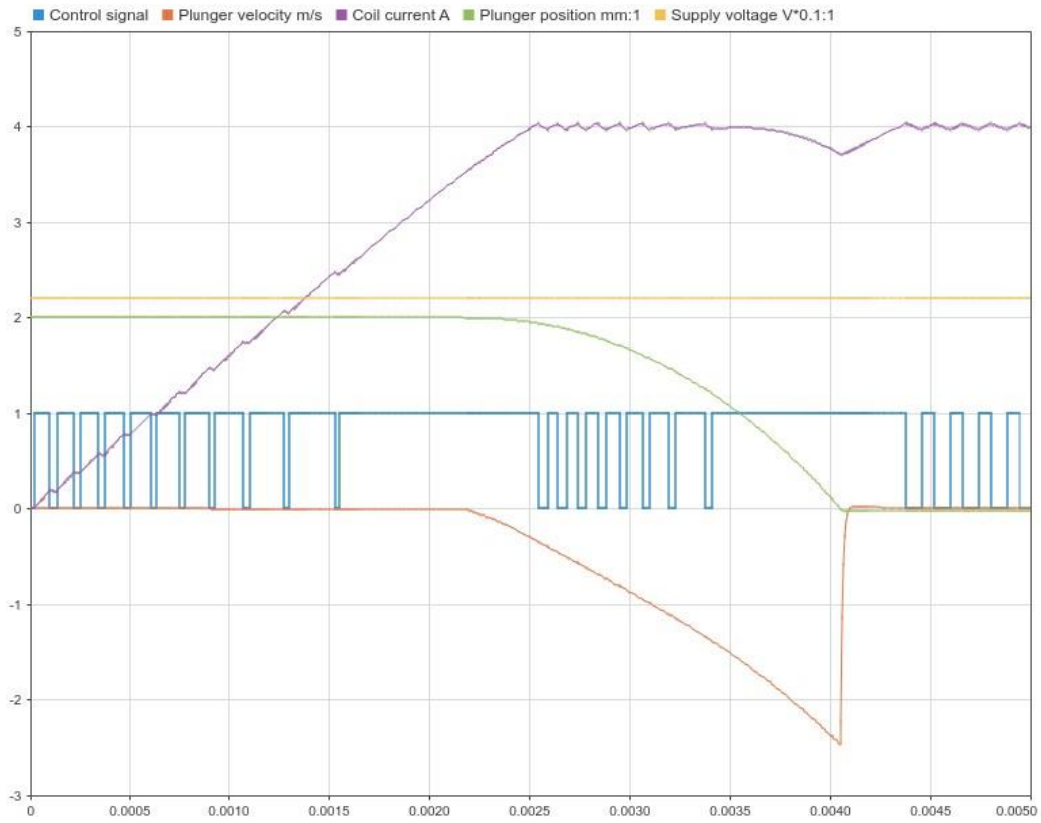

Figure 4.13. Linear current gradient control simulation results at supply voltage 22 V and added coil series resistance 0.6 Ohm.

Comparing the test results, it can be seen that the gradient of the coil current (purple waveform) is kept the same until the back-EMF induced by the plunger motion affects it, forcing the controller to saturate. However, this does not affect the plunger end-stop time, which can be confirmed by analysing the plunger position waveform (green) that in both cases riches the end-stop value (0 mm) at the same time (0.00405 ms), or by analysing the plunger velocity waveform (red) that in both cases reaches its peak value at the same time (0.00405 ms). Also, the peak of the current dip provoked by the back-EMF corresponds to the solenoid plunger end-stop time, which is the same in both cases.

Therefore, it can be concluded that the developed in this section coil current gradient control algorithm provides response time stabilisation of a cyclically operating solenoid valve within established ranges of the coil driver supply voltage and coil circuit resistance. The implementation of this algorithm in VHDL is feasible for low-cost FPGAs.

4.3.2.2 Power-law current gradient control

The next approach to provide a current gradient control of the coil current profile ramp stage was accomplished by generating an ongoing current reference value by using a power-law equation (34). Figure 4.14 shows some graphs generated by the power-law equation using random values for I_{peak}, T_{ramp}, and random values for the convex grade of the ramp defined by exponent c.

$$I_{ref} = i(t) = I_{peak} * \left(\frac{t}{T_{ramp}}\right)^{c} \quad (34)$$

Where I_{peak} is the current value of the peak phase, T_{ramp} is the period (time duration) of the ramp phase of the current coil current profile, t is a time (counter value) at the correspondent current reference value I_{ref}, and c is a constant in the range between 0 and 1 that defines the convex grade of the ramp.

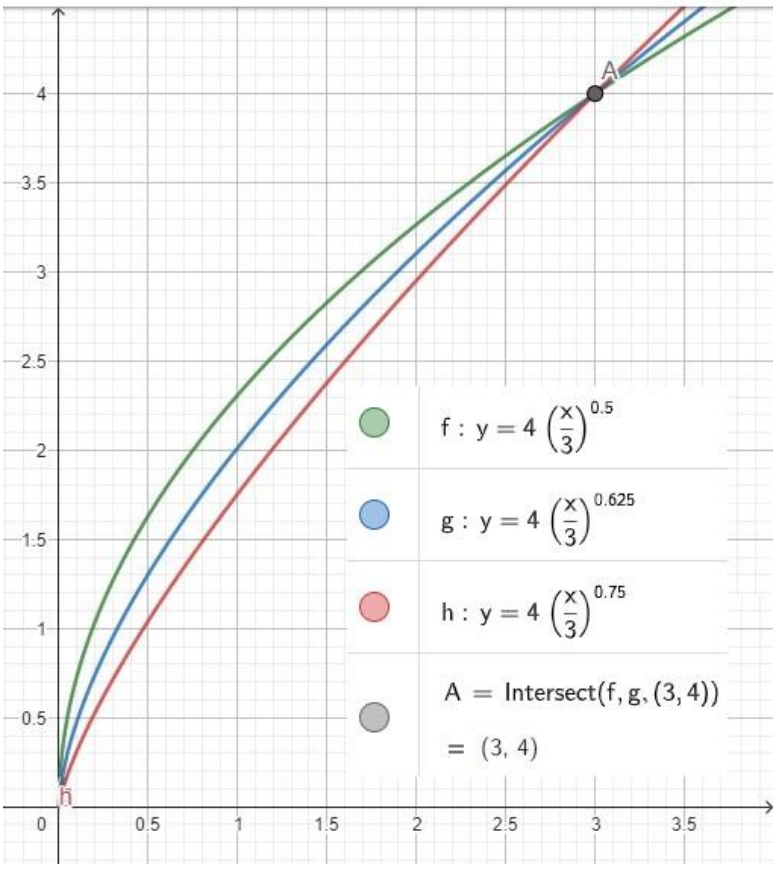

Figure 4.14. A graph generated by equation (34) for I_{peak}= 4 A, T_{ramp}= 3 ms, and a random convex grade of the ramp.

As was mentioned previously, the VHDL implementation of such arithmetic operation as exponentiation where the exponent is a variable of floating-point data type is not feasible. However, if rearranging equation (34) substituting the floating point exponents by a square root and an integer exponent, the VHDL implementation of such an equation will be possible by implementing the non-restoring square root algorithm (see [75] and [76]).

Equation (35) is the outcome of rearranging the equation (34), which can be implemented in VHDL. Figure 4.15 shows some graphs generated by the rearranged power-law equation using the same values for I_{peak}, T_{ramp}, and the same values for the convex grade of the ramp as in Figure 4.14.

$$I_{ref} = i(t) = I_{peak} * \sqrt[a]{\left(\frac{t}{T_{ramp}}\right)^{b}} \tag{35}$$

Where I_{peak} is the current value of the peak phase and T_{ramp} is the period (time duration) of the ramp phase of the current coil current profile, t is a time (counter value) at the correspondent current reference value I_{ref}, and a and b are integer constants that define the convex grade of the ramp (where a is an even number to enable the non-restoring square root algorithm application).

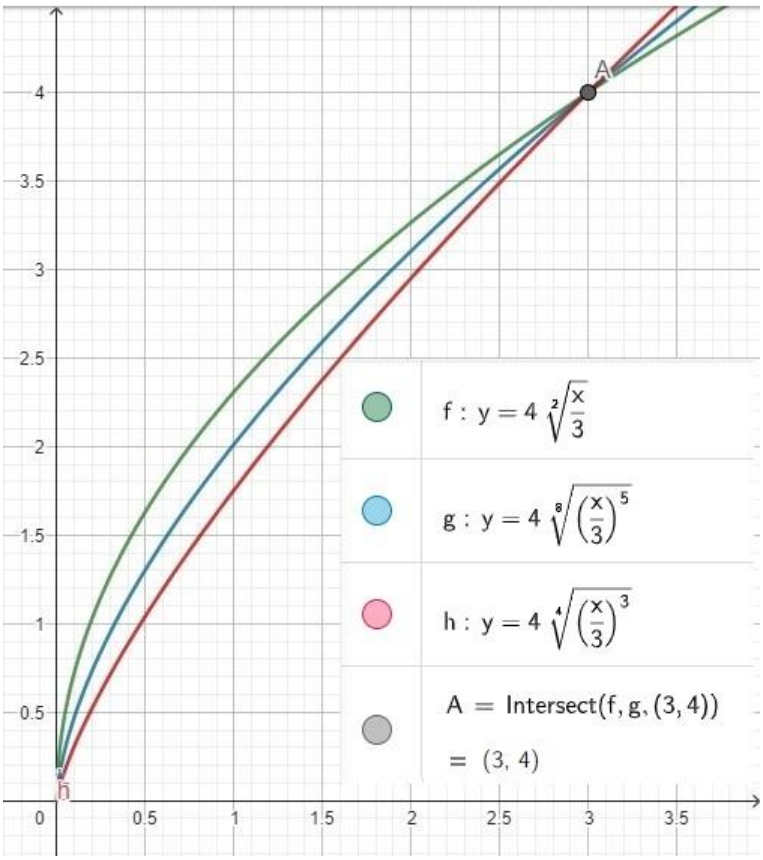

Figure 4.15. A graph generated by equation (35) for I_{peak}= 4 A, T_{ramp}= 3 A, and values convex grade of the ramp that were used in Figure 4.14.

The developed VHDL code for the ramp shapes *f* and *h* from Figure 4.15 can be found in Appendix B.

Figure 4.16 shows the coil current gradient control algorithm based on linear equation (31) and power-law equation (35) developed in Simulink. The simulation lasts for 5 ms. During the first 2.5 ms, the current reference is generated using equation (35) and the next 2.5 ms using equation (31), where the T_{ramp} is set to 2.5 ms, the I_{peak} is set to 4 A, and the convex of the ramp is defined by constants a and b. The error between reference and feedback values is continuously compared to the hysteresis limits. If the error is larger than the upper hysteresis limit, the control signal turns low. Or, if the difference is smaller than the lower hysteresis limit, the control signal turns high.

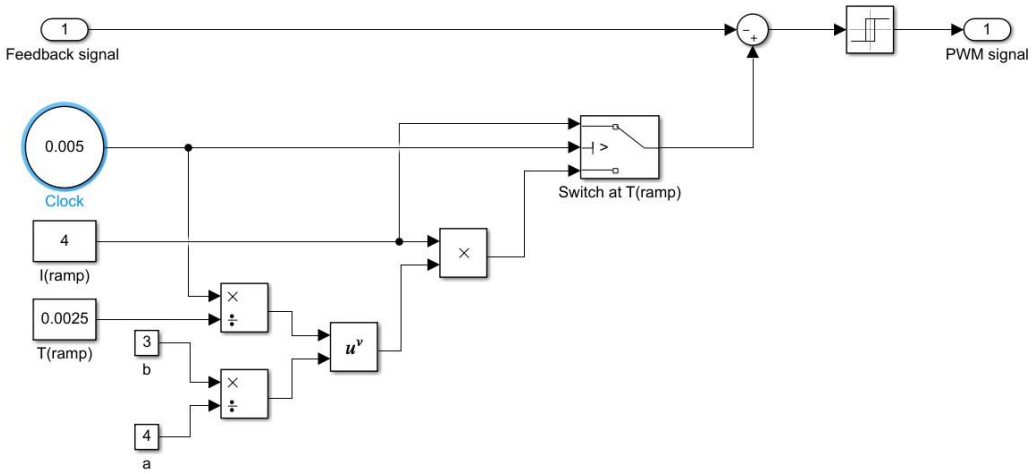

Figure 4.16. Power-law current gradient control algorithm.

The simulation was run for the maximum and minimum supply voltage and coil circuit resistance values established previously.

Figure 4.17 shows the test results at the maximum supply voltage of 32 V and the minimum coil series resistance 0.1 Ohm of the DD application. Figure 4.18 shows the test results at the minimum supply voltage of 32 V and the maximum coil series resistance 0.1 Ohm of the DD application.

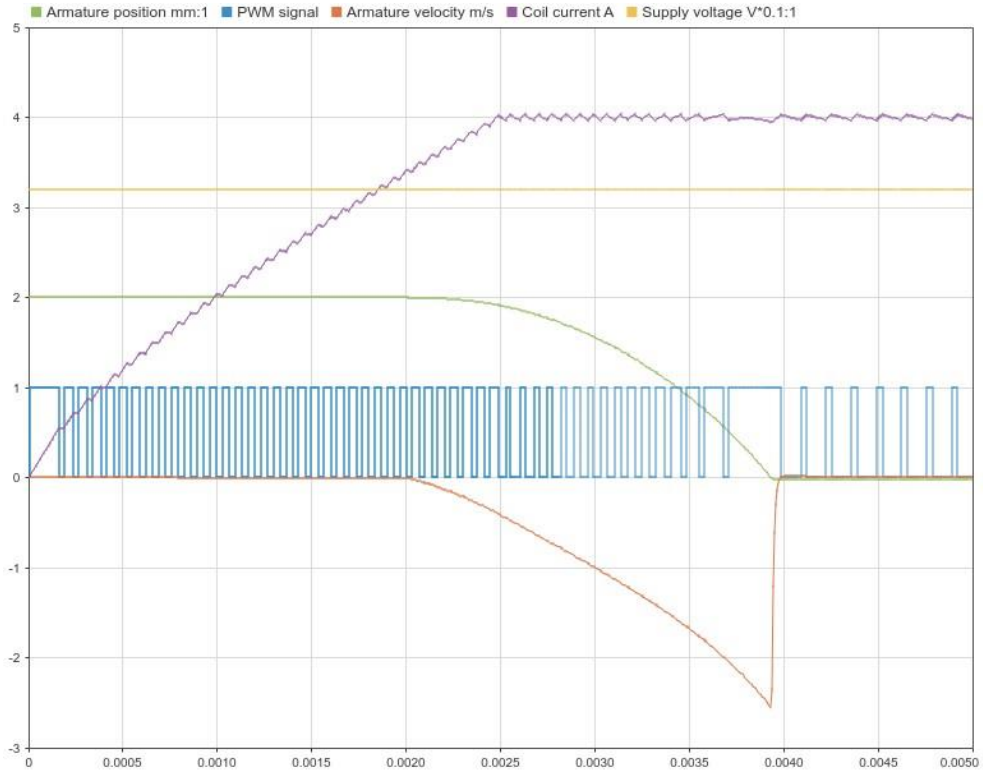

Figure 4.17. Power-law current gradient control simulation results at supply voltage of 32 V and added coil series resistance of 0.1 Ohm.

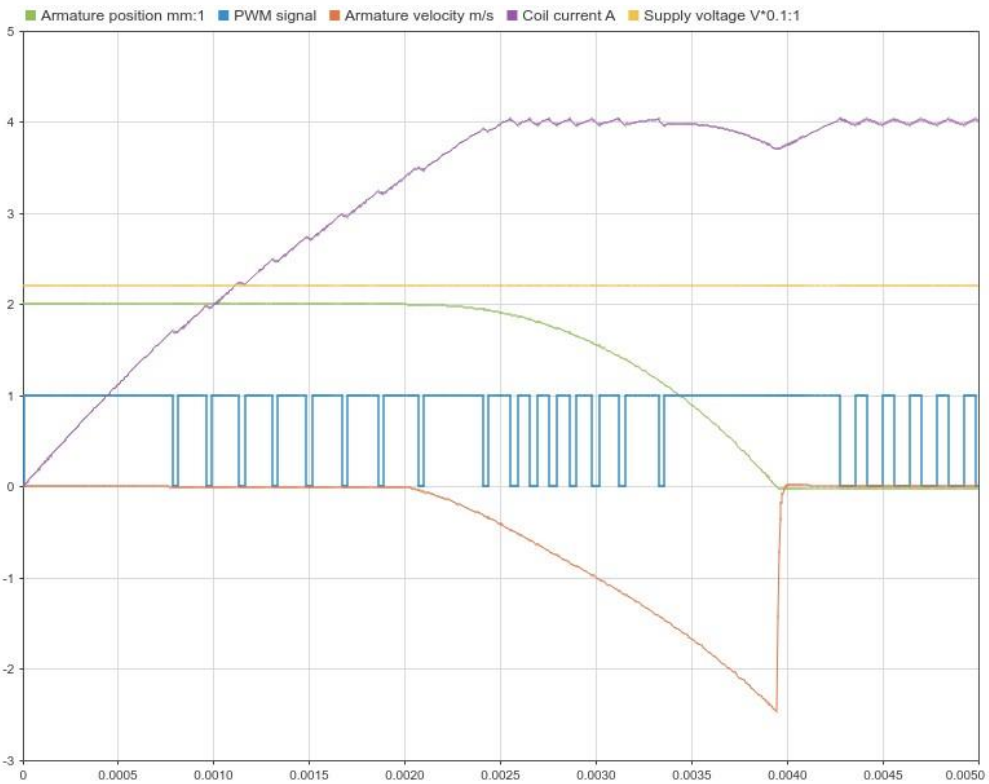

Figure 4.18. P[ower-law current gradient control simulation results at supply voltage of 22 V and added coil series resistance of 0.6 Ohm.

Comparing the test results, it can be seen that the gradient of the coil current (purple waveform) is kept nearly the same until the back-EMF induced by the plunger motion affects it, forcing the controller to saturate. However, this does not affect the plunger end-stop time, which can be confirmed by analysing the plunger position waveform (green) that in both cases riches the end-stop value (0 mm) at the same time (0.00394 ms), or by analysing the plunger velocity waveform (red) that in both cases reaches its peak value at the same time (0.00394 ms). Also, the peak of the current dip provoked by the back-EMF corresponds to the solenoid plunger end-stop time, which is the same in both cases. The valve response time achieved at power-law gradient control is faster by 0.11 ms than the response time when using linear gradient control.

Therefore, it can be concluded that the power-law coil current gradient control algorithm provides a constant response time of the solenoid valve within established ranges of the coil driver supply voltage and coil circuit resistance. Also, valve response time at the power-law gradient is faster than the response time provided by linear gradient control. The implementation of such an algorithm in VHDL is feasible.

4.3.2.3 Linear current gradient control with boost option

Figure 4.19 shows the current waveform generated by the linear current gradient controller (red) against the one that was generated by the power-law controller (blue). Both waveforms were generated using the previously described Simulink model at the same setup (supply voltage, coil circuit resistance…). As can be seen and as was mentioned previously, in the case of the power-law rising edge of the current profile the plunger reaches the end-stop faster than in the case with the linear rising edge. It happens because the coil current reaches the pull-in current faster. Also, it can be seen the power-law controller saturates at the beginning of the energising stage, which might keep the coil current below the reference values during the saturation region.

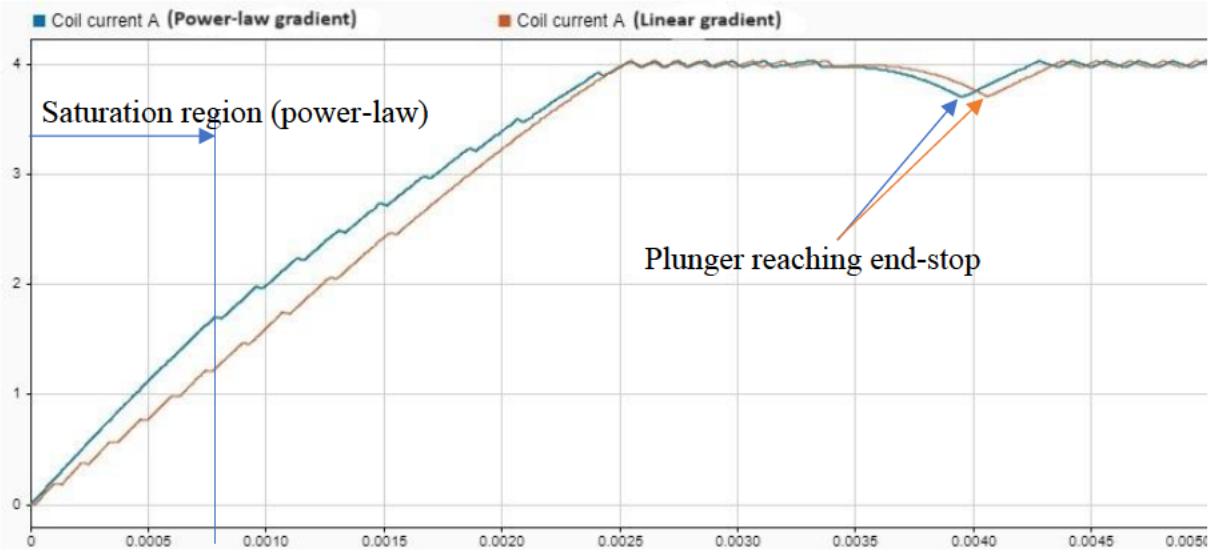

Figure 4.19. Coil current comparison at supply voltage of 22 V and added coil series resistance of 0.6 Ohm. Blue waveform - power-law current gradient control, red waveform - linear current gradient control.

Figure 4.20 shows current waveforms generated by the power-law current gradient controller at different supply voltages and coil circuit resistances. As can be seen, the coil of the blue waveform is slightly below the reference at the saturation region, which leads to a discrepancy in coil current at this region. However, this difference in the coil current profile does not affect the solenoid response time, which can be confirmed by analysing the plunger position change waveforms, which are shown in Figure 4.21. As can be seen in both cases plunger starts and finishes its travelling at the same time.

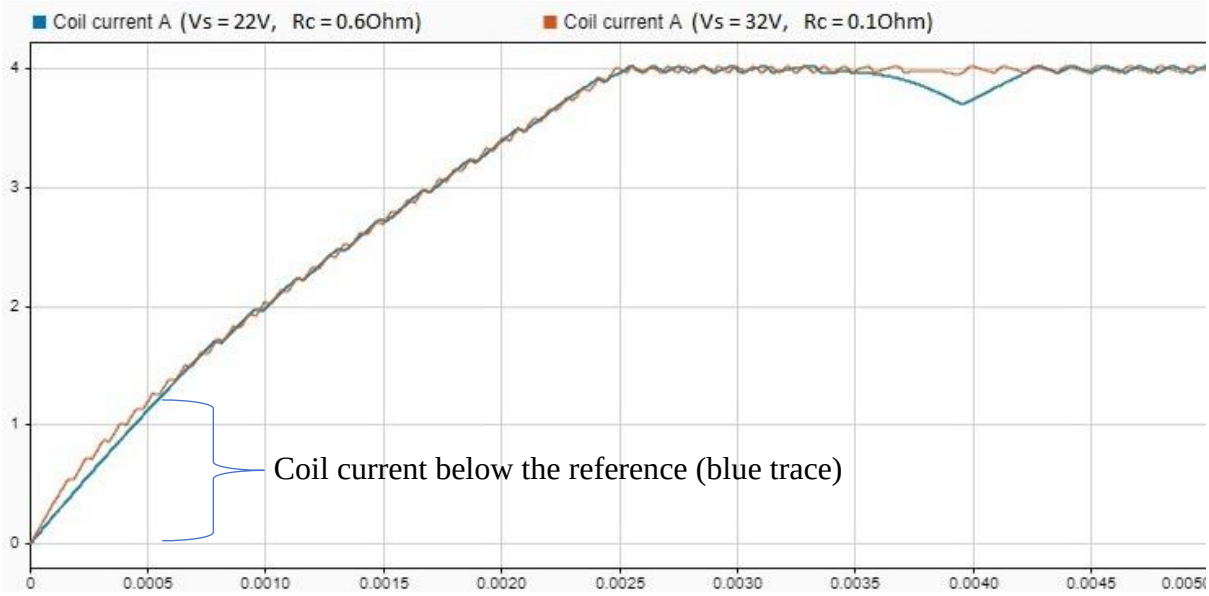

Figure 4.20. Coil current comparison at power-law current gradient control. Blue waveform - at supply voltage 22 V and added coil series resistance of 0.6 Ohm, red waveform - at supply voltage 32 V and added coil series resistance of 0.1 Ohm.

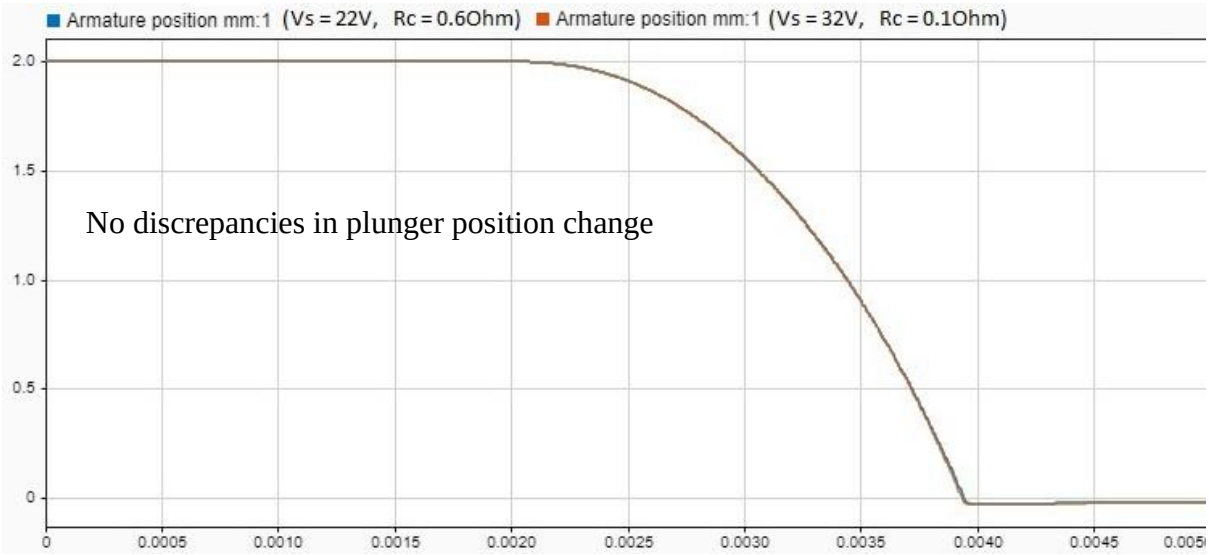

Figure 4.21. Plunger position change comparison at power-law current gradient control. Blue waveform - at supply voltage 22 V and added coil series resistance of 0.6 Ohm, red waveform - at supply voltage 32 V and added coil series resistance of 0.1 Ohm.

Therefore, the response time of the solenoid valve is not affected by the coil current discrepancy at the start of the energising phase, where the coil current is relatively small. This can be explained by analysing the solenoid force equation (36).

$$F = \frac{\mu_0 (NI)^2 S}{2\left(\frac{l_m}{\mu_r} + l_0\right)^2} \quad (36)$$

Where F is a solenoid force, N – number of turns of the solenoid coil, I – coil current, S – cross-section area of the core, μ_0 – magnetic permeability of air and vacuum, l_0 – length of the air gap, l_m – length of the path along ferromagnetic material, μ_r – relative magnetic permeability.

As can be seen from the equation, the solenoid force depends on coil current exponentially. Therefore, at the small values of the coil current, the change in the solenoid force is relatively small, and any discrepancies in the coil current profile at this stage will not affect the response time of the solenoid valve. Thus, there is no need to control the coil current at the start of the energising phase in order to keep the solenoid response time constant between the switching cycles.

Following this argument, a method of linear gradient control with a boost option was proposed, which can make valve response time smaller compared to the linear gradient. The method is based on the equation of a line in two-point form. The current gradient of the rising edge is defined by two values, I_{boost} and I_{peak}, where I_{boost} is the first point of the current reference that will be above 0 A. Therefore, the coil current will rise uncontrolled until it reaches a reference value thus, passing the region that is not affecting the solenoid response time as fast as allows the system and reaching the solenoid pull-in current faster than when using the linear gradient control.

Equation (37) describes the linear current gradient reference with the boost option.

$$I_{ref} = i(t) = I_{boost} + t\left(\frac{I_{peak} - I_{boost}}{T_{ramp}}\right) \quad (37)$$

Where I_{boost} is the initial value of the current reference, I_{peak} is the current value of the peak phase, T_{ramp} is the period (time duration) of the ramp phase of the current coil current profile, and t is a time (counter value) at the correspondent current reference value I_{ref}.

Figure 4.22 shows a graph generated by the linear current gradient reference equation (33) against a graph generated by the linear current gradient reference with the boost option equation (37).

The VHDL implementation procedure of equation (37) is the same as in case of equation (33). The developed VHDL code can be found in Appendix B.

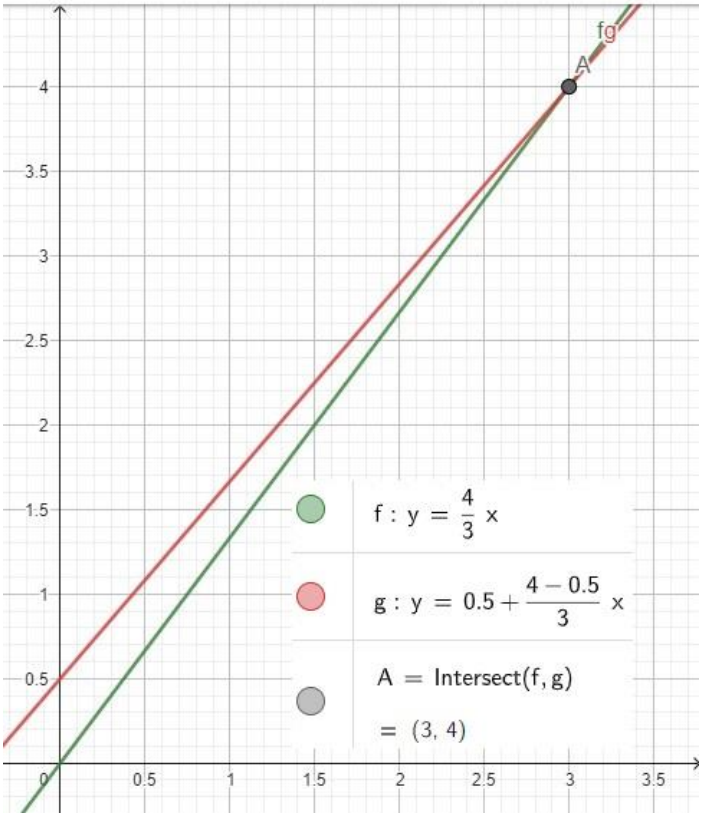

Figure 4.22. Linear current gradient reference (green) vs linear current gradient reference with boost option (red).

Figure 4.23 shows the coil current gradient control algorithm based on liner equations (31) and (37), developed in Simulink. The simulation lasts for 5 ms. During the first 2.5 ms, the current reference is generated using equation (37) and the next 2.5 ms using equation (31), where the T_{ramp} is set to 2.5 ms, the I_{peak} is set to 4 A, and I_{boost} is set to 0.7 A. The error between reference and feedback values is continuously compared to the hysteresis limits. If the error is larger than the upper hysteresis limit, the control signal turns low. Or, if the difference is smaller than the lower hysteresis limit, the control signal turns high.

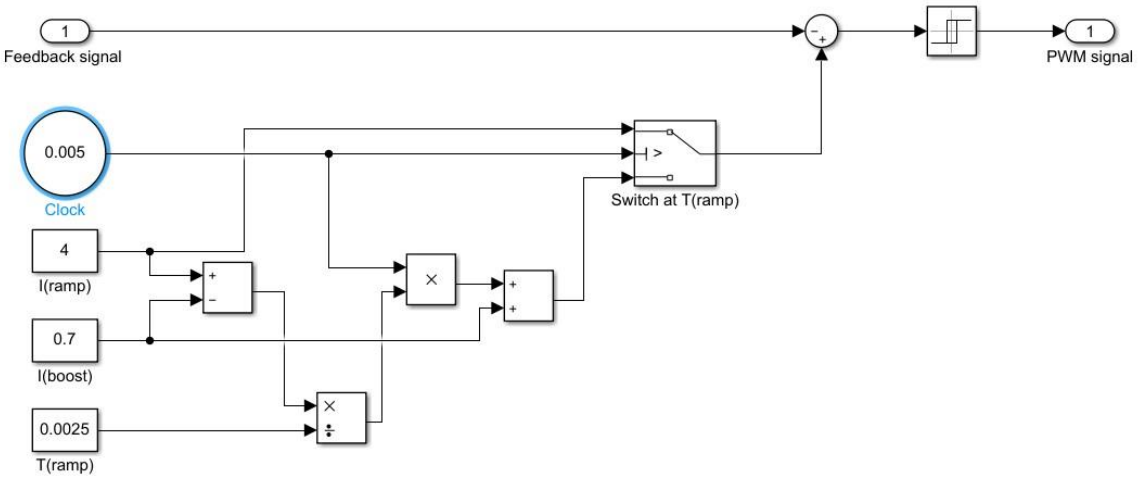

Figure 4.23. Linear current gradient control algorithm with boost option.

The simulation was run for the maximum and minimum supply voltage and coil circuit resistance values established previously.

Figure 4.24 shows the test results at the maximum supply voltage of 32 V and the minimum coil series resistance 0.1 Ohm of the DD application. Figure 4.25 shows the test results at the minimum supply voltage of 32 V and the maximum coil series resistance 0.1 Ohm of the DD application. Figure 4.26, Figure 4.27 and Figure 4.28 show a comparison of coil current, solenoid force, and solenoid plunger position traces accordingly.

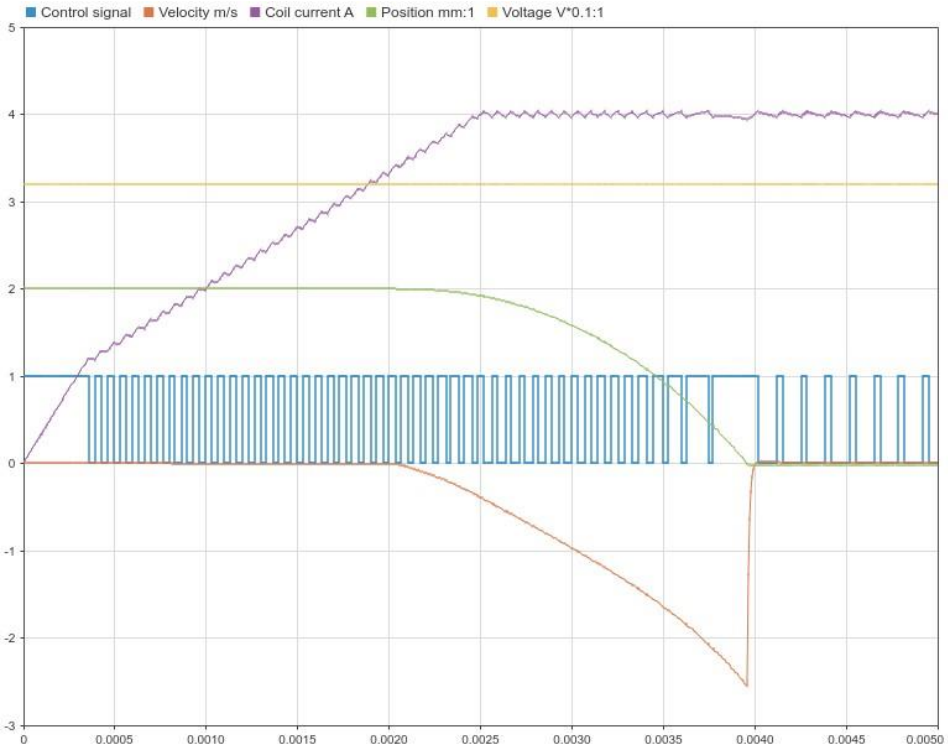

Figure 4.24. Linear current gradient control with boost option simulation results at supply voltage of 32 V and added coil series resistance of 0.1 Ohm.

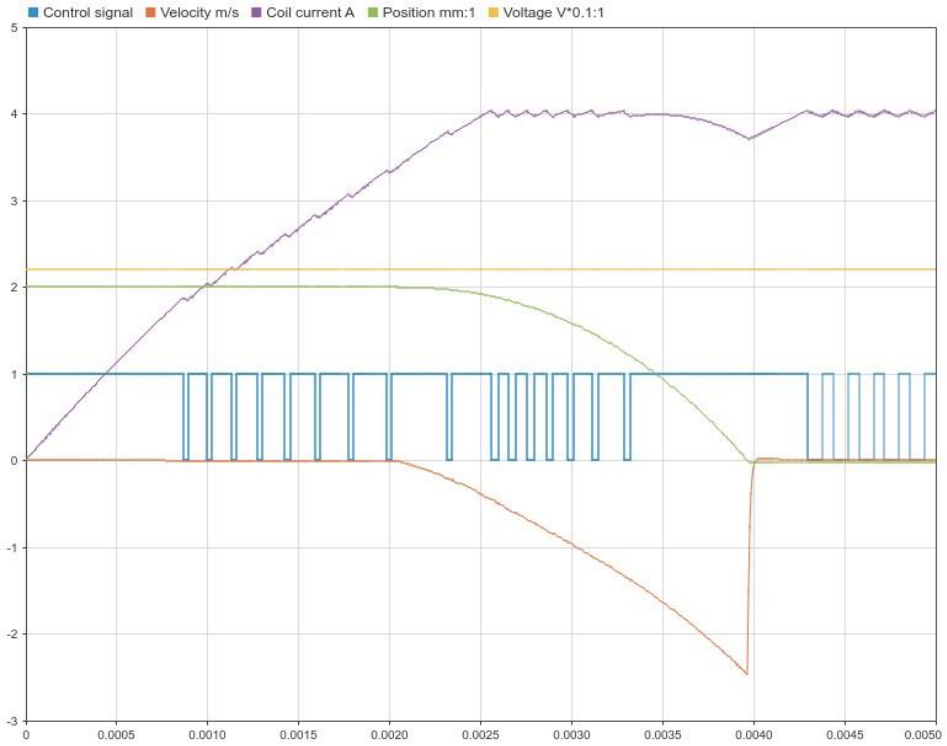

Figure 4.25. Linear current gradient control with boost option simulation results at supply voltage 22 V and added coil series resistance 0.6 Ohm.

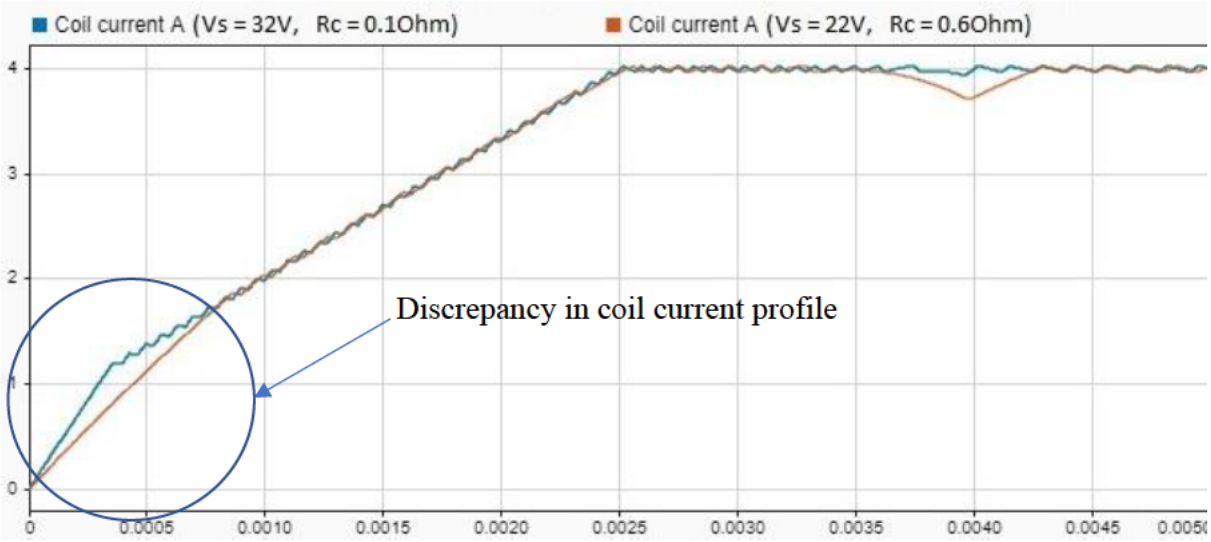

Figure 4.26. Coil current comparison at linear current gradient control with boost option. Red waveform - at supply voltage 22 V and added coil series resistance of 0.6 Ohm, blue waveform - at supply voltage 32 V and added coil series resistance of 0.1 Ohm.

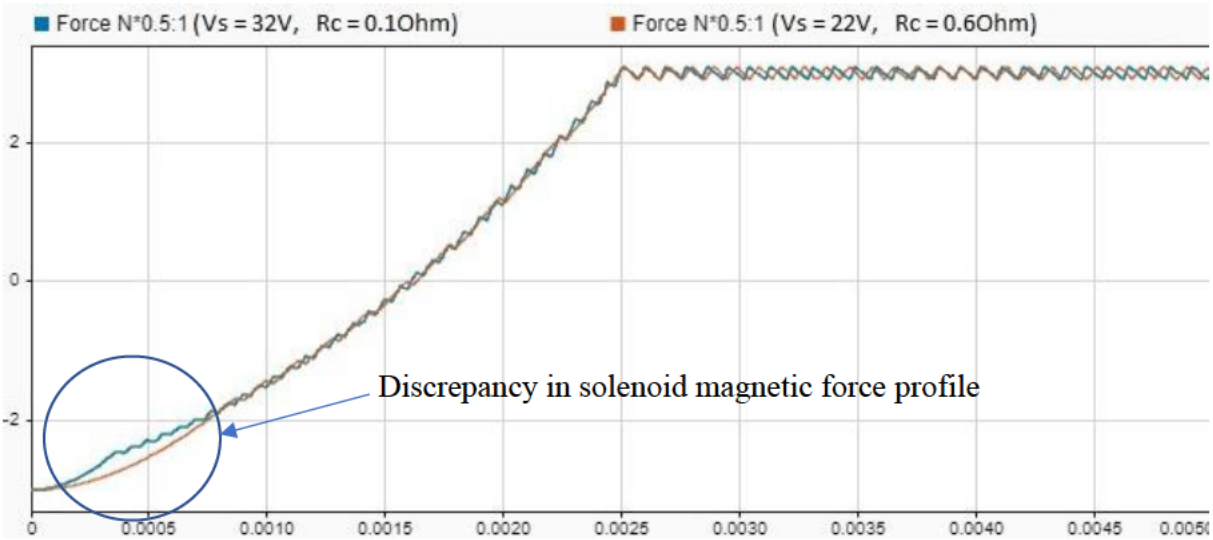

Figure 4.27. Solenoid force comparison at linear current gradient control with boost option. Red waveform - at supply voltage 22 V and added coil series resistance of 0.6 Ohm, blue waveform - at supply voltage 32 V and added coil series resistance of 0.1 Ohm.

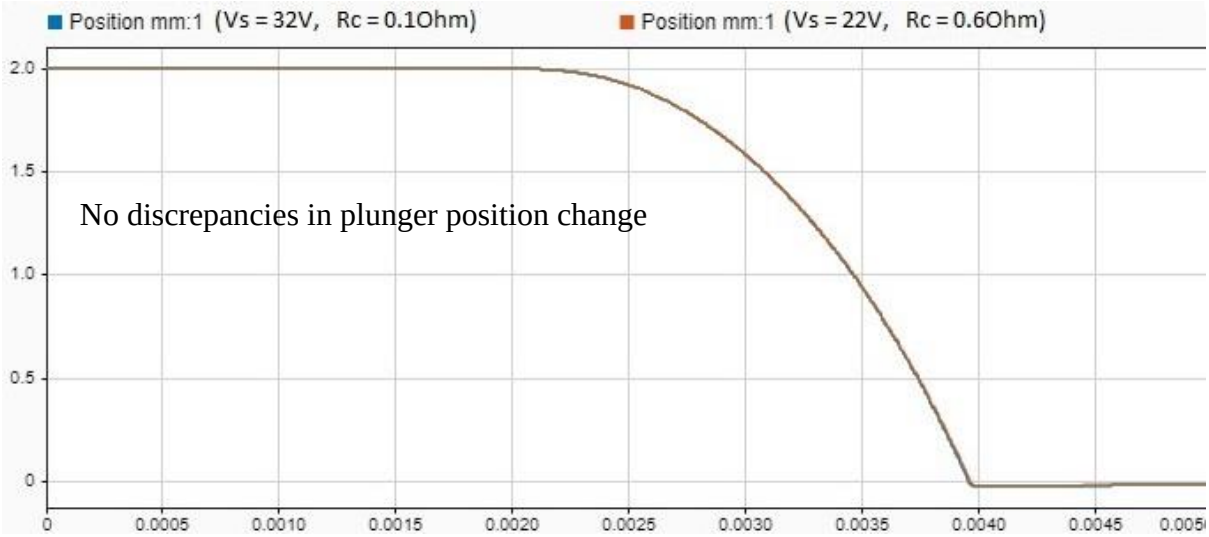

Figure 4.28. Plunger position change comparison at linear current gradient control with boost option. Red waveform - at supply voltage 22 V and added coil series resistance of 0.6 Ohm, blue waveform - at supply voltage 32 V and added coil series resistance of 0.1 Ohm.

Comparing the test results, it can be seen that the coil current rises differently during the open-loop stage, which causes a small difference between the force traces during the same period. However, these discrepancies do not affect the plunger travelling time or the end-stop time. In both cases, the plunger reaches the end-stop time at 0.00395 ms, which makes the solenoid response time faster by 0.1 ms than in the case of linear current gradient control without the boost option, which is 2.5% faster.

Therefore, it can be concluded that the developed in this section coil current gradient control algorithm provides response time stabilisation of a cyclically operating solenoid valve within established ranges of the coil driver supply voltage and coil circuit resistance and makes the solenoid valve faster by 2.5% comparing to linear-only gradient control. The implementation of such an algorithm in VHDL is feasible for low-cost FPGAs.

4.3.3 Test results of the developed current gradient control algorithms

The developed current gradient control algorithms were implemented in VHDL for the Arty-A7 FPGA board to control the next-generation coil driver (NGCD) prototype board described in Chapter 2 . The developed VHDL code is given in Appendix B.

Figure 4.29 shows the photo of the test bench used for testing the developed coil current gradient control algorithms that were discussed in this chapter. The setup was as follows.

Flashed with the developed firmware, the FPGA board is controlling the NGCD board, which in turn, is controlling DD valve PAV8. The NGCD board is powered by a variable power supply that provide required for testing voltage range 22-32 V established according to ISO 16750-2 (see section 4.3.2). A resistor of 0.68 Ohm was placed in series with the coil in order to simulate the coil circuit resistance change due to the temperature and wires length change. The 0.68 Ohm resistance variation corresponds to the temperature change from -40°C to +150°C of the MAV8 valve in series with 15 AWG cable of the length in a range of 2-10 meters. The valve closing time was detected using an accelerometer placed on top of the valve. The supply voltage, NGCD board coil current/voltage monitor circuit output (see Chapter 3), and accelerometer signal were measured using an oscilloscope. The current sensing circuit scaling constant is 7.143 A/V.

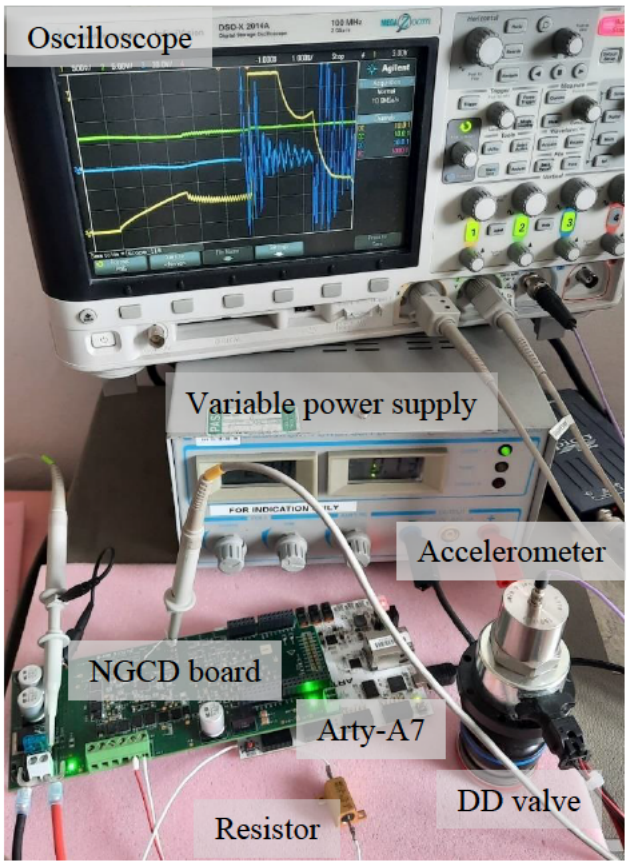

Figure 4.29. Photo of the test bench for the solenoid valve response time stabilisation method testing.

4.3.3.1 Linear current gradient control test results

This section describes the test results of the linear coil current gradient control at which the coil current profile was set to the following parameters:

- $T_{ramp} = 2.5\ ms$;
- $T_{peak} = 2.5\ ms$;
- $I_{peak} = 6\ A$.

Figure 4.30 shows the oscilloscope readings during the test when the supply voltage was set to 32 V, and the coil circuit additional resistor is 0 Ohm. Figure 4.31 shows the oscilloscope readings during the test when the supply voltage was set to 22 V, and the coil circuit additional resistor is 0.68 Ohm. In both figures green waveform is the supply voltage, the blue waveform is the accelerometer signal, and the yellow waveform is the output signal of the NGCD board coil current/voltage sensing circuit.

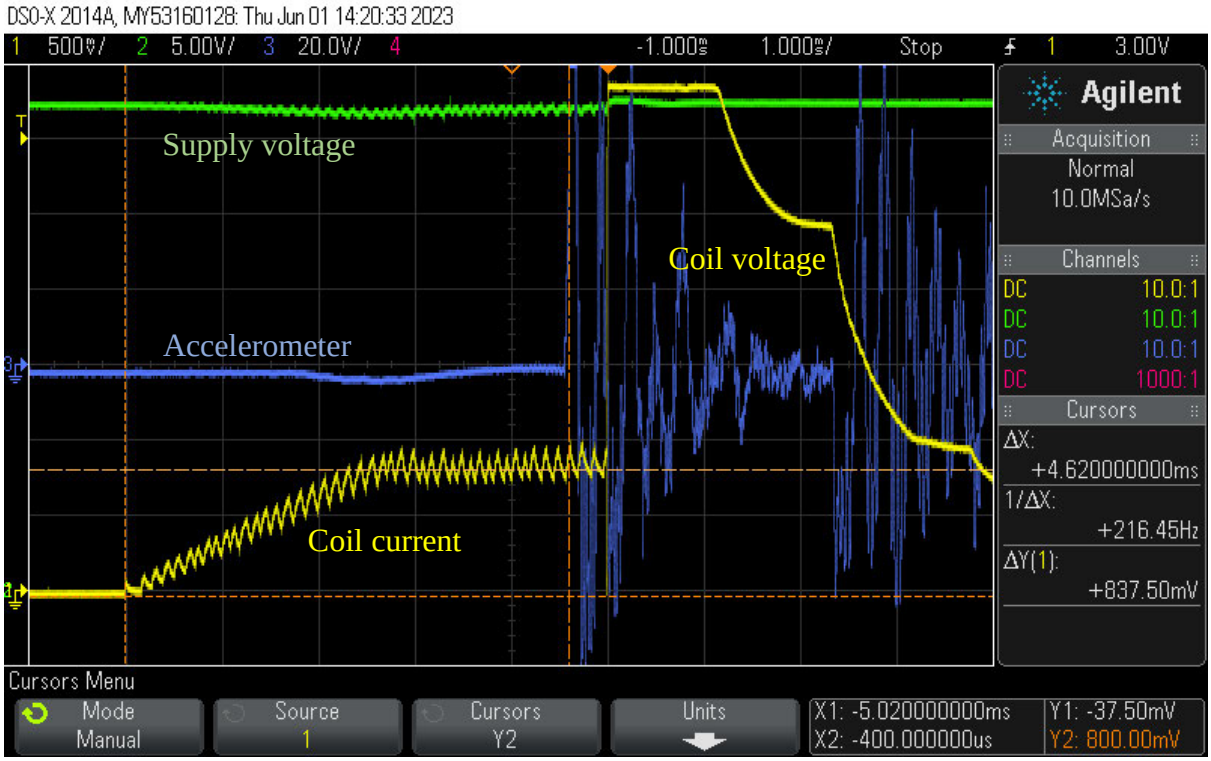

Figure 4.30. Linear current gradient control test results at added coil series resistor 0 Ohm and supply voltage 32 V. Green waveform – supply voltage, blue waveform – accelerometer signal, yellow waveform – NGCD board coil current/voltage sensing signal.

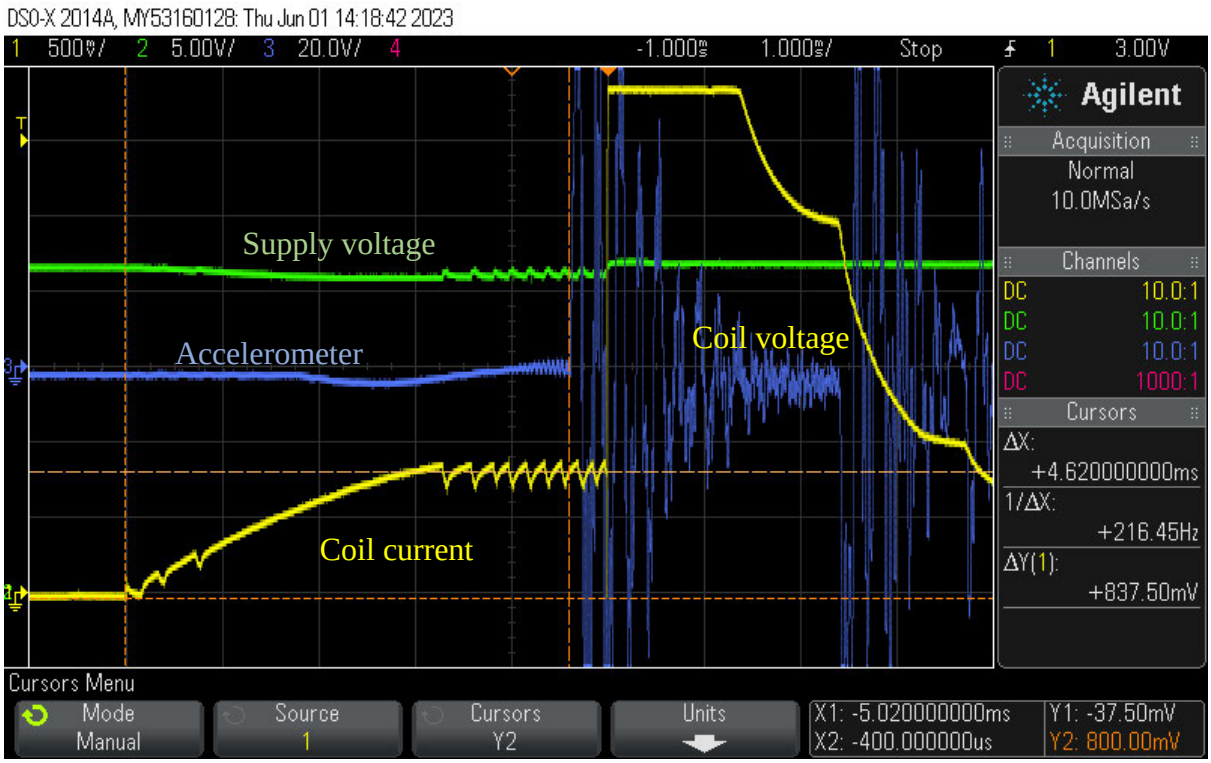

Figure 4.31. Linear current gradient control test results at added coil series resistor 0.68 Ohm and supply voltage 22 V. Green waveform – supply voltage, blue waveform – accelerometer signal, yellow waveform – NGCD board coil current/voltage sensing signal.

From the test results can be seen that the current controller operates as expected, keeping the coil current profile repeatable (constant) at each switching cycle and according to the pre-set parameters allowing almost complete saturation during the ramp phase at the minimum supply voltage and the maximum coil circuit resistance established for the test. The valve response time is constant within the voltage and resistance range established for the test and equal to 4.62 ms.

4.3.3.2 Power-law current gradient control test results

This section describes the test results of the power-law coil current gradient control at which the coil current profile was set to the following parameters:

- $T_{ramp} = 2.5\ ms$;
- $T_{peak} = 2.5\ ms$;
- $I_{peak} = 6\ A$;
- $a = 4$;

– $b = 3$.

Constants a and b define the convex grade of the ramp (see equation (35).

Figure 4.32 shows the oscilloscope readings during the test when the supply voltage was set to 32 V, and the coil circuit additional resistor is 0 Ohm. Figure 4.33 shows the oscilloscope readings during the test when the supply voltage was set to 22 V, and the coil circuit additional resistor is 0.68 Ohm. Figure 4.34 shows a sweep sampling in the voltage range 22-32 V with a 2 V step, the coil circuit additional resistor is 0 Ohm.

In all figures green waveform is the supply voltage, the blue waveform is the accelerometer signal, and the yellow waveform is the output signal of the NGCD board coil current/voltage sensing circuit.

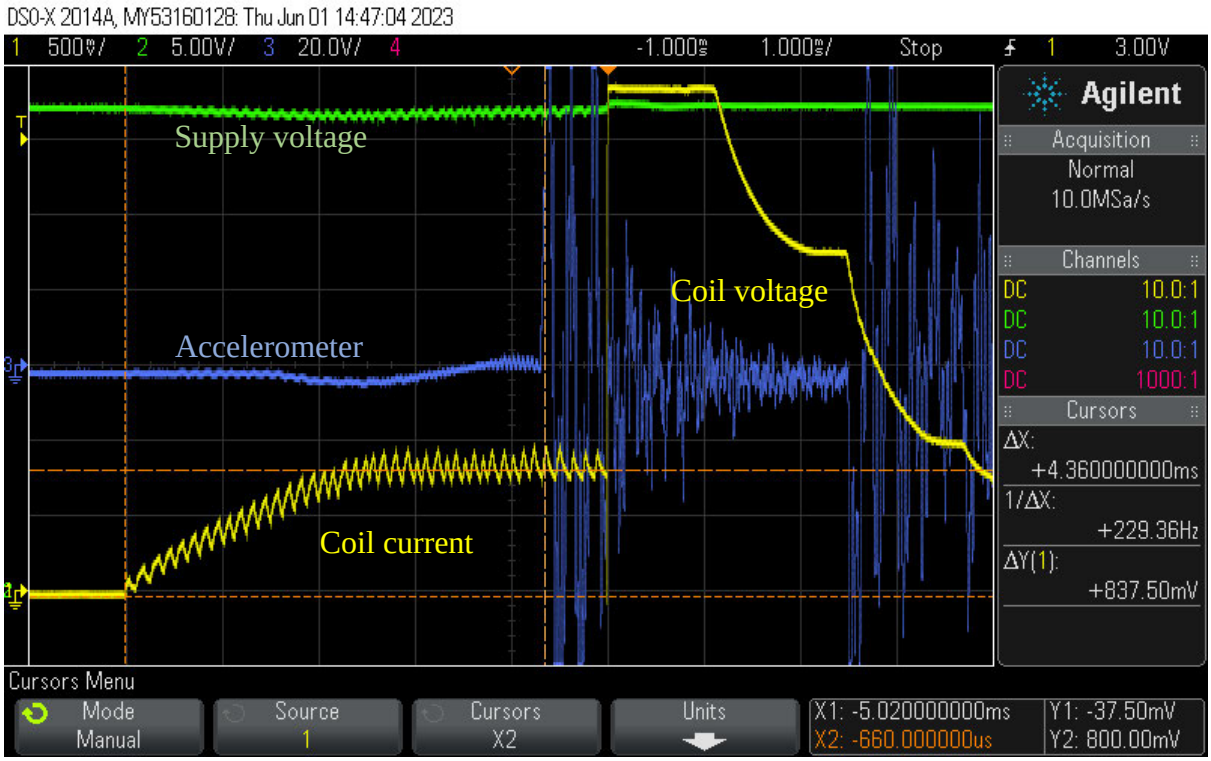

Figure 4.32. Power-law current gradient control test results at added coil series resistor 0 Ohm and supply voltage 32 V. Green waveform – supply voltage, blue waveform – accelerometer signal, yellow waveform – NGCD board coil current/voltage sensing signal.

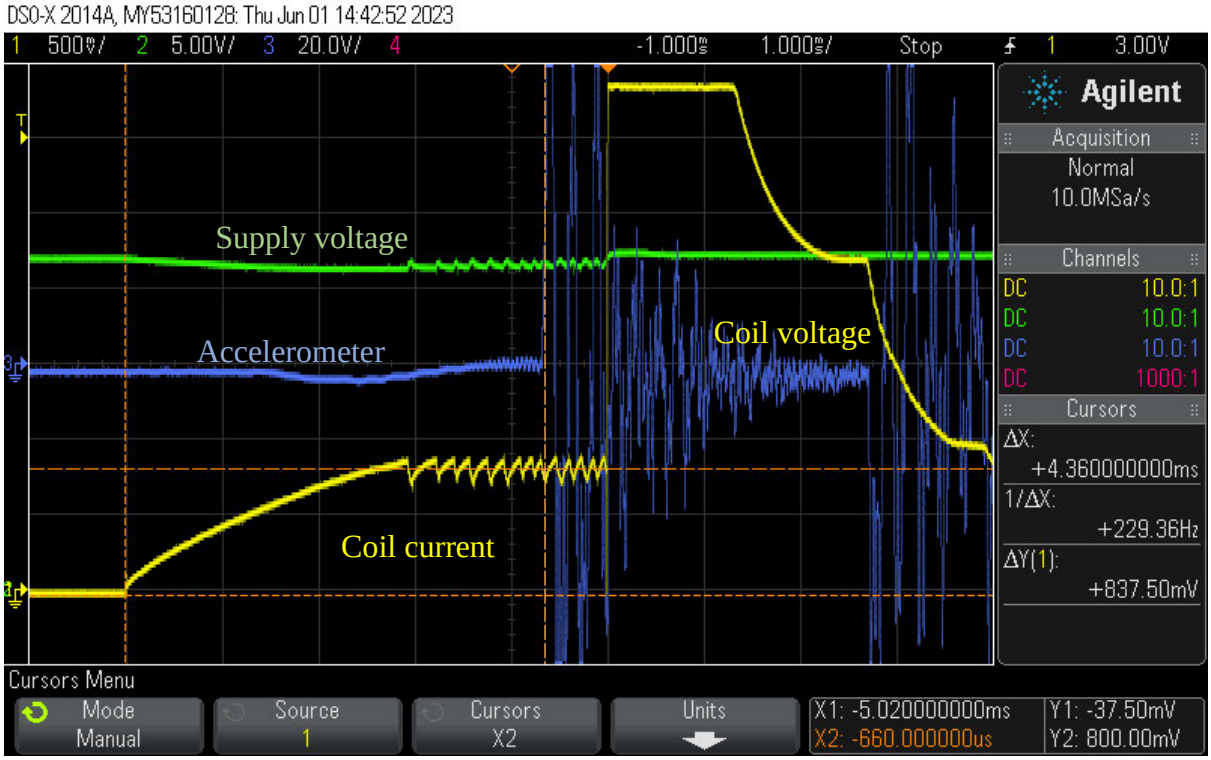

Figure 4.33. Power-law current gradient control test results at added coil series resistor 0.68 Ohm and supply voltage 22 V. Green waveform – supply voltage, blue waveform – accelerometer signal, yellow waveform – NGCD board coil current/voltage sensing signal.

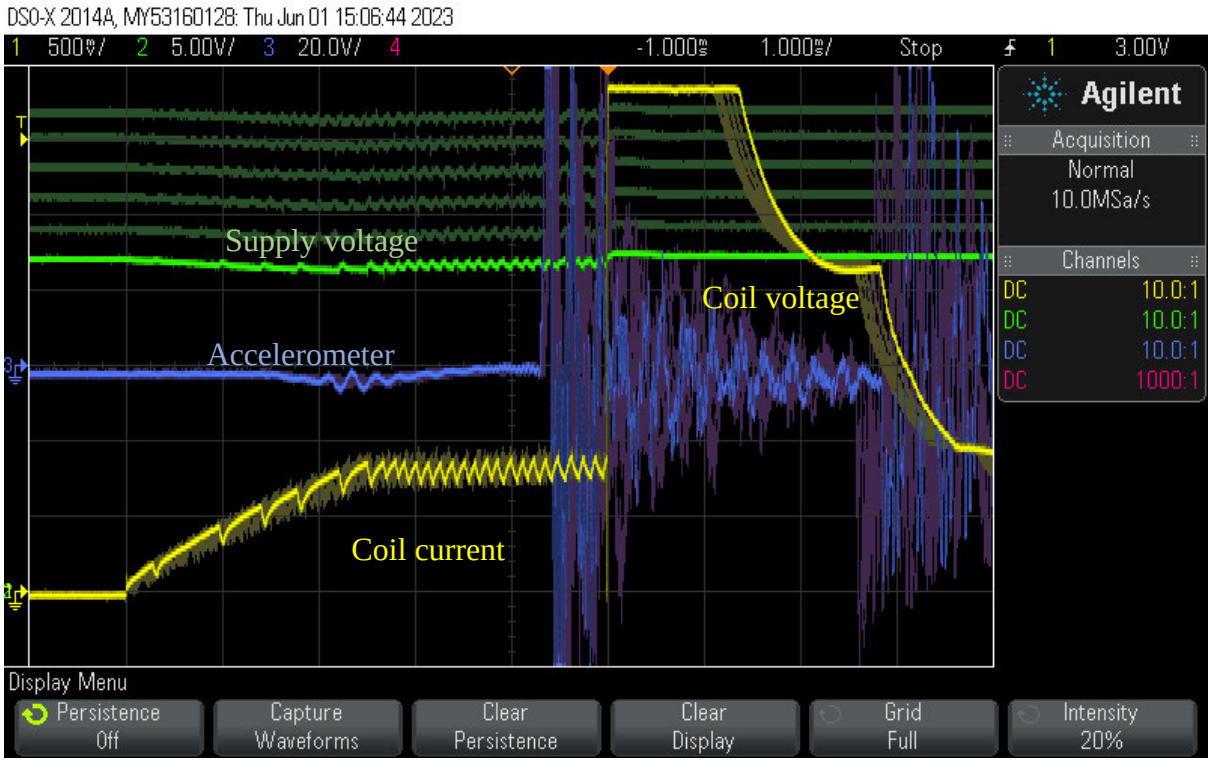

Figure 4.34. Power-law current gradient control test results, sweep sampling in the voltage range 22-32 V with 2 V step at 0 Ohm added series resistor. Green waveform – supply voltage, blue waveform – accelerometer signal, yellow waveform – NGCD board coil current/voltage sensing signal.

From the test results can be seen that the current controller operates as expected, keeping the coil current profile repeatable (constant) at each switching cycle and according to the pre-set parameters, allowing complete saturation during the ramp phase at the minimum supply voltage and the maximum coil circuit resistance established for the test. The valve response time is constant within the voltage and resistance range established for the test and equal to 4.36 ms, which is 5.6% faster that in the case of linear current gradient control. A faster response time allows for a decrease in the energising time of the valve, which might reduce the energy consumption of the controller.

Also, can be spotted a variation in the response time at the turn-off phase of the solenoid valve due to the voltage and resistance variation, which one more time proves the importance of developed in Chapter 3 the reliable back-EMF detection method that allows enabling of closed-loop reopening time optimisation at motoring of a DD machine.

4.3.3.3 Linear current gradient control with boost option test results

This section describes the test results of the linear coil current gradient control at which the coil current profile was set to the following parameters:

- $T_{ramp} = 2.5\ ms$;
- $T_{peak} = 2.5\ ms$;
- $I_{boost} = 1\ A$;
- $I_{peak} = 6\ A$.

Figure 4.35 shows the oscilloscope readings during the test when the supply voltage was set to 32 V, and the coil circuit additional resistor is 0 Ohm. Figure 4.36 shows the oscilloscope readings during the test when the supply voltage was set to 22 V, and the coil circuit additional resistor is 0.68 Ohm. Figure 4.37 shows a sweep sampling in the voltage range 22-32 V with a 2 V step, the coil circuit additional resistor is 0 Ohm.

In all figures green waveform is the supply voltage, the blue waveform is the accelerometer signal, and the yellow waveform is the output signal of the NGCD board coil current/voltage sensing circuit.

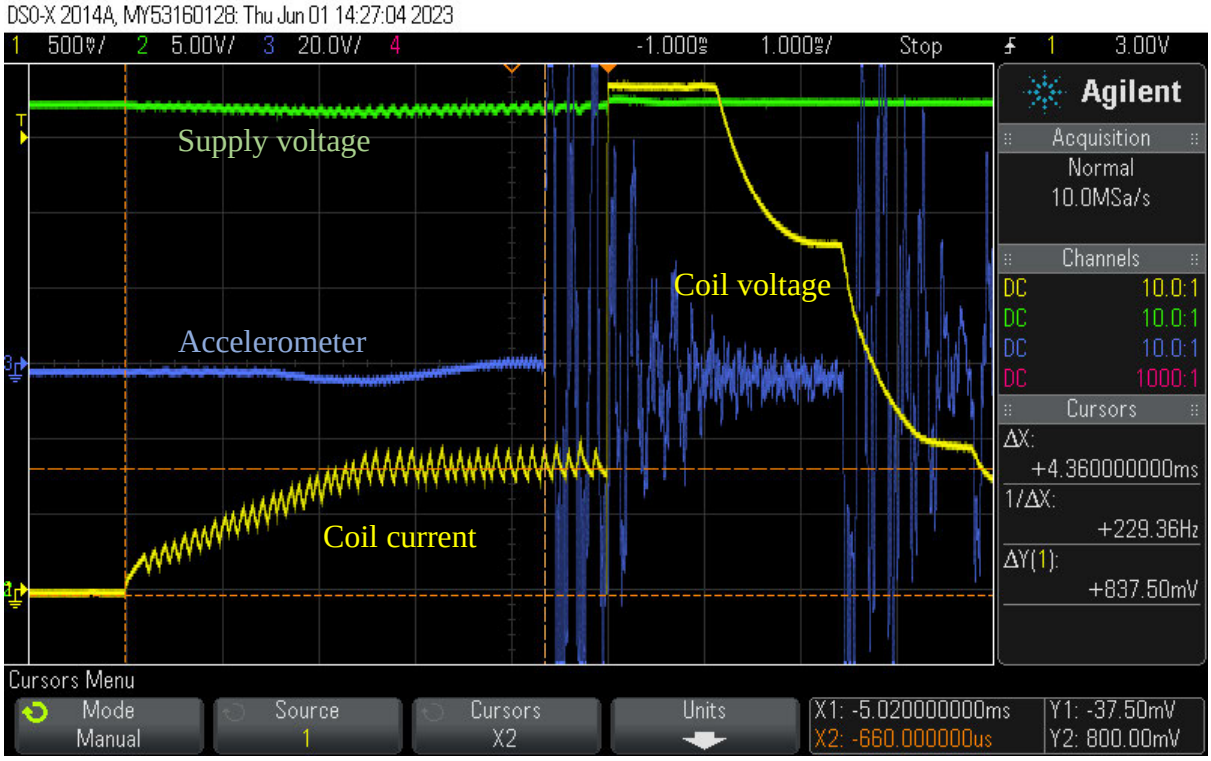

Figure 4.35. Linear current gradient control with boost option test results at added coil series resistor 0 Ohm and supply voltage 32 V. Green waveform – supply voltage, blue waveform – accelerometer signal, yellow waveform – NGCD board coil current/voltage sensing signal.

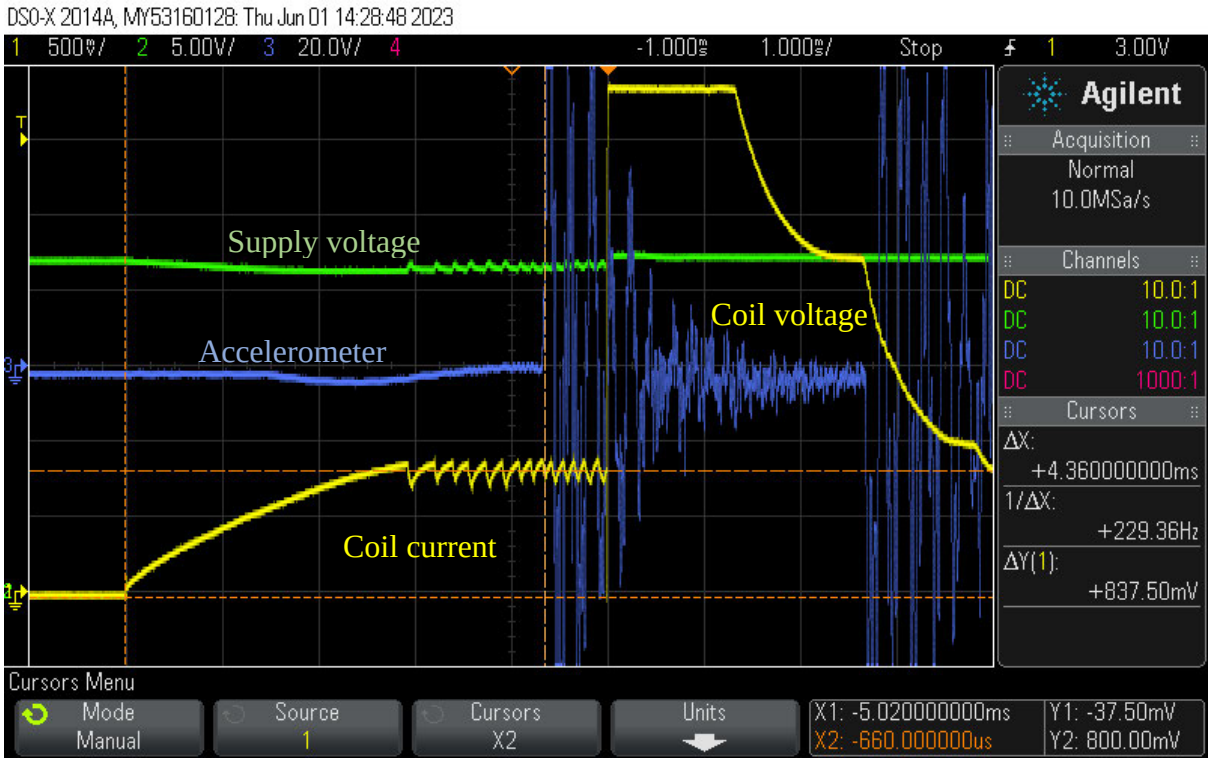

Figure 4.36. Linear current gradient control with boost option test results at added coil series resistor 0.68 Ohm and supply voltage 22 V. Green waveform – supply voltage, blue waveform – accelerometer signal, yellow waveform – NGCD board coil current/voltage sensing signal.

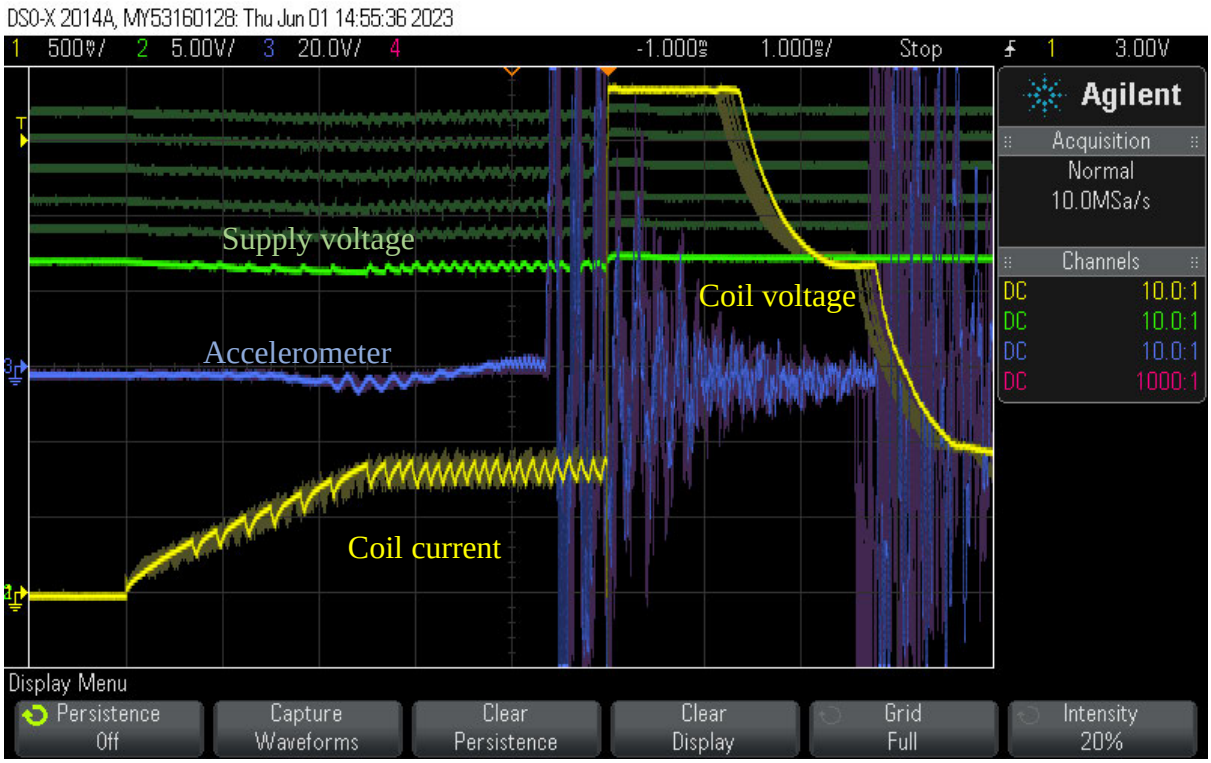

Figure 4.37. Linear current gradient control with boost option test results, sweep sampling in the voltage range 22-32 V with 2 V step at 0 Ohm added series resistor. Green waveform – supply voltage, blue waveform – accelerometer signal, yellow waveform – NGCD board coil current/voltage sensing signal.

From the test results can be seen that the current controller operates as expected, keeping the coil current profile repeatable (constant) at each switching cycle and according to the pre-set parameters, allowing complete saturation during the ramp phase at the minimum supply voltage and the maximum coil circuit resistance established for the test. The valve response time is the same as the case of the power-law current gradient control, which is equal to 4.36 ms.

4.3.3.4 DD valve control with vs without response time stabilisation

In order to compare to the actual open-loop control method of the DD valve, the firmware was developed similarly to one that is used in the present DD controllers. The method is based on limiting an excessive rise of current by applying a PWM technique during the peak and hold phase, the duty cycle of which must be defined prior to operating a DD machine (at the calibration phase of a DD valve, during the development process).

This section gives a comparison between the closed-loop control methods developed in this chapter and the actual open-loop control method of the DD valve. The coil current controller setup during the test was as follow:

- $T_{ramp} = 2.5\ ms$;
- $T_{peak} = 2.5\ ms$;
- $Duty\ Cycle_{ramp} = 100\%$;
- $Duty\ cycle_{peak} = 50\%$;
- $f_{PWM} = 10\ kHz$;

The purpose of the test was to define how the valve will respond to the supply voltage and solenoid coil resistance change when operating using the open-loop control method and then collate the results with the developed closed-loop gradient control methods to quantify potential improvements.

Figure 4.38 shows the test results between 0 Ohm and 0.68 Ohm of the coil circuit resistance that was applied at the constant voltage of 22 V. Figure 4.39 shows a sweep sampling in the voltage range 22-32 V with a 2 V step, the coil circuit additional resistor is 0 Ohm.

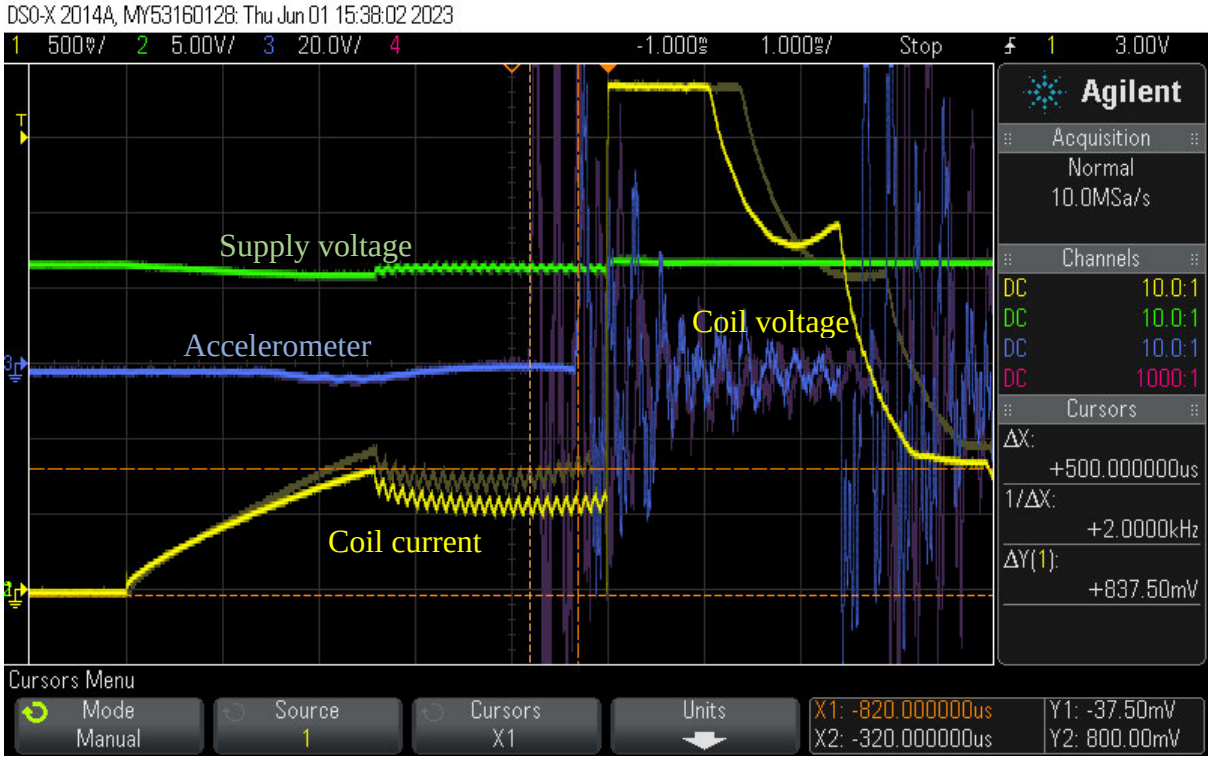

Figure 4.38. Open-loop control test results at supply voltage 22 V, 0 Ohm vs 0.68 Ohm added series resistor. Green waveform – supply voltage, blue waveform – accelerometer signal, yellow waveform – NGCD board coil current/voltage sensing signal.

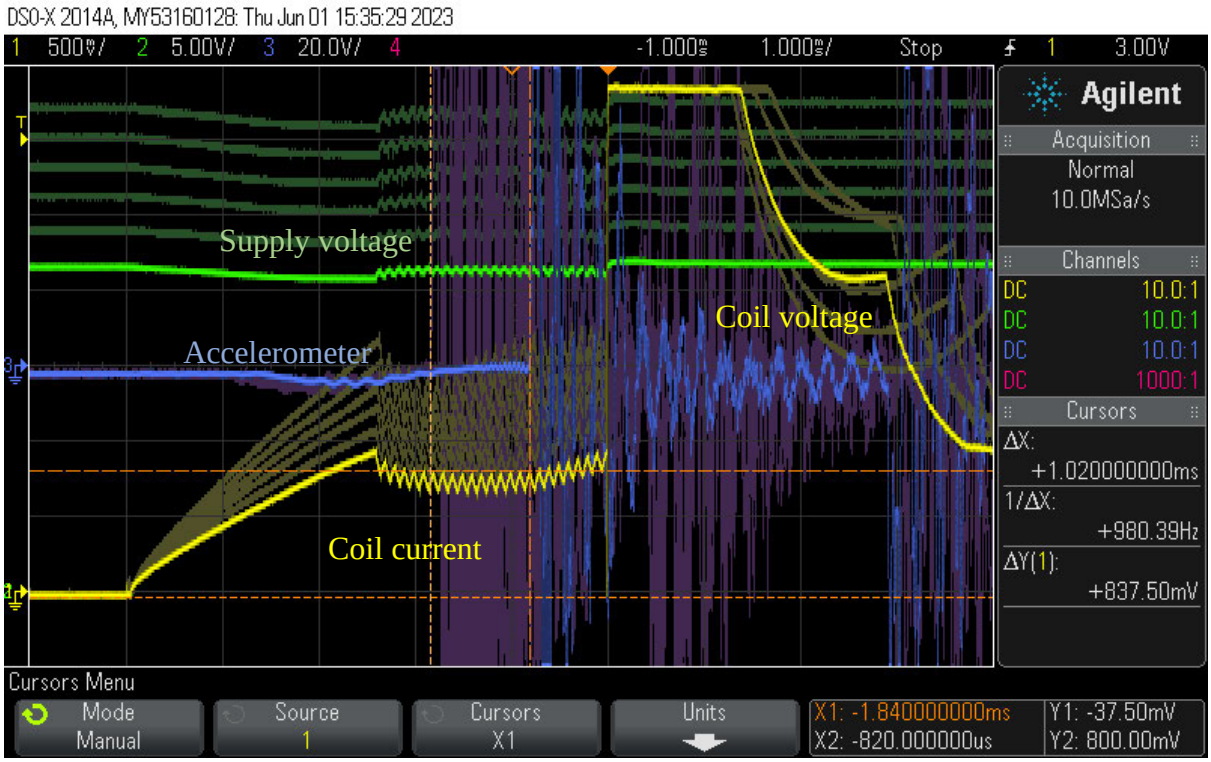

Figure 4.39. Open-loop control test results, sweep sampling in the voltage range 22-32 V with 2 V step at 0 Ohm added series resistor. Green waveform – supply voltage, blue waveform – accelerometer signal, yellow waveform – NGCD board coil current/voltage sensing signal.

As can be seen from the test results, the valve response time is significantly affected by the supply voltage and the coil circuit resistance. The supply voltage change in 10 V changes the valve response time by 1 ms, 24% of the maximum response time within the tested voltage range. However, if adding the 0.5 ms delay caused by resistance change within the established range, the full response time of the valve increases up to 4.7 ms, which increases the potential error of the valve response time up to 32% or 1.5 ms. This potential response time variation must be compensated by initiating the valve energising cycle in advance, which, according to [6], will cause a drop in displacement and efficiency of a DD machine and decrease its life cycle.

Table 4.3 summarises the test results of the developed in this chapter coil current gradient control technics and comparing them against the open-loop technic that is used in present DD controllers.

Table 4.3. Summary of the test results of the developed in this chapter coil current gradient control technics against the open-loop technic that is used in present DD controllers.

Controller	**Valve**	**Voltage range**	**Resistance range**	T_{ramp}	T_{peak}	I_{peak}	**Response time**
Linear	MAV8	22-32V	0-0.68Ohm	2.5ms	2.5ms	6A	4.62ms
Power-law	MAV8	22-32V	0-0.68Ohm	2.5ms	2.5ms	6A	4.36ms
Linear + boost	MAV8	22-32V	0-0.68Ohm	2.5ms	2.5ms	6A	4.36ms
Open-loop	MAV8	22-32V	0-0.68Ohm	2.5ms	2.5ms	13-5A	3.2-4.7ms

4.4 Summary and conclusions of the chapter

A new method based on coil current gradient control, which allows stabilising the response time of a cyclically operating solenoid valve at the turn-on phase, has been established in this chapter, thus reaching the third goal of this thesis.

A patent application for the invention has been filed.
Title: “Response time stabilisation (RTS) of cyclically operated valves”.
Application number: EP22168535.7.

A Simulink model was developed to prove the stable and correct operation of each algorithm before its implementation in VHDL. The developed VHDL code was integrated into the next-

generation coil driver (NGCD) board firmware and successfully tested by operating a single-coil DD valve PAV8 in the lab environment.

Experimentally was shown that applying the valve response time stabilisation method to DD valves allows for achieving its stable response time at each switching cycle within established ranges of the supply voltage and solenoid coil circuit resistance.

The developed closed-loop coil current gradient control algorithm based on a linear current reference generation equation with a boost option was approved to be integrated into the experimental and production firmware for DDC15 and DPC30 Digital Displacement controllers.

Chapter 5

Sensorless diagnostic of DD machine based on back-EMF signal

This chapter describes another invention (inventors: Peter McCurry, Christian Norgaard, **Andriy Tkachuk Volodymyrovych**), which is the outcome of this PhD work. The invention proposes a sensorless method for determining the conditions/abnormality of the DD machine before the shaft rotation. Also, a based on the invention algorithm for determining the low hydraulic liquid level of the DD machine is proposed.

The original idea of the invention belongs to Peter McCurry. My input to this invention consists in the development of practical methods of the invention and demonstration of its feasibility. Also, I was investigating the novelty of the invention and generating the invention report.

5.1 Introduction

It is vital to determine if the conditions of the DD machine meet/correspond to the safe operation requirements before the shaft starts rotating. Operation of the DD machine (i.e., rotating the shaft) under some conditions can permanently damage the machine. For example, DD machine running surfaces will become damaged quickly and the machine will fail quickly if the machine shaft is rotated without any oil or little oil within the crankcase volume (so-called 'dry running'). This can easily happen if the machine has been disconnected hydraulically, or is newly installed, or there is a hydraulic leakage in the system.

Cylinders can also fail to pump if they are airlocked – that or the oil level is low in a pump due to say a trapped air bubble inside the crankcase, thus, isolating valve(s) from oil. A machine that was not properly purged/bled during commissioning (when filling oil for the first time or refilling/replacing the oil) can suffer from a trapped air bubble inside the crankcase, thus, isolating some valves from oil.

5.1.1 Summary of the invention

The invention consists in determining an abnormality of the DD machine prior its operation, more specifically in terms of detecting:

– the physical state/condition of the fluid (e.g., abnormality being a high degree of oil aeration, presence of water/diesel/other contamination in the fluid), and/or

- the approximate fluid level within the crankcase (e.g., abnormality being low fluid level in the crankcase), and/or
- the functioning of individual valves (e.g., abnormality being the presence of air pockets in the crankcase around the valve, or broken valve, detached poppet, broken spring, etc.).

Each of these three detections is performed within individual cylinders, when the shaft is stationary, where comparing detections between cylinders, can provide/infer information on those cylinders as well as on other cylinders, and on the entire machine. Detection is done by analysing the response time and/or the amplitude of the back-EMF signal (can be voltage or current) in respect of individual cylinders. To deduce information on the entire machine, the analysis must take into account the spatial orientation and the proximity of the valves when triggering them before the shaft begins to spin.

5.2 Prior Art related to the invention

This section gives a list with a brief description of known engineering practice that relates to the ‘Sensorless diagnostic of DD machine based on back-EMF signal’.

Patent [77] "Method of measuring a property of entrained gas in a hydraulic fluid and fluid-working machine" from Artemis intelligent power Ltd, discloses a method of measuring a property of entrained gas in hydraulic liquid received by a working chamber of a fluid-working motor… The property is determined from the period of time elapsing between the closure of a first valve to isolate the working chamber and the passive opening of a second valve to bring the working chamber into fluid communication with a manifold. The shaft rotates during property determination, in contrast to the main embodiment of the present invention, requiring a static shaft.

Besides the rotating shaft, this method requires generating the hydraulic flow and pressure in order to open the second valve. None of these features is used in the present invention and cannot be used because the core of the present invention is to detect any abnormal condition of the DD machine before the shaft starts rotating thus avoiding its permanent damage due to such faults as low-level or absence of the hydraulic fluid. Using the method proposed in the above

prior art-doc will highly likely lead to permanent damage to the DD machine before the low level or absence of the hydraulic fluid will be detected.

Patent [78] "Speed control for diaphragm pump" discloses dry running detection. It apparently discloses using a running pump, i.e. a rotating shaft, in contrast to the present invention where the dry pump detection embodiment uses a stationary shaft. Furthermore, it relates to diaphragm pumps, rather than a radial-type pumps, and thus can't be applied to hydraulic DDP/DDM.

Patent [79] "Measuring hydraulic fluid pressure in a fluid working machine" discloses an invention that is very specific to guessing pressure. It is similar in the sense that it determines the physical characteristics of the system based on valve signature (reopening signal), however, it does not discuss determining the level of fill of the machine, oil condition, or the like and requires shaft rotation to function.

Patent [80] "Fluid working machine and method of operating a fluid working machine" discloses that if the valve inactivity test is met, then "…transmitting one or more additional actuator signals to the actuator of the said low-pressure valve, which additional actuator signals do not significantly change the net displacement of working fluid by the respective working chamber".

Thus, it discloses the idea of actuating LPV without a significant effect on the amount of fluid pumped.

More specifically it discloses "Preferably, the said low-pressure valve is closed and then opened again within 20%, 10%, 5%, 2.5% or 1% (72°, 36°, 18°, 9°, 3.6° of phase) of the period of a cycle of working chamber volume before bottom dead centre." Also, it discloses that "the one or more additional actuator signals are transmitted to the said actuator of a low-pressure valve, to cause the respective valve to open and then to close again while the respective working chamber remains sealed from the high-pressure manifold.".

However, it does not discuss the detection of 'valve not having its normal timing', and in contrast, requires a rotating shaft.

Patent [3] "Fluid-working machine valve timing" discloses amongst other things, the "ingress…of air" into the machine [para0009] changes the properties of the working fluid significantly and discusses the relation to potential cycle failure.

Both have relevance to the present invention because they deduce machine information from a back-EMF signal from LPV and are in that sense similarly sensorless. However, in relation to the dry valve detection embodiment of the present invention, both of the above in contrast require a rotating shaft.

Patent [81] "Fluid-working machine and methods of detecting a fault" discloses the idea of treating a working chamber as unavailable due to a detection of an associated fault.

Para[061] explicitly refers to fault detection for stationary shaft: “For example, the fault detection means may be configured to operate only when the shaft is stationary, when the fluid working machine is fluidically isolated from at least some work functions, when work functions have reached a certain condition such as an end stop, when a brake is applied, or when the fluid working machine is not operating at maximum capacity, and configured so as not to operate under any other conditions.”

Fault detection is disclosed including: “…a voltage or current sensor operable to measure one or more properties of the response of a valve associated with a working chamber to a control signal” and provides an output parameter.

However, this might be summarised as 'make a change, watch the system change' rather than the present invention of 'know the system characteristics/response and compare acquired data to the reference data', which is different.

A further difference is that the document does not disclose:

- diagnostics of the DD machine prior to starting or at stationary conditions.
- use of ‘spatial orientation’.
- proximity map of the valves of the DD machine.

Each of which of the above is required in the present invention.

5.3 Results

5.3.1 Invention description

5.3.1.1 Basics of the DD machine

Figure 5.1 shows a simplified schematic diagram of a DD machine that illustrates its basic principles of operation and Figure 5.2 shows a circuit diagram of a basic solenoid drive system. The DD machine comprises of at least one crankshaft (11), working chamber (10) with movable piston (9) and high- and low-pressure solenoid valve (8) that comprises at least an electromagnetically inductive coil (6) wound around a movable armature (7), a resetting/return spring (5), and a low-pressure poppet (4) that is physically attached to the armature, wherein the coil is electrically connected to an electronic controller that actively controls one or more said valves to determine the net displacement of fluid by the working chamber on a cycle-by-cycle basis.

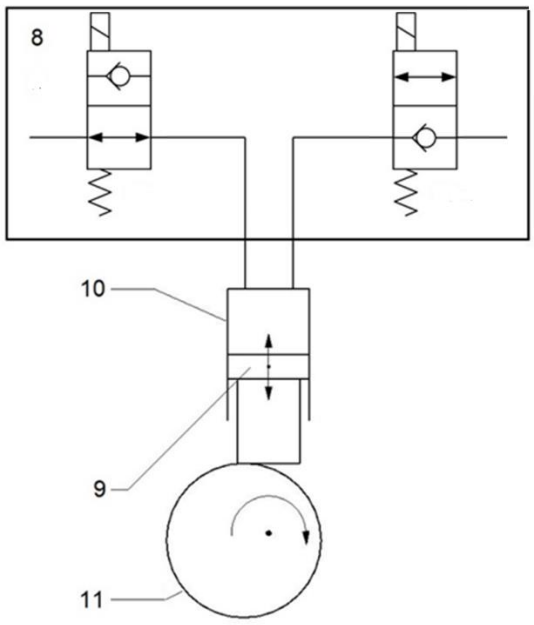

Figure 5.1. Simplified schematic diagram of a DD machine.

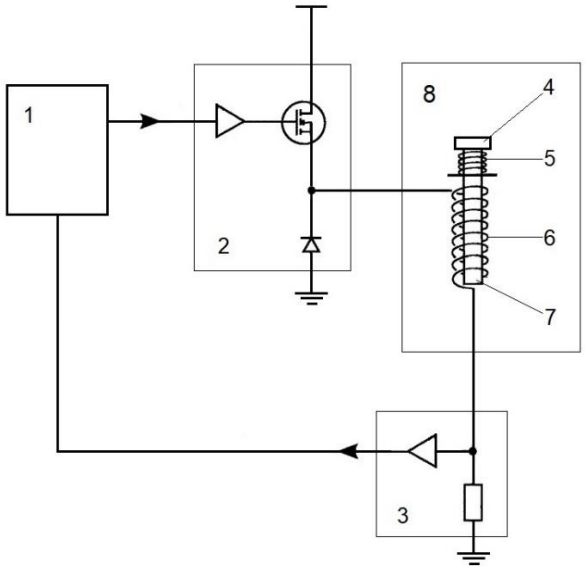

Figure 5.2. Circuit diagram of a basic solenoid drive system.

As shown in Figure 5.2, the controller for the DD machine comprises at least a coil driver circuit (2), a sensing circuit (3) that provides a feedback signal of coil current or voltage (or both) and allows to detect back-EMF signal generated by armature motion energising and/or de-energising stage, a CPU (1) that can be programmed at least to generate required signals for the coil driver circuit in order to energise or de-energise the solenoid valve and to compute the response time of the solenoid valve and/or the amplitude of the back-EMF signal induced during the reopening stage. The DD machine includes at least one solenoid valve (8), which comprises at least an electromagnetically inductive coil (6) wound around a movable armature (7), a resetting/return spring (5), and a low- or a high-pressure poppet (4) that is physically attached to the armature, wherein the coil is electrically connected to an electronic controller.

5.3.1.2 Response time and back-EMF signal infer characteristics of working fluid

The invention proposes a diagnostic method that allows determining/verifying if the conditions of the DD machine meet/correspond to the safe operation requirements. The test (or series of tests) may be performed at every start-up of the machine before the shaft starts rotating. Alternatively, the test may be performed at another frequency, or perhaps according to some other trigger.

For the diagnostics/test, the response time or/and the amplitude of the back-EMF signal generated by the armature motion at the energising or/and de-energising stage of the valve will be analysed considering 1) the map of spatial orientation, and 2) valve proximity of the valves within a DD machine.

The major benefit of the method is that it can be used to determine if the DD machine is full/empty or partially filled with hydraulic liquid before the shaft is commanded to rotate.

In the DD machine, when the low-pressure valve (LPV) is energised and the shaft is stationary, the armature and connected low-pressure poppet (LPP) will move towards a top end by means of the magnetic force, thus compressing the resetting/return spring. After the switch-off command is set, the solenoid magnetic field starts to decay, thus, decreasing the electromagnetic force, whilst the armature remains stationary (static phase). When solenoid magnetic force plus stiction force (that actuates onto the armature and physically attached to it LPP) is lower than the spring force, the armature will start to travel towards the bottom end (dynamic phase), this motion is inducing back-EMF in the solenoid coil. This period is defined as travel time and the peak of the back-EMF signal corresponds to the end of this period (i.e., corresponds to the time when the armature stopped its motion and the low-pressure valve become opened state). Forces developed by friction and eddy-making resistance as well as aerodynamic/hydrodynamic forces acting on the armature and the LPP during the motion, thus slowing down the armature velocity. The time between the switch-off command is set and the LPV becoming reopened is defined as the response time of the solenoid valve at the reopening (de-energising) stage (T_response in Figure 5.3).

If the energy transferred to the solenoid and the magnetic field decay setup is the same at each switching cycle, the valve response time and the amplitude of the back-EMF signal during reopening (de-energising) will vary proportionally with the following variables:

- the stiction force,
- aerodynamic/hydrodynamic forces,
- frictional forces,
- eddy-making resistance,

each of which forces may act on the armature and LPP during static and dynamic phases. These forces are predominantly defined by the physical characteristics of the medium the armature and LPP are travelling through. Therefore, the response time of the solenoid valve and the

amplitude of the back-EMF signal during the reopening (de-energising) stage will depend on the physical characteristics of the fluid which is drawn into the working chamber, during piston intake stroke (hydraulic liquid or air).

Thus, physical characteristics (e.g., viscosity, density) that influence the above-mentioned forces differ significantly between air and hydraulic fluid, and thus the response time and the amplitude of induced back-EMF signal during reopening (de-energising) will also significantly differ. The time/amplitude can thus be used for determining if the valve chamber is filled with air or hydraulic liquid.

Figure 5.3 shows an illustration of the coil current waveform of a solenoid valve filled with air (a) and filled with hydraulic liquid (b). Where is shown that the response time is smaller, and the amplitude of the back-EMF signal is larger when a solenoid valve is filled with air compared to when it is filled with hydraulic liquid.

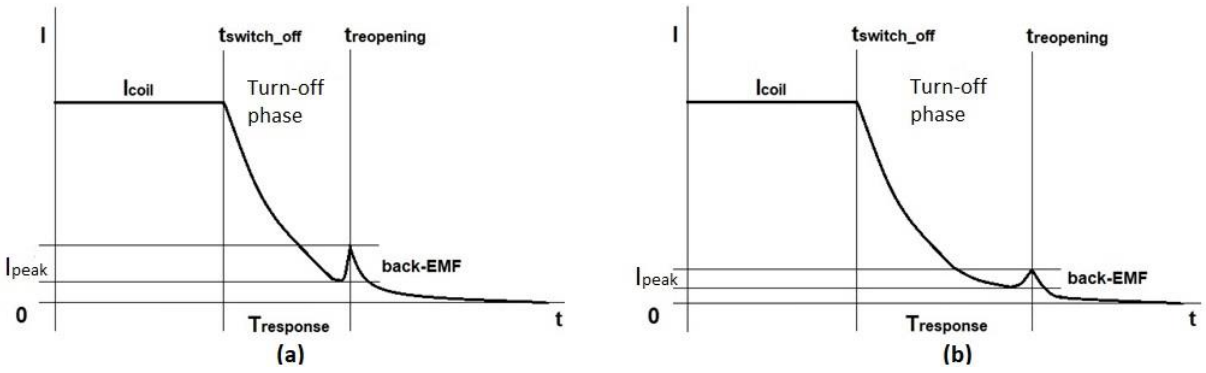

Figure 5.3. An illustration of the coil current waveform of a solenoid valve filled with air (a) and filled with hydraulic liquid (b). The response time is smaller, and the amplitude of the back-EMF signal is larger compared of (a) compared to (b).

5.3.1.3 Individual and group valve analysis, for special orientation and proximity

As it is shown in Figure 5.4, a DD machine contains valves that are evenly physically spaced in respect of the shaft axis, and which are submerged in a hydraulic fluid that fills the inner cavity of the DD machine body and the working chambers. Therefore, the information about spatial orientation and proximity of the valves that failed/passed the dry valve test is used to verify the false-positive. Once a false-positive is verified, and all other valves are confirmed 'good', this means the machine can be set to rotate, and further tests performed. If a false-positive is not confirmed this means that the valves are not submerged in the oil (are dry),

therefore the oil level of the crankcase is low, and the DD machine should not be started. The approximate oil level can be defined by spatial orientation and proximity analysis too.

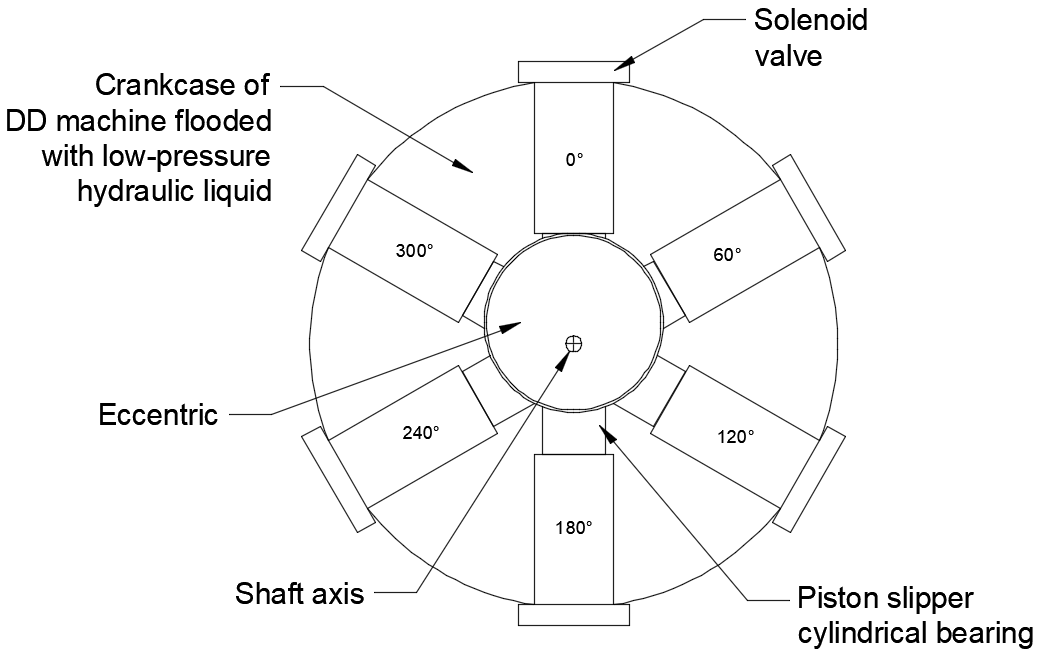

Figure 5.4. Schematic diagram of a DD® machine demonstrating the proximity and spatial orientation map of the solenoid valves.

Causes of the false positives include:

1) where the air is temporarily trapped adjacent to some part of the LPV, or
2) where a valve spring is perhaps broken, providing only partial spring force, or
3) the LPP can become detached from the plunger, etc.

So, even though the test potentially suggests a broken component, it still permits machine rotation (though subject to further specific tests, which hopefully will correctly identify the broken component, thus potentially disabling the corresponding valve/cylinder).

The ‘spatial orientation’ and the ‘proximity’ are analysed to determine the hydraulic liquid level in the inner cavity of the DD machine, and establish if the level is within the permitted range (i.e. suitable for starting the machine and operating normally).

Example 1:

If the valve with orientation of 60° (Figure 5.4) failed the dry valve test, but two neighbouring valves (with orientation of 0° and 120°) have passed the dry valve test, then the 60° valve is

highly likely has failed the dry valve test due to an air bubble inside the valve (or other causes that are listed above). Therefore, it can be marked as false-positive and is then ignored during the stationary testing of the present invention, and it is then suggested as a subject for further tests when the shaft is spinning during the machine is pumping or idling.

Example 2:

If the valves at 60°, 0°, and 300° have failed the dry valve test while the valves at 120°, 180°, and 240° have passed the dry valve test then it is highly likely that the hydraulic liquid level in the inner cavity of the DD machine low and it is below valves at 60° and 300° but above valves at 240° and 120°.

5.3.1.4 Proposed test & analysis steps to determine a low hydraulic fluid level of the DD machine

The procedure of the diagnostics is based on the following test and analysis:

1) Click test: to trigger all the LPVs of the DD machine before the shaft starts rotating for measuring and comparing to the reference the response time of each solenoid valve or/and the amplitude of the back-EMF signal generated by the armature motion at the energising or/and de-energising stage. Thus, detecting abnormal behaviour of the solenoid valves.

2) Proximity analysis: determine if those valves that fail the click test are ones which are directly adjacent to one another or not. If one solo, with good on either side, this means this is a local problem with the valve (this is a false positive detection). If two or more are adjacent, this means that the group of valves are true positive detections, thus indicating a macro issue (like a partially fluid-filled crankcase).

3) Spatial orientation analysis: To determine the spatial orientation (i.e., where the valve is in the machine) of the valves that failed the click test and the proximity analysis, defining where the failed valves are located (and thus their orientation), in respect to the shaft position. This allows us to confirm if the cause of the abnormal behaviour of the valves, is due to a problem with the whole machine (e.g., the crankcase oil level, where the special orientation analysis allows determination of the crankcase level), or

a problem which is a local issue around a specific valve (e.g., air bubble in/around that valve, spring break on that valve, etc).

Figure 5.5 shows a flow chart of an algorithm example that represents the present invention, which can be used for detecting a low hydraulic fluid level in the DD machine from Figure 5.4**.**

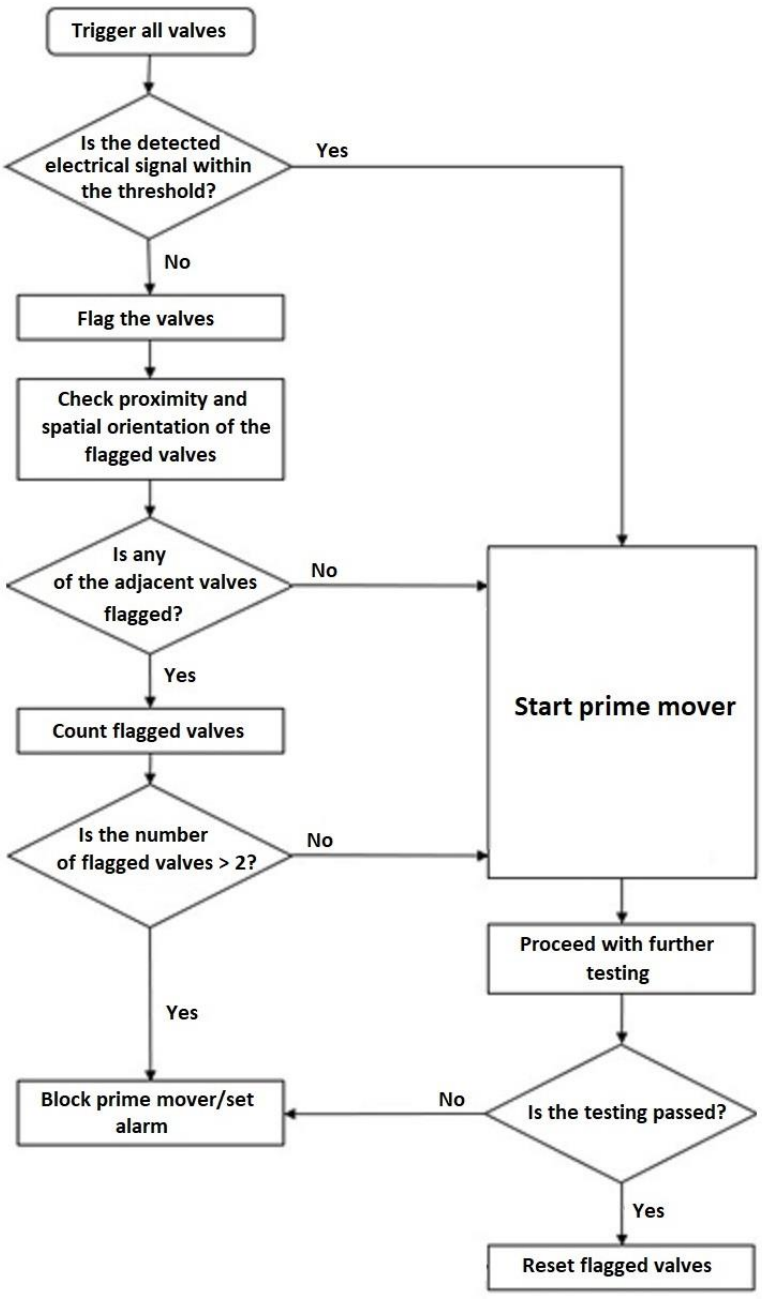

Figure 5.5. Flow chart of an algorithm example that represents the present invention, which can be used for detecting a low hydraulic fluid level in the DD machine from Figure 5.4.

5.3.2 Test results of the dry valve detection method

A bench test was run to determine if the implementation of the invention is feasible. During the test, the next-generation coil driver (NGCD) prototype board was used to switch a DD valve PAV8 in the air and oil of 32cSt kinematic viscosity, at different supply voltages and resistances established as potential real-life conditions for an automotive application.

The 22-32 V supply voltage range (see Table 4.2, code G, section 4.3.2) was assumed to be appropriate for a 24 V DD automotive application nominal operation conditions. The real-life dry valve detection test must be run before the shaft starts to rotate, which means the DD machine will be supplied from the battery, the voltage of which is assumed to be in the range of 22-26 V for the 24 V system. The temperature of the solenoid coil and cables will be equal to the ambient temperature, which is assumed to be from -20°C to +40°C. This temperature range and potential variation of 15 AWG coil cables length between 2m and 10m give around 0.27 Ohm of the potential solenoid coil circuit resistance variation.

As was shown in previous chapters, the time of the solenoid valve turn-off phase depends on the voltage applied across the coil at the fast-decay mode. The established supply voltage range of 22-32 V will introduce significant errors in dry valve detection when the solenoid response time during the turn-off phase is used as the reference. Therefore, (since the coil circuit resistance variation is relatively small and will not affect the current decay significantly) it was decided to decay most of the residual coil current using a slow-decay mode during 2.5 ms (until the "hold" current value) and then switch into the fast-decay mode, which will be the reference point of initiation of the solenoid valve turn-off phase. The time that corresponds to the peak of the back-EMF signal marks the end of the turn-off phase. During the test, the time of the solenoid valve turn-off phase and the amplitude of the back-EMF signal were measured.

The test coil current profile was as follows:

- $T_{ramp} = 2.5\ ms$;
- $T_{peak} = 3\ ms$;
- $T_{hold} = 2.5\ ms$;
- $I_{boost} = 1\ A$;
- $I_{peak} = 6\ A$.
- $I_{hold} = 2.5\ A$.

Figure 5.6 shows test results of PAV8 switching in the air at supply voltage 22 V and 32 V, and at solenoid coil added resistance 0 Ohm and 0.27 Ohm. Figure 5.7 shows test results of PAV8 switching in oil at supply voltage 22 V and 32 V, and at solenoid coil added resistance 0 Ohm and 0.27 Ohm. Figure 5.8 shows test results of PAV8 switched in the air against switched in oil at 24 V supply voltage, 0 Ohm solenoid coil added resistance at an ambient temperature of 20°C.

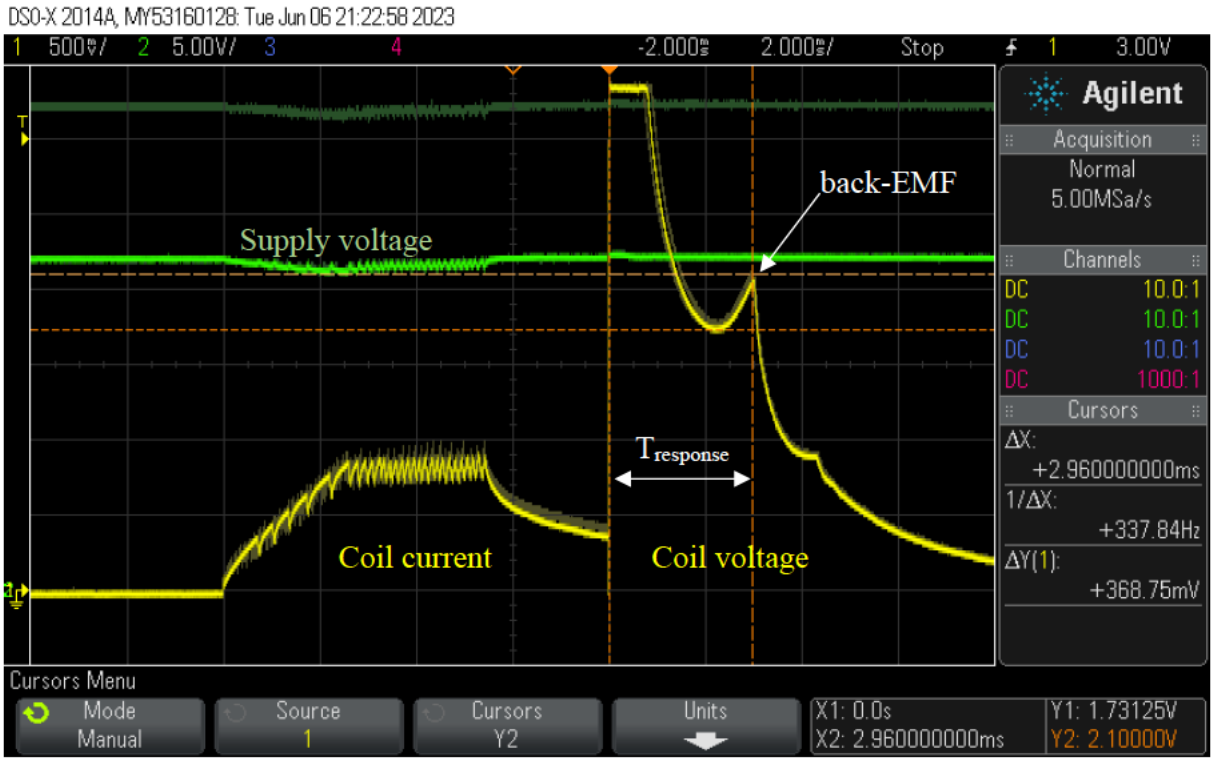

Figure 5.6. Bench test results of PAV8 switching in the air at different conditions: at supply voltage 2 2V and 32V, and at solenoid coil added resistance 0 Ohm and 0.27 Ohm (32 cSt oil at ambient temperature of 20°C). Green waveform – supply voltage, yellow waveform – coil current/voltage sensing circuit output.

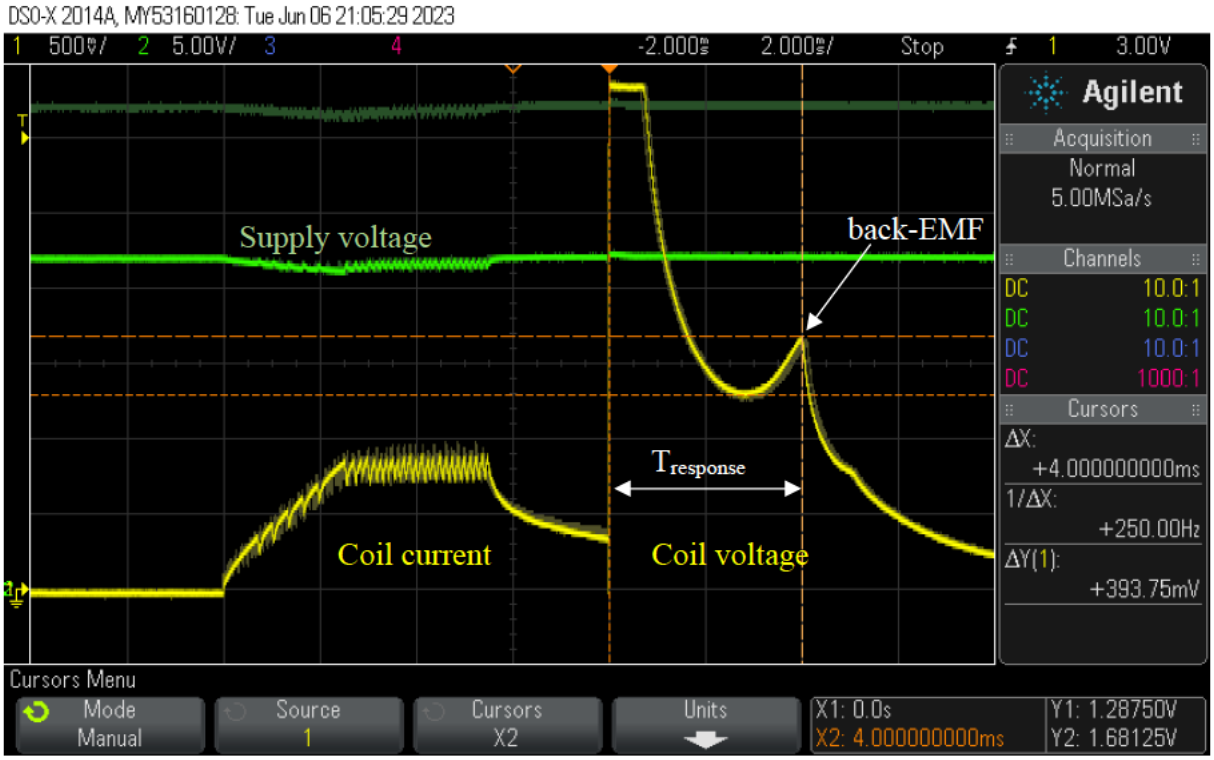

Figure 5.7. Bench test results of PAV8 switching in hydraulic oil at different conditions: at supply voltage 22 V and 32 V, and at solenoid coil added resistance 0 Ohm and 0.27 Ohm (32 cSt oil at ambient temperature of 20°C). Green waveform – supply voltage, yellow waveform – coil current/voltage sensing circuit output.

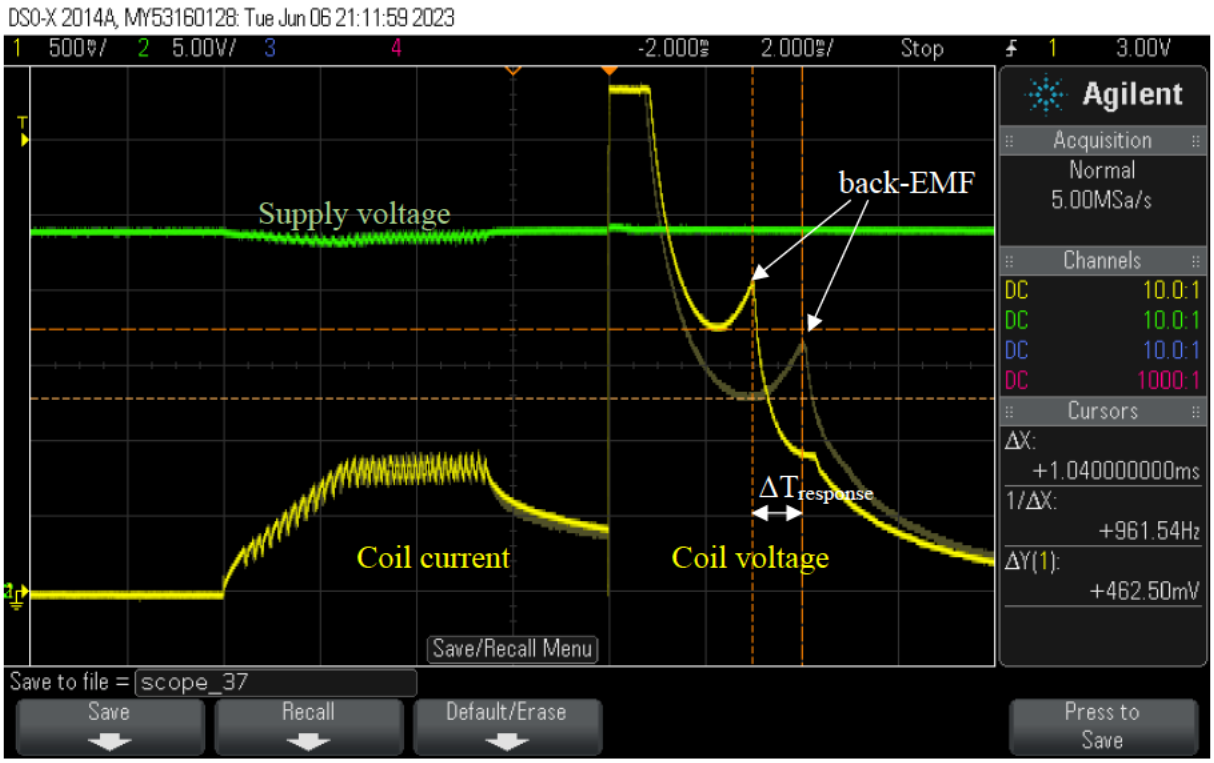

Figure 5.8. Bench test results of PAV8 switched in the air (yellow bright waveform) against switched in oil (yellow shadowed waveform) at 24 V supply voltage, 0 Ohm solenoid coil added resistance, 32 cSt oil at ambient temperature of 20°C. Green waveform – supply voltage, yellow waveform – coil current/voltage sensing circuit output.

As can be seen from the test results, during the turn-off phase, the response time of the solenoid valve and the amplitude of the back-EMF signal are not affected significantly by the supply voltage or solenoid series resistance. However, the response time ($T_{response}$) increases from 2.96 ms up to 4 ms when changing the environment of operation of the valve from air to oil, marking a difference ($\Delta T_{response}$) of 1.04 ms or 35%, which can be reliably detected.

The amplitude of the back-EMF is large by 14.2% when the valve is operating in oil (338 mV against 394 mV), which is not as expected (it was expected vice versa). However, the travel time of the poppet is larger in the case when operating the valve in oil than in air, which is due to the larger viscosity of the oil as was explained previously. Therefore, the speed of the poppet that travels through the oil is slower, which was expected.

The larger amplitude of the bac-EMF can be due to the lower residual current of the solenoid coil that opposes the back-EMF current, induced by the plunger motion through the solenoid coil. The plunger starts moving later due to the larger stiction forces caused by oil, thus, allowing the coil residual currents to decay more, compared to when the plunger is operated in the air.

Thus, it can be concluded that dry valve detection by comparing the valve response time ($\Delta T_{response}$) to the established reference is feasible.

5.4 Summary and conclusions of the chapter

A new method based on the low-pressure valve reopening back-EMF signal parameters that allows providing diagnostics of the Digital Displacement (DD) machine before its operation has been established in this chapter, thus reaching the fourth goal of this thesis.

A patent application for the invention has been filed.
Title: “Sensorless diagnostic of DD machine based on back-EMF signal”.
Application number: EP22187973.7.

The method can be used to determine if the DD machine can be safely started or/and suggest a particular valve as one in need of further testing during operation.

As an example, it was shown how to use this method for detecting an approximate hydraulic liquid level of the DD machine. If the hydraulic liquid level is defined below the minimum threshold, the DD machine will be defined as empty or partially filled and an action to prevent

damage to the DD machine will be taken (e.g., prohibiting a prime mover from rotation(‘blocking’), and/or setting an alarm).

Also, this method can be useful during the commissioning or servicing DD machine (i.e., during which processes, the machine may be filled, or refilled with oil), and if the controller indicates a dry valve to be detected, it will be suggested to purge/bleed the machine and repeat the test to confirm if the air pocket has disappeared.

The feasibility of implementation of the method was proven experimentally. The test results show the difference in turn-off response time to be 35% between valve clicking in oil and air, which can be reliably detected.

Chapter 6

Systems integration

This chapter describes the test results that demonstrate significant improvement of the DD technology achieved by implementing the developed next-generation valve actuation design in the 15-channel DD controller DDC15 designed to control a new DD pump/motor DDP1X0.

6.1 Prior art

6.1.1 DDP1X0 test rig setup overview

DDP1X0 is a new Digital Displacement (DD) pump/motor family of larger displacement with energy recovery capabilities currently developed by Danfoss Power Solutions. The DDP1X0 pump family consists of two primary models: the 15-cylindered Single pump/motor DDP1X0S and the 30-cylindered Double pump/motor DDP1X0D, specifically designed for excavators. The 'S' stays for a single and 'D' for a double pump arrangement, and the 'X' refers to the displacement options. Each DD module has 8-12 cc/rev geometric displacement, which enables total displacements of 120-180 cc/rev for a single pump and 240-360 cc/rev for a double pump. The DDP1X0 is successfully controlled by two 15-channel Digital Displacement® prototype controllers DDC15_01B configured for “master-slave” operation, which precisely deliver the current pulses needed by mechatronic valves to perform their intended operating cycles at the minimum losses. The next-generation valve actuation design, developed in this PhD project, is used in the DDC15_01B controller.

Currently, the system under test is a double DD pump/motor, DDP150D, with geometrical displacement up to 300 cc/rev (2x 150 cc/rev), which is designed to be the first commercial hydraulic pump/motor to be evolved in excavator systems of various sizes where the motoring cycle of the DD machine is used to recover the hydraulic energy. The system under test is designed to convert direct current electrical power to hydraulic power. The source power comes from an active front end, which acts as a constant 700 VDC voltage source simulating a battery setup in an electric excavator. The 700 VDC voltage source powers the Editron PMI375-T800 permanent magnet electric motor controlled by the Editron DUAL DC/AC inverter set (EC-C1200-450-L-SW11+MC350+CG1). The delivered continuous power is 154 kW with a 96% peak efficiency [2]. The DDP150D is installed on one end, and a tandem pump DDP096T (2x

96 cc/rev) is installed at the other end of the electric motor to provide a source flow for DDP150D when operating in motoring mode. Two 10 L high-pressure accumulators are used to store the pumped hydraulic energy, which can be recovered to the grid through the motoring and generator function of the DDP150D and the Editron electric motor and converter, respectively. The oil that is used in the rig is VG 46.

Figure 6.1 shows a simplified circuit diagram used for the steady-state efficiency mapping test, the dynamic energy recovery test, and the hydraulic transformation test within the DDP150D pump. To determine the efficiency of the system, the hydraulic power is measured at point *P*1, the mechanical rotational power is measured at point *P*2, and electrical power is measured at point *P*3. The full description of the tests can be found in [2]. Figure 6.2 shows a photograph of the test rig layout marking the key components, and Figure 6.3 shows the test rig control room where the DDC15_01B controllers are installed.

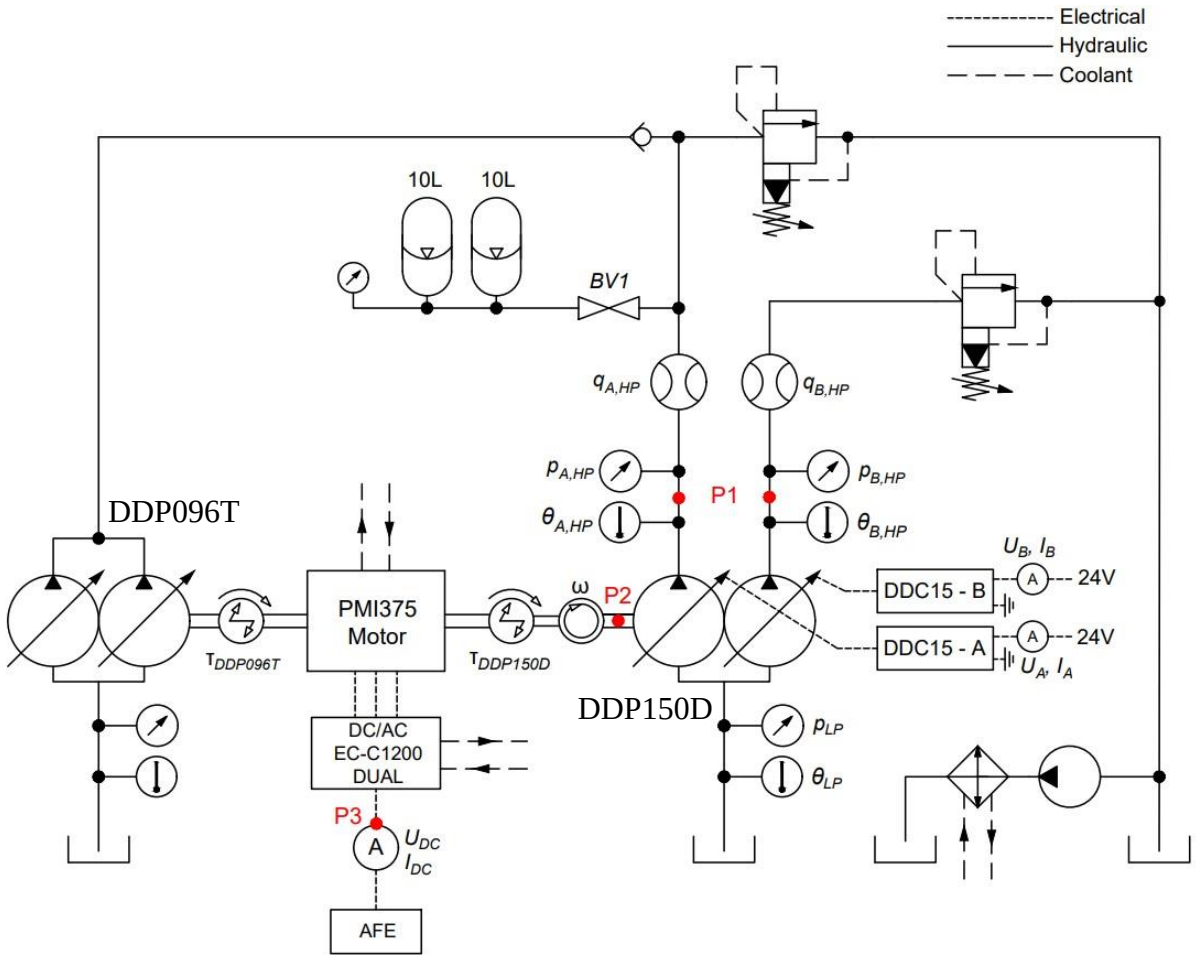

Figure 6.1. Simplified circuit diagram of the test rig setup [2].

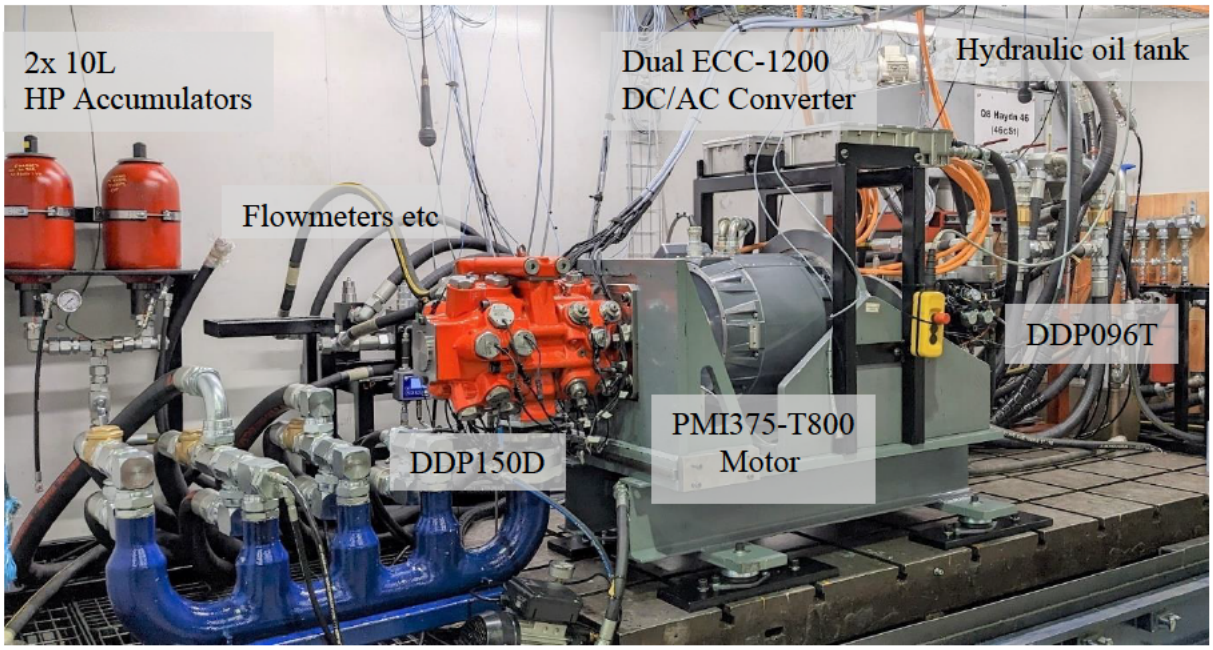

Figure 6.2. Photograph showing the inside of the test rig.

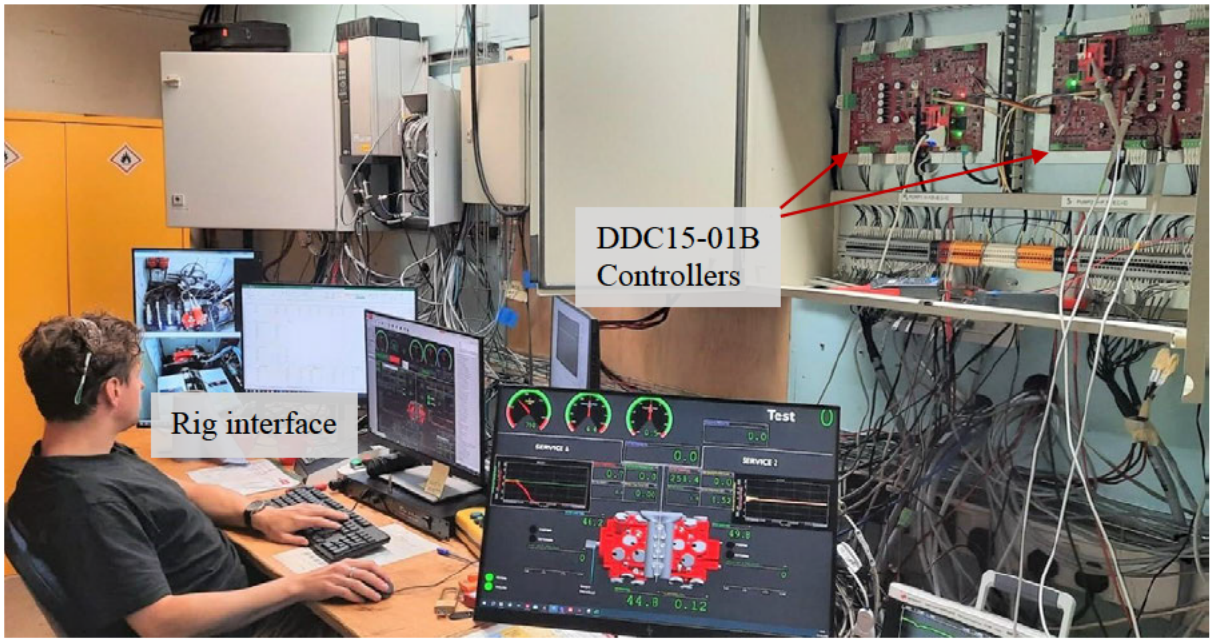

Figure 6.3. Test-rig control room photograph.

6.2 Results

6.2.1 15-channel Digital Displacement® controller (DDC15) overview

The Digital Displacement Controller DDC15 is a purpose-built electronic control unit for Danfoss' range of digital hydraulic machines. Its primary function is to control the high-speed solenoid valves at the heart of these machines to generate the required output flow and pressure.

The DDC15 controller was developed within two iterations especially designed to operate the DDP1X0 machine. The first iteration controller (DDC15_01A) is of industrial-only use allowing up to 1kW nominal load (power consumed by the valves of the DD machine) and 400 kHz SPI clock frequency. The second iteration controller (DDC15_01B) was developed for industrial and automotive use with up to 1kW nominal load and 800 kHz SPI clock frequency. The power electronic design (1st and 2nd iterations), high-speed signals routing supervision (2nd iteration), valve control algorithms development, their VHDL implementation and integration into the existing firmware (1st and 2nd iterations), development of the manufacturing documentation (1st and 2nd iterations), heat sink design and enclosure design supervision (1st and 2nd iterations), and commissioning (1st and 2nd iterations) were my direct contribution to the DDC15 controller development.

The DDC15_01A/B controller supports up to 15 DD valve output channels, but up to 30 channels are supported in a "master-slave" configuration. It has a range of inputs for sensors (e.g., speed, temperature, pressure) and features self-diagnostic capability. It supports CAN, RS232 and RS485 communication.

Figure 6.4 shows a functional block diagram of the DDC15_01B controller.

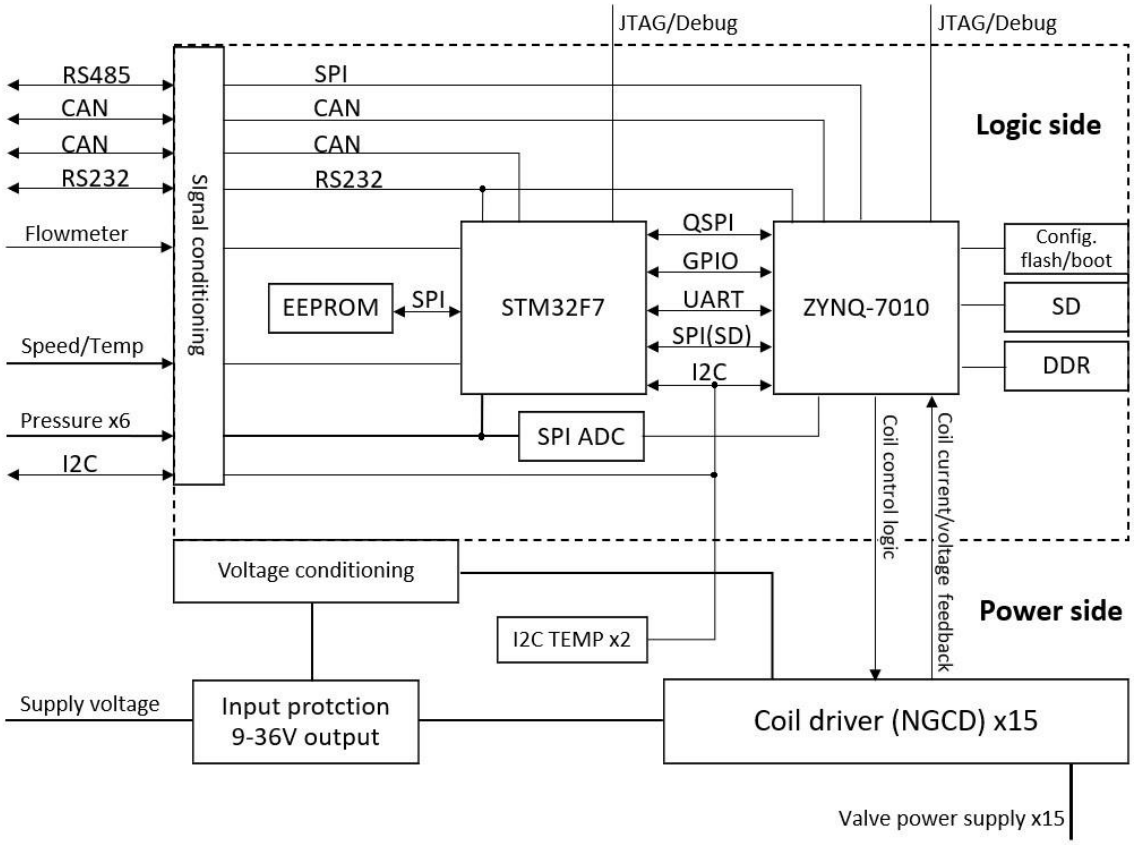

Figure 6.4. DDC15_01B functional block diagram.

The DDC15_01B controller is intended to be installed in off-highway mobile applications for prototyping purposes and in the Danfoss test rigs for DDPM testing purposes. It is designed to operate from a 24 V power supply, including 24 V automotive systems within the 9-36 V operating voltage range, enabling 100% of DDP1X0 features in the voltage range of 18-36 V. The power supply input protection circuit is based on LTC4368IMS-1, which is a -40 V to 100 V active surge suppressor integrated circuit (IC), which with the front end V20E23P 36 V varistor, provides complete protection at automotive transients specified in ISO 7637-2 and ISO 16750-2. The 15-channel coil driver circuitry is based on the next-generation coil driver (NGCD) design including the coil current/voltage monitoring circuit. The NGCD circuit was further improved according to the suggestions specified in the conclusions section of Chapter 2 . The voltage conditioning circuit provides a set of voltages (1.0 V, 1.8 V, 3.0 V, 3.3 V, 10 V and 15 V) and sequencing required for the digital and analogue circuits of the controller.

Two I2C temperature sensors are installed at the top and bottom layer of the circuit printed board (PCB) in the expected hottest spots of the controller, thus, providing general overtemperature protection of the controller.

The logic design comprises following modules.

Processing:

- STM32F765II (Application software, DD core)
- Zynq 7010 + DDR (firmware and diagnostics)
- SPI ADC
- QSPI, CAN, UART, GPIO between STM32 and Zynq

Storage:

- 128MB DDR2 memory (enhanced diagnostics)
- Micro SD card (storage of parameters, operating history, software update)
- 256 kB EEPROM memory

Communication:

- CAN
- RS232
- RS485 (“mater-slave” communication)

Inputs:

- Speed and temperature sensor
- Flowmeter
- 6x pressure sensors

Figure 6.5 shows the photograph of the DDC15_01B with the layout guidance. The PCB design is split between logic and power sides, where the power side of the board does not contain components on the bottom layer. This is done to increase the contact area of the board with the heat sink that will be placed directly under the power circuity of the board, thus, minimising the thermal resistance between the hot spots of the board and the heat sink. The power supply input (with input protection circuit and bulk capacitors) is placed in the centre of the board surrounded by the coil driver circuity, which was done to distribute the current across the board, thus, spreading the heat evenly. Most of the connectors are placed on the peripheral/perimeter of the PCB, which facilitates the wiring.

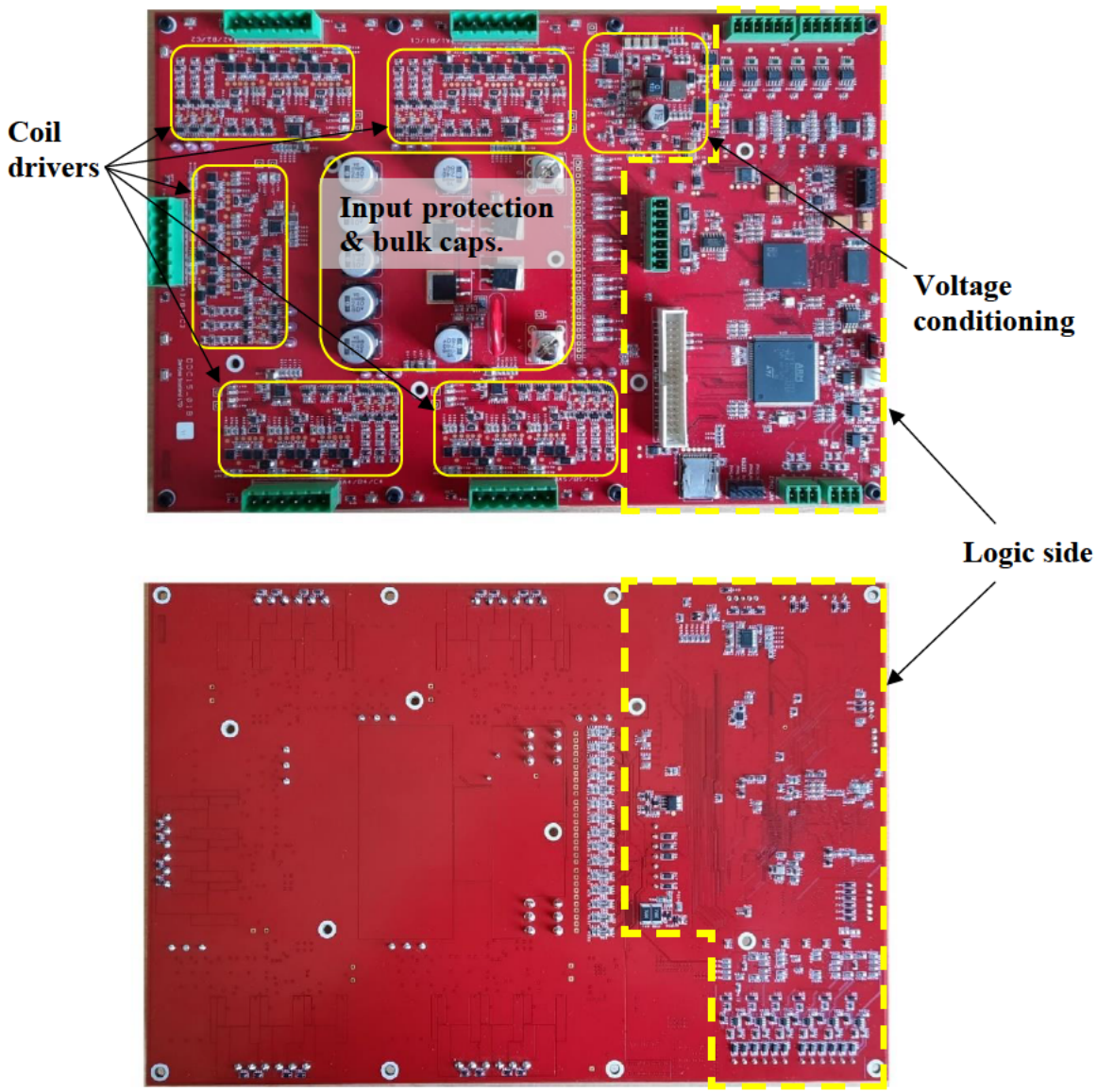

Figure 6.5. DDC15_01B photograph. (Top picture – top view, bottom picture – bottom view)

The coil current gradient control algorithm (described in Chapter 4) was integrated into the DDC15 firmware enabling the response time stabilisation of the valves during the energising phase. Also, the low-pressure valve (LPV) reopening detection algorithm (described in Chapter 3) was integrated into the DDC15 firmware enabling the closed-loop motoring control of the DDP1X0 machine.

Figure 6.6 shows the signal the controller sees during motoring. Up until the mStop (end of the valve energising cycle), the controller measures current for closed loop current control, after the mStop, the controller measures back-EMF voltage to detect the LPV reopening (end of the valve de-energising phase).

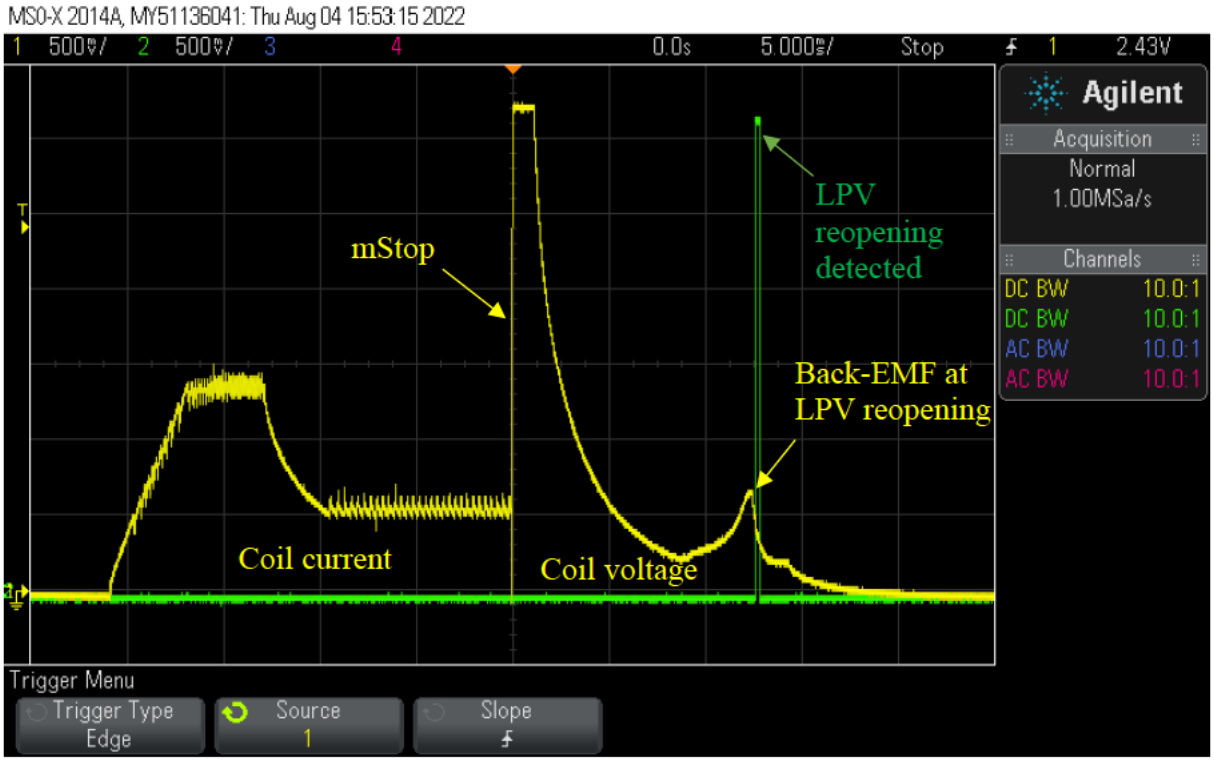

Figure 6.6. The DDC15_01B coil driver feedback signal at the DDP1X0 machine motoring mode of operation.

The DDC15_01B was designed to pass the testing criteria listed in Table 6.1. Currently, the enclosure design for DDC15_01B is under development, which is required to complete the testing.

Table 6.1. DDC15 testing criteria.

Description	Applicable standard
Climate environment	
Storage temperature	IEC 60068-2-1, test Ab, IEC 60068-2-2 test Bb
Operating temperature	IEC 60068-2-1, test Ab, IEC 60068-2-2 test Bb
Thermal cycle	IEC 60068-2-2, test Na, IEC 60068-2-38 (partial)
Humidity	IEC 60068-2-78, IEC 60068-2-30 test Db
Degree of protection	IEC 60529
Chemical environment	
Chemical resistance	ISO 16750-5

Mechanical environment	
Vibration	IEC 60068-2-6, test Fc, IEC 60068-2-64 test Fh
Bump	IEC 60068-2-29, test Eb
Shock	IEC 60068-2-27, test Ea
Free fall	IEC 60068-2-32, test Ed
Electrical/Electronics	
EMC emissions	EN ISO 14982, ISO 13766
EMC immunity	EN ISO 14982, ISO 13766
Electrostatic discharge	EN 60-1 000-4-2
Automotive transients	ISO 7637-2, ISO 7637-3
Short circuit protection	Danfoss test (inputs and outputs survive continuous short circuit, normal operation resumes when short circuit is removed)

6.2.2 Energy regeneration test results

This test was performed to demonstrate the energy-saving capability of the DDC15 controller, which is allowed by the coil residual energy regeneration feature of the next-generation coil driver (NGCD) design developed in this project (see Chapter 2).

The test consists of two stages, at which the power consumption of the controller was measured at various values of the DD machine speed, in the range from 750 rpm to 2500 rpm.

During the first stage, a modified DDC15 firmware was used that set the coil driver in the slow-decay mode during the turn-off stage of the valve decaying the coil energy across the coil circuit resistance. Therefore, the energy regeneration feature is disabled.

During the second stage, the original DDC15 firmware was used to set the coil driver in the fast-decay mode during the turn-off stage of the valve connecting the solenoid coil to the power supply with reverse polarity. Therefore, the energy regeneration feature is enabled.

The power supply voltage during the test was 28.5 V, and the coil current profile parameters were as follows:

- $T_{ramp} = 3\ ms;$

- $T_{peak} = 3\ ms$;
- $I_{boost} = 1\ A$;
- $I_{peak} = 6\ A$.

These are the expected nominal values for the DDP1X0 automotive application.

Table 6.2 and Figure 6.7 show the DDC15_01B energy regeneration test results comparison.

Table 6.2. DDC15_01B energy regeneration test result comparison.

Shaft speed (rpm)	**Controller power consumption without energy regeneration (W)**	**Controller power consumption with energy regeneration (W)**	**Difference in controller power consumption (%)**
750	68.56	61.01	11.01
1000	91.62	81.51	11.03
1200	110.55	98.59	10.82
1400	129.42	115.65	10.64
1600	147.60	132.05	10.54
1800	167.61	150.11	10.44
2000	184.45	165.71	10.16
2200	205.32	184.52	10.13
2400	223.55	201.02	10.08
2500	233.46	210.05	10.03

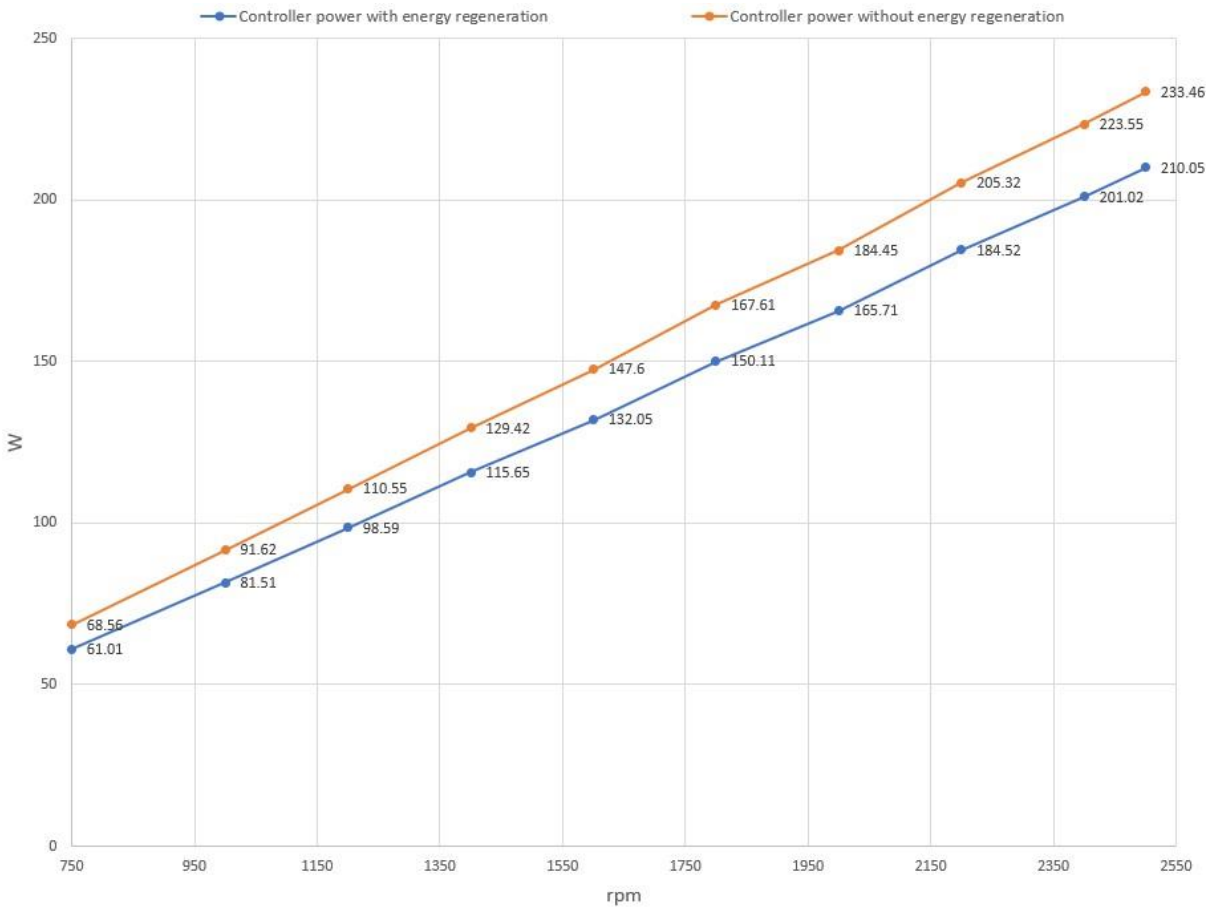

Figure 6.7. Test results comparison. DDC15_01B controller power consumption with coil residual energy regeneration (blue line) against without coil residual energy regeneration (orange line).

As can be seen from the test results, the controller power consumption proportionally increases with the increment of the shaft rotational speed. The controller consumes up to 11% less power when the solenoid coil residual energy regeneration is applied. Also, it can be spotted that energy regeneration value decreases with the increment of the shaft speed, which might be due to the increment of the energy loss across the coil circuit resistance. Because at the higher shaft speed, the valve switching is more frequent, thus, increasing the average current through the coil circuit, which, in turn, increases its resistance due to the temperature increase caused by the Joule heat effect.

Therefore, it can be concluded that the coil residual energy regeneration feature of the next-generation coil driver (NGCD) used in the DDC15_01B design allows for saving from 10% to 11% of the energy used for valves actuation of the DDP150S machine when operating at as a pump. Thus, bringing the maximum power consumption of the DDC15 controller from 233 W to 210 W (the assumption is made that the maximum speed of the DDP1X0 will be 2500 rpm).

The lower energy consumption allows for a decrease in the rating of the controller's electronic components, leading to a reduction in its price. Additionally, it results in a lower load on the alternator of an automotive system. These factors make DD technology more efficient and more attractive on the market.

6.2.3 Closed-loop motoring control test results

6.2.3.1 Overview of the open- and closed-loop motoring mode of operation of a DD machine

According to [6], it is crucial to ensure the precise timing for the low-pressure valve (LPV) reopening angle during the motoring mode of operation of the Digital Displacement (DD) machine. If the LPV reopening occurs too early before the piston reaches the bottom dead centre (BDC) the displacement of the machine will be partially lost at this motoring cycle. If the LPV reopening occurs after the piston reaches the BDC, the machine will enter an undesired pumping mode causing a total loss of the displacement at this motoring cycle and unstable operation (named “Juddering”) of the DD machine. Therefore, the target is to reopen the LPV when the piston reaches the BDC.

The DD machine requires to be calibrated to define the exact time/angle (named "mStop") when the valve begins the turn-off stage (i.e., the solenoid is set in the fast turn-off state).

Currently, DD software offers two motoring modes of operation: the closed-loop and the open-loop motoring mode.

For open-loop motoring, the mStop angle is defined by an engineer for the chosen speed and pressure of each valve of every single DD machine. During the operation, the mStop angle value will be adjusted with the speed change using extrapolation method.

For the closed-loop motoring, the mStop angle is adjusted during the operation by the closed-loop timing optimisation algorithm individually for each valve of the DD machine. The algorithm uses the reopening angle of the LPV as a feedback signal, which is generated by the LPV reopening detection algorithm, which in turn, uses the LPV back-EMF at reopening as the feedback signal (see Chapter 3). The main setup parameters for the closed-loop algorithm are the “Reopen Target”, the “Gain”, and the “Judder Backoff”. The Gain parameter defines the unit correction per valve switching cycle, the Reopen Target parameter defines the target LPV reopening angle with respect to the shaft position, and the Judder Backoff parameter

defines by how many degrees the mStop angle must be retreated (set earlier) from its previous value when juddering is detected. These parameters must be set once during the calibration of the closed-loop motoring algorithm.

6.2.3.2 Closed-loop motoring calibration

The calibration purpose was to define the setup parameters ("Reopen Target" and "Gain") of the closed-loop motoring mode at which the maximum possible displacement of the DD machine at its stable operation (no Juddering must occur) will be achieved over a defined speed range of the shaft. The shaft speed range for DD1X0D is 750-2200 rpm, at this stage of development, was defined by the mechanical department. A default -10 degrees for the Judder Backoff parameter was used throughout the test.

The first stage of the calibration process consisted of defining the most appropriate Reopen Target and Gain values over the shaft speed range with intervals of 2000-2200 rpm at a system pressure of 150 bar. The first stage calibration results are summarised in Table 6.3.

Table 6.3. The first stage calibration results for the DDP150S closed-loop motoring mode.

Shaft speed (rpm)	Displacement (cc/rev)	Reopen Target (degrees)	Gain
750	138.7	7	0.01
1000	137.6	7	0.01
1200	137.4	8	0.01
1400	137.5	11	0.01
1600	137.4	15	0.01
1800	134.8	13	0.01
2000	132	13	0.01
2200	129.2	12	0.01
-	$\Sigma/n = 135.6$	-	-

The second stage of the calibration consisted in testing the machine with the lowest value of the Reopen Target from the first calibration stage since an increased Reopening Target value of the correspondent speed will result in juddering of the DD machine. The second stage calibration results are summarised in Table 6.4.

Table 6.4. The second stage calibration results for the DDP150S closed-loop motoring mode.

Shaft speed (rpm)	Displacement (cc/rev)	Reopen Target (degrees)	Gain
750	138.5	7	0.01
1000	137.3	7	0.01
1200	137.1	7	0.01
1400	136.7	7	0.01
1600	135	7	0.01
1800	131.8	7	0.01
2000	128.2	7	0.01
2200	126.1	7	0.01
-	$\Sigma/n = 133.8$	-	-

Figure 6.8 shows the comparison of the DDP150S displacement results achieved at the first (blue line) and second (yellow line) stages of the closed-loop motoring calibration.

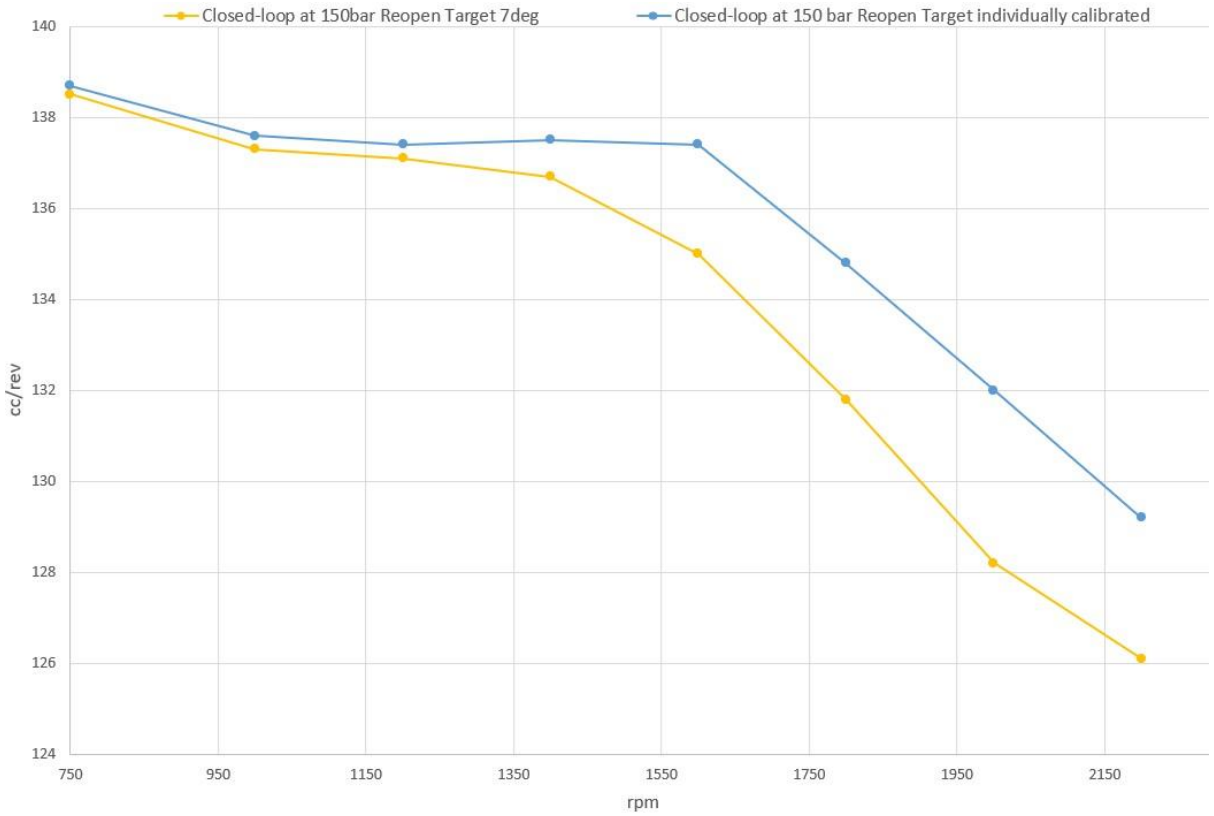

Figure 6.8. Comparison of DDP150S displacement results achieved at the first (blue line) and second (yellow line) stages of the closed-loop motoring calibration.

As can be seen from the calibration results, the DDP150S displacement drops steeper when the Reopen Target is the constant value and cannot be adjusted along the speed change of the shaft. However, since closed-loop motoring is still under development, the algorithm and software can be modified to allow improvements.

Therefore, the third stage of the calibration process was to improve the displacement of the DD machine by using two values for the Reopen Target parameter. One value will be for the lower speed range (750-1200 rpm), and the other one will be for the higher speed range (1200-2200 rpm). This solution will result in a minor software modification, such as adding a lookup table of two or more values used for the Reopen Target in a certain speed range. The third stage calibration results are summarised in Table 6.5.

Table 6.5. The third stage calibration results for the DDP150S closed-loop motoring mode.

Shaft speed (rpm)	Displacement (cc/rev)	Reopen Target (degrees)	Gain
750	138.4	7	0.01
1000	137.4	7	0.01
1200	137	7	0.01
1400	137	11	0.01
1600	136	11	0.01
1800	134.1	11	0.01
2000	131.1	11	0.01
2200	129.4	11	0.01
-	$\Sigma/n = 135$	-	-

Figure 6.9 shows a comparison of the DDP150S displacement produced during the calibration process of the closed-loop motoring (thick orange line is the final third stage calibration results) against the open-loop motoring results (dashed blue line).

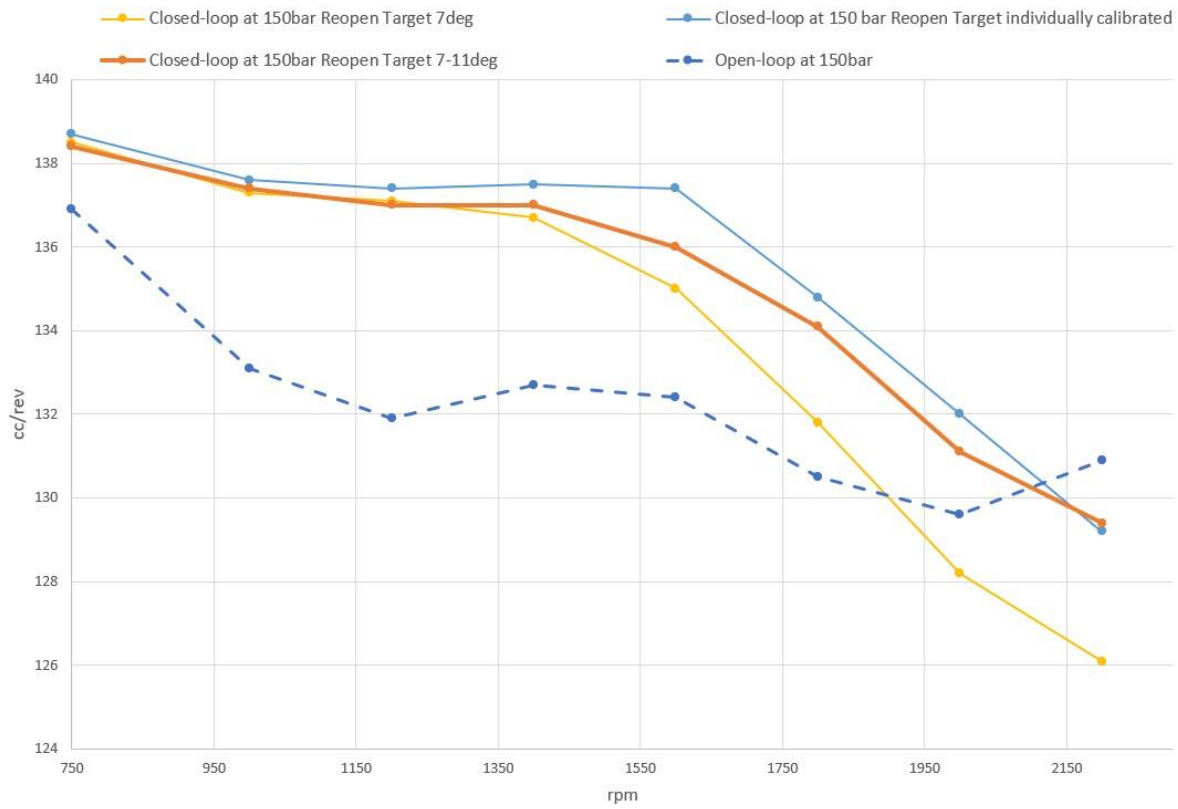

Figure 6.9. comparison of the DDP150S displacement produced at the closed-loop motoring during the calibration process (bold orange line is the final third stage calibration result) against the open-loop motoring results (dashed blue line).

As can be seen from the calibration results, the closed-loop motoring provides a 1.2 cc/rev larger displacement of the DDC150S when using two values for the Reopen Target instead of one (133.8 cc/rev against 135 cc/rev machine average displacement), and only 0.5 cc/rev lower than in the case when individual Reopen Target value is used for each speed point.

Also, it can be seen that at the constant pressure of 150 bar, the closed-loop motoring provides a larger displacement compared to the open-loop motoring, which is 135 cc/rev against 132 cc/rev of the DDP150S average displacement within the speed range of 750-2200 rpm.

6.2.3.3 Closed-loop vs open-loop motoring at different system pressure

The next step in evaluating the closed-loop motoring was to compare the DDP150S machine displacement delivered by the closed-loop motoring and the open-loop motoring at different system pressure.

Figure 6.10 shows the test results of the DDP150S displacement delivered at the closed-loop motoring (continuous line) and open-loop motoring (dashed line) at the system pressure of 150 bar and 250 bar.

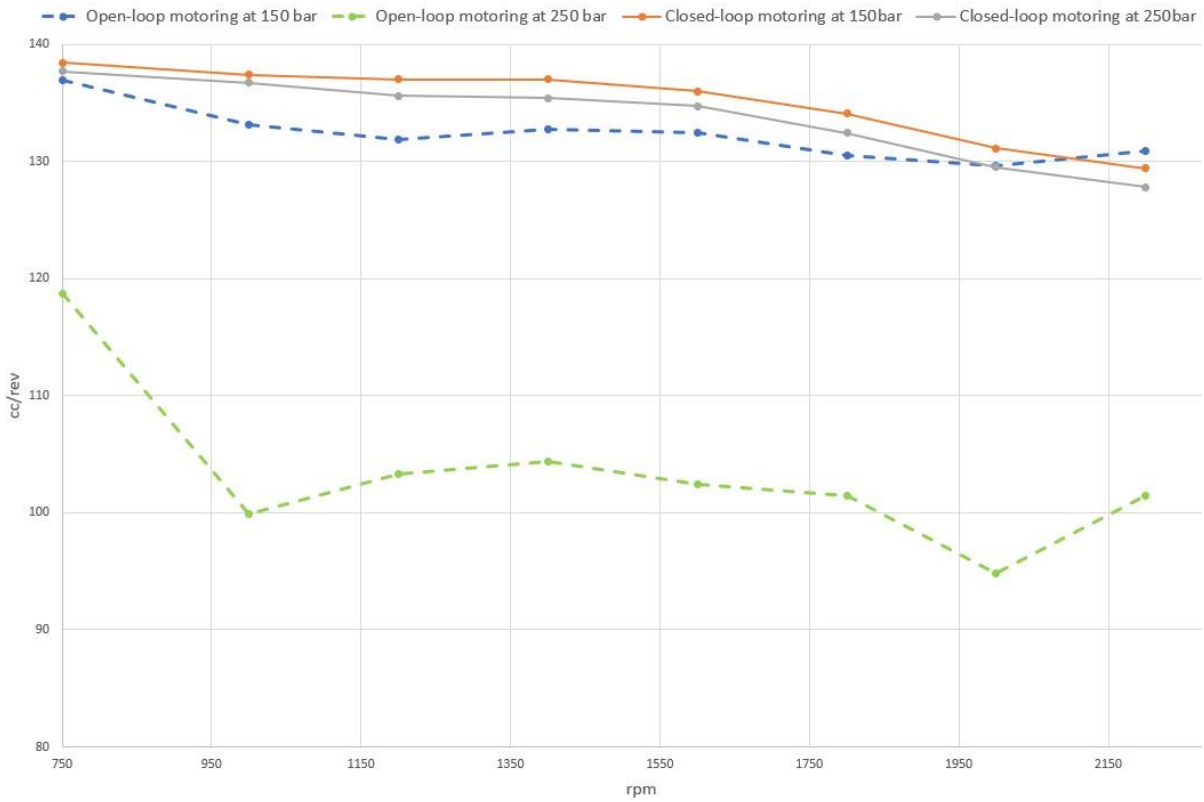

Figure 6.10. Test results of the DDP150S displacement delivered at the closed-loop motoring (solid line) and open-loop motoring (dashed line) at the system pressure of 150 bar and 250 bar.

As can be seen from the test results, the displacement of the machine at the closed-loop motoring stays almost the same (134cc/rev against 135cc/rev) when the system pressure increases from 150 bar to 250 bar. However, if the machine is operating in the open-loop motoring mode, its average displacement dramatically drops from 133 cc/rev up to 103 cc/rev, which is by 22%.

The drop in displacement will cause a drop in the torque produced by the DD machine, which leads to a decrement in the efficiency of the application (e.g., excavator) where the motoring cycle of the DD machine is used to recover the hydraulic energy.

Figure 6.11 shows the test results of the DDP150S torque produced at the closed-loop motoring (continuous line) and open-loop motoring (dashed line) at the system pressure of 150 bar and 250 bar.

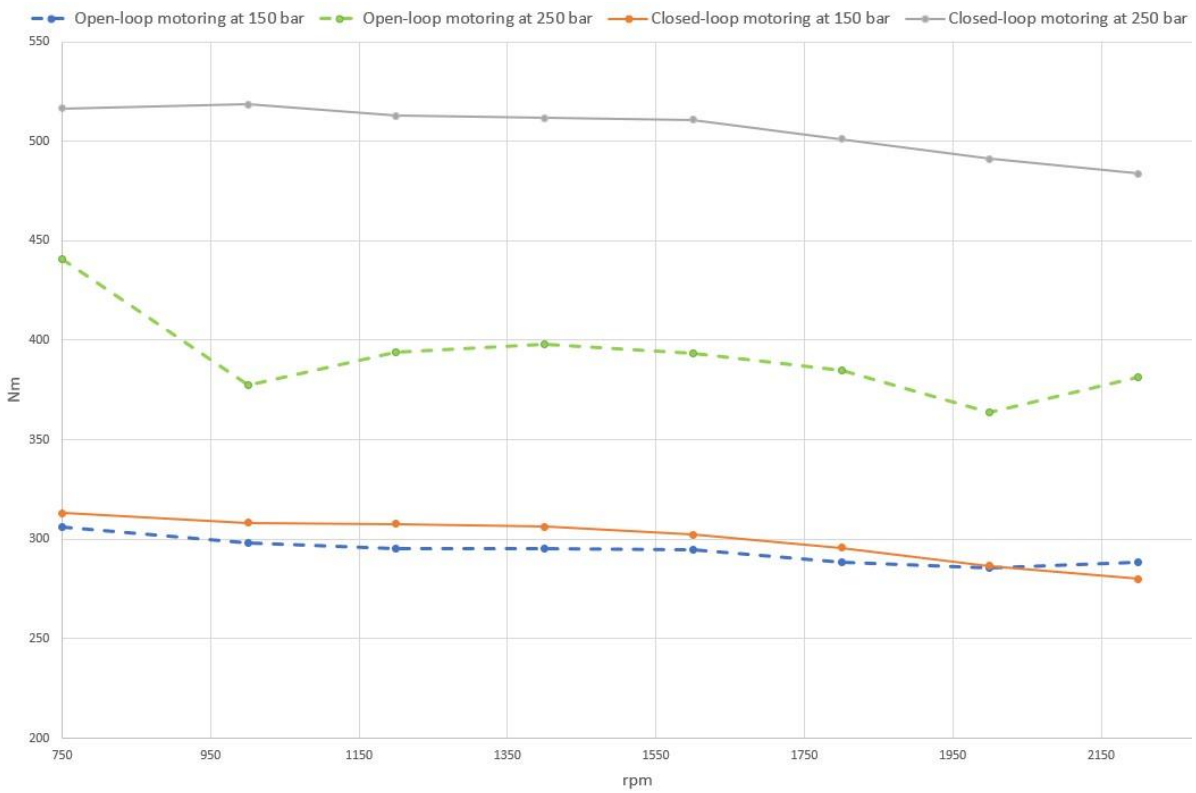

Figure 6.11. Test results of the DDP150S torque produced at the closed-loop motoring (solid line) and open-loop motoring (dashed line) at the system pressure of 150 bar and 250 bar.

As expected, the DDP150S torque produced at open-loop motoring mode is significantly lower (by 22% average) than the torque produced when the machine is operating at the closed-loop motoring mode.

Additionally, the open-loop motoring operation of the machine was not possible when the system pressure was decreased down to 50 bar, because the machine was continuously juddering. It is worth mentioning that continuous juddering for more than 5-10 minutes can cause unreversible damage to the DD machine. However, the closed-loop motoring software developed by Stephen Laird detects juddering and prevents damage to the mechanism.

To investigate what is causing the spread in displacement due to the system's pressure change, the valve voltage signature during its turn-off phase was examined within the shaft speed sweep at the system pressure of 50 bar, 150 bar, and 250 bar.

Figure 6.12, Figure 6.13, and Figure 6.14 show the scope reading obtained during the voltage signature examination of the DDP150S valve during its turn-off phase at the 28.5 V supply voltage within 750-2400 rpm speed range at the system pressure of 50 bar, 150 bar, and 250 bar accordingly. Only one valve of the DDP150S machine was examined in the closed-loop motoring mode of operation.

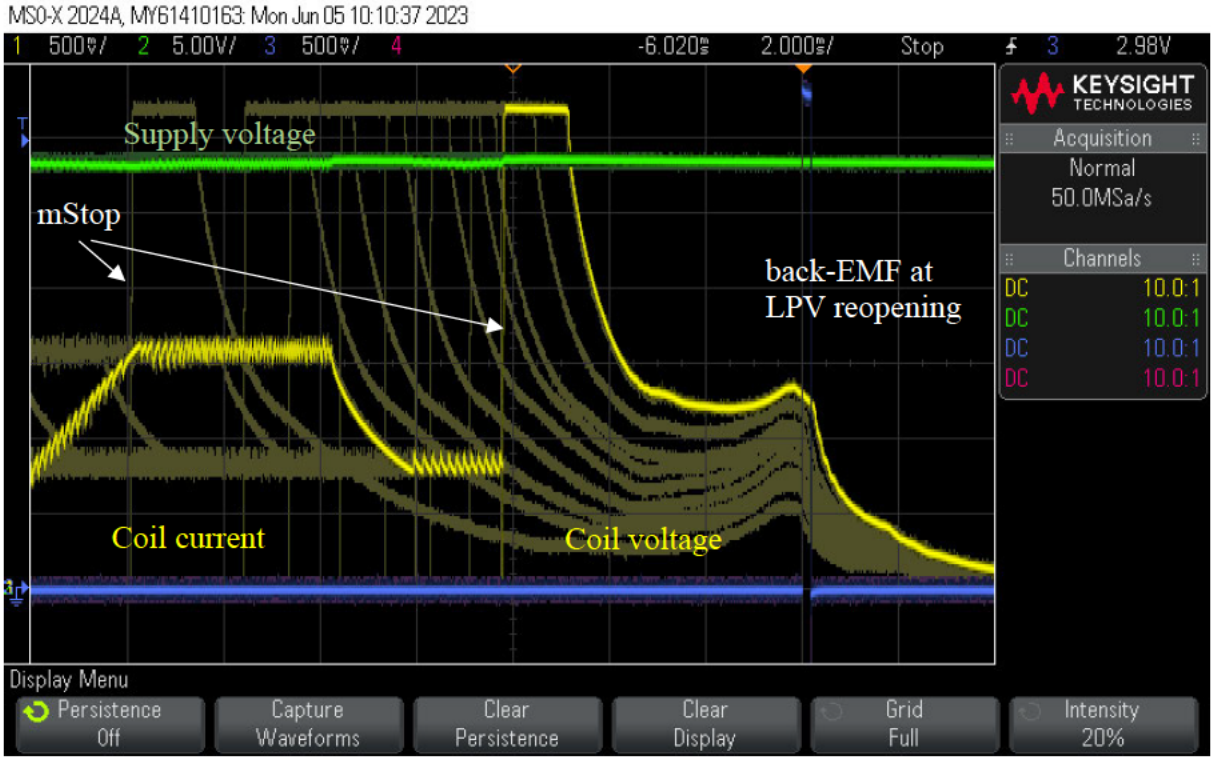

*Figure 6.12. Voltage signature examination of the DDP150S valve during its turn-off phase at **50 bar** system pressure (sweep in shaft speed at closed-loop motoring, speed range 750-2400 rpm).*

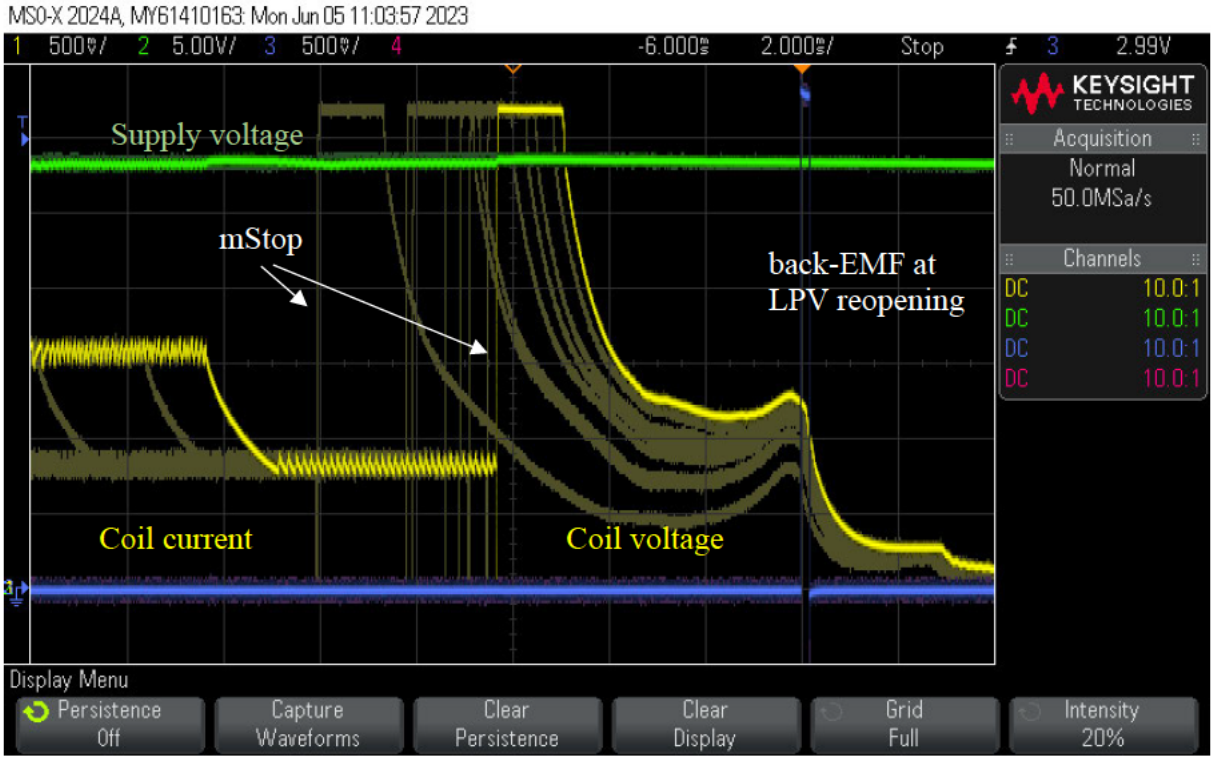

*Figure 6.13. Voltage signature examination of the DDP150S valve during its turn-off phase at **150 bar** system pressure (sweep in shaft speed at closed-loop motoring, speed range 750-2200 rpm).*

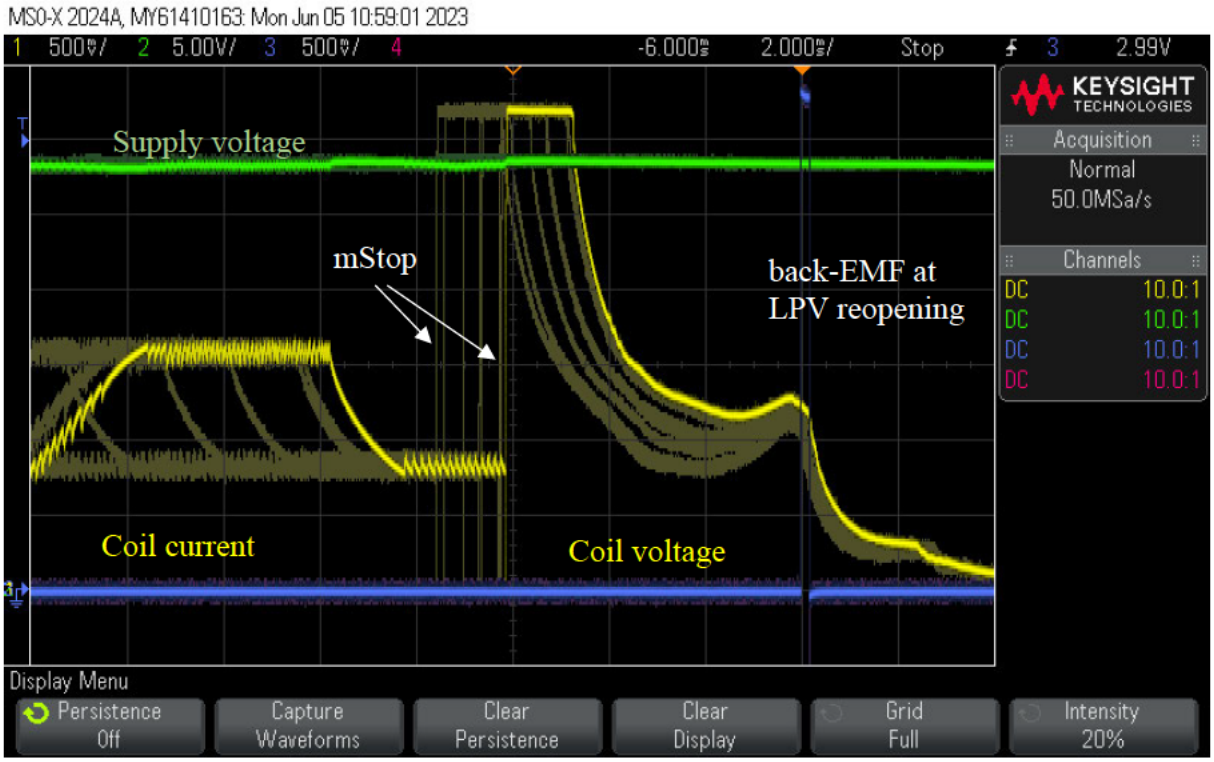

*Figure 6.14. Voltage signature examination of the DDP150S valve during its turn-off phase at **250 bar** system pressure (sweep in shaft speed at closed-loop motoring, speed range 750-2400 rpm).*

Table 6.6 summarises the experiment results of the valve turn-off time variation due to the shaft speed and system pressure.

Table 6.6. Spread in the valve turn-off time due to the shaft speed and system pressure.

System pressure	50 bar	150 bar	250 bar
Spread in the valve turn-off time due to the shaft speed	14 ms	10 ms	7.6 ms

As can be seen from the test results, the valve turn-off time (the time from the mStop until the peak of the back-EMF) varies not only with the shaft speed change but also with the system pressure change. The variation of the valve turn-off time with the shaft speed decreases with an increment in the system's pressure. The greater the pressure in the system, the shorter the valve closing time.

Therefore, as the open-loop algorithm does not take into account variation of the valve turn-off time with the pressure change and its calibration process is performed only for a single value of the system pressure (150 bar in this case), the LPV valve reopens (i.e., motoring cycle ends) earlier (regarding the piston position in respect to the BDC of the correspondent valve) if the system pressure increases above the calibration pressure or later if the system pressure decreases below the calibration pressure.

Therefore, during the experiment, a decrement of DDP150S displacement was observed when the system pressure was 250 bar (100 bar above the calibration pressure) and juddering when the system pressure was 50 bar (100 bar below the calibration pressure).

Additionally, the response time at the turn-off phase of all valves of the DDP150S was examined at the constant system conditions. Figure 6.15 shows the voltage and current profile of all DDP150S valves (superimposed, to show the spread in valve turn-off time) during its turn-off phase at the motoring cycle, 150 bar system pressure and 750 rpm shaft speed.

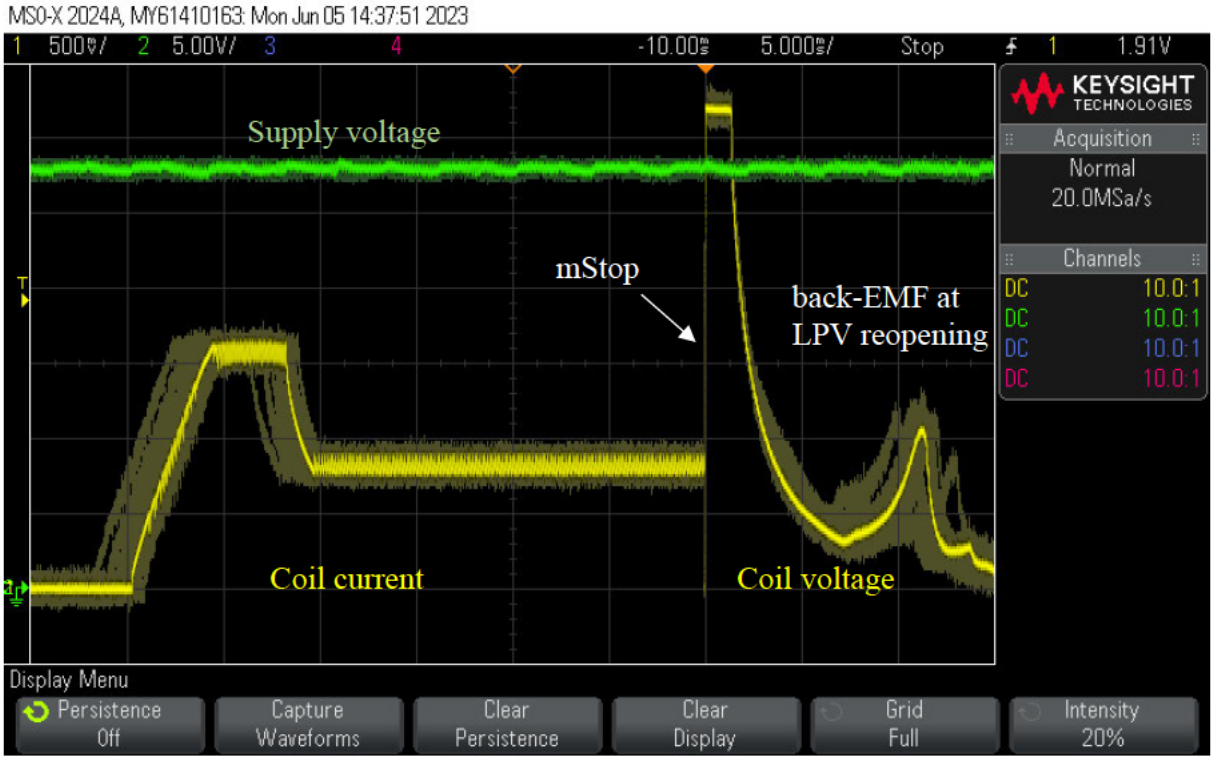

Figure 6.15. Voltage signature examination of all DDP150S valves during its turn-off phase at 150 bar system pressure and 750 rpm shaft speed (closed-loop motoring mode).

From the experiment results can be observed that the valve turn-off time (the time from the mStop until the peak of the back-EMF) varies from valve to valve, which can be due a minor difference in the valve assembly (manufacture tolerances in spring force, air gap length etc.), or valve's spatial orientation. The valve difference due to manufacture tolerances cannot be predicted, which means that each DD machine (and each valve of the DD machine) must be calibrated individually for the open-loop motoring to achieve its maximum displacement. This is not operationally feasible as the manual calibration takes too much time and effort (according to Dr Niall James Caldwell, more than four hours per machine), which hinders the mass production of the DD machine and, therefore, its commercialisation. Also, manual calibration doesn't account for valve characteristics variation over a lifetime caused by wear or other ageing effects, which will affect the displacement of the DD machine.

Thus, it can be concluded that enabling the closed-loop motoring feature for the DD machine is crucial for achieving its maximum displacement over the wide range of the system's conditions/parameters, such as the system's pressure, shaft speed, manufacturing tolerance, valve's spatial orientation, hydraulic oil characteristics, components wearing and others that influence the valve response time at the turn-off phase. Also, the closed-loop motoring mode

improves the stability of the operation, prevents juddering, and provides self-calibration of the DD machine, which makes feasible its mass production, therefore, its commercialisation, and enables its auto-adjustment over the life span.

6.2.4 Valve response time stabilisation test results

As it was mentioned previously, the low-pressure valve (LPV) closing angle concerning the shaft position (i.e., concerning the piston position regarding the bottom or top dead centre (BDC or TDC)) impacts the displacement of the DD module and its correct operation. Early or late closure of the LPV during the pumping cycle will lead to the displacement reduction of the DD module. During the motoring cycle, early closure of the LPV leads to an undesired pumping before the motoring commences, and late closure of the LPV leads to the collapse of the motoring stroke (the machine executes an idle cycle).

One of the main features of the DD machine is that it can provide real-time displacement control. This can be achieved by varying the number of operating DD modules (valves) at a constant firing angle (the angle that defines the start of the energizing phase of the solenoid valve) or by applying a part pump technique that involves varying the valve firing angle. This way, it becomes possible to control the amount of hydraulic fluid that will be displaced by each cylinder of the DD machine in real-time. More about displacement control of the DD machine can be found in the PhD thesis of Dr Niall James Caldwell [6] (section 5.3.1), and in [59], [82].

Therefore, it is crucial to provide a precise control of the LPV closing angle to enable a precise real-time displacement control of the DD machine and to ensure its correct operation.

Currently, the DD machine employs an open-loop control of the LPV closing angle. This control method relies on data obtained through experimental calibration of the machine. This acquired data is then utilized to set the appropriate LPV closing angles for different operating conditions without ongoing feedback during the machine's operation.

The calibration process for the DD machine involves performing a sweep in the LPV (low-pressure valve) firing angle. During this calibration procedure, the LPV firing angle is systematically varied across a range of values, and for each firing angle setting, the resulting displacement of the DD module is measured and recorded. By conducting this sweep and recording the corresponding displacement values, a map or table can be created that relates different LPV firing angles to the corresponding displacements achieved by the DD module.

This map establishes a functional relationship between the firing angle and the resulting hydraulic fluid displacement. Once this calibration map is established, it is used during the operation of the DD machine in the open-loop control scheme. When specific displacement levels are required, the firing angle can be set based on the values in the calibration map to achieve the desired amount of fluid displacement for a given task or application.

In the current control scheme, the firing angle that corresponds to the maximum displacement of the DD machine is selected for the full pumping stroke. This means that during the primary operation or when maximum hydraulic fluid displacement is required, the firing angle that provides the best performance is utilised. On the other hand, during the part-pump mode of operation, where a reduced displacement is desired, different firing angles are employed. By varying the firing angle during this mode, the amount of hydraulic fluid displaced by each cylinder can be controlled, allowing for partial or reduced pumping action as needed for specific tasks or operating conditions.

Figure 6.16 shows three waveforms of the sweep in the LPV firing angle (20 degrees step) of a DDP150S module (valve) without valve response time stabilisation (RTS) being applied. During the experiment, the system pressure was 50 bar.

The blue waveform corresponds to the 32 V supply voltage and 0 Ohm coil circuit series resistor. The orange waveform corresponds to the 22 V supply voltage and 0 Ohm coil circuit series resistor. The grey waveform corresponds to the 22 V supply voltage and 27 Ohm coil circuit series resistor. The voltage range of 22-32 V corresponds to the nominal supply voltage of the 24 V automotive system (see Chapter 4) and the 0.27 Ohm resistor simulates the coil circuit resistance variation due to the temperature variation (in the range of -20°C to +120°C) and coil power cables length variation (2-10 m range).

The coil current controller parameters were set as follows:

- $T_{ramp} = 2\ ms$;
- $T_{peak} = 5\ ms$;
- $PWM_{ramp} = 100\%$.
- $PWM_{peak} = 45\%$.

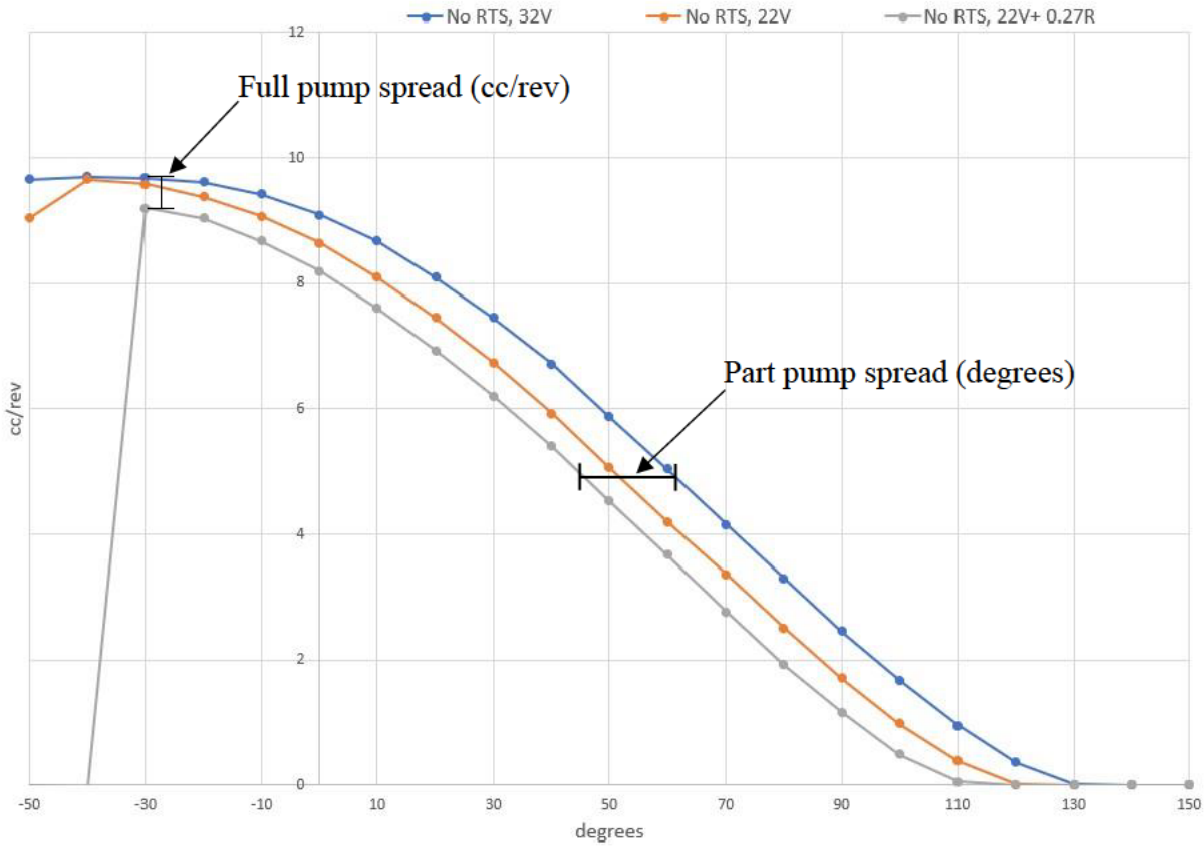

Figure 6.16. Sweep in the LPV firing angle of a DDP150S module (valve) without valve response time stabilisation (RTS). Blue line – 32 V supply voltage and 0 Ohm coil circuit series resistor, orange line – 22 V supply voltage and 0 Ohm coil circuit series resistor, grey line – 22 V supply voltage and 27 Ohm coil circuit series resistor.

Based on the test results, the full pump spread, defined as the variability of flow at the full pump, ranges between 9.2 cc/rev and 9.58 cc/rev, resulting in a 4% variation. This means that the hydraulic fluid displacement achieved during full pumping operation shows a slight difference, varying by 4% under the same firing angle and different values of the controller supply voltage and coil circuit resistance.

Similarly, the part pump spread, defined as the variability in firing angle required to obtain 50% of the rated displacement, is 10 degrees. This indicates that a range of 10 degrees in firing angles will take place to achieve 50% with the change of the controller supply voltage and coil circuit resistance.

Figure 6.17 shows the variation of the coil current profile with the corresponding variation of the controller supply voltage and coil circuit resistance during the test.

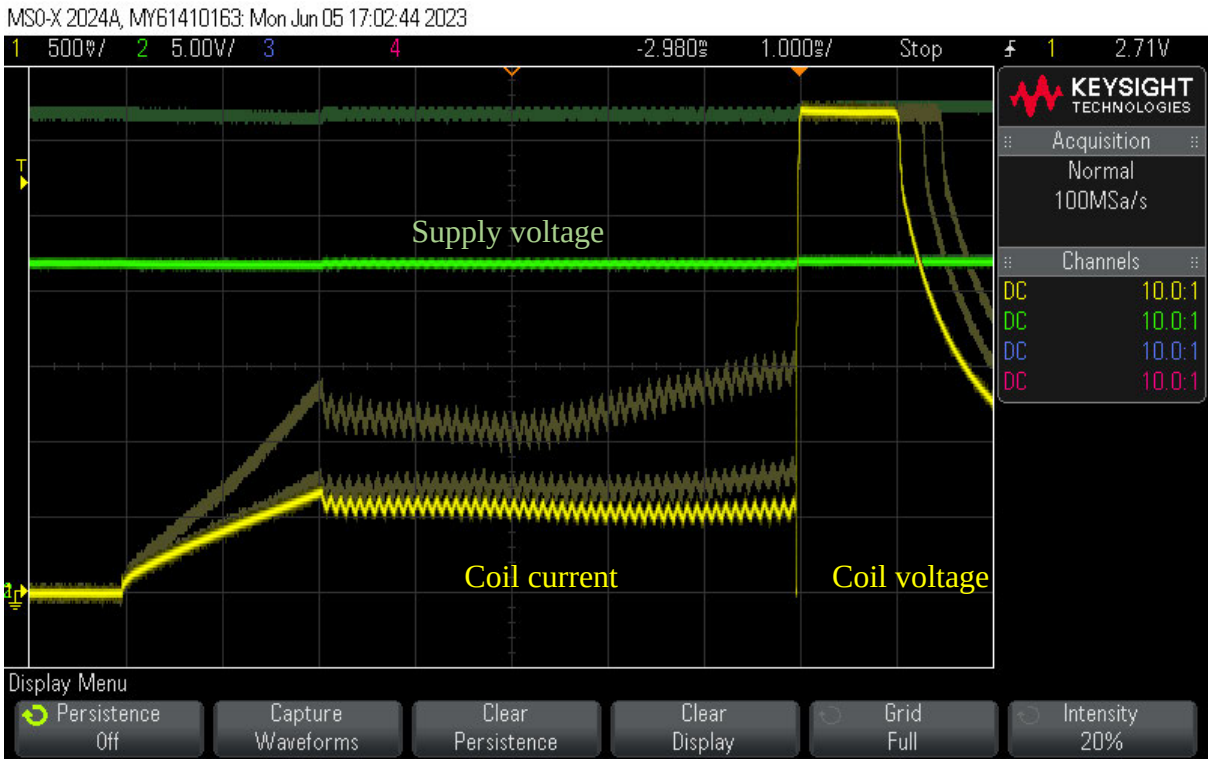

Figure 6.17. Coil current profile at the sweep in firing angle test without the valve response time stabilisation (RTS). The supply voltage switched from 32 V down to 22 V, and coil serious resistance increased by 0.27 Ohm.. DDP150S pumping cycle.

As can be seen, the gradient of the rising edge of the coil current profile (also its peak value) decreases with a decrement in the supply voltage of the controller and with an increment in the coil circuit resistance, which causes a delay in the build-up of the solenoid magnetic force, which in turn, delays the LPV closing angle (see Chapter 4).

At the next stage of the experiment, the sweeps of the LPV firing angle were obtained for the same valve and under the same system conditions. However, in this stage, a closed-loop control of the coil current profile was applied, which means that the valve response time stabilization (RTS) was implemented.

The coil current controller parameters were set as follows:

- $T_{ramp} = 4\ ms$;
- $T_{peak} = 3\ ms$;
- $I_{boost} = 1\ A$.
- $I_{peak} = 6\ A$.

Figure 6.18 shows three waveforms of the sweep in the LPV firing angle (20 degrees step) obtained by controlling the same DDP150S module (valve) using the valve response time stabilisation (RTS) technique, which involves closed-loop control of the solenoid coil current profile (see Chapter 4).

Similarly, to the first stage of the experiment, different values for the supply voltage (32 V and 22 V) and solenoid coil resistance (0 Ohm and 0.27 Ohm) were applied. The system pressure was 50 bar.

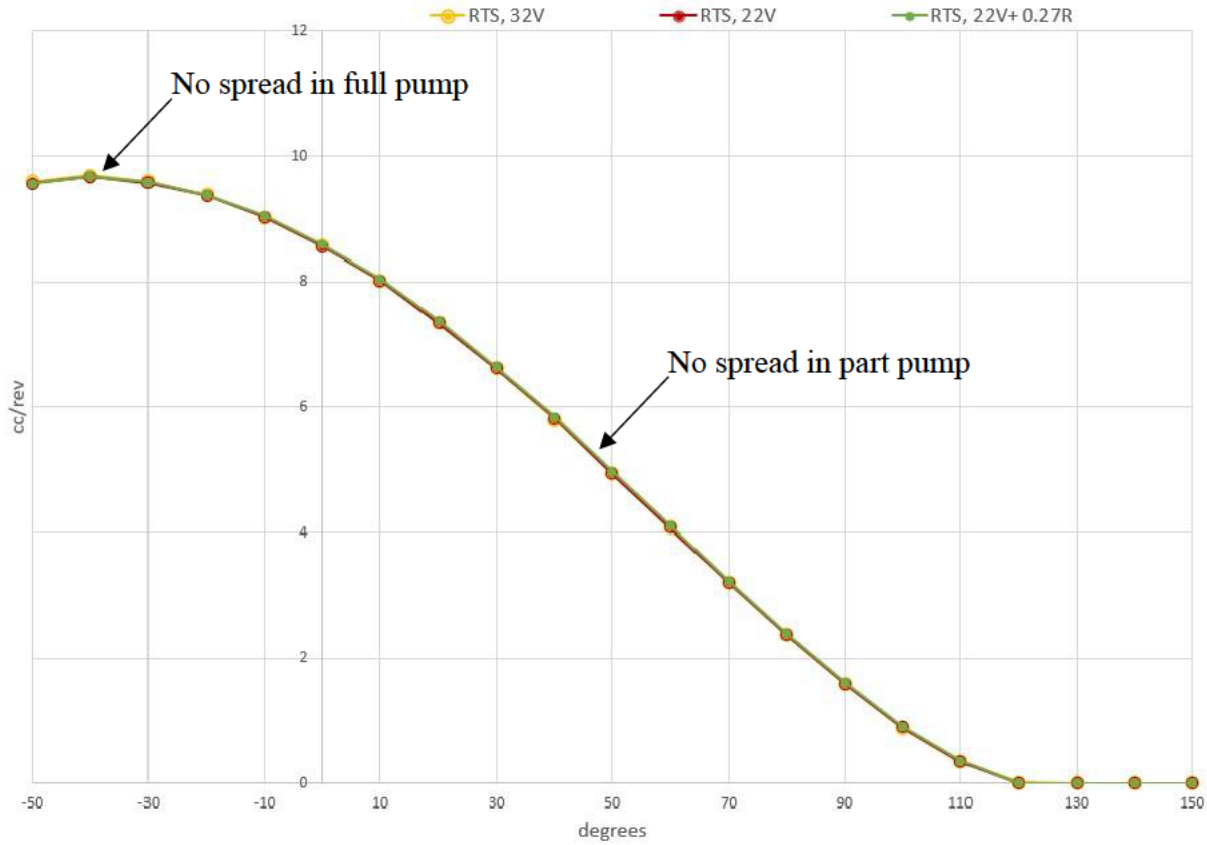

Figure 6.18. Sweep in the LPV firing angle of the same DDP150S module (valve) with valve response time stabilisation (RTS). Yellow line – 32 V supply voltage and 0 Ohm coil circuit series resistor, red line – 22 V supply voltage and 0 Ohm coil circuit series resistor, green line – 22 V supply voltage and 27 Ohm coil circuit series resistor.

As can be seen from the test results, all three waveforms are overlapping, and no discrepancy can be observed. This means that no spread in firing angle for the part pump either spread in displacement for the full pump will occurs if RTS is applied.

From the test results, it is evident that all three waveforms are overlapping, and no discrepancy can be observed. This finding implies that when the valve response time stabilization (RTS) is

applied through closed-loop control of the coil current profile, there is no spread in firing angle at the part pump, nor is there any spread in displacement at the full pump, regardless of variations in the supply voltage or coil resistance.

The absence of spread in firing angle at the part pump indicates that the closed-loop control effectively maintains a consistent firing angle to achieve required displacement. This precision in control ensures that the DD machine can consistently and accurately achieve the desired fluid displacement during part pumping operation.

Similarly, the lack of spread in displacement at the full pump signifies that the closed-loop control maintains a uniform and steady flow rate or fluid displacement during full pumping operation. This results in a stable and consistent performance of the DD machine at its maximum capacity.

Figure 6.19 shows the coil current profile at the corresponding variations of the controller supply voltage and coil circuit resistance during the second phase of the experiment when the RTS was applied. All three current profiles are overlapping.

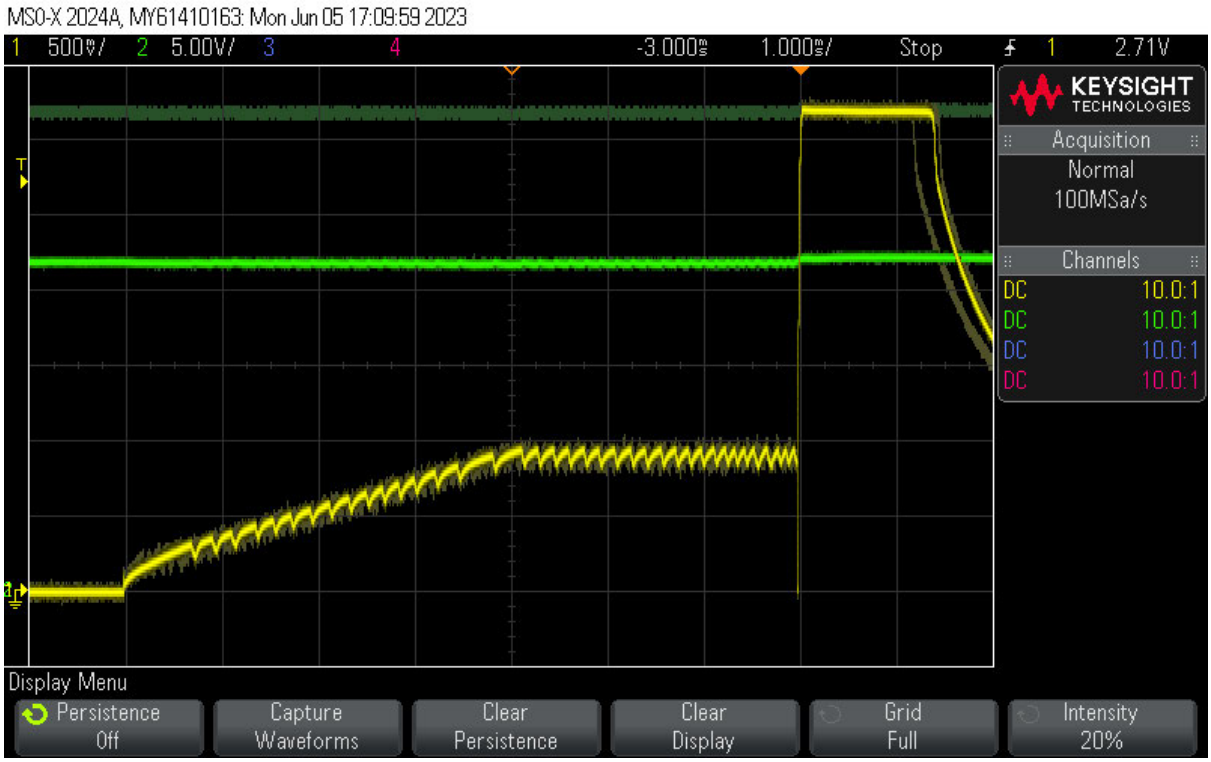

Figure 6.19. Coil current profile at the sweep in firing angle test with the valve response time stabilisation (RTS) enabled. DDP150S pumping cycle.

Overall, it can be concluded the application of RTS through closed-loop control of the coil current profile helps to overcome the challenges posed by changes in supply voltage and coil circuit resistance, which can cause variations in the valve response time. By continuously adjusting the coil current profile based on real-time feedback, the closed-loop control system eliminates the delays in the build-up of the solenoid magnetic force, ensuring precise and consistent valve operation.

The successful implementation of RTS improves the performance and reliability of the DD machine, making it highly suitable for applications that demand accurate and stable fluid displacement control.

6.3 Summary and conclusions of the chapter

Experimentally was demonstrated that the next-generation coil driver (NGCD) topology proposed in this PhD project and used in the new 15-channel Digital Displacement controller allows for decreasing the controller power consumption by 10-11% when operating the new larger displacement DD machine DDP150S as a pump.

Also, it was proven that enabling the closed-loop motoring feature for the DD machines is crucial to achieving its maximum displacement over the wide range of the system's pressure, shaft speed, manufacturing tolerance of the machine components and other system conditions/parameters that influence the valve response time at the turn-off phase.

Experimentally was demonstrated that the DDP150S displacement can vary by 30% with the systems pressure change of 100 bar if open-loop is used instead of closed-loop motoring.

Additionally, the closed-loop motoring control improves the stability of operation, prevents juddering (i.e., prevents permanent damage to the machine due to juddering), and provides auto-adjustment over the life span of the DD machine and its self-calibration, which allows for its mass production, therefore, its commercialisation.

Finally, it was shown that the turn-on phase valve response time stabilisation (RTS) feature, developed in this project, allows for precise and consistent control of the valve closing angle within a wide range of the controller power supply and coil resistance change. This improves precision in the control of the displacement fraction of the DD machine and its stability of operation.

Chapter 7
Conclusions

As stated in the introduction, this research work is related to the development of the next-generation solenoid valve actuation design for single-coil digital displacement (DD) modules, aiming to improve reliability, energy efficiency, and precision in the control of the valves; and to enable the closed-loop motoring control for the Digital Displacement Pump/Motor (DDPM) designed for automotive applications. The main goals of this thesis were successfully achieved. Each chapter contains detailed conclusions, which can be summarised as follows.

1. A new coil driver design for DD solenoid valves was developed, which is based on a combination of a new "smart" gate driver technology and pseudo-H-bridge topology. Its main benefits over the coil driver designs used in the present DD controllers are as follows.

   – Significant reduction of energy dissipation by synchronous rectification for the slow-decay mode and regeneration of the solenoid residual energy (up to 12.25%) for the fast-decay mode of operation. This is important to reduce the parasitic load on the vehicle alternator and to reduce cooling requirements of the controller.
   – Fast overcurrent protection (6.5 us maximum response time) with self-recovery option. This is important to improve reliability and fault tolerance in the harsh environment of off-road vehicles.
   – Footprint and cost reduction by 40%. This will make DD technology more accessible and increase the range of markets.

2. A method that allows reliable detection of the low-pressure valve (LPV) reopening, applicable to all existing designs of the DD modules, was developed and successfully implemented for a new DDPM DDP1X0 specially designed to be used in fluid-powered excavators. This method enables the closed-loop motoring technique to apply to new DDPMs. In turn, the closed-loop motoring improves the stability of the operation, prevents juddering (i.e., prevents permanent damage of the machine due to juddering), and provides self-calibration of the DD machine, which allows for its mass production, therefore its commercialisation, and enables its auto-adjustment over the life span.

3. A new method allowing stabilisation of the response time of a cyclically operating solenoid valve at the turn-on phase was developed, and it was successfully implemented for the new DDPM DDP1X0. The method enables precise control of the LPV closing angle within the established supply voltage and solenoid coil circuit resistance ranges, thus, improving the stability of operation and increasing the displacement of the DDPM. Additionally, it cancels a need for the front-end DC-DC converter, thus, improving efficiency and EMC performance and reducing the cost and size of DD controllers.

   A patent application for the invention (title: "Response time stabilisation (RTS) of cyclically operated valves") has been filed, which is pending the examiner's approval.

4. A new method allowing sensorless diagnostics of the DD machine before its operation was developed. The method is based on the back-EMF signal parameters analysis, which is generated by the LPV reopening. An algorithm based on the developed method for determining an approximate level of the hydraulic liquid inside the DD machine was proposed.

   A patent application for the invention (title: "Sensorless diagnostic of DD machine based on back-EMF signal") has been filed, which is pending the examiner's approval.

5. The next-generation coil actuation design developed in this PhD project was implemented in the new 15-channel Digital Displacement Controller (DDC15) designed to control a new DDPM DDP1X0. The test results demonstrate that the coil residual energy regenerating feature decreases the energy consumption of the DD controller by 10-11% at the pumping mode of operation. Up to 30% of displacement increment was demonstrated for the DDP1X0 by enabling the closed-loop motoring mode, which proportionally increases the developed torque, thus, leading to an increase in the regenerative efficiency of the DDPM. Finally, it was proven the valve response time stabilisation feature provides precise control of the LPV closing angle, thus, providing precise control of the DDPM displacement fraction at the static mode of operation.

7.1 Further work recommendations

Further work to promote the theme may include the following tasks.

1. Integration of the next-generation coil actuation design for DD valves into the new 30-channel Digital Displacement production controller DPC30.

2. To investigate possibilities for improvement of the closed-loop motoring algorithm. Test and quantify the improvement in the regenerative efficiency of the DDPM by enabling the closed-loop motoring feature. Publishing new results.

3. To investigate the necessity of any additional development of the LPV response time stabilisation for the dynamic mode of the operation of the DD machine (i.e., if any correction is required of the LPV response time at variable shaft speed, systems pressure, oil temperature etc.).

4. To implement the proposed algorithm for detecting an approximate level of the hydraulic fluid of the DD machine. Investigate the possibility of other applications of the sensorless diagnostic for DD machine based on the LPV reopening back-EMF signal parameters analysis.

5. To investigate possibility of development of sensorless determination of the solenoid coil temperature based on its current and voltage measurements.

6. Additionally, since most of the project material is commercially sensitive, whilst the other material first needed to be filed as a patent application, the publication of corresponding papers was impeded. However, when the patents that disclose the inventions presented in this PhD thesis will be published, the results of this PhD project can be summarised and written into a paper for submission to a suitable conference.

References

[1] Danfoss, “Digital Displacement paves the way for an off-highway revolution,” Danfoss Scotland Ltd, 5 November 2020. [Online]. Available: https://www.danfoss.com/en/about-danfoss/news/cf/digital-displacement-an-off-highway-revolution/. [Accessed 29 Jun 2023].

[2] V. Pavlis, C. McMillan, C. Nørgård and . N. J. Caldwell, “DIGITAL DISPLACEMENT MOTORING CHARACTERISTICS OF DYNAMIC ENERGY RECOVERY AND HYDRAULIC TRANSFORMATION,” ASME, Edinburgh, 2023.

[3] W. H. S. RAMPEN, U. B. P. STEIN, N. J. CALDWELL, S. M. LAIRD, P. R. OLY, M. R. FIELDING and D. S. DUMNOV, “FLUID-WORKING MACHINE VALVE TIMING”. GB Patent EP 2 386 026 B1, 14 10 2015.

[4] J. Quilter, “Windpower monthly,” Mitsubishi Power Systems Europe, 25 November 2011. [Online]. Available: https://www.windpowermonthly.com/article/1106330/mitsubishi-unveil-7mw-offshore-turbine. [Accessed 23 Jun 2023].

[5] U. STEIN, J. EILERS, J. LAVENDER and S. LAIRD, “VALVE UNIT A FLUID WORKING MACHINE COMPRISING A VALVE UNIT”. DE/FR/GB Patent EP 2 961 983 B1, 03 03 2014.

[6] N. J. Caldwell, “Digital Displacement Hydrostatic Transmission Systems,” The University of Edinburgh , Edinburgh , 2007.

[7] V. Masson-Delmotte, P. Zhai, H. O. Pörtner, J. Skea, P. Shukla, A. Pirani, W. Moufouma-Okia, C. Péan and R. Pidcock, “Global warming of 1.5°C,” IPCC, 2018.

[8] T. Stocker, D. Qin, G. Plattner, M. Tignor, S. Allen, J. Boschung and A. Nauels, “Summary for Policymakers. In: Climate Change 2013: The Physical Science Basis.

Contribution of Working Group I to the Fifth Assessment Report of the Intergovernmental Panel on Climate Change," IPCC, 2013.

[9] G. C. f. U. A. o. E. Efficiency, "Recommendations of the Global Commission," 2020.

[10] T. Abekawa, Y. Tanikawa and A. Hirosawa, "Introduction of Komatsu Genuine Hydraulic Oil KOMHYDRO HE," Komatsu, Yumpu, 2010.

[11] Center for Alternative Fuels, Engines & Emissions, "Heavy-Duty Vehicle Diesel Engine Efficiency Evaluation and Energy Audit," West Virginia University, 2014.

[12] M. Green, J. Macpherson, N. Caldwell and W. Rampen, "DEXTER: The Application of a Digital Displacement Pump to a 16 Tonne Excavator," in *Symposium on Fluid Power and Motion Control,* BATH/ASME, 2018.

[13] N. Caldwell, "Digital Displacement Technology for Heavy Vehicles," *Industrial Vehicle Technology (iVT Expo),* no. 2019, pp. 13-14, 2019.

[14] Danfoss, "Danfoss Power Solutions launches Dextreme systems pathway to increase excavator efficiency and productivity," Danfoss Scotland Ltd, 28 March 2023. [Online]. Available: https://www.danfoss.com/en/about-danfoss/news/dps/danfoss-power-solutions-launches-dextreme-systems-pathway-to-increase-excavator-efficiency-and-productivity/. [Accessed 2 July 2023].

[15] M. Green, J. MacPherson, N. Caldwell and W. Rampen, "DEXTER - THE APPLICATION OF A DIGITAL," in *Symposium on Fluid Power and Motion Control: FPMC2018 . American Society of Mechanical,* Bath/ASME, 2018.

[16] J. Budden and C. Williamson, "DANFOSS DIGITAL DISPLACEMENT® EXCAVATOR: TEST RESULTS AND ANALYSIS," in *Symposium on Fluid Power and Motion Control,* Sarasota, 2019.

[17] J. Lagarde, M. Green, A. Dole, J. Talvitie and J. Toikka, "Danfoss Digital Displacement & Editron: An efficient electro-hydraulic system for mobile applications," in *The 13th International Fluid Power Conference, 13. IFK,* Aachen, 2022.

[18] M. Pellegri, “Applying a multi-service Digital Displacement pump to an excavator to reduce valve losses,” in *12th International Fluid Power Conference (12IFK)*, Dresden, 2020.

[19] J. Macpherson, M. Green, C. Williamson and N. Caldwell, “ENERGY EFFICIENT EXCAVATOR HYDRAULIC SYSTEMS WITH DIGITAL DISPLACEMENT® PUMP-MOTORS AND DIGITAL FLOW DISTRIBUTION,” in *Symposium on Fluid Power and Motion Control*, Bath, 2020.

[20] B. N. M. Truong, D. Q. Truong, L. S. Young and L. S. Young, “Study on Energy Regeneration System for Hybrid Hydraulic Excavator,” in *International Conference on Fluid Power and Mechatronics*, Harbin, 2015.

[21] J. Hutcheson, D. Abrahams, J. Macpherson, N. Caldwell and W. Rampen, “DEMONSTRATION OF EFFICIENT ENERGY RECOVERY SYSTEMS USING DIGITAL DISPLACEMENT® HYDRAULICS,” in *Symposium on Fluid Power and Motion Control*, Bath, 2020.

[22] M. UMAYA, M. UCHIDA, Y. KAWAI, T. NOGUCHI, M. SHIBATA and R. NOTOMI, “Wind Power Generation, Development status of Offshore Wind Turbines,” *Mitsubishi Heavy Industries Technical Review*, vol. 50, no. 3, pp. 29-35, 2013.

[23] W. Bolton, Engineering Science, London and New York: Routledge of the Taylor & Francis Group, 2015.

[24] T. Denton, Automobile electrical and electronic systems, Oxford: Elsevier Butterworth-Heinemann, 2004.

[25] D. Righetti, Solenoid Actuators: Theory and Computational Methods, Perugia: Youcanprint SelfPublishing, 2017.

[26] M. Balakrishnan and N. Kumar, “Texas Instruments,” June 2015. [Online]. Available: https://www.ti.com/lit/wp/ssiy001/ssiy001.pdf?ts=1643788966117. [Accessed 2 February 2022].

[27] N. Bodo and A. Berry, “Nexperia,” 4 December 2020. [Online]. Available: https://www.nexperia.com/applications/interactive-app-notes/IAN50003_driving-automotive-solenoids.html. [Accessed 17 January 2022].

[28] B. Sotskov, Fundamental of Calculation and Design of Electromechanical Elements for Automated and Remote-Control Devices, Moscow: Energiya, 1965.

[29] S. Sihwan, C. Sungyeol, J. Hyuncheol, K. Dongkyu, K. Byunggon and J. Junchae, “A Heterogeneous Frequency PWM Controlled Scheme for Effective Operating of Proportionally Variable Force Solenoid Valve,” *KSAE,* vol. 28, no. 11, pp. 751-757, 2020.

[30] J. M. Perotti, “KEA-71 Smart Current Signature Sensor (SCSS),” 19 November 2010. [Online]. Available: https://ntrs.nasa.gov/citations/20110000497. [Accessed 12 March 2020].

[31] Z. Wilson, “E2E,” Texas Instruments, 28 February 2014. [Online]. Available: https://e2e.ti.com/blogs_/b/industrial_strength/posts/tips-for-solenoid-driving. [Accessed 22 March 2021].

[32] TI, “DRV832x 6 to 60-V Three-Phase Smart Gate Driver,” August 2018. [Online]. Available: https://www.ti.com/lit/ds/symlink/drv8323.pdf?ts=1645563315188&ref_url=https%253A%252F%252Fwww.ti.com%252Fproduct%252FDRV8323. [Accessed 15 Jun 2021].

[33] S. C. Industries, “NVMFS6H824N DATA SHEET,” May 2022. [Online]. Available: https://www.onsemi.com/pdf/datasheet/nvmfs6h824n-d.pdf. [Accessed 2 May 2023].

[34] N. Oborny and A. Ojha, “Understanding Smart Gate Drive,” Texas Instruments, Dallas, 2021.

[35] Toshiba Electronic Devices & Storage Corporation, “Power MOSFET Electrical Characteristics,” 2017. [Online]. Available: https://toshiba.semicon-storage.com/info/application_note_en_20230209_AKX00063.pdf?did=13415. [Accessed 14 May 2023].

[36] ONSEMI, “NVMFS6H824N Technical Documentation,” ONSEMI, 1 January 2023. [Online]. Available: https://www.onsemi.com/products/discrete-power-modules/mosfets/nvmfs6h824n#technical-documentation. [Accessed 3 May 2023].

[37] Nexperia, “PMBT2222A Product data sheet,” 27 July 2022. [Online]. Available: https://assets.nexperia.com/documents/data-sheet/PMBT2222A.pdf. [Accessed 2023 May 2023].

[38] TI, “INA381,” October 2019. [Online]. Available: https://www.ti.com/lit/ds/symlink/ina381.pdf?ts=1646816863336&ref_url=https%253A%252F%252Fwww.google.com%252F. [Accessed 11 March 2021].

[39] TI, “INAx180 Datasheet,” July 2022. [Online]. Available: https://www.ti.com/lit/ds/symlink/ina180.pdf?ts=1683184845053&ref_url=https%253A%252F%252Fwww.google.com%252F. [Accessed 4 May 2023].

[40] TI, “Fast-response overcurrent event detection circuit,” May 2019. [Online]. Available: https://www.ti.com/lit/an/sboa349/sboa349.pdf?ts=1683274732834&ref_url=https%253A%252F%252Fwww.google.com%252F. [Accessed 5 May 2023].

[41] A. Forbes, “Automotive Load Short-Circuit Reliability and Accurate Current Sensing Reference Design,” Texas Instruments, Dallas, 2019.

[42] D. D. Graovac, M. Pürschel and A. Kiep, “MOSFET Power Losses Calculation Using the Datasheet Parameters,” Infineon Technologies AG, Neubiberg, 2006.

[43] D. Incorporated, “SDT5H100SB datasheet,” January 2019. [Online]. Available: https://www.mouser.co.uk/datasheet/2/115/DIOD_S_A0007740194_1-2542897.pdf. [Accessed 8 May 2023].

[44] TI, “Layout Guide for the DRV832x Family of Three-Phase Smart Gate Drivers,” Texas Instruments Incorporated, Texas, 2018.

[45] TI, “AN-1149 Layout Guidelines for Switching Power Supplies,” Texas Instruments Incorporated, Texas, 2013.

[46] TI, “AN-1520 A Guide to Board Layout for Best Thermal Resistance for Exposed Packages,” Texas Instruments Incorporated, Texas, 2013.

[47] TI, “Best Practices for Board Layout of Motor Drivers,” Texas Instruments Incorporated, Texas, 2018.

[48] T. Hegarty, “Reduce buck-converter EMI and voltage stress by minimizing inductive parasitics,” Texas Instruments Incorporated, Texas, 2016.

[49] M. Rangu and A. Eadie, Getting EMC Design Right First Time, EMC FastPass, 2019.

[50] TI, “Ringing Reduction Techniques for NexFET_TM High Performance MOSFETs,” Texas Instruments Incorporated, Dallas, 2011.

[51] K. Kam, D. Pommerenke, F. Centola, C.-w. Lam and R. Steinfeld, “EMC Guideline for Synchronous Buck Converter Design,” in *International Symposium on Electromagnetic Compatibility*, 2009.

[52] D. Pommerenke, R. Steinfeld , K. Kam and C.-w. Lam, “EMI Analysis Methods for Synchronous Buck Converter EMI Root Cause Analysis,” in *IEEE International Symposium on Electromagnetic Compatibility*, Detroit, 2008.

[53] ST, “Mitigation technique of the SiC MOSFET gate voltage glitches with Miller clamp,” STMicroelectronics, 2019.

[54] EMC FastPass, EMC TESTING: THE BEGINNER'S GUIDE, EMC FastPass, 2018.

[55] T. Hegarty, “An overview of radiated EMI specifications for power supplies,” Texas Instruments Incorporated, Dallas, 2018.

[56] TI, “PCB Design Guidelines For Reduced EMI,” Texas Instruments Incorporated, Dallas, 1999.

[57] N. Oborny and A. Ojha, “Understanding Smart Gate Drive,” Texas Instruments Incorporated, Dallas, 2021.

[58] U. STEIN, J. EILERS, J. LAVENDER and L. Stephen, “Valve unit a fluid working machine comprising a valve unit”. GB Patent EP2961983, 1 March 2013.

[59] M. Ehsan, W. H. S. Rampen and S. H. Salter, “Modeling of Digital-Displacement Pump-Motors and Their Application as Hydraulic Drives for Nonuniform Loads,” *Journal of Dynamic Systems, Measurement, and Control*, vol. 122, no. ASME, pp. 211-215, 2000.

[60] M. S. LAIRD, “LPV Reopening Detection and Automatic Tuning,” Artemis Inteligent Power Ltd, Loanhead, 2013.

[61] S. Fink and M. Saterbak, “METHOD AND DEVICE FOR DETERMINING THE STATE OF AN ELECTRICALLY CONTROLLED VALVE”. USA Patent US10429427B2, 1 October 2019.

[62] D. S. Association, INTERNATIONAL STANDARD ISO 11452-4, Nordhavn: DANSK STANDARD, 2020.

[63] H. Matthias Werner, “DEVICE FOR DETERMINING THE STRENGTH OF THE MAGNETIC FELD OF ANELECTROMAGNET”. USA Patent US7898243B2, 21 April 2008.

[64] W. Holger Menges, “SOLENOID - ACTUATOR WITH PASSIVE TEMPERATURE COMPENSATION”. USA Patent US2017/0256350A1, 2 March 2017.

[65] K. Barnickel, “Verfahren zum Betreiben eines Magnetventils”. Germany Patent DE102013201134A1, 24 January 2013.

[66] J. Bedingfield, “MEDICAL FLUID MACHINE HAVING SOLENOD CONTROL SYSTEM WITH TEMPERATURE COMPENSATION”. USA Patent US7746620B2, 27 August 2009.

[67] S. Coakley and M. Binnard, “COMPENSATING TEMPERATURE EFFECTS IN MAGNETIC ACTUATORS”. USA Patent US8705222B2 , 22 April 2014.

[68] Y. Kinbara, “ELECTROMAGNETIC CONTACTOR”. USA Patent US6845001B1, 18 January 2005.

[69] S. D. Jacob, F. Najjar, G. W. Meyer and R. D. Ross, “METHOD OF CONTROLLING SOLENOID VALVE”. USA Patent US2011/0094589A1, 28 April 2011.

[70] C. Haggenmiller and A. Mayer-Dick, “METHOD FOR ACTUATING ASOLENOID VALVE AND ASSOCATED DEVICE”. USA Patent US2010/0193036A1, 5 August 2010.

[71] W. E. Schultz, D. Kleinert, P. Tappe, J. Heinzmann and H. E. Wassermann, “METHOD AND CIRCUIT FOR DETECTING THE ARMATURE POSITION OF AN THE ARMATURE POSITION OF AN”. USA Patent US6949923B2 , 27 September 2005.

[72] M. Koch and R. Rösel, “MODIFIED ELECTRICAL ACTUATION OF AN ACTUATOR FOR DETERMINING THE TIME AT WHICH AN ARMATURE STRIKES A STOP”. USA Patent US9412508B2, 9 August 2016.

[73] O. Ohligschläger, “Verfahren zur Ansteuerung eines zyklisch betriebenen Elektromagneten”. Germany Patent DE102019131388A1, 21 November 2019.

[74] ISO, “ISO 16750-2: Road vehicles — Environmental conditions and testing for electrical and electronic equipment,” ISO copyright office, Geneva, 2012.

[75] L. Yamin and C. Wanming, “A New Non-Restoring Square Root Algorithm and Its VLSI Implementations,” in *International Conference on Computer Design,* Austin, 1996.

[76] T. Sutikno, “An Efficient Implementation of the Non Restoring Square Root Algorithm in Gate Level,” *International Journal of Computer Theory and Engineering,* vol. Vol.3, no. No.1, 2011.

[77] N. J. Caldwell and S. M. Laird, “METHOD OF MEASURING A PROPERTY OF ENTRAINED GAS IN A HYDRAULIC FLUID AND FLUID - WORKING MACHINE”. USA Patent US9828986B2, 28 November 2017.

[78] M. Orndorff, S. Driscoll and J. Roberts, “SPEED CONTROL FOR DIAPHRAGM PUMP”. USA Patent US8926291B2, 6 January 2015.

[79] M. Brett and P. McCurry, “MEASURING HYDRAULIC FLUID PRESSURE IN A FLUID-WORKING MACHINE”. USA Patent US11073147B2, 27 July 2021.

[80] F. McIntyre and S. Laird, “FLUID WORKING MACHINE AND METHOD OF OPERATING A FLUID WORKING MACHINE”. USA Patent US10584691B2, 10 March 2020.

[81] W. H. S. Rampen, N. J. Caldwell, M. R. Fielding, U. Stein and J. T. Campbell, “FLUID-WORKING MACHINE AND METHOD OF DETECTING AFAULT”. USA Patent US9133839B2, 15 September 2015.

[82] D. Dumnov and N. Caldwell, “A CYLINDER ENABLING ALGORITHM FOR REDUCTION IN LOW FREQUENCY PULSATION FROM DIGITAL DISPLACEMENT PUMPS,” in *Symposium on Fluid Power and Motion Control*, Bath, 2022.

[83] I. Baptiste and A. Wood, “Allegro Microsystems,” 25 January 2021. [Online]. Available: https://www.allegromicro.com/-/media/files/application-notes/an296220-bootstrap-supply.pdf?sc_lang=en&hash=DC1AE9D311CE6301F40020DADFD60464. [Accessed 12 February 2022].

[84] IXYS, “IX4310T,” 9 January 2021. [Online]. Available: https://www.ixysic.com/home/pdfs.nsf/www/IX4310T.pdf/$file/IX4310T.pdf. [Accessed 10 March 2021].

[85] S. Fraisse, “Smart High Side Switches,” Infineon Technologies, Munich, 2010.

[86] Infineon Technologies, “Dynamic thermal behavior of MOSFETs,” Infineon Technologies AG, Munich, 2017.

[87] Toshiba Electronic Devices & Storage Corporation, “Power MOSFETs’ thermal design and attachment of a thermal fin,” Toshiba Electronic Devices & Storage Corporation, 2017.

[88] VISHAY, “Power MOSFET Basics: Understanding Gate Charge and Using It To Assess Switching Performance,” 16 February 2016. [Online]. Available: https://www.vishay.com/docs/73217/an608a.pdf. [Accessed 22 March 2021].

[89] J. M. Perotti, “KEA-71 Smart Current Signature Sensor (SCSS),” 25 August 2013. [Online]. Available: https://ntrs.nasa.gov/citations/20110000497. [Accessed May 12 2020].

Appendices

Appendix A

Next-generation coil driver (NGCD) evaluation board schematics

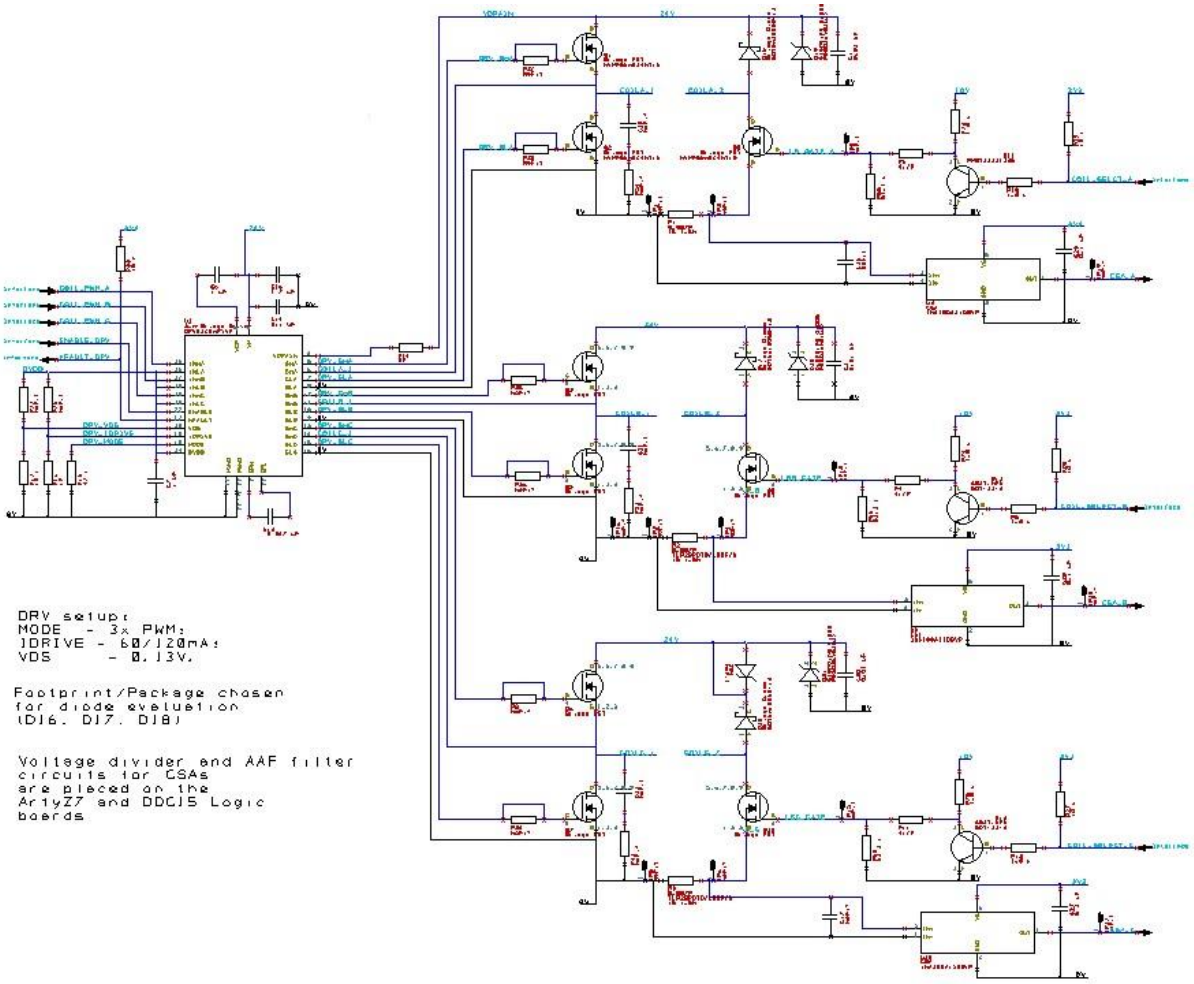

	Project: NGCD evaluation board	Number: 01	Rev.:A
Designed for: Danfoss internal use	Page title: 3x Coil driver and coil current sensing		
Eng.: Andriy Tkachuk	Date: __/__/2020		Danfoss

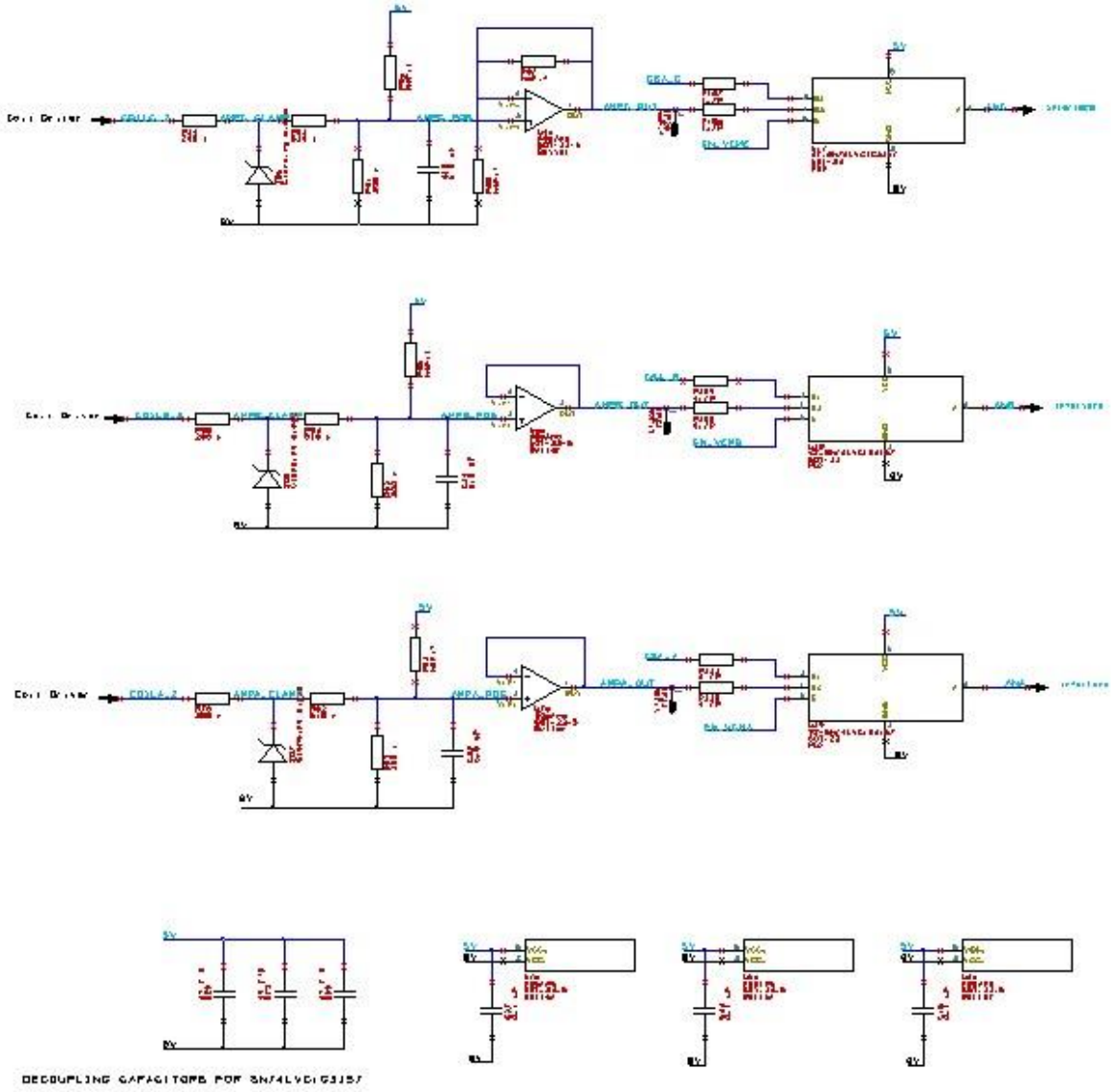

	Project: NGCD evaluation board	Number: 01	Rev.:A
Designed for: Danfoss internal use	Page title: 3x Coil voltage sensing		
Eng.: Andriy Tkachuk	Date: __/__/2020		Danfoss

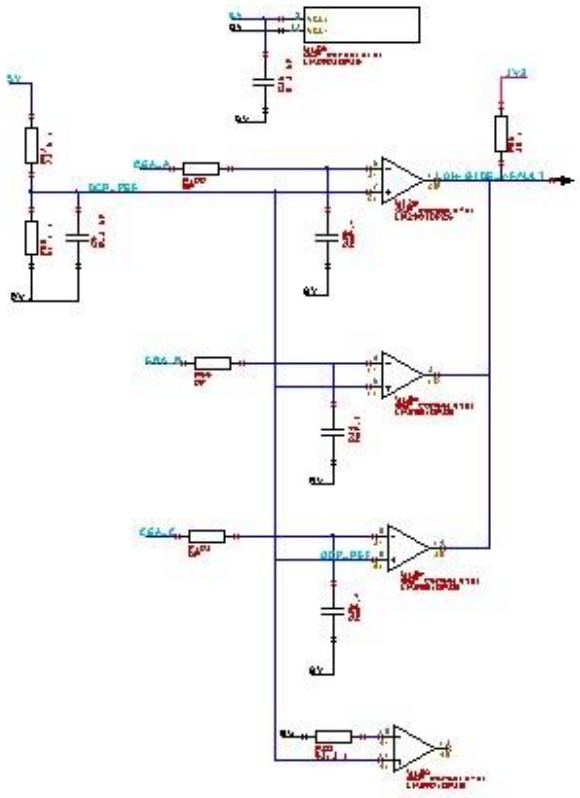

OCP reference is set to 2.1V. Which is 16A

	Project: NGCD evaluation board	Number: 01	Rev.:A
Designed for: Danfoss internal use	Page title: Low-side OCP		
Eng.: Andriy Tkachuk	Date: __/__/2020		Danfoss

Input protection

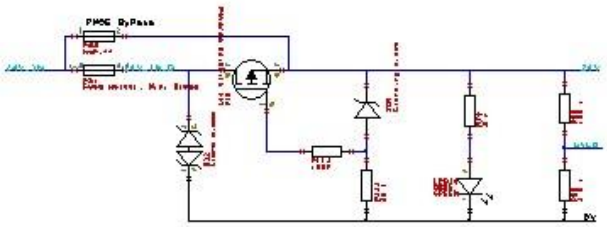

5V power supply

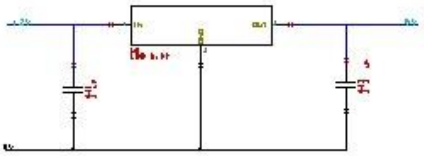

12V power supply

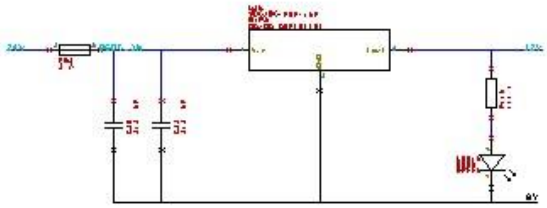

3.3V power supply

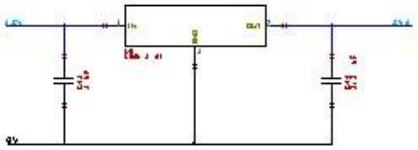

10V power supply

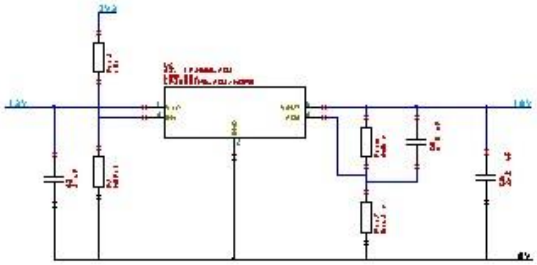

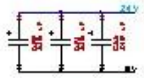

	Project: NGCD evaluation board	Number: 01	Rev.:A
Designed for: Danfoss internal use	Page title: Power supply		
Eng.: Andriy Tkachuk	Date: __/__/2020		Danfoss

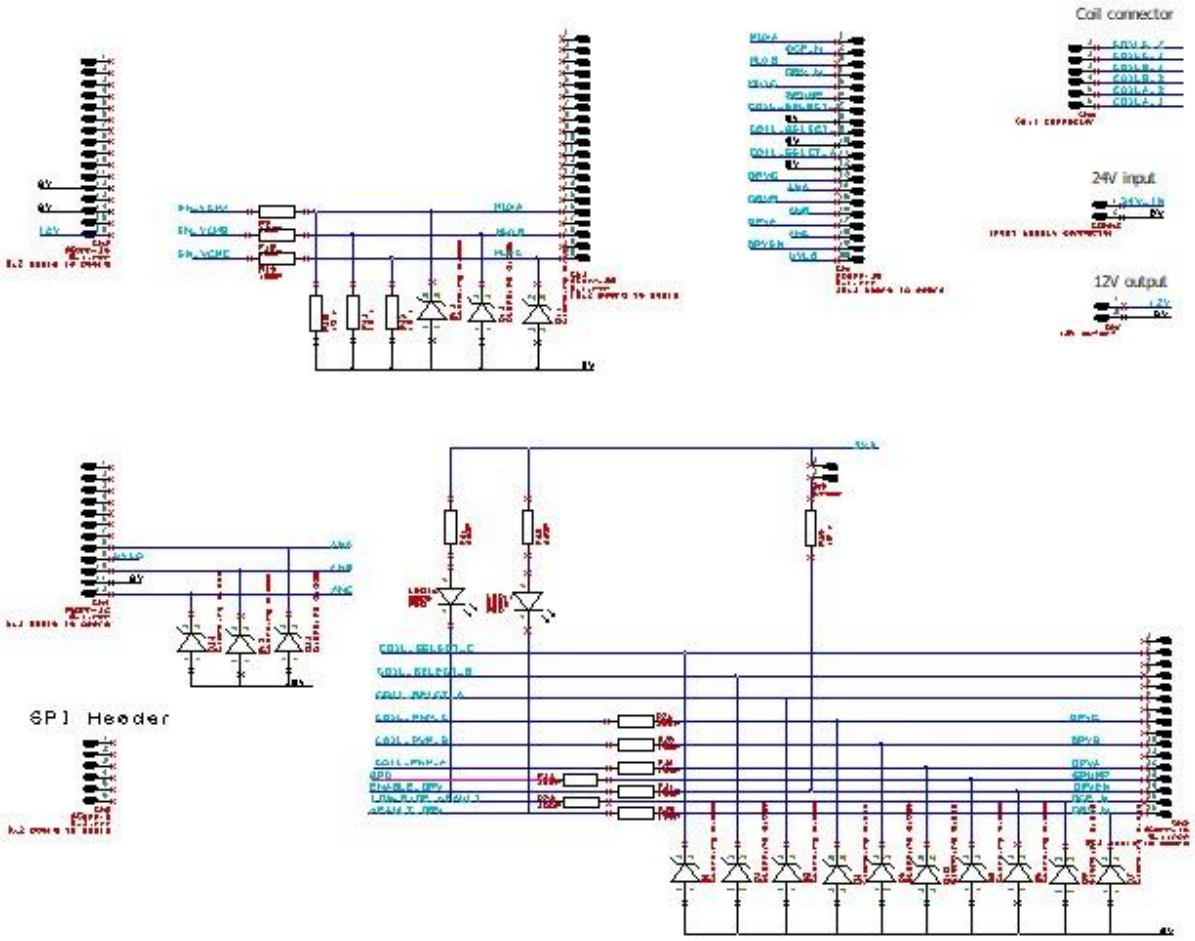

	Project: NGCD evaluation board	Number: 01	Rev.:A
Designed for: Danfoss internal use	Page title: Connectors and Interface and ESD protection		
Eng.: Andriy Tkachuk	Date: __/__/2020		Danfoss

Next-generation coil driver (NGCD) evaluation board artwork

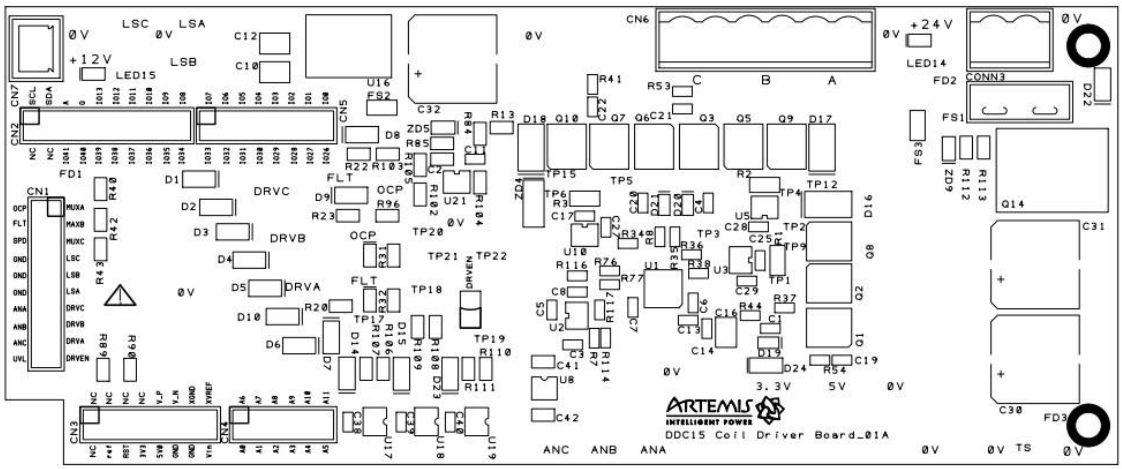

Not to scale	Project: NGCD evaluation board	Number: 01	Rev.:A
Viewed from top side	Plot name: Board Layer = Top Silk Screen		
Eng.: Andriy Tkachuk	Date: __/__/2020		Danfoss

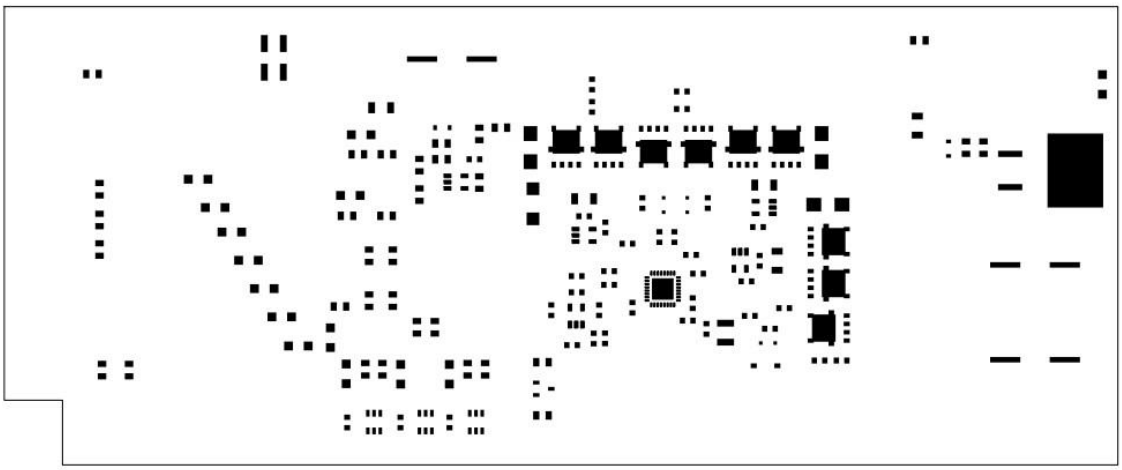

Not to scale	Project: NGCD evaluation board	Number: 01	Rev.:A
Viewed from top side	Plot name: Board Layer = Top Solder Paste		
Eng.: Andriy Tkachuk	Date: __/__/2020		Danfoss

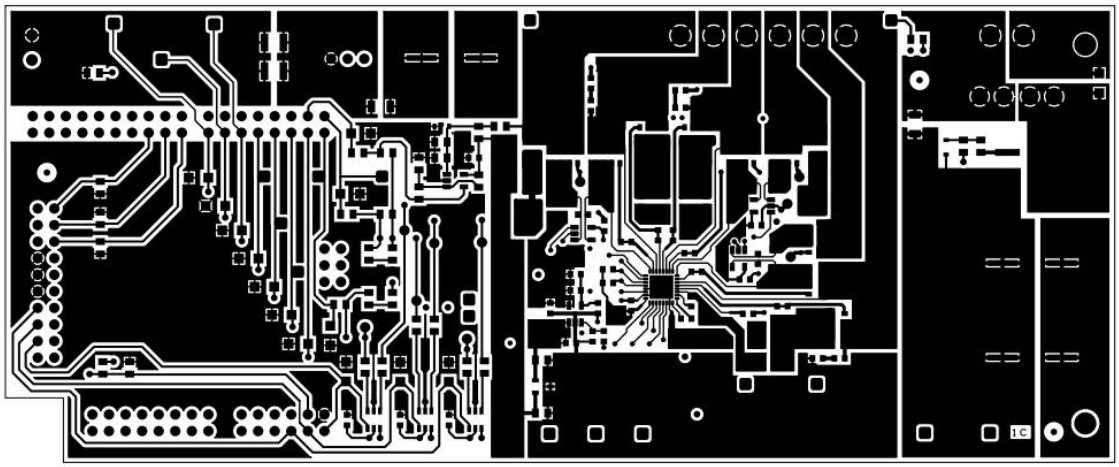

Not to scale	Project: NGCD evaluation board	Number: 01	Rev.:A
Viewed from top side	Plot name: Board Layer = Top Copper		
Eng.: Andriy Tkachuk	Date: __/__/2020		Danfoss

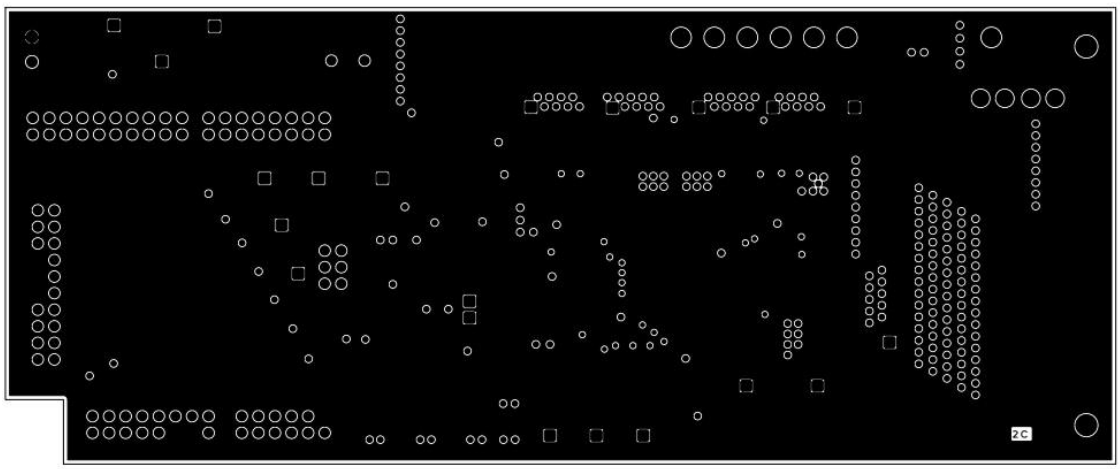

Not to scale	Project: NGCD evaluation board	Number: 01	Rev.:A
Viewed from top side	Plot name: Board Layer = Ground A		
Eng.: Andriy Tkachuk	Date: __/__/2020		Danfoss

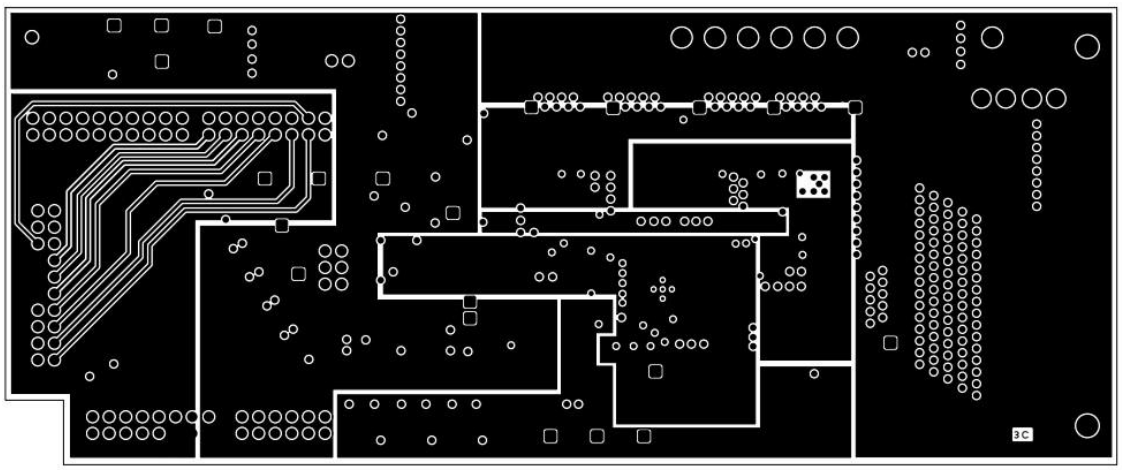

Not to scale	Project: NGCD evaluation board	Number: 01	Rev.:A
Viewed from top side	Plot name: Board Layer = Power A		
Eng.: Andriy Tkachuk	Date: __/__/2020		Danfoss

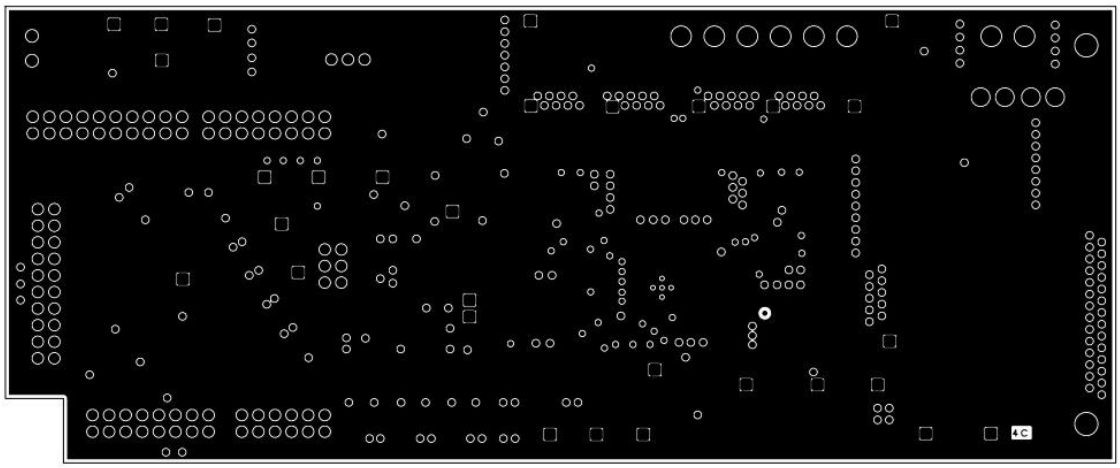

Not to scale	Project: NGCD evaluation board	Number: 01	Rev.:A
Viewed from top side	Plot name: Board Layer = Power B		
Eng.: Andriy Tkachuk	Date: __/__/2020		Danfoss

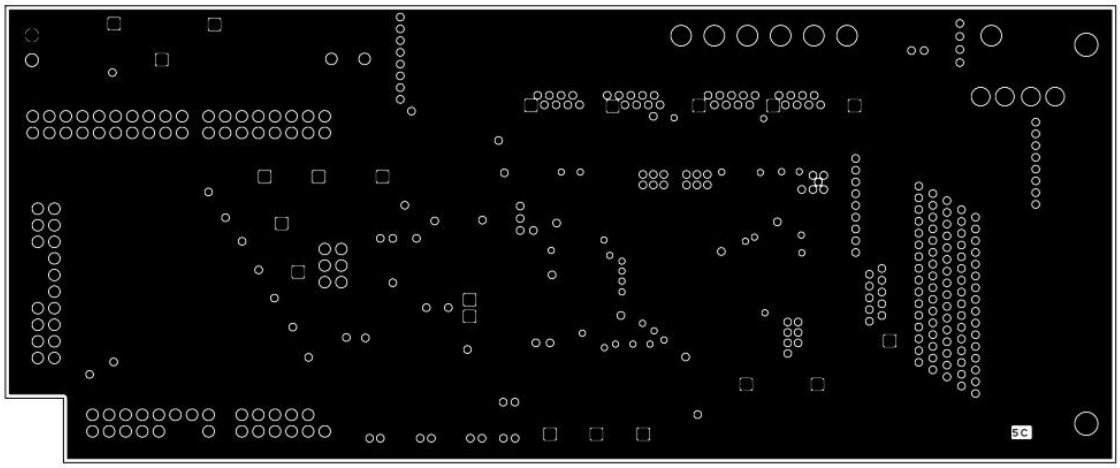

Not to scale	Project: NGCD evaluation board	Number: 01	Rev.:A
Viewed from top side	Plot name: Board Layer = Ground B		
Eng.: Andriy Tkachuk	Date: __/__/2020		Danfoss

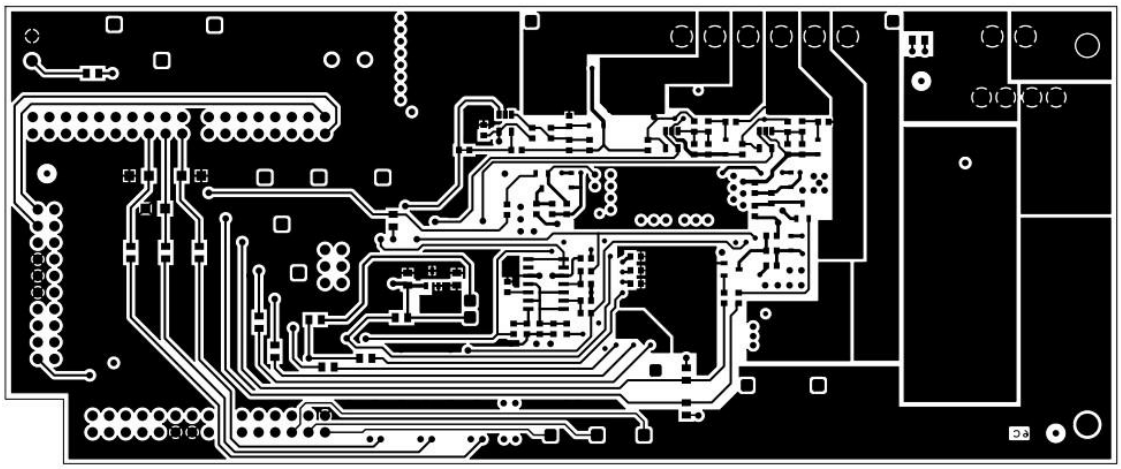

Not to scale	Project: NGCD evaluation board	Number: 01	Rev.:A
Viewed from top side	Plot name: Board Layer = Bottom Copper		
Eng.: Andriy Tkachuk	Date: __/__/2020		Danfoss

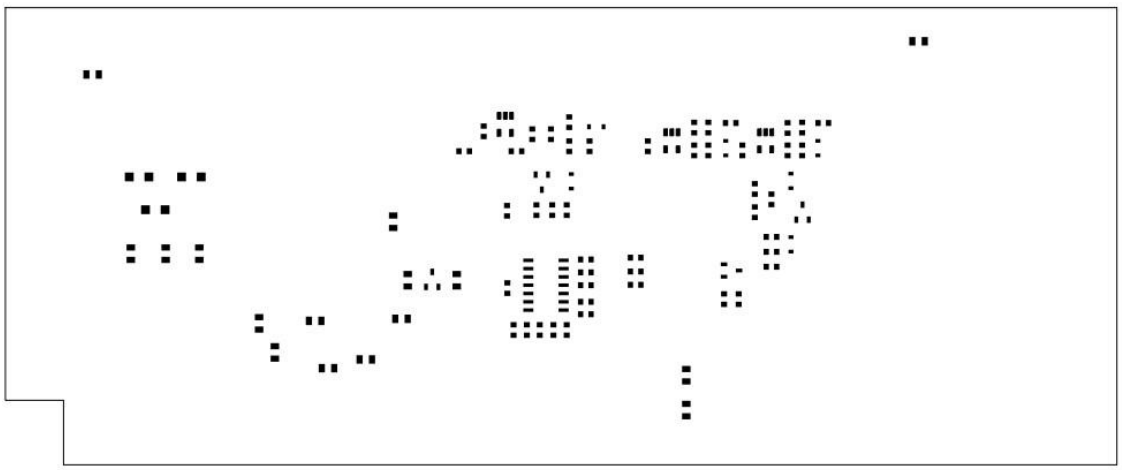

Not to scale	Project: NGCD evaluation board	Number: 01	Rev.:A
Viewed from top side	Plot name: Board Layer = Bottom Solder Paste		
Eng.: Andriy Tkachuk	Date: __/__/2020		Danfoss

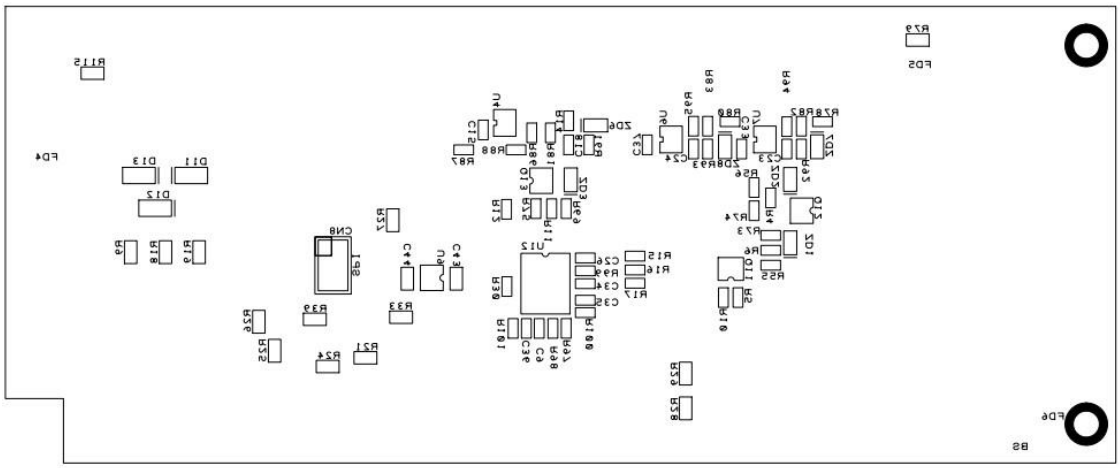

Not to scale	Project: NGCD evaluation board	Number: 01	Rev.:A
Viewed from top side	Plot name: Board Layer = Silk Screen		
Eng.: Andriy Tkachuk	Date: __/__/2020		Danfoss

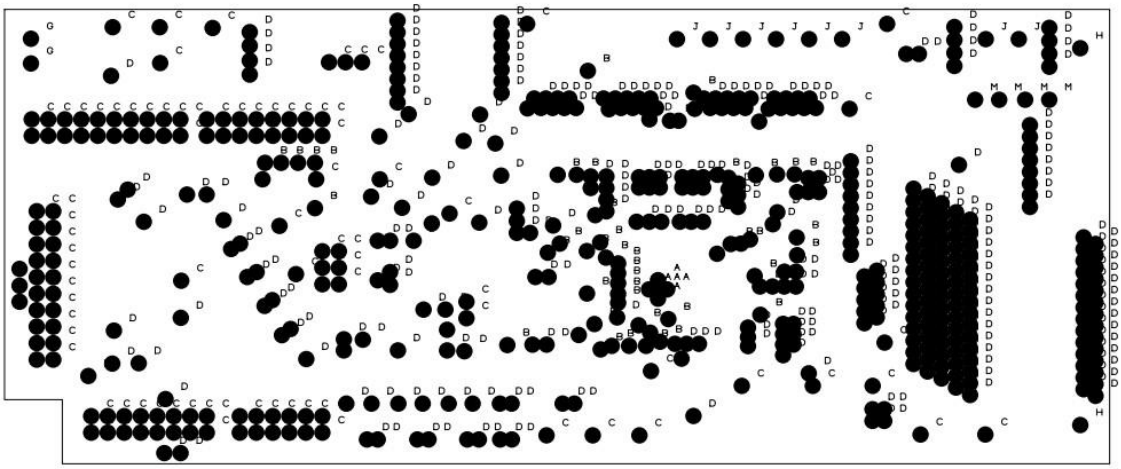

Drill Table

All Holes

Tool	Size	Count	ID	Symbol
T001	0.00787	5	A	
T002	0.01575	46	B	
T003	0.02400	346	D	
T004	0.03937	123	C/N	
T005	0.04724	2	G	
T006	0.05512	8	J	
T007	0.07087	4	M	
T008	0.13386	2	H	
All		536		

Sizes in Inches

Not to scale	Project: NGCD evaluation board	Number: 01	Rev.:A
Viewed from top side	Plot name: Drill Drawing		
Eng.: Andriy Tkachuk	Date: __/__/2020		Danfoss

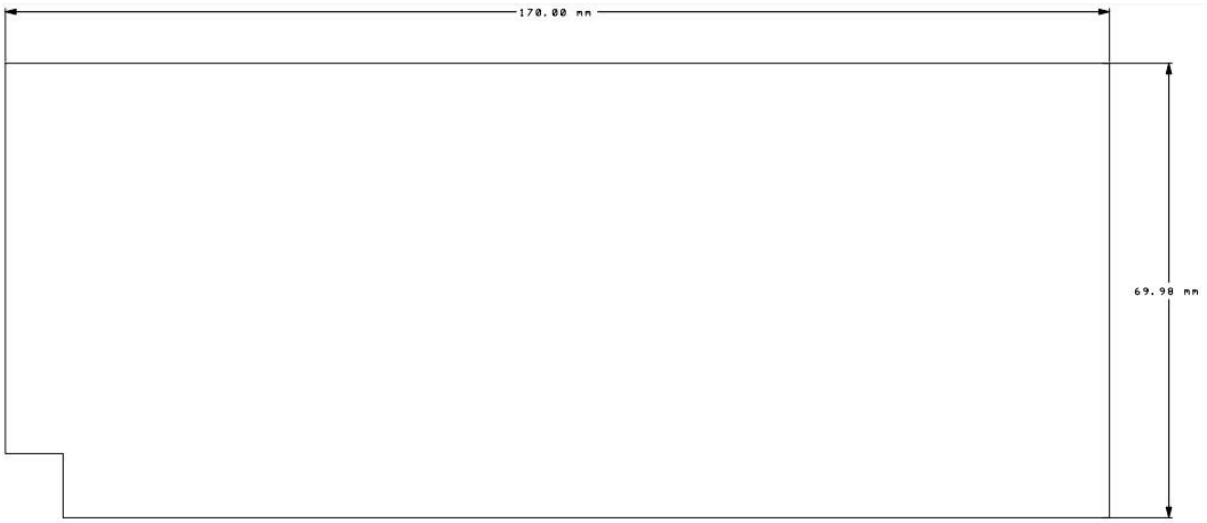

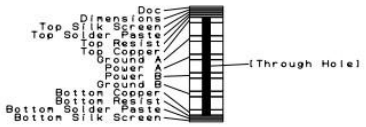

Not to scale	Project: NGCD evaluation board	Number: 01	Rev.:A
Viewed from top side	Plot name: Board Dimensions		
Eng.: Andriy Tkachuk	Date: __/__/2020		Danfoss

Appendix B

Next-generation coil driver (NGCD) evaluation board firmware

```
----------------------------------------------------------------------------------
-- Company: Danfoss
-- Engineer: Andriy Tkachuk
--
-- Create Date: --/--/2021
-- Design Name:
-- Module Name: Valve_Actuation - Behavioral
-- Project Name: Next Generation Valve Actuation for Digital Displacement® Machines
-- Target Devices: Arty A7 + NGCD evaluation board_01A
-- Tool Versions:
-- Description:  Top level
--
-- Dependencies:
--
-- Revision:
-- Revision 0.01 - File Created
-- Additional Comments: AHDL
--
----------------------------------------------------------------------------------


library ieee;
use ieee.std_logic_1164.all;
use ieee.numeric_std.all;

entity Valve_Actuation is
   Generic (
            g_sys_clk         : integer := 100_000_000;    --system clock frequency in Hz
            g_ce_clk          : integer := 5_000_000;      --new clock frequency in Hz
            g_adc_bits        : integer := 12;
            g_Number_of_valves  : integer := 3
          );
   Port    (
            CLK           : in  std_logic;                  -- system clock
            Reset         : in  std_logic;
            Vp_in         : in  std_logic;                  -- Dedicated Analog Input Pair
            Vn_in         : in  std_logic;
            vaux0_p       : in  std_logic;                  -- Auxiliary Channel 0
            vaux0_n       : in  std_logic;
            vaux7_p       : in  std_logic;                  -- Auxiliary Channel 7
            vaux7_n       : in  std_logic;
            vaux15_p      : in  std_logic;                  -- Auxiliary Channel 15
            vaux15_n      : in  std_logic;
            Turn_on_command : in  std_logic;
```

```
            Nfault_drv     : in std_logic;
            Nfault_low_side : in std_logic;
            Valve_select    : in std_logic_vector (g_Number_of_valves - 1 downto 0);
            Coil_pwm        : out std_logic_vector (g_Number_of_valves - 1 downto 0);
            Coil_select     : out std_logic_vector (g_Number_of_valves - 1 downto 0);
            Mux             : out std_logic_vector (g_Number_of_valves - 1 downto 0);
            Led             : out std_logic_vector (g_Number_of_valves - 1 downto 0);
            Enable_drv      : out std_logic;
            Valve_reopening : out std_logic_vector (g_Number_of_valves - 1 downto 0);
            Led_start_fault_detection : out std_logic
        );
end Valve_Actuation;

architecture Behavioral of Valve_Actuation is


component xadc_wiz_0 is                                 -- declaring component
  port
  (
   daddr_in      : in  STD_LOGIC_VECTOR (6 downto 0);     -- Address bus for the dynamic
reconfiguration port
   den_in        : in  STD_LOGIC;                      -- Enable Signal for the dynamic reconfiguration port
   di_in         : in  STD_LOGIC_VECTOR (15 downto 0);    -- Input data bus for the dynamic
reconfiguration port
   dwe_in        : in  STD_LOGIC;                      -- Write Enable for the dynamic reconfiguration port
   do_out        : out  STD_LOGIC_VECTOR (15 downto 0);   -- Output data bus for dynamic
reconfiguration port
   drdy_out      : out  STD_LOGIC;                      -- Data ready signal for the dynamic reconfiguration
port
   dclk_in       : in  STD_LOGIC;                      -- Clock input for the dynamic reconfiguration port
   reset_in      : in  STD_LOGIC;                      -- Reset signal for the System Monitor control logic
   vauxp0        : in  STD_LOGIC;                       -- Auxiliary Channel 0
   vauxn0        : in  STD_LOGIC;
   vauxp7        : in  STD_LOGIC;                      -- Auxiliary Channel 7
   vauxn7        : in  STD_LOGIC;
   vauxp15       : in  STD_LOGIC;                       -- Auxiliary Channel 15
   vauxn15       : in  STD_LOGIC;
   busy_out      : out  STD_LOGIC;                      -- ADC Busy signal
   channel_out    : out  STD_LOGIC_VECTOR (4 downto 0);    -- Channel Selection Outputs
   eoc_out       : out  STD_LOGIC;                       -- End of Conversion Signal
   eos_out       : out  STD_LOGIC;                       -- End of Sequence Signal
   ot_out        : out  STD_LOGIC;                      -- Over-Temperature alarm output
   vccaux_alarm_out : out  STD_LOGIC;                       -- VCCAUX-sensor alarm output
   vccint_alarm_out : out  STD_LOGIC;                      -- VCCINT-sensor alarm output
   user_temp_alarm_out : out  STD_LOGIC;                       -- Temperature-sensor alarm output
   alarm_out     : out STD_LOGIC;                        -- OR'ed output of all the Alarms
   vp_in         : in  STD_LOGIC;                      -- Dedicated Analog Input Pair
   vn_in         : in  STD_LOGIC
   );
end component;
```

```
component Coil_Current_Control is                    -- declaring component
   Port(
      Clk            : in std_logic;            -- system clock
      Current_control_ce : in std_logic;            --new clock, used to run controller proces and pwm
generation process
      Adc_ready       : in std_logic;
      Reset           : in std_logic;
      Valve_select     : in std_logic;
      Turn_on_command   : in std_logic;
      Fault           : in std_logic;
      Adc_data        : in std_logic_vector;
      Start_detection   : out std_logic;
      Coil_pwm        : out std_logic;
      Coil_select      : out std_logic;
      Mux             : out std_logic;
      Led             : out std_logic
      --Start_reopening_detection : out std_logic        --turns on for one clock cycle
      );
end component Coil_Current_Control;

component Valve_Reopening_Detection is
         Port(
                  Reset           : in std_logic;
                  CLK             : in std_logic;                  --system clock
                  Adc_ready       : in std_logic;                  --if '1' ADC value is ready
                  Start_detection    : in std_logic;                  --turns '1' for valve reopening
detection
      Adc_data        : in std_logic_vector(g_adc_bits-1 downto 0); --analogue input data measured
coil voltage
                  Reopened        : out std_logic                  --active high
                  );
end component Valve_Reopening_Detection;

component Coil_driver_fault_detection is
         Port(
      Reset           : in std_logic;
      CLK             : in std_logic;          --system clock
      Nfault_low_side    : in std_logic;
      Nfault_drv       : in std_logic;
      Enable_drv       : out std_logic;
      Faulty_drv       : out std_logic;
      Led_start_fault_detection : out std_logic
         );
end component Coil_driver_fault_detection;

constant ADC_LSB_NEW      : integer := 15-g_adc_bits+1;    --new LSB index to define the  ADCs
data size to be used
constant CE_CLK_PERIOD    : integer := g_sys_clk/g_ce_clk;  --number of clocks in new clock
period
```

```
signal s_current_control_ce : std_logic;
signal xadc_data          : std_logic_vector (15 downto 0);
signal xadc_adress        : std_logic_vector (6 downto 0):= "0010000";      --16 is the number of the
ADC channel 0
signal xadc_ready         : std_logic := '0';
signal xadc_not_ready     : std_logic := '0';
signal enable             : std_logic;
type t_xadc_data  is array (0 to g_number_of_valves - 1) of std_logic_vector(g_adc_bits-1 downto 0);
signal s_xadc_data        : t_xadc_data ;
signal s_adc_ready        : std_logic;
signal s_faulty_drv       : std_logic;

-- valve reopening detection data
type Type_start_reopening_detection is array (0 to g_number_of_valves - 1) of std_logic;
signal s_start_reopening_detection : Type_start_reopening_detection;
type Type_reopened is array (0 to g_number_of_valves - 1) of std_logic;
signal s_reopened                : Type_reopened;
-- end valve reopening detection data

begin

ADC: xadc_wiz_0                              --maping ports
  port map
  (
   daddr_in       =>  xadc_adress,              -- Address bus for the dynamic reconfiguration port
   den_in         =>  enable,                   -- Enable Signal for the dynamic reconfiguration port
   di_in          =>  (others => '0'),          -- Input data bus for the dynamic reconfiguration port
   dwe_in         =>  '0',                      -- Write Enable for the dynamic reconfiguration port
   do_out (15 downto 0)   => xadc_data,         -- Output data bus for dynamic reconfiguration port
not in use
   drdy_out       =>  xadc_ready,               -- Data ready signal for the dynamic reconfiguration port
   dclk_in        =>  CLK,                      -- Clock input for the dynamic reconfiguration port
   reset_in       =>  '0',                      -- Reset signal for the System Monitor control logic
   vauxp0         =>  vaux0_p,                  -- Auxiliary Channel 0
   vauxn0         =>  vaux0_n,
   vauxp7         =>  vaux7_p,                  -- Auxiliary Channel 7
   vauxn7         =>  vaux7_n,
   vauxp15        =>  vaux15_p,                 -- Auxiliary Channel 15
   vauxn15        =>  vaux15_n,
   busy_out       =>  open,                     -- ADC Busy signal
   channel_out    =>  open,                     -- Channel Selection Outputs
   eoc_out        =>  enable,                   -- End of Conversion Signal
   eos_out        =>  open,                     -- End of Sequence Signal
   alarm_out      =>  open,                     -- OR'ed output of all the Alarms
   vp_in          =>  Vp_in,                    -- Dedicated Analog Input Pair
   vn_in          =>  Vn_in
);

--Report constant usage
```

```
assert false report "Using generic constant g_Number_of_valves : " &
natural'image(g_Number_of_valves) severity NOTE;

--Generate main valves
--
--Generate the required number of valves.

Valve_array_CC : for i in 0 to  g_Number_of_valves - 1 generate
Inst_current_controller_valve: Coil_Current_Control           --maping  ports
port map
 (
   Clk              => CLK,                          -- system clock
   Current_control_ce => s_current_control_ce,              --current profile controller clock
   Adc_ready        => s_adc_ready,
   Reset            => Reset,
   Valve_select     => Valve_select(i),
   Turn_on_command   => Turn_on_command,
   Fault            => s_faulty_drv,
   Adc_data         => s_xadc_data(i),
   Start_detection   => s_start_reopening_detection(i),
   Coil_pwm         => Coil_pwm(i),
   Coil_select      => Coil_select(i),
   Mux              => Mux(i),
   Led              => Led(i)
);
end generate Valve_array_CC;

Valve_array_RD : for i in 0 to  g_Number_of_valves - 1 generate
Inst_Valve_Reopening_Detection: Valve_Reopening_Detection           --maping  ports
port map
 (
   Reset            => Reset,
   CLK              => CLK,
   Adc_ready        => s_adc_ready,
   Adc_data         => s_xadc_data(i),
   Start_detection   => s_start_reopening_detection(i),
   Reopened         => Valve_reopening(i)
);
end generate Valve_array_RD;

Inst_coil_driver_fault_detection : Coil_driver_fault_detection
port map
 (
   Reset        => Reset,
   CLK          => CLK,
   Nfault_low_side => Nfault_low_side,
   Nfault_drv    => Nfault_drv,
   Enable_drv    => Enable_drv,
   Faulty_drv    => s_faulty_drv,
   Led_start_fault_detection => Led_start_fault_detection
```

```
);

--* VALVE TIMING BASE CLOCK ENABLE GENERATOR
--*
--* Generates a clock enable signal to be used as a base by the valves
--*
--* Output CE is one CLK cycle pulse every VALVE_BASE_US microseconds
current_control_ce : process (CLK)
variable v_count : integer range 0 to CE_CLK_PERIOD - 1 := 0;
begin
        if (CLK ' event and CLK = '1') then
                if (Reset = '1') then
                        v_count := CE_CLK_PERIOD - 1;
                        s_current_control_ce <= '0';
                else
                        if (v_count = 0) then
                                v_count := CE_CLK_PERIOD - 1;
                                s_current_control_ce <= '1';
                        else
                                v_count := v_count - 1;
                                s_current_control_ce <= '0';
                        end if;
                end if;
        end if;
end process current_control_ce;



ADC_channel_select: process(CLK)

begin
  if(CLK'event and CLK = '1')then
    xadc_not_ready <= xadc_ready;
  if(xadc_ready = '1' AND xadc_not_ready = '0') then
    s_adc_ready <= '1';
    case xadc_adress is
      when "0010111" =>  --ADC channel 7
      s_xadc_data (0)    <= xadc_data(15 downto ADC_LSB_NEW); --Write data ANA
      when "0011111" =>  --ADC channel 15
      s_xadc_data (1)    <= xadc_data(15 downto ADC_LSB_NEW); --Write data ANB
      when "0010000" =>  --ADC channel 0
      s_xadc_data (2)    <= xadc_data(15 downto ADC_LSB_NEW); --Write data ANC
      when others => null;
    end case;
  elsif (xadc_ready = '0' AND xadc_not_ready = '1') then
    s_adc_ready <= '0';
    case xadc_adress is
      when "0010111" =>
      xadc_adress <= "0011111";
```

```
            when "0011111" =>
            xadc_adress <= "0010000";
            when "0010000"=>
            xadc_adress <= "0010111";
            when others => null;
        end case;
    else
        s_adc_ready <= '0';
    end if;
END IF;
end process ADC_channel_select;

end Behavioral;
```

```
----------------------------------------------------------------------------------
-- Company:  Danfoss
-- Engineer: Andriy Tkachuk
--
-- Create Date: --/--/2021
-- Design Name:
-- Module Name: Coil_Current_Control - Behavioral
-- Project Name: Next Generation Valve Actuation for Digital Displacement Machines
-- Target Devices: Arty A7 + NGCD evaluation board_01A
-- Tool Versions:
-- Description: Coil current profile control based on hysteresis closed-loop current control.
--                    Linear refference generation with boost option
-- Dependencies:
--
-- Revision:
-- Revision 0.01 - File Created
-- Additional Comments: VHDL
--
----------------------------------------------------------------------------------


library ieee;
use ieee.std_logic_1164.all;
use ieee.numeric_std.all;


entity Coil_Current_Control is
    Generic (
        g_T_rammp          : integer := 3_000; --in us
        g_T_plateau        : integer := 3_000; --in us
        g_T_hold           : integer := 2_500; --in us
        g_T_decay          : integer := 1_000_000; --in us
        g_I_rammp          : integer := 6_000; --in uA
        g_I_plateau        : integer := 6_000; --in uA
```

```
        g_I_hold          : integer := 3_000; --in uA
        g_hysteresis      : integer := 250;   --in uA
        g_I_boost         : integer := 1_000; --in uA
        g_adc_bits        : integer := 12;       --used bits of ADC
        g_cs_const        : integer := 23_571;    --Scaling constant of the CSA in mA
        g_ce_clk          : integer := 5_000_000  --clock frequency for current control timing in Hz



        );


    Port(
        Clk             : in std_logic;             -- system clock
        Current_control_ce : in std_logic;              --new clock, used to run controller proces and pwm
generation process
        Adc_ready       : in std_logic;
        Reset           : in std_logic;
        Valve_select    : in std_logic;
        Turn_on_command   : in std_logic;
        Fault           : in std_logic;
        Adc_data        : in std_logic_vector;
        Start_detection   : out std_logic;
        Coil_pwm        : out std_logic;
        Coil_select     : out std_logic;
        Mux             : out std_logic;
        Led             : out std_logic
        --Start_reopening_detection : out std_logic        --turns on for one clock cycle
        );


end Coil_Current_Control;


architecture Behavioral of Coil_Current_Control is
constant MULTIPLIER_SCALING_CONSTANT : integer := 2**11;                        --scaling
constant for ramp multiplier value
```

```
constant CURRENT_SCALING_CONSTANT : integer := 2**g_adc_bits*1000/g_cs_const;              --
scaling constant for current value (174 codes)

constant TIME_SCALING_CONSTANT  : integer := g_ce_clk/1_000_000;

constant T_RAMP              : integer := g_T_rammp*TIME_SCALING_CONSTANT;             --in clock
cycles

constant T_PLATEAU           : integer := g_T_plateau*TIME_SCALING_CONSTANT;           --in
clock cycles

constant T_HOLD              : integer := g_T_hold*TIME_SCALING_CONSTANT;              --in clock
cycles

constant T_DECAY             : integer := g_T_decay*TIME_SCALING_CONSTANT;             --in clock
cycles

constant I_BOOST             : integer := g_I_boost*CURRENT_SCALING_CONSTANT/1000;      --in
codes, current reference for boost stage

constant I_RAMP              : integer := g_I_rammp*CURRENT_SCALING_CONSTANT/1000;      --in
codes, current reference for ramp stage

constant I_PLATEAU           : integer := g_I_plateau*CURRENT_SCALING_CONSTANT/1000;    --
in codes, current reference for plat stage

constant I_HOLD              : integer := g_I_hold*CURRENT_SCALING_CONSTANT/1000;       --in
codes, current reference fro hold stage

constant I_HYSTERESIS        : integer := g_hysteresis*CURRENT_SCALING_CONSTANT/1000;   --
-in codes

constant I_RAMP_MULTIPLIER     : integer := (I_RAMP - I_BOOST) *
MULTIPLIER_SCALING_CONSTANT / T_RAMP;  --in codes, current reference for ramp stage

signal s_I_reference         : integer;                    --ongoing current reference

signal s_tc_counter          : integer;                    --counter used to switch on stages of the
current profile

signal s_I_coil              : integer;

signal s_switch_on_flag      : std_logic  := '0';                --

signal s_switch_off_flag     : std_logic  := '0';                --HIGH when valve switch on cycle is
over

signal s_start_flag          : std_logic  := '0';

signal s_sync_start          : std_logic  := '0';

type tc_state is (start_tc, ramp_stage, plateau_stage, hold_stage, decay_stage);

signal s_tc_state            : tc_state;

type cc_state is (cc_state_1, cc_state_2, cc_state_3, cc_state_4);

signal s_cc_state            : cc_state;
```

```
begin


--the process to turn on or turn off the curretn controller
switch_controller: process (CLK)
begin
   if(CLK'event and CLK = '1')then
      if(Reset = '1')then
         s_switch_on_flag  <= '0';                    --resets s_switch_on_flag when global reset is HIGH
      else
         if(Fault = '0')then
            if((Turn_on_command = '1' OR Valve_select = '1') AND s_switch_on_flag  = '0')then   --when Turn_on_comand and Valve_select are HIGH sets HIGH the s_switch_on_flag
               s_switch_on_flag  <= '1';
            elsif(s_switch_off_flag = '1')then
               s_switch_on_flag  <= '0';                --resets s_switch_on_flag when s_switch_off_flag is HIGH
            end if;
         else
            s_switch_on_flag  <= '0';
         end if;
      end if;
   end if;
end process switch_controller;


--the process to control the timing of the current control according to the custom current profile
timing_controller: process (CLK)
begin
if(CLK'event and CLK = '1') then
   if(s_switch_on_flag = '0')then                    --resets the controller process variables to the initial values
      s_tc_counter        <=  0;
      s_switch_off_flag    <= '0';
      s_start_flag        <= '0';
      s_tc_state          <= start_tc;
```

```
    elsif(Current_control_ce = '1') then
      s_tc_counter  <= s_tc_counter  + 1;                    --incrementing the switch_on counter
      case s_tc_state is
        when start_tc =>
          s_start_flag <= '1';                          --initiating Current Control
          s_tc_state <= ramp_stage;
        when ramp_stage =>                              --initiating the ramp stage of the current profile
          if(s_tc_counter = T_ramp) then
            s_tc_counter  <= 0;
            s_tc_state <= plateau_stage;
          end if;
        when plateau_stage =>                           --initiating the plateau stage of the current profile
          if(s_tc_counter = T_PLATEAU) then
            s_tc_counter  <= 0;
            s_tc_state <= hold_stage;
          end if;
        when hold_stage =>                              --initiating the hold stage of the current profile
          if(s_tc_counter = T_HOLD) then
            s_tc_counter  <= 0;
            s_tc_state <= decay_stage;
          end if;
        when decay_stage =>                             --initiating the hold stage of the current profile
          if(s_tc_counter = T_DECAY) then
            s_switch_off_flag <= '1';
          end if;
        when others => null;
      end case;
    end if;
end if;
end process timing_controller;

--the process to control solenoid valve current according to the custom current profile
current_controller: process (CLK)
```

```
begin
if(CLK'event and CLK = '1') then
   if(s_start_flag = '0')then                                  --resets the current_controller process variables
to the initial values
      Coil_pwm     <= '0';
      Coil_select   <= '1';
      Mux          <= '0';
      Led          <= '0';
      s_sync_start  <= '0';
      s_cc_state    <= cc_state_1;
      Start_detection <= '1';
   else
      if(s_sync_start = '0')then
         Coil_select   <= '0';                                --Switch-on flywheel mosfet
         Coil_pwm      <= '1';                                 --Switch-on PWM mosfet
         Mux          <= '0';
         Led          <= '1';
         s_sync_start  <= '1';
         Start_detection <= '0';
       else
          case s_cc_state is
            when cc_state_1 =>
               if(Adc_ready = '1')then                             --synchronising PWM with ADC sampling
frequency
                  s_I_coil <= to_integer(unsigned(Adc_data));
                  case s_tc_state is
                     when ramp_stage =>
                        s_I_reference <= s_tc_counter * I_RAMP_MULTIPLIER;   --multiplying counter
value by ramp reference
                        s_cc_state <= cc_state_2;
                     when plateau_stage =>
                        s_I_reference  <= I_PLATEAU;                 --assigning the ongoing current
reference value for plateau stage
                        s_cc_state <= cc_state_4;
                     when hold_stage =>
```

```
                    s_I_reference  <= I_HOLD;                    --assigning the ongoing current
reference value for hold stage
                    s_cc_state <= cc_state_4;
                  when decay_stage =>
                    Coil_pwm     <= '0';
                    Coil_select   <= '1';
                    Mux          <= '1';
                    Led          <= '0';
                    Start_detection <= '1';
                  when others => null;
                end case;
              end if;
            when cc_state_2 =>
              s_I_reference <= s_I_reference / Multiplier_scaling_constant;
              s_cc_state <= cc_state_3;
            when cc_state_3 =>
              s_I_reference  <= s_I_reference + I_BOOST;          --assigning the ongoing ramp
reference value
              s_cc_state <= cc_state_4;
            when cc_state_4 =>
              if((s_I_reference - I_HYSTERESIS) > s_I_coil)then      --comparing ongoing current
reference with the actual current reading multiplied by the correction constant
                Coil_pwm  <= '1';                          --Switch-on PWM mosfet
              elsif((s_I_reference + I_HYSTERESIS) < s_I_coil)then    --comparing ongoing current
reference with the actual current reading multiplied by the correction constant
                Coil_pwm  <= '0';                          --Switch-off PWM mosfet
              end if;
              s_cc_state <= cc_state_1;
            when others => null;
          end case;
        end if;
      end if;
    end if;
end process current_controller;
end Behavioral;
```

```
----------------------------------------------------------------------------------
-- Company:  Danfoss
-- Engineer: Andriy Tkachuk
--
-- Create Date: __/__/2021
-- Design Name:
-- Module Name: Coil_Current_Control - Behavioral
-- Project Name: Next Generation Valve Actuation for Digital Displacement Machines
-- Target Devices: Arty A7 + NGCD evaluation board_01A
-- Tool Versions:
-- Description: Coil current profile control based on hysteresis closed-loop current control
--                      power-law gradient reference generation
-- Dependencies:
--
-- Revision:
-- Revision 0.01 - File Created
-- Additional Comments: VHDL
--
----------------------------------------------------------------------------------


library ieee;
use ieee.std_logic_1164.all;
use ieee.numeric_std.all;


entity Coil_Current_Control is
   Generic (
      g_T_rammp         : integer := 2_500; --in us
      g_T_plateau       : integer := 2_500; --in us
      g_T_hold          : integer := 0_000; --in us
      g_T_decay         : integer := 1_000_000; --in us
      g_I_rammp         : integer := 6_000; --in uA
      g_I_plateau       : integer := 6_000; --in uA
      g_I_hold          : integer := 4_000; --in uA
      g_hysteresis      : integer := 250;   --in uA
      g_adc_bits        : integer := 12;       --used bits of ADC
      g_cs_const        : integer := 23_571;    --Scaling constant of the CSA in mA
      g_ce_clk          : integer := 5_000_000  --clock frequency for current control timing in Hz

      );

   Port(
      Clk             : in std_logic;              -- system clock
      Current_control_ce : in std_logic;              --new clock, used to run controller proces and pwm
generation process
      Adc_ready       : in std_logic;
      Reset           : in std_logic;
      Valve_select      : in std_logic;
      Turn_on_command    : in std_logic;
```

```
    Fault           : in std_logic;
    Adc_data        : in std_logic_vector;
    Coil_pwm        : out std_logic;
    Coil_select     : out std_logic;
    Mux             : out std_logic;
    Led             : out std_logic
    --Start_reopening_detection : out std_logic        --turns on for one clock cycle
    );

end Coil_Current_Control;

architecture Behavioral of Coil_Current_Control is
constant MULTIPLIER_SCALING_CONSTANT : integer := 2**11;                          --scaling
constant for ramp multiplier value
constant CURRENT_SCALING_CONSTANT : integer := 2**g_adc_bits*1000/g_cs_const;             --
scaling constant for current value (174 codes / A)
constant TIME_SCALING_CONSTANT  : integer := g_ce_clk/1_000_000;
constant T_RAMP             : integer := g_T_rammp*TIME_SCALING_CONSTANT;             --in clock
cycles
constant T_PLATEAU          : integer := g_T_plateau*TIME_SCALING_CONSTANT;           --in
clock cycles
constant T_HOLD             : integer := g_T_hold*TIME_SCALING_CONSTANT;              --in clock
cycles
constant T_DECAY            : integer := g_T_decay*TIME_SCALING_CONSTANT;             --in clock
cycles
constant I_PLATEAU          : integer := g_I_plateau*CURRENT_SCALING_CONSTANT/1000;   --in
codes, current reference for plat stage
constant I_HOLD             : integer := g_I_hold*CURRENT_SCALING_CONSTANT/1000;      --in
codes, current reference fro hold stage
constant I_HYSTERESIS       : integer := g_hysteresis*CURRENT_SCALING_CONSTANT/1000;   -
-in codes
signal s_I_reference        : integer;                          --ongoing current reference
signal s_I_coil             : integer;
signal s_tc_counter         : integer;                          --counter used to switch on stages of the
current profile
signal s_switch_on_flag     : std_logic  := '0';                --
signal s_switch_off_flag    : std_logic  := '0';                --HIGH when valve switch on cycle is
over
signal s_start_flag         : std_logic  := '0';
signal s_sync_start         : std_logic  := '0';
type tc_state is (start_tc, ramp_stage, plateau_stage, hold_stage, decay_stage);
signal s_tc_state           : tc_state;
type cc_state is (cc_state_1, cc_state_2, cc_state_2_1, cc_state_3, cc_state_4);
signal s_cc_state           : cc_state;
signal s_adc_data           : std_logic_vector (23 downto 0):= (others => '0');
signal s_I_hysteresis       : integer := 0;
signal s_counter_value      : integer := 0;

signal s_controller_mode    : std_logic  := '0';
signal s_reset_counter      : integer := 0; -- in clock cycles
```

```
constant I_RAMP_MULTIPLIER_0     : integer := 1_840;  --
(CURRENT_SCALING_CONSTANT*g_I_rammp) * MULTIPLIER_SCALING_CONSTANT
/((g_T_rammp*TIME_SCALING_CONSTANT)**(3/4)) for 10kHz is 1_094; for 5kHz is 1_840
constant I_RAMP_MULTIPLIER_1     : integer := 20_367; --
(CURRENT_SCALING_CONSTANT*g_I_rammp) * MULTIPLIER_SCALING_CONSTANT
/((g_T_rammp*TIME_SCALING_CONSTANT)**(1/2)) for 10kHz is 14_401; for 5kHz is 20_367

begin

--the process to turn on or turn off the curretn controller *
switch_controller: process (CLK)
begin
   if(CLK'event and CLK = '1')then
      if(Reset = '1')then
         s_switch_on_flag  <= '0';                          --resets s_switch_on_flag when global reset is
HIGH

         if(s_reset_counter  = 1_000_000)then
            s_controller_mode <= not s_controller_mode;
            s_reset_counter <= 0;
         else
            s_reset_counter <= s_reset_counter +1;
         end if;

      else
         if(Fault = '0')then
            if((Turn_on_command = '1' OR Valve_select = '1') AND s_switch_on_flag  = '0')then   --when
Turn_on_comand and Valve_select are HIGH sets HIGH the s_switch_on_flag
               s_switch_on_flag  <= '1';
            elsif(s_switch_off_flag = '1')then
               s_switch_on_flag  <= '0';                    --resets s_switch_on_flag when
s_switch_off_flag is HIGH
            end if;
         else
            s_switch_on_flag  <= '0';
         end if;
      end if;
   end if;
end process switch_controller;

--the process to control the timing of the current control according to the custom current profile
timing_controller: process (CLK)
begin
if(CLK'event and CLK = '1') then
   if(s_switch_on_flag = '0')then                          --resets the controller process variables to the
initial values
      s_tc_counter       <=  0;
      s_switch_off_flag   <= '0';
      s_start_flag       <= '0';
      s_tc_state         <= start_tc;
```

```
   elsif(Current_control_ce = '1') then
      s_tc_counter  <= s_tc_counter  + 1;                    --incrementing the switch_on counter
      case s_tc_state is
         when start_tc =>
            s_start_flag <= '1';                          --initiating Current Control
            s_tc_state <= ramp_stage;
         when ramp_stage =>                               --initiating the ramp stage of the current profile
            if(s_tc_counter = T_ramp) then
               s_tc_counter  <= 0;
               s_tc_state <= plateau_stage;
            end if;
         when plateau_stage =>                            --initiating the plateau stage of the current profile
            if(s_tc_counter = T_PLATEAU) then
               s_tc_counter  <= 0;
               s_tc_state <= hold_stage;
            end if;
         when hold_stage =>                               --initiating the hold stage of the current profile
            if(s_tc_counter = T_HOLD) then
               s_tc_counter  <= 0;
               s_tc_state <= decay_stage;
            end if;
         when decay_stage =>                              --initiating the hold stage of the current profile
            if(s_tc_counter = T_DECAY) then
               s_switch_off_flag <= '1';
            end if;
         when others => null;
      end case;
   end if;
end if;
end process timing_controller;

--the process to control solenoid valve current according to the custom current profile
current_controller: process (CLK)

--variables for sqr
variable a : unsigned(31 downto 0):=(others => '0');  --original input.
variable q : unsigned(15 downto 0):=(others => '0');  --result.
variable left,right,r : unsigned(17 downto 0):=(others => '0');  --input to adder/sub.r-remainder.
variable i : integer range 0 to 16 :=0;
variable q_int : integer range 0 to 65_535;

begin
if(CLK'event and CLK = '1') then
   if(s_start_flag = '0')then                              --resets the current_controller process variables
to the initial values
      Coil_pwm     <= '0';
      Coil_select   <= '1';
      Mux          <= '0';
      Led          <= '0';
      s_sync_start  <= '0';
```

```
      s_cc_state    <= cc_state_1;
      s_adc_data    <= (others => '0');
   else
      if(s_sync_start = '0')then
         Coil_select   <= '0';                              --Switch-on flywheel mosfet
         Coil_pwm      <= '1';                               --Switch-on PWM mosfet
         Mux           <= '0';
         Led           <= '1';
         s_sync_start  <= '1';
       else
          case s_cc_state is
            when cc_state_1 =>
               if(Adc_ready = '1')then                          --synchronising PWM with ADC sampling
frequency
                  case s_tc_state is
                     when ramp_stage =>
                        s_adc_data (g_adc_bits-1 downto 0) <= Adc_data;       --assigning the ongoing
current reference value for ramp stage
                        s_I_coil <= to_integer(shift_left(unsigned(s_adc_data), 11));   --multiplying the coil
current measured value by a scaling constant
                        s_counter_value <= s_tc_counter;
                        a    := to_unsigned((s_counter_value), a'length);
                        q    :=(others => '0');
                        left  :=(others => '0');
                        right :=(others => '0');
                        r    :=(others => '0');
                        if(s_controller_mode = '0')then
                           s_cc_state <= cc_state_2;
                        else
                           s_cc_state <= cc_state_2_1;
                        end if;
                     when plateau_stage =>
                        s_I_reference  <= I_PLATEAU;                  --assigning the ongoing current
reference value for plateau stage
                        s_I_coil <= to_integer(unsigned(Adc_data));
                        s_I_hysteresis <= I_HYSTERESIS;
                        s_cc_state <= cc_state_4;
                     when hold_stage =>
                        s_I_reference  <= I_HOLD;                     --assigning the ongoing current
reference value for hold stage
                        s_I_coil <= to_integer(unsigned(Adc_data));
                        s_I_hysteresis <= I_HYSTERESIS;
                        s_cc_state <= cc_state_4;
                     when decay_stage =>
                        Coil_pwm      <= '0';
                        Coil_select   <= '1';
                        Mux           <= '1';
                        Led           <= '0';
                     when others => null;
                  end case;
```

```
    end if;
when cc_state_2 =>
    if(i < 16)then
        i := i + 1;
        right(0):='1';
        right(1):=r(17);
        right(17 downto 2):=q;
        left(1 downto 0):=a(31 downto 30);
        left(17 downto 2):=r(15 downto 0);
        a(31 downto 2):=a(29 downto 0);    --shifting by 2 bit
        if ( r(17) = '1') then
            r := left + right;
        else
            r := left - right;
        end if;
        q(15 downto 1) := q(14 downto 0);
        q(0) := not r(17);
    else
        q_int := to_integer(q);
        a     := to_unsigned((q_int * s_counter_value), a'length);
        q     :=(others => '0');
        left  :=(others => '0');
        right :=(others => '0');
        r     :=(others => '0');
        i     := 0;
        s_cc_state <= cc_state_2_1;
    end if;
when cc_state_2_1 =>
    if(i < 16)then
        i := i + 1;
        right(0):='1';
        right(1):=r(17);
        right(17 downto 2):=q;
        left(1 downto 0):=a(31 downto 30);
        left(17 downto 2):=r(15 downto 0);
        a(31 downto 2):=a(29 downto 0);    --shifting by 2 bit
        if ( r(17) = '1') then
            r := left + right;
        else
            r := left - right;
        end if;
        q(15 downto 1) := q(14 downto 0);
        q(0) := not r(17);
    else
        i := 0;
        s_I_hysteresis <= I_HYSTERESIS * MULTIPLIER_SCALING_CONSTANT;
        s_cc_state <= cc_state_3;
    end if;
when cc_state_3 =>
```

```
            if(s_controller_mode = '0')then
               s_I_reference  <= I_RAMP_MULTIPLIER_0 * to_integer(q);  --assigning the ongoing
current reference value for ramp stage
             else
               s_I_reference  <= I_RAMP_MULTIPLIER_1 * to_integer(q);  --assigning the ongoing
current reference value for ramp stage
             end if;
               s_cc_state <= cc_state_4;
            when cc_state_4 =>
               if(s_I_reference - s_I_hysteresis > s_I_coil)then          --comparing ongoing current
reference with the actual current reading multiplied by the correction constant
                  Coil_pwm  <= '1';                              --Switch-on PWM mosfet
               elsif(s_I_reference + s_I_hysteresis < s_I_coil)then       --comparing ongoing current
reference with the actual current reading multiplied by the correction constant
                  Coil_pwm  <= '0';                              --Switch-off PWM mosfet
               end if;
               s_cc_state <= cc_state_1;
            when others => null;
         end case;
      end if;
   end if;
end if;
end process current_controller;

end Behavioral;
```

```
----------------------------------------------------------------------------------
-- Company: Danfoss
-- Engineer: Andriy Tkachuk
--
-- Create Date:  __/__/2021
-- Design Name:
-- Module Name: Coil_driver_fault_detection - Behavioral
-- Project Name: Next Generation Valve Actuation for Digital Displacement Machines
-- Target Devices: Arty A7 + NGCD evaluation board_01A
-- Tool Versions:
-- Description: Low- side overcurrent protection (OCP) based on nFault state detection.
--
-- Dependencies:
--
-- Revision:
-- Revision 0.01 - File Created
-- Additional Comments: VHDL
--
----------------------------------------------------------------------------------

library ieee;
use ieee.std_logic_1164.all;
use ieee.numeric_std.all;


entity Coil_driver_fault_detection is
   Generic (
      g_sys_clk        : integer := 100_000_000;       --system clock frequency in Hz
      g_fault_blank_time : integer := 2;               --in us
      g_drv_wake_time    : integer := 2_000            --in us
   );

   Port (
      Reset            : in std_logic;
      CLK              : in std_logic;           --system clock
      Nfault_low_side     : in std_logic;
      Nfault_drv        : in std_logic;
      Enable_drv        : out std_logic;
      Faulty_drv        : out std_logic;
      Led_start_fault_detection : out std_logic
   );
end Coil_driver_fault_detection;

architecture Behavioral of Coil_driver_fault_detection is
constant TIME_SCALING_CONSTANT   : integer := g_sys_clk / 1_000_000;
constant FAULT_BLANK_TIME       : integer := TIME_SCALING_CONSTANT * g_fault_blank_time;
constant DRV_WAKE_TIME          : integer := TIME_SCALING_CONSTANT * g_drv_wake_time;
signal s_blank_time_counter     : integer := 0;
signal s_start_detection_counter : integer := 0;
```

```
signal s_start_detection        : std_logic := '0';

begin
fault_detection: process (CLK)
variable i : integer range 0 to 8 := 4;
begin
if(CLK'event and CLK = '1')then
   if(Reset = '1')then
      Enable_drv  <= '0';
      Faulty_drv  <= '0';
      s_start_detection    <= '0';
      s_blank_time_counter <= 0;
      s_start_detection_counter <= 0;
      Led_start_fault_detection <= '0';
   else
      if(s_start_detection ='0')then
         Enable_drv  <= '1';
         if(s_start_detection_counter > DRV_WAKE_TIME - 1)then
            s_start_detection         <= '1';
            Led_start_fault_detection  <= '1';
         else
         s_start_detection_counter <= s_start_detection_counter + 1;
         end if;
      else
         if(Nfault_drv = '1' AND Nfault_low_side = '1')then
            s_blank_time_counter <= 0;
         else
            if(s_blank_time_counter > FAULT_BLANK_TIME - 1)then
               Enable_drv  <= '0';
               Faulty_drv  <= '1';
               Led_start_fault_detection <= '0';
            else
               s_blank_time_counter <= s_blank_time_counter + 1;
            end if;
         end if;
      end if;
   end if;
end if;
end process fault_detection;

end Behavioral;
```

```
----------------------------------------------------------------------------------
-- Company: Danfoss
-- Engineer: Andriy Tkachuk
--
-- Create Date: --/--/2021
-- Design Name:
-- Module Name: Valve_Reopening_Detection - Behavioral
-- Project Name: -- Project Name: Next Generation Valve Actuation for Digital Displacement Machines
-- Target Devices: Arty A7 + NGCD evaluation board_01A
-- Tool Versions:
-- Description:
--
-- Dependencies:
--
-- Revision:
-- Revision 0.01 - File Created
-- Additional Comments: VHDL
--
----------------------------------------------------------------------------------


library ieee;
use ieee.std_logic_1164.all;
use ieee.numeric_std.all;


entity Valve_Reopening_Detection is
   Generic (
      g_adc_bits              : integer := 12;                --used bits of ADC
      g_start_threshold       : integer := 3000;                --in mV
      g_signal_deviation      : integer := 30;                --in mV
      g_filter_constant       : integer := 1                  --filter time constant coefficient (0 - deactivates filtering)
      );

            Port(
                  Reset             : in std_logic;
                  CLK               : in std_logic;                         --system clock
                  Adc_ready         : in std_logic;                         --if '1' ADC value is ready
                  Start_detection   : in std_logic;                         --turns '1' for valve reopening detection
      Adc_data          : in std_logic_vector(g_adc_bits-1 downto 0); --analogue input data measured coil voltage
                  Reopened          : out std_logic                         --active high
                  );
end Valve_Reopening_Detection;

architecture Behavioral of Valve_Reopening_Detection is
```

```
constant START_THRESHOLD       : integer := 2**g_adc_bits*g_start_threshold/3300;
constant SIGNAL_DEVIATION      : integer := 2**g_adc_bits*g_signal_deviation/3300;
signal s_filtered_signal       : integer range 0 to 2**g_adc_bits := 0;
signal s_filtered_signal_prev   : integer range 0 to 2**g_adc_bits := 0;
signal s_min                   : integer range 0 to 2**g_adc_bits := 0;
signal s_max                    : integer range 0 to 2**g_adc_bits := 0;
signal s_start                 : std_logic_vector (1 downto 0):= (others => '0');

begin

Reopening_detection: process (CLK)
variable v_signed_temp : signed (g_adc_bits+2 downto 0);
begin
   if(CLK'event and CLK = '1')then
      if(Reset = '1' OR Start_detection = '0')then
         s_filtered_signal <= 0;
         s_filtered_signal_prev <= 0;
         s_min <= 0;
         s_max <= 0;
         s_start <= "00";
         Reopened <= '0';
      else
         if(Adc_ready = '1')then
            --first order low pass filter
            v_signed_temp := to_signed((to_integer(unsigned(Adc_data)) - s_filtered_signal_prev),
v_signed_temp'length);
            s_filtered_signal <= s_filtered_signal_prev + to_integer(shift_right(v_signed_temp,
g_filter_constant));
            s_filtered_signal_prev <= s_filtered_signal;
            --end first order low pass filter
            case s_start is
               when "00" =>
                  if(s_filtered_signal > START_THRESHOLD)then    --meeting starting condition 1
                     s_start <= "01";
                  end if;
               when "01" =>
                  if(s_filtered_signal < START_THRESHOLD)then    --meeting starting condition 2
                     s_min <= START_THRESHOLD;
                     s_start <= "10";
                  end if;
               when "10" =>
                  if(s_filtered_signal < s_min)then            --looking for minimum
                  s_min <= s_filtered_signal;
                  elsif(((s_filtered_signal - SIGNAL_DEVIATION) > s_min ) AND (s_filtered_signal >
s_max))then  --looking for maximum
                     s_max <= s_filtered_signal;
                  elsif((s_filtered_signal + SIGNAL_DEVIATION) < s_max )then  --looking for reopening
                     Reopened <= '1';                    --set reopening flag
                     s_start <= "11";
                  end if;
```

```
                when "11" =>
                    Reopened <= '0';                    --reset reopening flag
                when others => null;
            end case;
        end if;
    end if;
  end if;
end process Reopening_detection;
end Behavioral;
```

```
-- Company: Danfoss
-- Engineer: Andriy Tkachuk
--
-- Create Date: --/--/2021
--
-- This file is an .xdc for the Arty A7 board + NGCD evaluation board_01A
-- To use it in a project: Next Generation Valve Actuation for Digital Displacement Machines
--
----------------------------------------------------------------------------------

## Clock signal
set_property -dict { PACKAGE_PIN E3    IOSTANDARD LVCMOS33 } [get_ports { CLK }];
create_clock -add -name sys_clk_pin -period 10.00 -waveform {0 5} [get_ports {CLK}];

## Switches
set_property -dict { PACKAGE_PIN A8    IOSTANDARD LVCMOS33 } [get_ports { Valve_select[0] }];
set_property -dict { PACKAGE_PIN C11   IOSTANDARD LVCMOS33 } [get_ports { Valve_select[1] }];
set_property -dict { PACKAGE_PIN C10   IOSTANDARD LVCMOS33 } [get_ports { Valve_select[2] }];
set_property -dict { PACKAGE_PIN A10   IOSTANDARD LVCMOS33 } [get_ports {
Turn_on_command }];

## LEDs
set_property -dict { PACKAGE_PIN H5    IOSTANDARD LVCMOS33 } [get_ports { Led[0] }];
set_property -dict { PACKAGE_PIN J5    IOSTANDARD LVCMOS33 } [get_ports { Led[1] }];
set_property -dict { PACKAGE_PIN T9    IOSTANDARD LVCMOS33 } [get_ports { Led[2] }];
set_property -dict { PACKAGE_PIN T10   IOSTANDARD LVCMOS33 } [get_ports {
Led_start_fault_detection }];

## Buttons
set_property -dict { PACKAGE_PIN D9    IOSTANDARD LVCMOS33 } [get_ports { Reset }];

## ChipKit Outer Digital Header
set_property -dict { PACKAGE_PIN V15   IOSTANDARD LVCMOS33 } [get_ports { Nfault_low_side
}];
set_property -dict { PACKAGE_PIN P14   IOSTANDARD LVCMOS33 } [get_ports {
Valve_reopening[0] }];
set_property -dict { PACKAGE_PIN T11   IOSTANDARD LVCMOS33 } [get_ports {
Valve_reopening[1]  }];
set_property -dict { PACKAGE_PIN R12   IOSTANDARD LVCMOS33 } [get_ports {
Valve_reopening[2]  }];

## ChipKit Inner Digital Header
set_property -dict { PACKAGE_PIN U11   IOSTANDARD LVCMOS33 } [get_ports { Nfault_drv }];
set_property -dict { PACKAGE_PIN V16   IOSTANDARD LVCMOS33 } [get_ports { Enable_drv }];
set_property -dict { PACKAGE_PIN M13   IOSTANDARD LVCMOS33 } [get_ports { Coil_pwm[0] }];
set_property -dict { PACKAGE_PIN R10   IOSTANDARD LVCMOS33 } [get_ports { Coil_pwm[1] }];
set_property -dict { PACKAGE_PIN R11   IOSTANDARD LVCMOS33 } [get_ports { Coil_pwm[2] }];
set_property -dict { PACKAGE_PIN R13   IOSTANDARD LVCMOS33 } [get_ports { Coil_select[0] }];
set_property -dict { PACKAGE_PIN R15   IOSTANDARD LVCMOS33 } [get_ports { Coil_select[1] }];
```

```
set_property -dict { PACKAGE_PIN P15   IOSTANDARD LVCMOS33 } [get_ports { Coil_select[2] }];
set_property -dict { PACKAGE_PIN R16   IOSTANDARD LVCMOS33 } [get_ports { Mux[2] }];
set_property -dict { PACKAGE_PIN N16   IOSTANDARD LVCMOS33 } [get_ports { Mux[1] }];
set_property -dict { PACKAGE_PIN N14   IOSTANDARD LVCMOS33 } [get_ports { Mux[0] }];


## ChipKit Outer Analog Header - as Single-Ended Analog Inputs
set_property -dict { PACKAGE_PIN A1    IOSTANDARD LVCMOS33 } [get_ports { vaux7_n }];
set_property -dict { PACKAGE_PIN B1    IOSTANDARD LVCMOS33 } [get_ports { vaux7_p }];
set_property -dict { PACKAGE_PIN B2    IOSTANDARD LVCMOS33 } [get_ports { vaux15_n }];
set_property -dict { PACKAGE_PIN B3    IOSTANDARD LVCMOS33 } [get_ports { vaux15_p }];
set_property -dict { PACKAGE_PIN C14   IOSTANDARD LVCMOS33 } [get_ports { vaux0_n }];
set_property -dict { PACKAGE_PIN D14   IOSTANDARD LVCMOS33 } [get_ports { vaux0_p }];
```